Controlled generation of unidirectional irregular sea states in experimental and numerical wave tanks

Maxime Canard

COLLEGE SCIENCES
DOCTORAL DE L'INGENIERIE
PAYS DE LA LOIRE ET DES SYSTEMES

CENTRALE NANTES

MÉMOIRE DE DOCTORAT DE

L'ÉCOLE CENTRALE DE NANTES

ÉCOLE DOCTORALE N° 602
Sciences de l'Ingénierie et des Systèmes
Spécialité : *Mécanique des Milieux Fluides*

Par
Maxime CANARD

Controlled generation of unidirectional irregular sea states in experimental and numerical wave tanks

Projet de recherche doctoral présenté et soutenu à Nantes, le 17 janvier 2024
Unité de recherche : UMR 6598, Laboratoire de Recherche en Hydrodynamique, Energétique et Environnement Atmosphérique (LHEEA)

Rapporteurs avant soutenance :

Miguel ONORATO	Full Professor, Universita di Torino (Italie)
Jaak MONBALIU	Full Professor, KU Leuven (Belgique)

Composition du Jury :

Présidente :	Anne-Claire BENNIS	Professeure des Universités, Université Caen-Normandie (France)
Examinateurs :	Miguel ONORATO	Full Professor, Universita di Torino (Italie)
	Jaak MONBALIU	Full Professor, KU Leuven (Belgique)
	Ioannis KARMPADAKIS	Assistant Professor, Imperial College London (Royaume-Uni)
	Jang Whan KIM	Senior Scientist, Front Energies (États-Unis)
	Sébastien FOUQUES	Senior Scientist, SINTEF Ocean (Norvège)
Dir. de recherches doctorales :	Guillaume DUCROZET	Professeur des Universités, École Centrale de Nantes (France)
Co-enc. de recherches doctorales :	Benjamin BOUSCASSE	Chargé de recherche, École Centrale de Nantes (France)

ACKNOWLEDGEMENT

Comment tous vous remercier ? De nombreuses personnes ont partagé ma route le long de ces 3 ans et demi de thèse, et je m'excuse par avance si je ne mentionne pas tout le monde.

Avant toute chose, je tiens à remercier mon directeur de thèse, Guillaume, sans qui rien n'aurait été possible. Passionné, rigoureux, présent, impliqué, et pédagogue il a su guider mes recherches et n'a pas hésité à mettre la main à la patte dés qu'il le fallait. Mes pensées vont ensuite à Benjamin, co-encadrant de cette thèse, que je remercie pour son point de vue plus industriel, son foisonnement d'idée, sa curiosité, ses injonctions à "envoyer du lourd", sa bonne humeur et ses conseils de vie.

Viennent ensuite bien évidemment mes amis Gaspard et Théo, camarades de thèse depuis le début, compagnons de travail, de galère, de dépression, d'euphorie et de vie nocturne. Gaspard, un grand merci pour ces 3 ans de collocation en D228, haut lieu de génie scientifique (et d'interprétation musicale). Parmi les autres doctorants et postdoctorant (nombreux!), je citerai ceux du début, Shinwoong (gomawo for the joie de vivre, maegjuleul masija in Hamburg), Rudy, Seung-Yoon (gomawo for the crous), Youngjun, Sithik, Tommaso, *Moran* (italique amplement mérité), Louis (dépanneur sans pareil bash et C++), et de la fin, Matthieu (ne lui laissez jamais la clé de votre bureau, il n'en part pas), Claire, Fabio, Solène, Giacomo.

Je tiens aussi à remercier les divers acteurs du laboratoire, enseignants chercheurs, techniciens et ingénieurs de recherche qui m'ont aidé sans hésitation lorsque j'en avais besoin (Félicien, Jérémy, Lionel, Pierre, Sonia, Florent, Sylvain). Un merci tout particulier à Anne pour nos heures à démêler des câbles dans le bassin de traction. Et des pensées aux collègues de footing, Sylvain, Benjamin (co-marathonien), Jérémy, Yzan.

Un dernier merci à tous ceux qui ont partagé ma vie en dehors des murs du laboratoire, Raphaëlle (évidemment en premier), Professeur Daroux (merci pour tes avis d'expert en physique) , Maxime, Lucie (vice major d'océan), Guigui, Roman, Grégoire, Thomas, Antoine, Emmanuelle, Diego, Rozenn, les archis, la mifa (merci Olivier pour la formation beamer), et j'en passe évidemment pleins que je n'oublie pas pour autant. Enfin, car comme le dit ma grand mère , "on porte en nous 7 générations d'aïeux", je tiens à remercier ma famille, mon frère, mes parents et tout particulièrement ma mère qui m'a transmis sa curiosité, son goût pour la réflexion et la conscience du travail bien fait.

TABLE OF CONTENTS

LIST OF SYMBOLS

Symbol	Description	Unit
$\overline{X(t)}$	Temporal mean of a signal $X(t)$	-
$\hat{X(t)}$	Hilbert transform of a signal $X(t)$	-
$\lfloor X \rfloor$	Integer part of a scalar X	-
X^*	complex conjugate of a scalar X	-
X^{conv}	Statistically converged value of X estimate	-
A	Wave amplitude	m
A_{input}	Input amplitude	m
A_{design}, A_{target}	Design/target amplitude	m
BFI	Benjamain Feir Index	-
B_x	Barthemely ratio	-
C	Maximum relative error tolerated for the measured spectrum	-
C_R	Non-dimensional wave gauge correction factor estimated from a repeatability dataset	-
C_x^{crest}	Crest speed	ms^{-1}
c_g	Group velocity	ms^{-1}
c_ϕ	Phase velocity	ms^{-1}
d	Water depth	m
d_{hinge}	Depth of the hinge of the wave maker (from bottom)	m
$E(X)$	Expected value of a random variable X	-
$E\{\}$	Average operator over several time windows	-
$E_S(f)$	Spectrum relative error from a target shape at frequency f	-
$E_{S,\text{conv}}^{\text{mean}}$	Relative difference from the statistically-converged spectrum estimate, averaged across the frequency range $f \in [\frac{3}{4}f_p, \frac{3}{2}f_p]$	-
$E_{\text{Welch}}(f)$	Relative Welch 95% confidence intervals amplitude at frequency f	-
f	Frequency	s^{-1}

f_0	Carrier frequency of a wave train	Hz
$f_{\max}$	Maximum frequency contained in a given signal	Hz
$f_{\max}^{\text{wvmk}}$	Largest frequency that the wave maker can generate	Hz
$f_{\max}^{\text{input}}$	Largest frequency contained in the wave maker inputs	Hz
f_{sample}	Sampling frequency	s^{-1}
f_η	Probability density function of the free surface elevation	-
$\mathscr{F}_X$	Fourier transform of the signal $X(t)$	-
$\mathscr{F}_X^d$	Discrete Fourier transform of the discrete signal $X(t_n)$	-
g	Gravity acceleration	m.s^{-2}
GF	Groupiness factor computed from the envelope	-
GF_{SIWEH}	Groupiness factor computed from the instantaneous wave energy	-
G_{WG}	Corrected wave gauge calibration factor	mV^{-1}
G_{WG}^B	Wave gauge calibration factor obtained from the calibration bench	mV^{-1}
H	Wave height of a given zero-crossing wave	m
H_c	Crest height of a given zero-crossing wave	m
H_s	Significant wave height	m
$I_S(t)$	Instantaneous wave energy	m^2
k	Norm of the wavenumber vector	m^{-1}
k_p	Peak wavenumber	m^{-1}
k_1	Mean wavenumber	m^{-1}
$k_{\max}^{\text{HOS}}$	Maximum x-axis wavenumber solved in a 1D `HOS-NWT` simulation	m^{-1}
k^{interact}, f^{interact}	wavenumber/frequency of a wave field component involved in a nonlinear interaction	m^{-1}, Hz
L_{dissip}	Dissipation length	m
L_x	Length of the tank	m
L_y	Width of the tank	m
M	Nonlinarity order of an `HOS-NWT` simulation	-
m_n	n^{th} Spectrum moment	m^2s^{-n}
n_{harmo}	harmonic number	-
N	Number of point of a given discrete signal	-
N_{harmo}	Number of harmonics in a wave maker input signal	-
N_{run}	Number of realizations	-

$N_{\text{run}_{\text{iter}}}$	Number of realizations per corrective iteration	-
N_x, N_z	Number of points in a `HOS-NWT` mesh in the x and z directions (spatial discretzation)	-
N_{paddle}	Number of wave maker paddle	-
O_{Welch}	Overlap ratio of the Welch windows	-
P_{design}	Probability of design	-
POE	Probability Of Exceedance	-
$r(X_1, X_2)$	Pearson correlation coefficient of $X_1(t)$ and $X_2(t)$ signals	-
S	Wave spectrum	$\text{m}^2.\text{s}$
S_{input}	Input spectrum	$\text{m}^2.\text{s}$
S_{design}, S_{target}	Design/target spectrum	$\text{m}^2.\text{s}$
S_{xxx}	Bispectrum	m^3s^2
S_{xxxx}	Trispectrum	m^4s^3
S_{xxxx}^{BFI}	Trispectrum slice focusing on the Benjamin Feir Four waves interactions	m^4s^3
t	Time	s
t_{beg} ; t_{end}	Beginning and end time of the analysis time window	s
T	Period of a given zero-crossing wave	s
T_p	Peak period	s
T_1	Mean period	s
T_2	mean zero-up-crossing period	s
T_{repeat}	Duration of the input signals for the wave maker	s
T_{analyzed}	Total duration of the analyzed series, including all the realizations	s
T_{Welch}	Size of the Welch windows (for spectrum smoothing)	s
T_{WVMK}	Time at which the wave maker stops	s
TF	Wave maker transfer function	-
U_x^{crest}	Water particle velocity at top of the crest	ms^{-1}
$U_{\text{Welch}}^{up}(f)$ / $U_{\text{Welch}}^{low}(f)$	95% confidence intervals of the spectral estimation based on the Welch method	
$U(X)$	Expanded uncertainty of a quantity X	-
$u_A(X)$	Type A uncertainty of a quantity X	-
$u_B(X)$	Type B uncertainty of a quantity X	-
$u_s(X)$	Standard uncertainty of a quantity X	-
$u_s^{\text{meas}}(X)$	Measurement Type B uncertainty of a quantity X	-

$u_s^{\text{samp}}(X)$	Sampling variability uncertainty of a quantity X	-
V	Tension	V
$var_t(X(t))$	Variance over time of a signal $X(t)$	-
$W(t)$	Wave maker motion time series	m
x	Distance from the wave maker	m
X_t	Target position	m
X_{target}	Quantity computed from the target spectrum (notation used when possibility of confusion)	-
X_{meas}	Quantity computed from the measured spectrum (notation used when possibility of confusion)	-
y	Lateral position	m
z	Vertical position	m
γ	Spectrum peak enhancement factor	-
δ_{BF}	Side-band size parameter of the Benjamin Feir instability quartet	Hz
δf	Frequency resolution	Hz
δf_{repeat}	Frequency resolution of the input wave maker signal	Hz
δt	Time step	s
δ_n	Dissipation length of the evanescent mode n	m
δ_x	misalignment of a y-axis line of measurement, between $y = 0$ and $y = L_y$	m
ΔT	Duration of the analyzed time window	s
Δ_f	Dimensional spectral width	s^{-1}
ε_p	Peak steepness	-
ε_1	Mean steepness	-
η	Free surface elevation	m
κ	Longitudinal wavenumber (x-axis)	m^{-1}
λ	Wavelength	m
λ_p	Peak wavelength	m
λ_3	Skewness of the free surface elevation	-
λ_4	Kurtosis of the free surface elevation	-
λ_{40}^d	Dynamic excess kurtosis	-
λ_{40}^b	Bound harmonics kurtosis	
μ	Transverse wavenumber (y-axis)	m^{-1}
ν	Kinematic water viscosity	m^2s^{-1}

ν_{eddy}	Eddy viscosity of the Tian breaking model	m^2s^{-1}
ν_w	Non-dimensional spectral width	-
ρ	Water density	kg.m^{-3}
ϕ	Phase	rad
ϕ_{input}	Input phase	rad
Φ	Velocity potential	m^2s^{-1}
Ψ	Wave envelope	m
σ_X	Standard deviation over time of a signal $X(t)$	-
ω	Angular frequency	rad.s^{-1}

INTRODUCTION

The ocean plays a crucial role in our society. It is extensively exploited for its natural resources, such as wind, oil, gas, and fish. It is also widely used for transportation. Since 2015, more than 10 million tons are loaded each year. This represents 90% of global trade (Unctad, 2022). To support these significant activities, the ocean engineering community has faced the challenge of constructing reliable ships and offshore installations, such as offshore oil platforms and offshore wind farms. More recently, in the context of climate change and global warming, the engineers face the tasks of decarbonizing offshore activities, increasing marine renewable energy capacity, and ensuring the security of marine operations while storms are more frequent and powerful (Konar and Ding, 2020).

The oceanic environment can be harsh and unsafe, with huge forces at play. Waves, currents, and winds can reach extreme levels, sometimes leading to accidents and damage. In this context, understanding the oceanic environment becomes necessary to ensure the safety and efficiency of human offshore activities. Among oceanic conditions, surface gravity waves hold significant importance. Swells, generated by wind and driven by gravity, crowd the ocean. Offshore wave heights can exceed 10 meters, with typical wavelengths ranging from 40 to 600 meters and periods spanning from 5 to 20 seconds. These waves consistently exert loads on ships and offshore structures.

The study of offshore structures' and ships' ability to withstand waves is a significant area of research. During the design phase, assessments are conducted through sea-keeping tests performed at model scale in wave basins or numerical simulations relying on Computational Fluid Dynamics (CFD). Note that here, CFD also refers to the numerical methods based on potential flow approximations. In these controlled experimental and numerical environments, the generated waves are designed to model the ocean sea states that the structure will encounter. Wave generation and qualification procedures have been developed by classification societies, Joint Industry projects (JIP), and international NGOs such as ITTC [1]. Their efficiency is directly linked to advancements in the scientific understanding of ocean wave physics. The severity of the waves is usually characterized by the ratio of amplitude to wavelength, denoted as steepness. Since the last century, the propagation of low-steepness waves has been well understood. However,

1. https://ittc.info/

large-steepness sea states involve complex mechanisms such as breaking and nonlinear wave interactions. Research in this field is still at a stage of development.

Within this framework, one of the main challenges for ocean engineering is to take account of extreme wave conditions. Current industrial procedures for assessing extreme responses are not accurate, and as a result classification society regulations use significant safety factors. The current Ph.D. thesis is founded on the necessity of incorporating the latest research advancements to standardize, control, and qualify the reproduction of extreme wave fields for the specific requirements of ocean engineering.

Overview of the research

The following paragraphs will explore the current state of the art, starting with ocean wave research and then focusing on the generation of wave fields in tanks or numerical simulations for ocean engineering applications. This overview does not claim to be exhaustive; its purpose is to present the context of the research conducted in this PhD thesis. Lastly, the scope and the objectives of the thesis will be defined.

Ocean waves propagation

Understanding the generation, propagation, and dissipation of ocean surface waves remains a challenging and intriguing line of research. Waves are generated by the wind stress over the water surface and grow through intricate resonance mechanisms. Their shape mainly depends on the wind fetch (contact distance in the direction of the wind) and water depth. As a result, the sea surface is crowded with waves of different frequencies and directions.

Their propagation is also known to be a complex phenomenon. They are dispersive, which means that their velocity is a function of their wavelength. And they are nonlinear, the frequency components of the wave fields interact with each other. The nature and intensity of the wave interactions are driven by the wave steepness, the relative water depth (ratio of depth to wavelength), and other elements such as the frequency and the directional bandwidths. The resulting sea states can be extreme and impressively large outlier events named "rogue waves" can occur (Onorato et al., 2013).

Lastly, the steepest waves break. The mechanisms behind wave breaking and the induced energy cascade among frequencies are extremely nonlinear and involve complex fluid mechanics notions such as turbulence or intermittency.

The following paragraphs will provide an overview of ocean wave research. The scope is limited to the description of ocean waves in deep and intermediate water depths. It will not address the effect of current, wind, and bathymetry variations on waves' propagation. See for instance Massel (1996) and Mei et al. (2005) books for a detailed description of ocean waves physics.

First theoretical works

The scientific interest in water waves rose in the 19^{th} century. Airy (1845) derived from the free surface boundary conditions a mathematical formulation for monochromatic linear water waves and established the dispersion relation

$$\omega^2 = gk\tanh(kd) \tag{1}$$

that led to the associated phase and group velocities:

$$c_\phi = \frac{\omega}{k} \tag{2}$$

$$c_g = \frac{\partial\omega}{\partial k} = \frac{\omega}{k}\frac{1}{2}\left(1+\frac{2kd}{\sinh(2kd)}\right) = \frac{c_\phi}{2}\left(1+\frac{2kd}{\sinh(2kd)}\right) \tag{3}$$

; with ω the angular frequency (in rad/s), k the wavenumber, g the gravity acceleration and d the water depth. This linear theory predicts a sinusoidal free surface elevation η and a circular trajectory of water particles below the disturbed interface.

$$\eta(x,t) = A\cos(\omega t - kx + \phi) \tag{4}$$

with A the amplitude, k the wavenumber, x the position, and ϕ the phase at $x = 0$. This Airy wave solution is valid for deep or intermediate water-depth waves of limited steepness (i. e. $kd \geq O(1)$ and $kA << O(1)$).

Additionally, using a perturbation series approach, Stokes (1847) derived a class of nonlinear solutions at different orders of nonlinearity. This work allows for the study of nonlinear features of wave propagation. Second-order terms lead to the development of bound waves, that do not obey the dispersion relation but affect the shape of η profile, making the troughs flatter and the crests sharper. They also induce a constant drift following the direction propagation, namely the Stokes drift. Furthermore, third-order terms modify the phase velocity, decreasing

the wavelength at a given frequency. More details about the origin of water waves theory can be found in Craik (2004) review. Rigorous analysis and derivations of the Stokes solutions from the Euler's equation (approximation of the Navier–Stokes equations neglecting the fluid viscosity) and the free surface boundary conditions can be found for example in Massel (1996) and Mei et al. (2005) books. The latter also provides solutions for shallow water waves, which are beyond the scope of the current thesis, which is limited to deep or intermediate water depth.

Description of ocean's wave fields through the wave spectrum

Airy and Stokes solutions are monochromatic, they model the propagation of a single-frequency wave and its harmonics. However, in the ocean, complex wave fields occur, composed of several frequencies and directions.

Since the 20^{th} century, to describe the sea state, the scientific community uses the variance spectrum of the free surface elevation (hereafter called wave spectrum). The wave fields are modeled as linear sums of frequency and direction components. Thanks to buoy observations and in-situ measurement campaigns, semi-empirical wave spectrum shapes were derived. The most known and used are the Bretschneider and the JONSWAP spectra (Bretschneider, 1959; Hasselmann et al., 1973). Their analytical formula takes as parameters the significant wave height H_s (which is equal to the standard deviation of the free surface elevation times four) and the peak period T_p (period of the most energetic component of the wave field).

Long-term statistics

In a specific ocean region, a wave spectrum is stable for 30 minutes to 1 hour. Consequently, thousands of sea states occur throughout the year. To study the occurrence of the sea states at a given geographical location, (H_s, T_p) scatter diagrams can be created. They provide the joint probability of given (H_s, T_p) pairs. Usually, this probability is represented by the return period, i. e. the average period separating two occurrences of given (H_s, T_p) pairs. The scatter diagrams are built from several-year datasets, including return periods larger than 100 years. Such information corresponds to what is called "long-term statistics".

Long-term statistics are essential for the design of offshore structures or ships. They determine the wave conditions that they should be able to withstand (see Bureau Veritas (2019) guidelines). This statistical information can be obtained with in-situ measurement databases (see for example Christou and Ewans (2014); Karmpadakis et al. (2020) for analyses of such database), or numerical hindcast data. Numerical hindcasts and forecasts at a given time and

geographical location are provided by large time-scale meteo-ocean solvers, which propagate the frequency/direction wave spectra over ocean-size domains. See for instance the meteo-ocean solver Wavewatch 3 (Tolman et al., 2009) and the European database ERA5 [2].

Wave propagation within a short time and space scale

The core of the present thesis and a flourishing line of research is the propagation of waves within the duration of a single specified sea state (30 minutes to 1 hour) over a domain whose size reaches maximum tens of wavelengths.

Using a linear approximation, the wave spectrum models the irregular (i.e. polychromatic) wave field as a linear sum of regular (i.e. monochromatic) Airy waves with random phases. However, the wave field components interact with each other. In steep conditions, the linear approximation is not sufficient to capture the evolution of the stochastic quantities of interest (wave-by-wave statistics, wave spectrum). See for instance Onorato et al. (2006); Fedele et al. (2010). The nonlinear interactions lead to several specific phenomena such as bound waves or modulational instabilities, namely Benjamin Feir instabilities (3^{rd} order near-resonant interaction of a disturbed wave train leading to extreme crests heights (Benjamin and Feir, 1967)).

Several theoretical frameworks have been developed to study the nonlinearities. Among them, the most popular is the nonlinear Schrodinger equation for water waves (see Peregrine (1983); Trulsen and Dysthe (1996)). It has the particularity to propagate the envelope of the wave trains rather than the free surface elevation. Even if it is limited to deep and intermediate relative water depths and narrow-band spectra, it successfully predicts numerous nonlinear features of water wave fields such as wave group asymmetries (Lo and Mei, 1985), Benjamin Feir instabilities (Zakharov and Shabat, 1971), modulations of wave train edges (Bonnefoy et al., 2020), the shape the extreme events (Peregrine, 1983; Michel et al., 2020; Chabchoub et al., 2012), or the development of non-gaussian wave height statistics Janssen (2003); Fedele et al. (2010).

Short-term statistics

As the wave fields are composed of hundreds of frequency components, with random phases (at least in a linear approximation), in addition to the wave spectrum, the characterization of the sea states also relies on statistical quantities. The so-called "short-term statistics" include for instance the distributions of the free surface elevation, the zero-crossing wave height and

2. https://cds.climate.copernicus.eu/cdsapp#!/home

period distributions, or the crest height probability of exceedance (i. e. probability to find events over given thresholds). They are of great interest to the ocean engineering community as they provide the probability of extreme events, which can be critical for the safety of offshore structures and ships.

A key research topic is predicting these statistical quantities based on the wave spectrum and environmental conditions (depth, current, wind). In the context of this thesis, which aims to improve wave conditions for ocean engineering studies, we are primarily interested in the theoretical distributions of crest heights and we do not investigate current and wind effects. Note that we are addressing the analysis of wave fields within time scales in which the spectrum is stationary.

By definition, linear wave fields are Gaussian. The free surface elevation is distributed according to the normal law, parametrized by the standard deviation which is related to H_s. The associated wave and crest height probability of exceedance distributions were derived in Komen et al. (1996); Lindgren (1972); Longuet-Higgins (1975); Boccotti (1989). They follow Rayleigh-type distributions, with specific corrections to account for finite spectral width effects.

However, the linear distributions significantly under-predict the observed crest height for steep conditions (Forristall, 2000). Considering the asymmetry of second-order nonlinear waves, Tayfun (1990) developed a theoretical shape better agreeing with the ocean observations. Complementary, Forristall (2000) built a semi-empirical distribution, now used as a benchmark by the ocean engineering community (Det Norske Veritas, 2010; ITTC, 2021). These distributions are parametrized by spectrum parameters such as H_s, mean period, and steepness (see Sec. 1.3.2 for definitions of spectrum parameters).

More recently, higher-order effects were studied. They are known to induce departures from the second-order references in wave tank laboratories, due to the development of modulational instabilities, especially for steep and narrow band spectra (Onorato et al., 2006, 2009; Shemer et al., 2010). In Tayfun and Fedele (2007) and Alkhalidi and Tayfun (2013), the authors provided new theoretical reference distributions that account for the deviations. They use as a parameter the excess kurtosis of the free surface elevation, characterizing the severity of the extreme events. Its evolution in space or time from a Gaussian wave field was theoretically predicted in Fedele (2015) based on Janssen (2003) works. Note that Chapter 2 provides the detailed formulas of the distributions mentioned above.

Several studies compared the theoretical references to in-situ data. See for example Forristall (2000); Tayfun and Fedele (2007); Casas-Prat and Holthuijsen (2010); Karmpadakis et al. (2020) (non-exhaustive sample). Various conditions were investigated, with varying relative

depth, steepness, and directional spreading. For most of the cases, linear references were sufficient to capture the wave height distributions. For the crest distribution, second-order references were more adapted. Nonetheless, some field data from steep but non-breaking sea states exhibit departures from the second-order references (see Karmpadakis et al. (2019)). More generally, no single distribution appears to be the most accurate. The efficiency of the models is dependent on the studied configuration (water depth, frequency and directional bandwidth, steepness). Recently, Karmpadakis and Swan (2022) derived an improved crest distribution model built to match a wide range of environmental conditions, including the effects of nonlinear wave interactions and breaking. It combines the existing theoretical references mentioned above with terms parametrized with field and experiment data.

Rogue waves

Examining the short-term statistics reveals that at low probabilities extreme events with large height or crest height relative to H_s do occur. These events are often referred to as "rogue waves". Several definitions can be found in the literature. For instance, in Haver (2001) rogue waves are defined as events verifying $H_c/H_s > 1.25$ (H_c being the crest height), and in Onorato et al. (2013) they corresponds to events verifying $H/H_s > 2$ (H being the crest-to-trough height). Such large waves were first noticed in the ocean during the second half of the 20th century. A famous example is the "New Year's wave" measured at the Draupner platform in the North Sea (Walker et al., 2004; Dysthe et al., 2008).

The observations raised the interest of the scientific community and opened the way to a significant number of studies. Several mechanisms were suggested to explain the formation of the rogue waves. It includes i) the nonlinear focusing of modulated waves trains leading to "breather" type solutions of the nonlinear Schrodinger equations (Chabchoub et al., 2012; Shemer and Alperovich, 2013; Michel et al., 2020), ii) the random linear focusing of directional waves fields (Fedele et al., 2016; Christou and Ewans, 2014), iii) the crossing sea states (Støle-Hentschel et al., 2018; Luxmoore et al., 2019), iv) the wave-current interactions (Toffoli et al., 2019), and v) the bathymetry variations effects (Ducrozet and Gouin, 2017). See Onorato et al. (2013) review for more possible references.

More recently, new approaches to model the formation and predict the occurrence of rogue waves were explored, relying on the wave turbulence notion (Choi et al., 2005; Zakharov et al., 2012; Fadaeiazar et al., 2020a; Skvortsov et al., 2022)) or the large deviation mathematical framework (Grafke and Vanden-Eijnden, 2019) leading to the concept of "instanton" (Dematteis et al., 2019).

Breaking

The study of ocean wave physics in the last decades also focused on breaking. Breaking events can be induced by several mechanisms, such as wind stress, current effects, variations in bathymetry, or linear and nonlinear focusing in steep irregular wave fields. See Babanin (2011) book for detailed explanations on the formation of breaking events. The scope of this thesis is limited to breaking occurring offshore in deep or intermediate water depth, without wind forcing, bathymetry variations, and currents.

Breaking events dissipate the energy of the wave field (Kendall Melville, 1994). This process is complex and difficult to model (Toffoli et al., 2010), no analytical solution allows for the full resolution of a breaking event. Several studies addressed the problem by developing breaking onset criteria, first for regular waves (Ochi and Tsai, 1983; Katsardi, 2007) and then for irregular wave fields (Tian et al., 2008; Banner and Peirson, 2007). See for instance Barthelemy et al. (2018) criteria, relying on the ratio of the water particle speed over the crest velocity. Complementary, works were carried out to understand the energy dissipation turbulent mechanisms (Drazen et al., 2008; Nepf et al., 1998), quantify the energy loss (Liang et al., 2017), investigate the properties of the waves prior and after breaking (Tian et al., 2010), and study the influence of breaking on short-term crest or wave height statistics (Onorato et al., 2006; Latheef and Swan, 2013).

Numerous works have also been carried out to simulate breaking events with Computational Fluid Dynamic methods. See for example Mostert et al. (2022) relying on Direct Numerical Simulations (DNS), solving directly Navier Stokes equations, and Lubin et al. (2006); Derakhti and Kirby (2014) tackling the problem with Large Eddy Simulation models (LES). This sample is obviously non-exhaustive.

Wave tank experiments

Conducting on-site observations requires expensive measurement systems and the wave condition under study cannot be controlled. As a result, many of the studies mentioned earlier are based on tank experiments. Ocean waves are reproduced at a smaller scale in basins equipped with wave generators and wave gauges. These facilities are very useful for the ocean engineering field, as they provide a monitored environment to conduct wave-structure interaction tests.

Wave tanks over the world

Depending on their applications, wave tanks present different shapes and features. Ocean engineering tanks are usually rectangular, equipped with a wave maker on at least one side and with an absorbing beach at the other side (configuration of the Ecole Centrale de Nantes (ECN) ocean engineering tank). The wave generator can be made of plungers, pistons, or flaps (with one or two hinges). It is sometimes settled at two or more sides of the domain to generate multidirectional sea states within a larger range of directions and/or to perform active absorption. See for example the the SINTEF Ocean Basin Laboratory, the MARIN offshore basin in the Netherlands, or the COB in Ostende (Belgium) managed by Ghent University, KU Leuven and Flanders Hydraulics Research. Bridges and hexafloats are usually settled over the tank to facilitate the installation of a model structure and wave gauges. Current and wind generation features can also be provided (see for example the Research Institute of Medium & Small Shipbuilding (RIMS) or the Technology Centre for Offshore and Marine Singapore (TCOMS) facilities in South Korea and Singapour respectively).

Wave-maker-equipped towing tanks, which consist of long channels with moving carriages allowing for the study of ship resistance, can also be used for waves-only studies (interesting to capture phenomena that need tens of wavelengths to occur). See for instance the ECN Towing tank or the B600 (managed by the DGA, French government).

The examples mentioned above are not exhaustive. Many other tanks exist, each with various features and fields of application.

Specificity of tank environments

The restrictive domains of wave tank facilities affect the realistic reproduction of ocean sea states. First, the shape of the wave-maker paddle does not lie on the wave-induced water velocity profile. As a consequence evanescent modes are generated near the wave generator (up to one wavelength of distance), see for example Kusumawinahyu et al. (2017) for an analytical description of the problem. Additionally, the absorbing beach usually located at the end of the domain does not totally prevent reflection. See for instance Bonnefoy (2005) that presents methods to quantify the reflected waves and isolate their influence. Note that more efficient active absorbing systems are now used (Andersen et al., 2018). However, even for these absorbing systems, the efficiency is limited to a specific range of frequencies. Besides, even for unidirectional wave generation, side walls induce transverse disturbances. See again Bonnefoy (2005) which studies the excitation of the natural transverse modes of the tank or Garrett (1970)

which describes the nonlinear excitation of cross waves by the wave maker. Lastly, for long tanks (for example towing tanks) the side walls' friction dissipates a noticeable fraction of the wave field energy. See Henderson et al. (2015) for an analytical description of the phenomenon.

Experimental propagation of irregular waves fields

The present PhD focuses on the propagation of irregular wave fields in wave tank environments. Research in this area has been booming in recent decades. For example, one should refer to Onorato et al. (2006); Shemer and Sergeeva (2009); Shemer et al. (2010); Derbanne et al. (2009) for studies of unidirectional sea states, and to Latheef and Swan (2013); Onorato et al. (2009) for the study of directional spectra. The water depth influence was explored for instance in Tang and Adcock (2021); Karmpadakis et al. (2019). Complementary, Lu et al. (2019); Michel et al. (2020); Huang and Dong (2021) focused on the generation of rogue waves in tanks.

Note that the above references are a non-exhaustive sample. From these studies, it appears that, as the distance from the wave maker increases, the wave spectrum broadens (due to high-order nonlinear effects) and dissipation occurs, especially in high-frequency ranges (due to side wall friction and breaking events). It is also shown that the statistical properties of the waves (crest and wave height distributions, kurtosis of the free surface elevation) evolve along the tank, again as a result of high-order nonlinear interactions such as modulational/Benjamin Feir instabilities. The probability of the extreme events increases with the distance from the wave maker. This evolution is limited for directional wave fields and is counteracted by breaking for the steepest wave fields. In addition, shallower water depths amplify the second-order nonlinear effects such as bound waves, but reduce the modulational instabilities.

In the current thesis, Chapter 4 will address the experimental propagation of a unidirectional narrow-band spectrum in deep water, and explore in detail its statistical features.

Numerical waves propagation

Complementary to tank experiments, numerical wave solvers have been developed, modeling open sea domains or mimicking wave tank environments, namely numerical waves tank (NWT). They present numerous advantages. As wave physics is accurately modeled by the potential flow of an ideal fluid (assuming non-viscous and incompressible fluid and irrotational flow), the computational time is not excessive. NWT are also free from the experimental issues previously mentioned such as the reflection or the transverse perturbations. Eventually, they

allow for the full measurement of the free surface elevation over the 2D domain (wave tank experiments usually only provide points of measurement). This is very interesting for the study of directional sea states.

Various specific nonlinear irregular wave modeling methods were reviewed in the International Towing Tank Conference (ITTC) recommended procedures and guidelines for laboratory modeling of waves (ITTC, 2021). Among them, the High-Order Spectral (HOS) method, relying on a surfacic extension of the water surface boundary conditions, is relatively low computational demanding and accurately propagates the waves up to an arbitrary order of nonlinearity (West et al., 1987; Dommermuth and Yue, 1987). In the present thesis, we make use of the extension of the HOS method to a numerical wave tank environment, using the open-source `HOS-NWT` program (Ducrozet et al., 2012). The latter is described in detail in Chapter 5. A review of different nonlinear potential flow solvers and the limitation of their applicability can be found in Ducrozet et al. (2017).

Application to ocean engineering

The ocean engineering community addresses a large panel of topics such as ship performance, maneuvering, fluid-structure interactions of floating or fixed platforms, automatization of floating objects, risk assessment of marine activities, or optimization of wave/wind/tidal energy converters. This list is non exhaustive, a detailed review is provided for example in Tavakoli et al. (2023). To deal with most of those fields, experimental and numerical wave tanks appear as relevant tools. They offer a controlled environment for conducting seakeeping tests, enabling the measurement of realistic responses to loads that simulate the ocean environment. The experimental tests are performed at model scale relying on the Froude similitude. The latter preserves wave dynamics. However the Reynold similitude cannot be achieved simultaneously. This means that vorticity and viscous phenomena are not well reproduced in experiments. Numerical solvers, based on Computational Fluid Dynamics (CFD), enable full-scale simulations which make it possible to avoid the partial similitude imposed in experimental facilities. Note that hybrid numerical/ experimental approaches can be used (validation of the CFD solver with experiments and numerical extension at full scale, see Pinguet (2021)).

Procedures to generate relevant wave conditions

Different types of wave conditions can be used for experimental and numerical seakeeping tests. The most fundamental approach consists of generating regular waves. For numerical tests,

the target waves correspond to nonlinear solutions such as stream function waves (Rienecker and Fenton, 1981) or the Stokes fifth-order waves (Fenton, 1985). These potential-flow theory solutions are known to match well with experimental and numerical results (Huseby and Grue, 2000; Choi et al., 2020). Sets of regular wave cases are usually run, varying the frequency at constant steepness, for several values of steepness. This kind of test provides the force or motion RAO (response amplitude operators). See for instance Greco et al. (2012) or Copuroglu and Pesman (2018) studies.

However, the use of irregular wave conditions is needed to evaluate more realistic structure responses. In this context, the classification companies establishing rules and procedures use the notion of design sea state (Det Norske Veritas, 2010; Bureau Veritas, 2019; NWT Preparation Workgroup, 2019). Based on long-term statistics, they select the extreme wave spectra that the ship or structure should be able to withstand. The duration T_{design} associated to a given sea state in design is typically 3 hours at full scale. It is directly associated with a probability $P_{\text{design}} \approx T_p/T_{\text{design}}$ (inverse of the number of waves occurring within the duration T_{design}). It gives the probability of exceedance of the maximum response that one should be able to evaluate. As an example, for $T_p \approx 10$s, and $T_{\text{design}} = 3$ hours, T_{design} corresponds to approximately 1000 waves, resulting in $P_{\text{design}} = 1/1000$. This means that the study must provide the representative maximum response of the structure occurring at a probability $P_{\text{design}} = 1/1000$.

On these grounds, two main approaches are used by the ocean engineering community to define relevant irregular wave conditions. The first approach, which is the scope of the present thesis, is stochastic. A set of realizations (long free surface elevation sequences, each equivalent to three hours at full scale) are run. The method requires that, i) the generated wave field at the position of interest corresponds to the design spectrum and that ii) the number of waves is large enough so that the response at P_{design} is statistically reliable. It is important to note that, consequently, the total duration of recorded waves must be significantly greater than T_{design}. Within this context, the quantities of interest used to qualify the wave field are i) the wave spectrum and ii) the wave statistics (mainly the crest distribution). Examples of such experiments can be found in Onorato et al. (2006); Shemer et al. (2010); Latheef and Swan (2013) (waves only in experimental wave tanks), Fouques et al. (2021) (waves only in numerical waves tank), Stansberg (2020); Han and Kinoshita (2012) (experimental waves structure interaction study), and Belenky et al. (2011) (numerical wave-structure interaction study). This approach is the most straightforward. However, it requires long-duration experimental campaigns or long computation time.

The second approach is the deterministic approach. One design wave is generated,

corresponding to a typical event of the sea state at a given P_{design}. Different methodologies were developed to derive the profile to generate. See for instance the "New Wave method" (Tromans et al., 1991), being the most probable linear wave profile at a certain probability; the FORM (first-order reliability method), solving a minimization problem to provide the wave profile and the associated probability (even if the response distribution is not known) (Jensen and Capul, 2006) ; or more recently the EDW (equivalent design waves), based on a FORM approach coupled with a nonlinear wave solver (Kim et al., 2022). These deterministic methods will not be investigated in this thesis.

Numerical wave structure interaction study

At this point, it is important to emphasize the particularity of numerical seakeeping studies relying on CFD solvers dedicated to fluid interaction modeling (which differ from the wave-only solvers previously mentioned). Note that here, 'CFD solver' term also includes the nonlinear wave-structure interaction solvers based on potential flow approximations. In these numerical environments, the accurate nonlinear generation of the target wave condition is not straightforward. A first natural approach is to model the entire tank using the CFD solvers, including a wave maker. However, the CFD-NWT waves tend to lose accuracy during wave propagation in the CFD domain (Choi et al., 2020). Especially, unrealistic numerical dissipation affects the waves. To avoid this phenomenon, the mesh needs to be very accurate all across the domain. Therefore, the computational cost needed to model the entire tank is huge.

To overcome these difficulties, a new wave generation approach has been developed. The incident wave velocity and elevation are imposed into specific boundaries or regions surrounding a limited-size CFD domain. These target incident fields can be produced from the dedicated nonlinear potential wave-only solvers modeling the NWT. Then, the generated waves are used as input to the smaller-size CFD domain centered around the structure. Within this area, the CFD solver, fed by the numerical nonlinear potential waves, solves the wave-structure interaction problem. This method is widely used in various NWT applications, such as the simulation of moored semisubmersible (Wang et al., 2022) and SPAR type platforms (Aliyar et al., 2022). Note that the approach enables relevant comparisons with experimental wave-structure interaction tests, as the nonlinear potential wave solver models the entire wave tank.

Objectives and outlines of the thesis

In a tank environment, the waves are generated by a wave maker, which motion is controlled. In the case of a seakeeping study, the structure is located further in the tank. Consequently, the wave field needs to be qualified in this area of interest. However, as detailed in the first part of this introduction, the wave properties are affected by numerous physical phenomena, and as a result, they evolve along the tank. It is therefore difficult to control the quantities of interest (spectrum and wave height statistics) in the area of interest. As a result, the standard industry practices to evaluate extreme responses are not accurate and the classification societies have to use large safety correction factors (Det Norske Veritas, 2010).

On these grounds, the objective of this Ph.D. thesis is to develop procedures, considering complex wave propagation, for accurately controlling the wave spectrum and the statistics of the sea states generated through a stochastic approach, whether in experimental wave tanks or numerical simulations. Special attention is focused on the tail of the crest height distributions, which represents the probability of extreme events. The thesis incorporates experimental and numerical works. The nonlinear potential wave solver `HOS-NWT` (Ducrozet et al., 2012), developed by ECN, is employed for numerical studies. Experimental campaigns are conducted using the ECN facilities, including a 2D towing tank (140m$\times$5m$\times$2.8m) and a 3D ocean engineering (O.E.) tank (50m$\times$30m$\times$5m), see Sec. 1.1.2. The framework is limited to unidirectional irregular deep-water wave conditions, and the research is exclusively focused on wave studies, without structures present in the domain.

This document is divided into two parts. The first part addresses various research topics related to irregular wave generation and propagation in experimental or numerical wave tanks. The objectives are to define the mathematics of the problem, present the available tools and procedures, and explore the physical phenomena at stake. Particular attention is given to a clear understanding of the evolution in space of the wave spectrum and statistics. The second part applies the conclusions drawn in the first part to enhance and develop wave generation and qualification procedures for ocean engineering studies.

PART I

Generation and characterization of irregular sea states in a wavetank environment

---

This part addresses various research topics related to irregular wave generation and propagation in experimental or numerical wave tanks. The objectives are to define the mathematics of the problem, present the available tools and procedures, and explore the physical phenomena at stake. First, the problem is clearly settled. The concept of 'wave tank environment' is defined, and the analysis procedures used to study the generated wave fields are presented (Chapter 1). Then, the problem is addressed from a theoretical point of view, introducing theories and tools that predict the propagation of the irregular wave fields in wave tank environments (Chapter 2). To ensure a relevant analysis of the experimental results, the third chapter is dedicated to the study and quantification of the experimental uncertainties. Complementary, relying on the data analysis procedures, the theoretical predictions, and the uncertainty ranges introduced in Chapter 1, 2 and 3 respectively, the experimental propagation of a typical narrow-band design sea state is studied in detail, focusing on the analysis of the probability of the extreme events (Chapter 4). Eventually, the wave propagation is studied from a numerical point of view, introducing the open source nonlinear potential wave solver `HOS-NWT` *developed at ECN and used in the current thesis as a powerful numerical twin of the experimental facilities (Chapter 5). The second part of the thesis will have the objective of applying the conclusions drawn in this first part to enhance and develop wave generation and qualification procedures for ocean engineering studies.*

CHAPTER 1

FRAMEWORK OF THE STUDIES

The objective of this chapter is to clearly settle the problem. We will examine the wave tank characteristics, introduce the standard procedure for generating stochastic wave fields, and clearly define the data analysis processes employed to study the generated wave fields.

1.1 Wave tank environment

The scope of the study is limited to 'wave tank environments'. We will here define this notion by presenting the characteristics of such domains. This section also contains an overview of the different experimental and numerical wave tanks used for the present thesis.

1.1.1 Domain definition

What we refer to as a 'wave tank environment' is a numerical or experimental basin equipped with a wave maker. The latter generates waves that propagate toward an absorbing beach that prevents reflection. The scope of the studies will be limited to unidirectional propagation. A target position is typically located at a distance denoted as X_t from the wave maker. This position corresponds to the location of the model in wave-structure interaction studies. Figure 1.1 illustrates the domain.

Wave gauges or numerical probes are settled to provide time series data of the free surface elevation at specific single-point positions. We note x and y the longitudinal and the transverse coordinates.

1.1.2 ECN experimental facilities

A significant part of the studies presented in this thesis were carried out in two tanks of the Ecole Centrale de Nantes (ECN) facilities, the Towing tank and the Ocean Engineering wave tank. They will often be denoted as Towing tank (or T. tank) and O.E. tank. Their characteristics

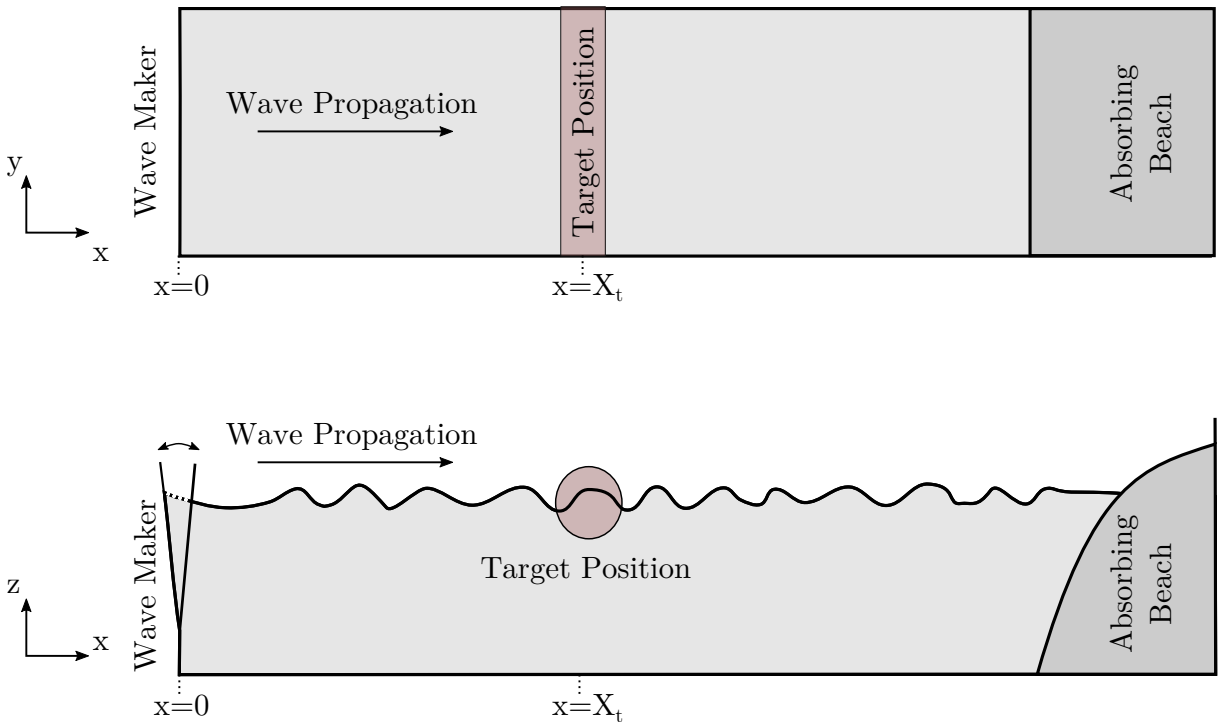

Figure 1.1 – Sketch of a wave tank equipped with a flap wave maker in (x, y) and (x, z) plans

(a) ECN Ocean Engineering tank

(b) ECN Towing Tank

Figure 1.2 – Photos of the ECN facilities

are detailed in Table 1.1. More information can be found on the ECN website [1] and Figure 1.3

1. https://lheea.ec-nantes.fr/english-version/test-facilities/ocean-tanks

Table 1.1 – Characteristics of ECN facilities

	O.E. tank	**T. tank**
Length (L_x)	50 m	150 m
Width (L_y)	30 m	5 m
Depth (d)	5 m	2.9 m
Wave maker type	flap	flap
Hinge depth from bottom (d_{hinge})	2.15 m	0.47 m
Number of flaps (N_{paddle})	48	1

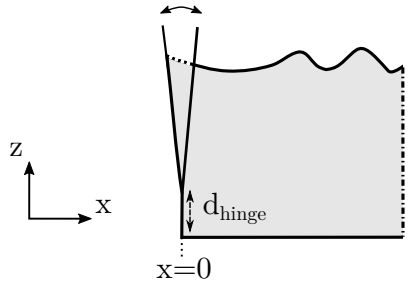

Figure 1.3 – Sketch of a flap wave maker with d_{hinge} definition

shows a sketch of a single-hinge wave maker. The O.E. tank is a large size rectangular basin equipped with a 48-paddle wave maker (single hinge) at one side ($x = 0$). It is designed to generate unidirectional and multidirectional deep-water sea states. Its capabilities cover periods from 0.5 to 5.0 s and significant wave heights H_s up to 0.8 m. The Towing tank is a long channel equipped with a one-flap wave maker (single hinge) that can generate waves from 0.5 s to 5 s and significant wave heights up to 0.3 m. A moving carriage is set up to perform towing experiments and measure ship resistance. The latter is removed for the wave-only studies. The passive absorbing system of the facilities has been studied in Bonnefoy (2005). The reflection coefficients, in terms of wave amplitude, do not exceed 5% to 10% within the range of frequencies covered by the wave makers. A detailed analysis specific to the setup adopted for this thesis is provided in Chapter 2.

The wave makers are mechanically limited to frequencies below $f_{\text{max}}^{\text{wvmk}} = 2$ Hz. They take as input the free surface elevation series wanted at $x = 0$. The latter are provided in the Fourier space, as a list of harmonics. Then, the wave maker transfer function, implemented in the wave generation software, converts the input harmonics into wave maker motion time series. A ramp in time is usually applied to the motion at the beginning and the end of the runs

to prevent mechanical issues. Its duration ranges from 2 to 20 s.

1.1.3 Numerical wave tank `HOS-NWT`

Additionally, numerical wave tank simulations were conducted using the `HOS-NWT` solver (Ducrozet et al., 2012), which is developed by ECN and released open-source [2]. A comprehensive description of the code is provided in Chapter 5. This solver is based on potential flow theory and incorporates nonlinear features of water wave propagation up to an arbitrary order. It is utilized within the framework of intermediate and deep water depths ((i. e. $kd \geq O(1)$). The numerical environment includes a realistic wave maker and an absorbing zone at the end of the domain (set to prevent reflection). The version used in the present study includes breaking models that enable the generation of the most extreme sea states.

As for the experimental ECN facilities, it takes as input a list of harmonics describing η at $x = 0$ and converts it into wave maker motion sequences. The similarity with the experimental mode of operation allows for the accurate and easy numerical reproduction of the experimental waves.

Chapter 5 provides the parametrization of `HOS-NWT`, adapted to propagate the sea states studied in this thesis (introduced in the next section) in environments mimicking the ECN O.E. and Towing tanks characteristics.

1.2 Wave conditions

1.2.1 Design wave spectra

The framework of the study is limited to the stochastic generation of unidirectional wave spectra in deep or intermediate water depth. Three design sea states were studied. Their characteristics are presented in Table 1.2 and plots are provided in Figure 1.4. λ_p corresponds to the peak wavelength. The shapes of the spectra follow the JONSWAP semi-empirical model (Komen et al., 1996),

$$S(\omega) = \frac{\alpha_p g^2}{\omega^5} \exp\left[-\frac{5}{4}\left(\frac{\omega}{\omega_p}\right)^{-4}\right] \gamma^{\exp[-(\omega-\omega_p)^2/(s_{\text{JONSWAP}}{}^2\omega_p^2)]} \tag{1.1}$$

2. `https://github.com/LHEEA/HOS-NWT`

with ω the wave angular frequency, α_p the Phillips parameter, $\omega_p = 2\pi f_p$ the peak wave angular frequency, γ the peak enhancement factor, $s_{\text{JONSWAP}} = 0.07$ for $\omega < \omega_p$ and $s_{\text{JONSWAP}} = 0.09$ for $\omega \geq \omega_p$.

Table 1.2 – Sea state characteristics at full scale (JONSWAP spectra).

	ss6	ss6g5	GOM
γ	1.0	5.0	2.6
H_s	6 m	6 m	17 m
T_p	12.25 s	12.25 s	15.5 s
λ_p	234 m	234 m	375 m
$\varepsilon_p = \frac{H_s}{\lambda_p}$	2.5%	2.5%	4.5%

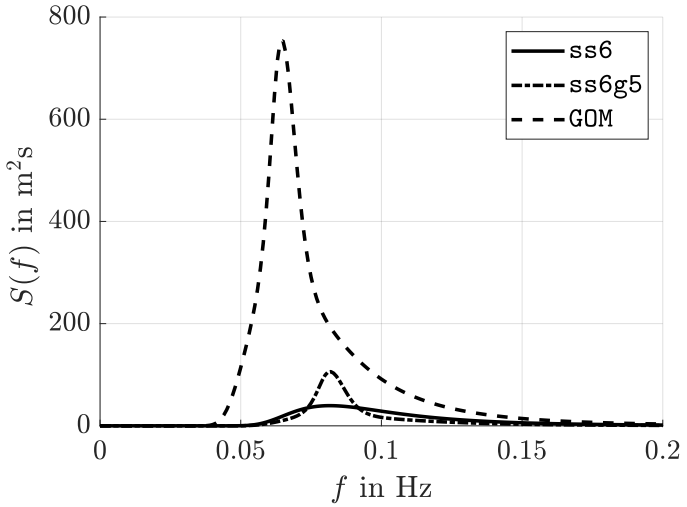

Figure 1.4 – Design sea states studied (full scale)

ss6 and GOM design sea states are references already studied by the ocean engineering community, see NWT Preparation Workgroup (2019) and Fouques et al. (2021) works. They represent mild and extreme conditions. ss6 is broad-banded and has a moderate peak steepness $\varepsilon_p = 2.5\%$. No breaking occurs. On the opposite, GOM is an extreme sea state. It corresponds to the 1000-year return period conditions of the Gulf of Mexico area (Kim et al., 2019). The large peak steepness ($\varepsilon_p = 4.5\%$) induces numerous and strong breaking events. In addition, ss6g5 sea state was built as a narrow band version of ss6 (γ increased from 1 to 5). The objective was to study nonlinear but non-breaking conditions, which are known to induce modulational

instabilities leading to extreme statistics (Onorato et al., 2006). These three design sea states were generated experimentally in the O.E. and Towing tanks at various scales, and numerically using the `HOS-NWT` numerical version of those facilities.

1.2.2 Standard stochastic generation procedure

As previously mentioned, within the scope of this thesis the sea states of interest are generated through a stochastic approach (generation of N_{run} random long-duration realizations). Figure 1.5 presents the procedure.

Each realization is associated with a set of input amplitudes $A_{\text{input}}(f)$ and phases $\phi_{\text{input}}(f)$, related to a free surface elevation time sequence $\eta_{\text{input}}(t)$ defined as

$$\eta_{\text{input}}(t) = \sum_{j=0}^{N_{\text{harmo}}} A_{\text{input}}(f_j)\cos(2\pi f_j t + \phi_{\text{input}}(f_j)) \tag{1.2}$$

with (f_j) the discrete frequency vector of constant resolution δf_{repeat} and N_{harmo} the number of harmonics. The maximum frequency to generate is denoted as $f_{\text{max}}^{\text{input}}$. The duration T_{repeat} of the series is defined by $T_{\text{repeat}} = 1/\delta f_{\text{repeat}}$. The phases are random and the amplitudes are built using the input spectrum $S_{\text{input}}(f)$ which corresponds to the target design spectrum: $S_{\text{input}}(f) = S_{\text{target}}(f)$. More exactly,

$$A_{\text{input}}(f) = \sqrt{2S_{\text{input}}(f)\delta f_{\text{repeat}}} \tag{1.3}$$

and,

$$\phi_{\text{input}}(f) = 2\pi U_{[0;1[} \tag{1.4}$$

with $U_{[0;1[}$ a random variable following the uniform probability law between 0 and 1.

The corresponding wave maker motion $\mathscr{F}_W(f)$ in Fourier space is built using the transfer function TF of the wave maker,

$$\mathscr{F}_W(f) = TF(A_{\text{input}}(f), \phi_{\text{input}}(f)) \tag{1.5}$$

The transfer function is dependent on the geometry of the wave maker (shape, d, d_{hinge}).

Then, at a position x (distance from the wave maker), the generated free surface elevation $\eta(x,t)$ can be expressed as

$$\eta(x,t) = \sum_{j=0}^{N} A(f,x)\cos(2\pi f_j t + \phi(f_j,x)) \tag{1.6}$$

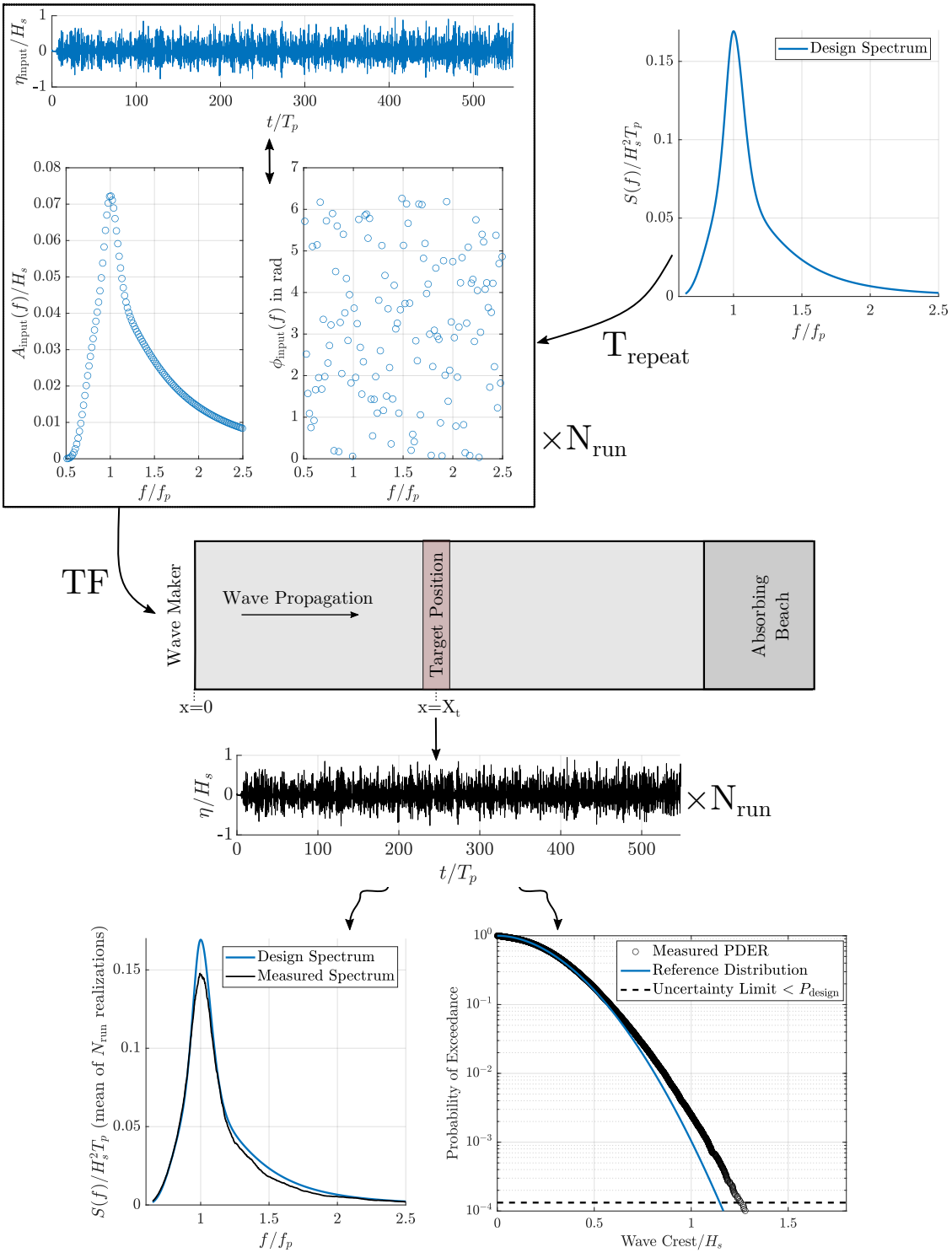

Figure 1.5 – Stochastic generation of a design sea state

with $A(f,x)$ and $\phi(f,x)$ the Fourier amplitude and the phase at position x and frequency f. N corresponds to the number of point in the frequency vector and the frequency resolution is denoted as δf. $\eta(x,t)$ is the quantity measured by the wave gauge / numerical probe. N and δf depend respectively on the measured signal's sampling frequency and duration.

The linear theory predicts $S(f,x) = S_{\text{input}}(f)$ and $\phi(f,x) = -k(f)x + \phi_{\text{input}}(f)$, with $k(f)$ the wavenumber at frequency f. More particularly $\phi(f,0) = \phi_{\text{input}}(f)$ and $S(f,0) = S_{\text{input}}(f)$.

However, the irregular waves propagation is not linear. Therefore, to ensure that at the area of interest $S(f,X_t) = S_{\text{input}}(f)$, corrections need to be applied. In the second part of the present thesis, such a procedure is described and validated (see Chapter 7). It adapts the input amplitudes with a calibration factor $C(f,X_t)$,

$$A_{\text{input}}^{\text{corrected}}(f) = A_{\text{input}}(f)\,.\,C(f,X_t) \tag{1.7}$$

Procedures with random amplitudes In this thesis, the input amplitudes $A_{\text{input}}(f)$ are deterministic, which means that they are fully determined by the input spectrum (see eq. 1.3). However, some wave generation procedures add randomness in the definition of $A_{\text{input}}(f)$ (ITTC, 2021). For instance, Rayleigh-distributed amplitudes can be used. This means that for each frequency component f_j, the amplitude is obtained from a Rayleigh distribution whose mean equals $\sqrt{2S_{\text{input}}(f_j)\delta f_{\text{repeat}}}$.

Indeed, linear wave fields built with deterministic amplitudes are not exactly Gaussian. They are Gaussian only if the number of frequency components tends towards infinity (which implies $\delta f_{\text{repeat}} \to 0$ i. e. $T_{\text{repeat}} \to \infty$). Using Rayleigh-distributed amplitudes enables to have a fully Gaussian free surface elevation with finite duration (finite T_{repeat} values).

In Tucker et al. (1984), the authors argue that when comparing linear wave fields built with deterministic amplitude with linear wave fields built with randomly-distributed amplitudes, differences are observed in terms of groupiness (distribution of wave group length) and sampling variability (sensitivity of stochastic quantities depending on the analyzed sample, i.e., the set of realizations and the analysis time window).

However, this concerns linear wave fields. In this thesis, we analyze wave fields generated either in experimental facilities or with the nonlinear wave solver `HOS-NWT`. Even for the less steep case (`ss6`), nonlinear effects are observed. In this context, the nonlinear interactions among the wave field components introduce randomness to the amplitudes. The effect is expected to be similar to that induced by randomly-distributed input amplitudes. Moreover, in this thesis, sampling variability intervals are systematically provided when presenting stochastic quantities,

see Sec 1.3.3. Any change in sampling variability would therefore be included in these intervals.

1.3 Data analysis procedures

The qualification of the wave fields requires the computation of quantities of interest, computed from the measured $\eta(x,t)$ time series. For the sake of reproducibility, this section entirely describes the analysis carried out. The accuracy of the methods will be discussed.

1.3.1 Selection of relevant time windows

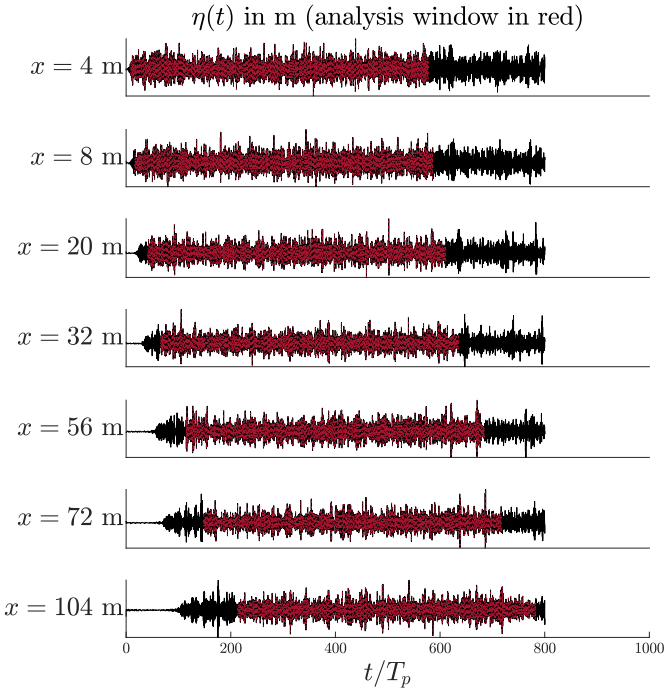

Figure 1.6 – Selection of time window for the analysis

In a unidirectional wave tank configuration, a network of probes measures time series of free surface elevation at single-point positions. To analyze the recorded data, one must choose appropriate time windows that remove the non-stationary development of the wave field at the probe location. The sea states generated for the present study are characterized by an energy spectrum centered around a peak frequency f_p and containing most of energy up to $2f_p$. Then,

for each probe, we use the following analysis window, depending on the probe position x:

$$t_{\text{beg}} = x/c_g(2f_p) \tag{1.8}$$

$$t_{\text{end}} = \Delta T + x/c_g(2f_p) \tag{1.9}$$

with $c_g(2f_p)$ the group velocity at twice the peak frequency, and ΔT a duration, constant for all the probes, fixed as $\Delta T \leq T_{\text{WVMK}} - \max(x)/c_g(2f_p)$ (T_{WVMK} is the time at which the wave maker stops, and $\max(x)$ denotes the position of the furthest probe in the network). This procedure allows for the analysis of an equal number of waves at each probe and enables the tracking of wave groups. As an example, Figure 1.6 presents the time windows applied to analyze a realization of `ss6g5` sea state generated in the Towing tank at scale 120.

The total duration of the analyzed series, including all the realizations is consequently $T_{\text{analyzed}} = N_{\text{run}}\Delta T$.

1.3.2 Stochastic Quantities of interest

a) Estimators of the wave spectrum

A design sea state is modeled and defined by a wave spectrum. Therefore, the most significant quantity of interest computed from the $\eta(t)$ measurements is the wave spectrum.

Definitions The Fourier transform of a continuous free surface elevation signal $\eta(t)$ of duration ΔT is defined as

$$\mathscr{F}_\eta(f) = \int_0^{\Delta T} \eta(t) e^{-i2\pi ft} dt \tag{1.10}$$

The associated variance spectrum (namely wave spectrum) follows as

$$S(f) = \lim_{\Delta T \to +\infty} \frac{1}{\Delta T} \mathscr{F}_\eta(f) \mathscr{F}_\eta{}^*(f) \tag{1.11}$$

with $i^2 = -1$ and * denoting the complex conjugate.

However the data recorded by the wave gauges are discrete. The definitions need to be adapted for discrete time-series $\eta(t_n) = \eta_n$ of duration $\Delta T - \delta t$, time step δt and number of

points $N = \Delta T / \delta t$. The discrete Fourier transform is usually defined as

$$\mathscr{F}_\eta^d(f_j) = \sum_{n=0}^{N-1} \eta_n e^{-i2\pi jn/N} \tag{1.12}$$

and the associated frequency vector is $f_j = j/(N\delta t) = j\delta f$ for $j \leq \lfloor N/2 \rfloor$ and $f_j = (j - N)/(N\delta t)$ for $j > \lfloor N/2 \rfloor$. $\lfloor N/2 \rfloor$ denotes the integer part of $N/2$. With this definition, $\mathscr{F}_\eta^d(f_j)$ has the same unit as η. To be consistent with the formulation for continuous signals, we can consider the quantity $\mathscr{F}_\eta^d(f_j)\delta t = \mathscr{F}_\eta^d(f_j)\Delta T/N$.

For the analysis of wave records, we use the moduli and arguments of the complex Fourier series coefficients, which correspond to the amplitudes and phases of the frequency components of the wave fields:

$$A(f_j) = |2/N \sum_{n=0}^{N-1} \eta_n e^{-i2\pi jn/N}| \tag{1.13}$$

and

$$\phi(f_j) = \arg\left(2/N \sum_{n=0}^{N-1} \eta_n e^{-i2\pi jn/N}\right) \tag{1.14}$$

with $j \in [1 : \lfloor N/2 \rfloor]$. Removing frequencies larger than $\lfloor N/2 \rfloor \delta f$ and multiplying by 2 removes the negative frequencies while preserving the energy of the signal. We refer to this latter quantity as Fourier amplitude.

The discrete wave spectrum can be expressed either as

$$S^{j\in[1:N]}(f_j) = \lim_{N\to+\infty} \frac{\delta t^2}{\Delta T} |\sum_{n=0}^{N-1} \eta_n e^{-i2\pi jn/N}|^2 = \lim_{N\to+\infty} \frac{\delta t^2}{\Delta T} |\mathscr{F}_\eta^d(f_j)|^2 \tag{1.15}$$

or

$$S^{j\in[1:\lfloor N/2 \rfloor]}(f_j) = \lim_{N\to+\infty} \frac{1}{2}\frac{\delta t^2}{\Delta T} |2 \sum_{n=0}^{N-1} \eta_n e^{-i2\pi jn/N}|^2 = \lim_{N\to+\infty} \frac{1}{2}\Delta T |2/N \sum_{n=0}^{N-1} \eta_n e^{-i2\pi jn/N}|^2 \tag{1.16}$$

which can be expressed using the Fourier amplitudes as

$$S^{j\in[1:\lfloor N/2 \rfloor]}(f_j) = \lim_{N\to+\infty} \frac{1}{2}\Delta T A(f_j)^2 = \lim_{N\to+\infty} \frac{1}{2}\frac{1}{\delta f} A(f_j)^2 \tag{1.17}$$

The integration of $S^{j\in[1:\lfloor N/2 \rfloor]}$ and $S^{j\in[1:N]}$ over their respective domains leads to the same value

which corresponds to the variance of the free surface elevation time series.

The spectrum is computed for each realization. The quantity of interest is the spectrum obtained by averaging all the individual-realization spectra.

Smoothing In this thesis, for each realization, $\Delta T > 100T_p$. This corresponds to frequency resolutions $\delta f < 0.01 f_p$. For these signals, the direct computation of the spectrum results in a very noisy quantity. Indeed, the input amplitudes, built from a smooth input spectrum, are defined with a frequency resolution δf_{repeat},which corresponds to a T_{repeat} duration in the time domain (see Eq. 1.3). Nevertheless, the signals that we analyze are obtained from experiments or nonlinear numerical simulations. They are recorded at a distance x from the wave maker within an analysis time window of length $\Delta T \neq T_{\text{repeat}}$. For all these reasons, the spectrum computed with (eq. 1.15) and (eq. 1.17) is noisy compared to the input spectrum.

Smoothing procedures are needed. To investigate this phenomenon, an artificial linear dataset of 10 free surface elevation sequences (realizations) was generated, based on `GOM` spectrum at model scale 100, with random phases (see eq. 1.2). The adopted T_{repeat} is 1024 s, and $T_p = 1.55$ s. When analyzing entirely the sequences (exactly from $t = 0$ to $t = T_{\text{repeat}}$), as the data is linear, (eq. 1.15) and (eq. 1.17) directly lead to the exact `GOM` spectrum. However, when analyzing smaller time windows, the computed spectrum becomes noisy, similar to what is observed with experimental and numerical data records. Consequently, it was chosen to test smoothing procedures on this artificial linear dataset, using windows of duration $\Delta T = 80\% T_{\text{repeat}}$.

Figure 1.7 displays the raw spectrum, averaged over the 10 realizations (black dotted line). The strong noise prevents a meaningful analysis of the spectrum. To face this issue, we make use of the Welch procedure (Welch, 1967a). η time series are divided into Hamming windows of length T_{Welch} with an overlap of O_{Welch} percents. The wave spectrum is computed for each segment, and then the spectra of individual segments are averaged. The frequency resolution δf of the resulting quantity is inversely proportional to the size of the windows. Consequently, when using sufficiently short windows, the spectrum becomes smoothed. This smoothing process is performed for each realization, and the resulting smoothed spectra are averaged to obtain the final mean spectrum.

Figure 1.7 presents the smoothed spectrum for different T_{Welch} (computed using the previously mentioned 10-realizations artificial dataset). As advised in (Welch, 1967a) O_{Welch} was fixed to 50%. T_{Welch} was parametrized as a function of the number of waves (counted with the peak period T_p), and values of 10, 30, 50, and $70T_p$ were tested. Even for the least

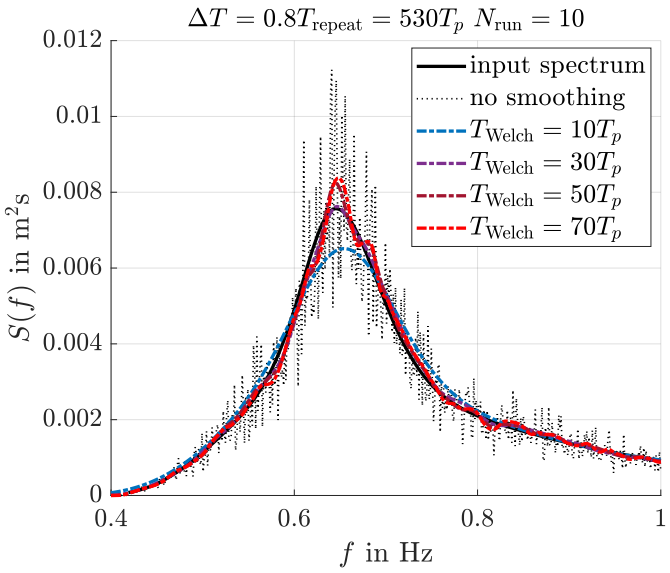

Figure 1.7 – Influence of welch window size on a linear artificial waves dataset

active smoothing case ($T_{\text{Welch}} = 70T_p$), the resulting spectrum is considerably easier to interpret than the raw one and approximately matches the input design spectrum. For $T_{\text{Welch}} < 30T_p$, the smoothing is too strong and the spectrum's peak is not captured. Therefore, $T_{\text{Welch}} = 30T_p$ was adopted for the studies of the present thesis. Note that in section 1.3.3 confidence intervals resulting from the Welch smoothing are introduced.

b) Spectrum Parameters

Sets of parameters are derived from the spectra. They give a quick and efficient overview of the wave field characteristics. We first define the n^{th} spectrum moment as

$$m_n = \int_0^{f_{\text{max}}} f^n S(f)\,\mathrm{d}f \tag{1.18}$$

Per definition m_0 equals the variance of the free surface elevation time series, and $\sigma_\eta = \sqrt{m_0}$ is associated the standard deviation. The significant wave height H_s follows as

$$H_s = 4\sqrt{m_0} \tag{1.19}$$

As the spectrum is smoothed and sensitive to the number of waves in the record, H_s values obtained from (Eq. 1.19) are less accurate than those obtained by directly using the variance of

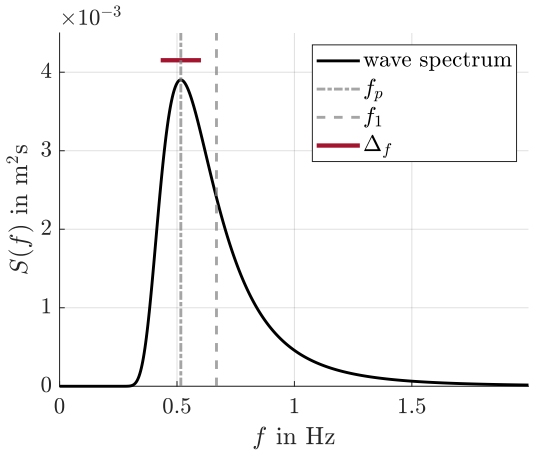

Figure 1.8 – Spectral parameters (GOM scale 100 shape)

the temporal signals,

$$H_s = 4\sqrt{\mathrm{var}_t(\eta(t))} \tag{1.20}$$

The latter definition will be used.

Figure 1.8 presents two characteristic frequencies. The first one is the peak frequency f_p (associated with the peak period T_p), which is computed as the abscissa of the maximum spectrum value. The second one is the mean frequency (associated with the mean period T_1). It is defined as

$$f_1 = m_1/m_0 \tag{1.21}$$

The corresponding wavelengths and wavenumbers λ_p, λ_1, k_p and k_1 are deduced using the dispersion relation (see eq. 1).

The red line in Figure 1.8 displays the dimensional spectral width Δ_f. Several methods can be used to compute the latter quantity. In this thesis, we follow Serio et al. (2005) recommendations. The non-dimensional spectral width ν_w is defined with the peakedness method,

$$\nu_w = \frac{1}{Q_p\sqrt{\pi}} \tag{1.22}$$

with $Q_p = \frac{2}{m_0^2}\int_0^{f_{\max}} f\,S^2(f)\,\mathrm{d}f$. Δ_f follows as

$$\Delta_f = \nu_w\sqrt{2log(2)}f_p \tag{1.23}$$

The steepness is computed either as mean steepness $\varepsilon_1 = k_1\sigma_\eta$ or as peak steepness $\varepsilon_p = H_s/\lambda_p$.

c) Statistical moments

$\eta(t)$ can be analyzed as a statistical random variable. The probability density function f_η can be estimated and its moments are interesting indicators that quantify the linear and nonlinear features of the data. For a given free surface elevation value h, $f_\eta(h)$ is defined so that the probability $P(\eta \in [h;h+dh]) = f_\eta(h)dh$. The moments of interest, estimated from the recorded discrete η time series, are:

$$\overline{\eta} = \sum_n \eta_n/N \tag{1.24}$$

the mean value,

$$var_t(\eta) = \overline{((\eta-\overline{\eta})^2} \tag{1.25}$$

the variance (linked to the standard deviation as $\sigma_\eta = \sqrt{var_t(\eta)}$),

$$\lambda_3 = \overline{(\eta-\overline{\eta})^3}/\sigma_\eta^3 \tag{1.26}$$

the skewness and,

$$\lambda_4 = \overline{(\eta-\overline{\eta})^4}/\sigma_\eta^4 \tag{1.27}$$

the kurtosis. The linear theory predicts that for sufficiently long records, η is a Gaussian variable (see for instance a demonstration in Massel (1996)), i. e.

$$f_{\eta_{\text{linear}}}(h) = \frac{1}{\sigma_\eta\sqrt{2\pi}}\exp\left(-\frac{1}{2}\left(\frac{h-\overline{\eta}}{\sigma_\eta}\right)^2\right) \tag{1.28}$$

In order to facilitate the interpretation of the moments, Figure 1.9 presents f_η for three datasets, all generated using `GOM` sea state as input. `Dataset A` corresponds to the artificial linear signals already studied in the paragraph a). `Dataset B` consists of O.E. tank measurements at $x = 1.5\lambda_p$, while `Dataset C` gathers towing tank measurements at $x = 28\lambda_p$. For all the three cases $\overline{\eta} = 0$, which is a consistent characteristic of free surface elevation signals. Additionally,

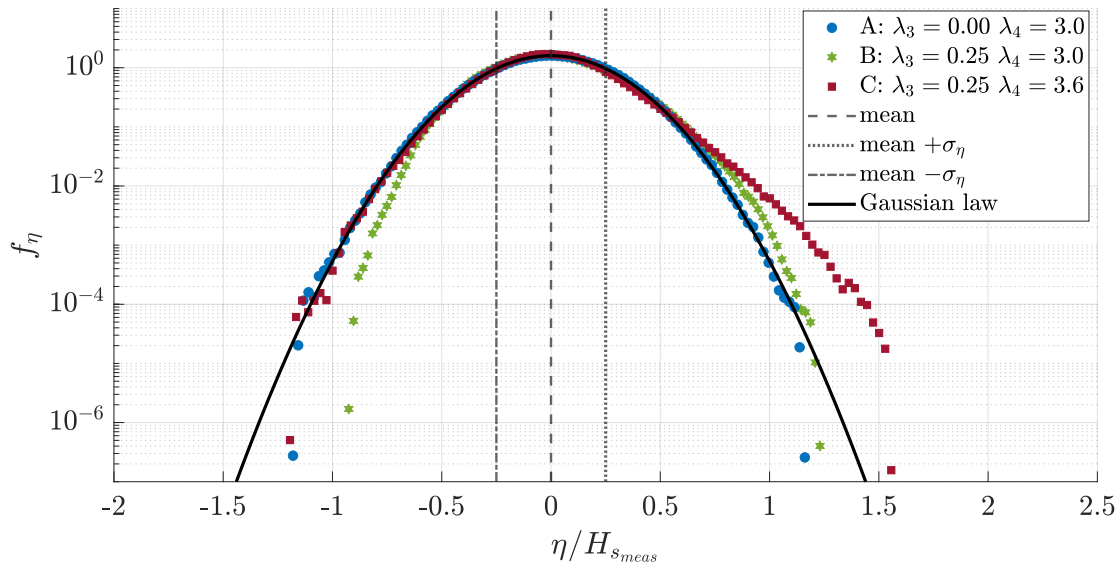

Figure 1.9 – η probability density function; data from `GOM` sea state; A: artificial linear signal; B: O.E. tank measurements at $x = 1.5\lambda_p$; C: Towing tank measurements at $x = 28\lambda_p$

by definition $\sigma_\eta = 1/4H_{s_{meas}}$. See the dotted and dashed vertical lines in Figure 1.9.

As expected, the linear `Dataset A` lies on the Gaussian shape exhibiting $\lambda_3 = 0$ and $\lambda_4 = 3$. The skewness measures the asymmetry of the distribution. In the two experimental datasets `Dataset B` and `Dataset C` $\lambda_3 = 0.25$. This means that the negative η values are smaller and the positive values larger than those predicted by the Gaussian model. Concretely, the wave's troughs are flatter and the crests are sharper. As will be further explained in Sec. 2.1.1, the asymmetry is induced by bound waves that do not obey the dispersion relation and result from second-order nonlinear interactions.

Kurtosis characterizes the distribution tail. Consequently, it is often used a simple indicator of the presence of extreme events in a time series (see for example Kirezci et al. (2021); Annenkov and Shrira (2009); Christou and Ewans (2014)). For Gaussian signals, $\lambda_4 = 3$. Values larger than three indicate larger $|\eta|$ values at a given probability level, implying more extreme waves than those predicted by the Gaussian distribution, both for troughs ($\eta < 0$) and crests ($\eta > 0$). For instance, see the comparison between `Dataset B` and `Dataset C`. They have the same skewness but `Dataset C` have a larger kurtosis.We observe that the tail of the `Dataset C` distribution show significant deviations from the `Dataset B` data, indicating more extreme $|\eta|$ values. As it will be explained in Sec. 2.1.2, the kurtosis increases with the distance from the wave maker due to third-order nonlinear wave interactions.

d) Zero crossing waves distributions

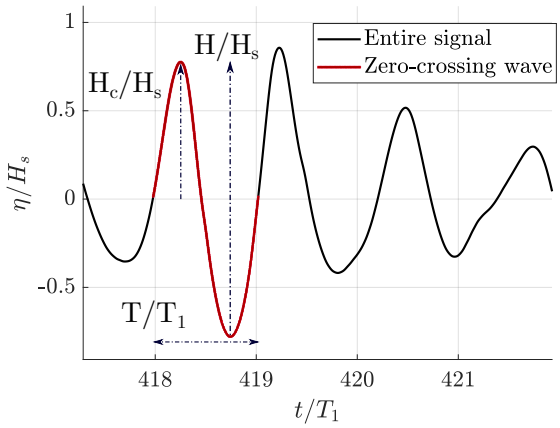

Figure 1.10 – Definition of a up-zero-crossing wave

The $\eta(x,t)$ time series can be decomposed into a list of individual up-zero-crossing waves, each characterized by a crest height H_c, a period T, and crest-to-trough height H, see Figure 1.10. The statistics of the wave-by-wave features are analyzed by computing the probability of exceedance (POE) of the wave heights, crests, and periods. For example, for a given H_c value, the crest POE corresponds to the probability to find a crest of size h_c larger than H_c.

$$POE(H_c) = P(h_c > H_c) \tag{1.29}$$

For a data sample $(H_c)_i$ the POE estimate is computed as

$$POE(H_{c_i}) = (N - n_i)/(N) \tag{1.30}$$

with n_i the number of events smaller than H_{c_i} and N the total number of events. In this thesis we will mainly focus on the crest distribution. The latter is usually compared to references, in order to assess the severity of the wave field ITTC (2021); Det Norske Veritas (2010). Various benchmarks will be provided in Sec. 2.2.

The crest probability distribution of a single realization is denoted as PDSR. In ocean engineering studies, the duration of a realization usually do not exceed $1000T_p$. As a result, the PDSR curve can be very different from one realization to another (Huang and Zhang, 2018). To characterize entire datasets, we use the ensemble realization, denoted as PDER, which is the probability distribution that includes all the events measured over the N_{run} realizations.

It is also interesting to evaluate the joint distribution of H and T to have a more complete view of the wave fields composition. See for instance Forristall (2017) for a detailed analysis of this quantity, along with theoretical predictions.

e) Wave Envelope characteristics / Wave groupiness

Besides, to analyze the structure of the wave field (the organization of wave packets), particular attention will be given to the properties of the wave envelope. These aspects have been extensively studied over the past years, as they have a significant role in coastal and offshore engineering (Mase, 1989; List, 1991; Haller and Dalrymple, 1995; Saulnier et al., 2011; Huang and Dong, 2021). A wave group is usually defined as a sequence of waves over a given threshold. Its properties are known to have a strong influence on offshore structures' stability, wave breaking, and the number of extreme events in the wave field (Huang and Dong, 2021). To account for the number and the severity of the wave groups in a given wave field, the notion of groupiness has been established. A set of groupiness factors (GF) can be defined (Haller and Dalrymple, 1995; Huang and Guo, 2017), the main idea being to quantify the intensity of the wave groups through the use of the standard deviation of the envelope or the instantaneous energy of the wave field. Here follows a brief description of the two groupiness factors computed in the present PhD thesis. More detailed definitions and characteristics of those quantities can be found in Huang and Dong (2021).

The first definition relies on the wave envelope estimation. The envelope $\Psi(t)$ is computed through the use of the Hilbert transform $\hat{\eta}(t)$ of the free surface elevation time series (Hudspeth and Medina (1989)).

$$\Psi(t) = |\eta(t) + i\hat{\eta}(t)| \tag{1.31}$$

Then, the groupiness factor is computed as

$$\mathrm{GF} = \frac{\sqrt{2}\sigma_\Psi}{\overline{\Psi}} \tag{1.32}$$

with $\overline{\Psi}$ and σ_Ψ the mean and the standard deviation of the wave envelope.

Through the use of the smoothed instantaneous wave energy history approach (hereafter SIWEH), another definition of the groupiness factor was established in Funke and Mansard

(1980). The procedure relies on the computation of the instantaneous wave energy

$$I_S(t) = \frac{1}{T_p}\int_{-\infty}^{+\infty} \eta^2(t+\xi)Q(\xi)d\xi \tag{1.33}$$

with

$$Q(\xi) = \begin{cases} 1-|\xi/T_p| & \text{if } \xi \in [-T_p, T_p] \\ 0 & \text{otherwise.} \end{cases} \tag{1.34}$$

Similarly to the envelope method, the groupiness factor is then obtained by computing the standard deviation of $I_S(t)$.

$$\mathrm{GF_{SIWEH}} = \frac{1}{\overline{I_S(t)}}\sqrt{\frac{1}{t_{\mathrm{end}}-t_{\mathrm{beg}}}\int_{t_{\mathrm{beg}}}^{t_{end}}(I_S(t)-\overline{I_S(t)})^2 dt} \tag{1.35}$$

with t_{beg} and t_{end} defining the time window analysis of the considered free surface elevation time series.

Groupiness factors together with interpretations and visualizations in the time domain will be provided, for instance, in Sec. 4.3.1.

f) High-Order spectral analysis

Water wave propagation is nonlinear. This means that the frequency components of the wave fields interact with each other and produce new frequency components. To track these interactions, high-order spectral analysis can be used. The wave spectrum is the spectrum of the 2^{nd} moment of the free surface elevation distribution (the variance). Similarly, high-order spectra are the spectra of higher-order f_η-moments (skewness and kurtosis). They evaluate the phase coherence between 3 frequency components (bispectrum) or 4 frequency components (trispectrum). This allows for the identification and quantification of the 3 and 4 waves nonlinear interactions (second and third-order nonlinear effects respectively). We will begin by defining the bispectrum and then shift our focus to the trispectrum. Note that more definitions, interpretations, and applications can be found in Collis et al. (1998); Lagoutte et al. (1989); Ewans et al. (2021).

Bispectrum For a continuous free surface elevation signal $\eta(t)$, the power density bispectrum is a 2D complex quantity defined for a frequency couple (f_1,f_2) as

$$S_{xxx}(f_1,f_2) = \lim_{\Delta T\to+\infty} \frac{1}{\Delta T} E\{\mathscr{F}_\eta(f_1)\mathscr{F}_\eta(f_2)\mathscr{F}_\eta{}^*(f_1+f_2)\} \tag{1.36}$$

$\mathscr{F}_\eta(f)$ is for the Fourier transform of a $\eta(t)$ segment with a duration of ΔT, and $E\{\}$ is the mean operator over several $\eta(t)$ segments. The segment can be either an entire realization or a smaller window. The mean operation is necessary to discriminate the frequencies resulting from nonlinear interactions from the frequencies already present in the initial linear wave field. It becomes clearer when writing the 1-window bispectrum as:

$$\frac{1}{\Delta T}\mathscr{F}_\eta(f_1)\mathscr{F}_\eta(f_2)\mathscr{F}_\eta{}^*(f_1+f_2) = B_{12}e^{i\phi_{12}} \tag{1.37}$$

with B_{12} the modulus of the complex bispectrum evaluated at (f_1,f_2) and ϕ_{12} its phase. Noting, ϕ_1, ϕ_2 and ϕ_{1+2} the phase of the f_1, f_2 and f_1+f_2 components,

$$\phi_{12} = \phi_1 + \phi_2 - \phi_{1+2} \tag{1.38}$$

In all cases, when ΔT is sufficiently large, B_{12} is the same for all the windows. However, for the phases, it depends on whether the f_1+f_2 frequency results from an interaction of f_1 and f_2 or not. If f_1+f_2 results from an interaction of f_1 and f_2, ϕ_{12} is the same for all the windows, so $E\{B_{12}e^{i\phi_{12}}\}$ is a priori a nonzero value. Conversely, if the frequency component at $f = f_1+f_2$ corresponds to an independent component, ϕ_{12} is a random value varying from one window to another, and $E\{B_{12}e^{i\phi_{12}}\}$ approaches zero with a sufficient number of windows. Consequently, the bispectrum characterizes for each frequency couple (f_1,f_2) the amplitude of their interaction.

Moreover, we can also interpret the bispectrum as the identification of the contribution of each couple (f_1,f_2) to the asymmetry of the η distribution. Its integration over all (f_1,f_2) pairs equals the skewness of the free surface elevation (see the demonstration in Collis et al. (1998)).

As the measured free surface elevation signals are discrete data, we rely on the following definition:

$$S_{xxx}^{(k,l)\in[1:N]^2}(f_k,f_l) = \lim_{N\to+\infty} \frac{\delta t^3}{\Delta T} E\{\mathscr{F}_\eta^d(f_k)\mathscr{F}_\eta^d(f_l)\mathscr{F}_\eta^{d*}(f_k+f_l)\} \tag{1.39}$$

Trispectrum The bispectrum characterizes the interaction of two frequency components f_1 and f_2. Similarly, the trispectrum characterizes the interaction of three frequencies f_1, f_2 and f_3. It is a 3D complex quantity.

For a continuous free surface elevation signal $\eta(t)$, the power density trispectrum is defined as

$$S_{xxxx}(f_1,f_2,f_3) = \lim_{\Delta T\to+\infty} \frac{1}{\Delta T} E\{\mathscr{F}_\eta(f_1)\mathscr{F}_\eta(f_2)\mathscr{F}_\eta(f_3)\mathscr{F}_\eta{}^*(f_1+f_2+f_3)\} \tag{1.40}$$

We can also interpret the trispectrum as the identification of the contribution of each triplet (f_1,f_2,f_3) to the kurtosis of the η distribution. Its integration over its 3D frequency domain equals the kurtosis of the free surface elevation. The demonstration can again be found in Collis et al. (1998).

As the measured free surface elevation signals are discrete data, we rely on the following definition:

$$S_{xxxx}^{(k,l,m)\in[1:N]^3}(f_k,f_l,f_m) = \lim_{N\to+\infty} \frac{\delta t^4}{\Delta T} E\{\mathscr{F}_\eta^d(f_k)\mathscr{F}_\eta^d(f_l)\mathscr{F}_\eta^d(f_m)\mathscr{F}_\eta^{d*}(f_k+f_l+f_m)\} \tag{1.41}$$

Trispectrum slices The trispectrum is a 3D quantity, making it challenging to visualize. To overcome this difficulty, the analysis will focus on relevant 2D slices.

The trispectrum analysis will be primarily used to track the nonlinear interactions responsible for the spatial evolution of the wave field statistics (see Chapter 4). The literature often emphasizes the significant role of modulational instabilities, also known as Benjamin Feir instabilities (Benjamin and Feir, 1967), which result from the degenerate four waves interaction:

$$(f_1^{\text{interact}} = f_0 - \delta_{\text{BF}}\,,\quad f_2^{\text{interact}} = f_0 + \delta_{\text{BF}}\,,\quad f_3^{\text{interact}} = f_0\,,\quad f_4^{\text{interact}} = f_0) \tag{1.42}$$

verifying

$$f_1^{\text{interact}} + f_2^{\text{interact}} = f_3^{\text{interact}} + f_4^{\text{interact}} \tag{1.43}$$

with f_i^{interact} the frequencies of the four interacting wave field components. (eq. 1.42) represents the interaction between a leading frequency f_0 and its side bands $f_0 \pm \delta_{\text{BF}}$.

To track this interaction, we will study the following trispectrum slice

$$S_{xxxx}^{BFI}(f_1,f_2) = S_{xxxx}(f_1,f_2,-(f_1+f_2)/2) \tag{1.44}$$

Indeed, per definition,

$$S^{BFI}_{xxxx}(f_1,f_2) = \lim_{\Delta T\to+\infty}\frac{1}{\Delta T}E\{\mathscr{F}_\eta(f_1)\mathscr{F}_\eta(f_2)\mathscr{F}_\eta(-(f_1+f_2)/2) \\ \mathscr{F}_\eta{}^*(f_1+f_2-(f_1+f_2)/2)\} \tag{1.45}$$

and using the property of the Fourier transform for a real function (which applies to η), $\mathscr{F}_\eta(-f) = \mathscr{F}_\eta{}^*(f)$, we obtain:

$$S^{BFI}_{xxxx}(f_1,f_2) = \lim_{\Delta T\to+\infty}\frac{1}{\Delta T}E\{\mathscr{F}_\eta(f_1)\mathscr{F}_\eta(f_2)\mathscr{F}_\eta{}^*((f_1+f_2)/2)\mathscr{F}_\eta{}^*((f_1+f_2)/2)\} \tag{1.46}$$

Therefore, $S^{BFI}_{xxxx}(f_1,f_2)$ tracks the interaction quartets of type

$$(f_1^{\text{interact}} = f_1\,,\quad f_2^{\text{interact}} = f_2\,,\quad f_3^{\text{interact}} = (f_1+f_2)/2\,,\quad f_4^{\text{interact}} = (f_1+f_2)/2) \tag{1.47}$$

which is equivalent to (eq. 1.42), by writing $f_0 = (f_1+f_2)/2$ and $\delta_{\text{BF}} = |f_2-f_1|/2$.

This leads to a 2D quantity (degree of freedom f_1 and f_2) that can be more easily displayed. As the trispectrum definition includes the raw Fourier transform of the free surface elevation, f_1 and f_2 can be negative frequencies. This leads to several symmetries:

$$S^{BFI}_{xxxx}(f_1,f_2) = S^{BFI}_{xxxx}(f_2,f_1) \tag{1.48}$$

which makes $f_2 = f_1$ line an axis of symmetry; and

$$S^{BFI}_{xxxx}(-f_1,-f_2) = S^{BFI}_{xxxx}(f_1,f_2) \tag{1.49}$$

together with,

$$S^{BFI}_{xxxx}(-f_1,f_2) = S^{BFI}_{xxxx}(f_1,-f_2) \tag{1.50}$$

which make $f_2 = -f_1$ line an axis of symmetry.

Examples of trispectra slices will be provided in Chapter 4, together with interpretation.

1.3.3 Sampling Variability

The quantities of interest computed from the wave measurements are stochastic, due to the randomness of the wave phases. Enough data should then be analyzed to compute relevant spectrum and wave-by-wave statistics. The statistical convergence, namely the sampling variability,

is studied in this subsection.

Description of the datasets To quantify sampling variability, quantities of interest (spectrum, H_s, λ_3, λ_4, crest PDER) were computed from 6 datasets, varying the analysis duration T_{analyzed}. The latter is normalized by the peak period of the design spectrum $T_{p_{\text{target}}}$.

The first three datasets are artificial linear data computed from `ss6g5` scale 120, `GOM` scale 50, and `ss6` scale 40 design spectra. The three others are experimental results of `ss6g5` scale 120 measured at $x = 53\lambda_p$, `GOM` scale 50 measured at $x = 2\lambda_p$ and `ss6` scale 40 measured at $x = 3\lambda_p$. The objective is to investigate the statistical convergence respectively for nonlinear extreme but nonbreaking conditions, nonlinear breaking conditions, and mild wave conditions. Complementary, the linear artificial data allow for discriminating nonlinear and experimental phenomena from pure sampling variability effects.

Each artificial dataset is composed of 30 $2048s$-realizations. Only 60% of the time series are analyzed to induce noise in the spectrum (i. e. for one realization, $\Delta T = 0.6T_{\text{repeat}} = 1230s$ which corresponds to $\Delta T \in [500, 1000]T_{p_{\text{target}}}$ depending on the wave condition). Each experimental dataset also contains 30 realizations of duration $\Delta T \in [500, 1000]T_{p_{\text{target}}}$. When analyzing all the realizations, this leads to T_{analyzed} values larger than $15000T_{p_{\text{target}}}$. To vary T_{analyzed}, we change the number of realizations included in the analysis.

Influence of T_{analyzed} on the stochastic quantities Figure 1.11 presents the results. The convergence of the spectrum is estimated using the relative spectrum error

$$E_{S,\text{conv}}(f) = (S(f) - S_{\text{conv}}(f))/S_{\text{conv}}(f) \tag{1.51}$$

across the range $f \in [\frac{3}{4}f_p, \frac{3}{2}f_p]$. $S_{\text{conv}}(f)$ is the estimation of the statistically converged spectrum, computed with all the 30-realization data (maximum T_{analyzed} available). Figure 1.11b displays,

$$E^{\text{mean}}_{S,\text{conv}} = \frac{1}{N}\sum_{j=1}^{N} |E_{S,\text{conv}}(f_j)| \tag{1.52}$$

as a function of $T_{\text{analyzed}}/T_{p_{\text{target}}}$. In (eq. 1.52), (f_j) with j from 1 to N corresponds to the frequency vector covering the frequency range $f \in [\frac{3}{4}f_p, \frac{3}{2}f_p]$.

The convergence of H_s, skewness, and kurtosis is assessed by computing the relative or absolute difference from H_s^{conv}, λ_3^{conv} and λ_4^{conv}, the converged values obtained by analyzing the entire datasets.

With the exception of the `ss6g5` experiments, there is no significant difference among

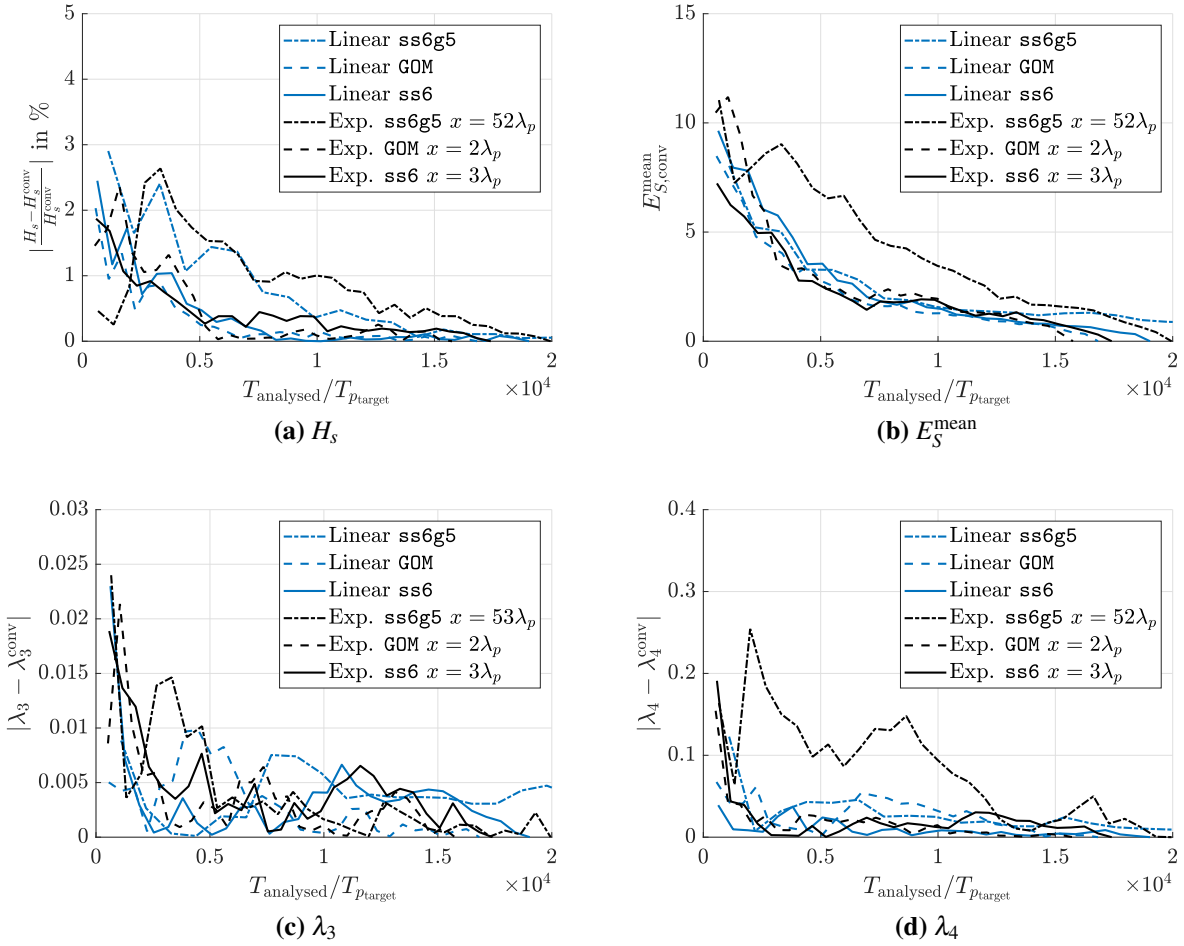

(a) H_s **(b)** E_S^{mean}

(c) λ_3 **(d)** λ_4

Figure 1.11 – Evolution of the stochastic quantities of interest as a function of the number of analyzed events

the datasets (either they are artificial, experimental, breaking, or non-breaking). With only one realization (the first point of the curves), the H_s error is already small ($\approx 3\%$). However, $E_{S,\text{conv}}^{\text{mean}} \approx 10\%$; $|\lambda_3 - \lambda_3^{\text{conv}}|$ reaches 0.025, representing more than 10% of error relative to the measured skewness values, which range from 0.1 to 0.3; and $|\lambda_4 - \lambda_4^{\text{conv}}|$ reaches 0.2, representing more than 5% of error.

For all the cases except `ss6g5` experiments, the convergence errors of spectrum, skewness and kurtosis can be considered as acceptable respectively for $T_{\text{analyzed}} \geq 4000 T_{p_{\text{target}}}$ ($E_{S,\text{conv}}^{\text{mean}} \leq 5\%$), $T_{\text{analyzed}} \geq 2500 T_{p_{\text{target}}}$ ($|\lambda_3 - \lambda_3^{\text{conv}}| \leq 0.01$), and $T_{\text{analyzed}} \geq 2500 T_{p_{\text{target}}}$ ($|\lambda_4 - \lambda_4^{\text{conv}}| \leq 0.1$).

For `ss6g5` experiments data, the sampling variability is larger. This wave field exhibits

a significant kurtosis $\lambda_4^{\text{conv}} = 3.6$, indicating a high probability of occurrence for extreme events. As detailed in Chapter 4, numerous nonlinear interactions occurred. This appears to affect the sampling variability. For this wave field, the kurtosis and spectrum need respectively $T_{\text{analyzed}} \geq 10000 T_{p_{\text{target}}}$ and $T_{\text{analyzed}} \geq 7000 T_{p_{\text{target}}}$ to be considered as statistically converged ($|\lambda_4 - \lambda_4^{\text{conv}}| \leq 0.1$ and $E_{S,\text{conv}}^{\text{mean}} \leq 5\%$).

From these results, it appears that i) the significant wave height is almost statistically converged with one realization only, ii) $T_{\text{analyzed}} \geq 4000 T_p$ allows for the convergence of the spectrum, kurtosis, and skewness for most of the cases, iii) for nonlinear wave fields exhibiting large kurtosis values $T_{\text{analyzed}} \geq 10000 T_p$ is needed, and iv) breaking has no specific effects.

Theoretical intervals Complementary, theoretical tools exist to quantify sampling variability. Each spectrum can be bounded by a 95% confidence interval, characterizing the error induced by the Welch estimator (Welch, 1967a). We define the Welch error at frequency f,

$$E_{\text{Welch}}(f) = \frac{U_{\text{Welch}}^{up}(f) - U_{\text{Welch}}^{low}(f)}{2S(f)} \tag{1.53}$$

with $U_{\text{Welch}}^{up}(f)$ and $U_{\text{Welch}}^{low}(f)$ the 95% confidence intervals of the spectral estimation based on the Welch method. As $S(f)$ is the mean spectrum over N_{run}, $U_{\text{Welch}}^{up}(f)$ and $U_{\text{Welch}}^{low}(f)$ are actually averages of the individual spectra confidence intervals, divided by $\sqrt{N_{\text{run}}}$ (following the usual uncertainty laws (ISO/IEC, 2008)). Additionally, binomial confidence intervals such as Jeffrey's intervals (see Brown et al. (2001)) can be computed to estimate the sampling variability error of the crest POE.

Figure 1.12 presents the evolution of the later bounds for the 6 datasets previously studied. $E_{\text{Welch}}(f)$ is provided at peak frequency $f = f_p$ and the Jeffrey intervals are plotted for the sole probability 10^{-3}. The results only depend on the number of waves T_{analyzed}. Therefore, no differences are observed between the datasets. $E_{\text{Welch}}(f_p)$ curve shape follows the already observed $E_{S,\text{conv}}^{\text{mean}}$ convergence pattern. At $T_{\text{analyzed}} = 4000 T_{p_{\text{target}}}$ (previously recommended value) the error reaches 13%, and at $T_{\text{analyzed}} = 20000 T_{p_{\text{target}}}$ it decreases to 6%. These values are greater than the corresponding $E_{S,\text{conv}}^{\text{mean}}$ ones. This difference is attributed to the fact that Welch confidence intervals consider both the sampling variability and the bias of the smoothing method.

The Jeffrey intervals, bounding the estimated POE values (here 10^{-3}), reach a pseudo convergence state for $T_{\text{analyzed}} > 10000 T_{p_{\text{target}}}$ (for larger-duration datasets the reliability of the results improves but the error does not significantly decreases). This is in accordance with the kurtosis convergence previously studied. Figures 1.11 and 1.12 will be used as references to

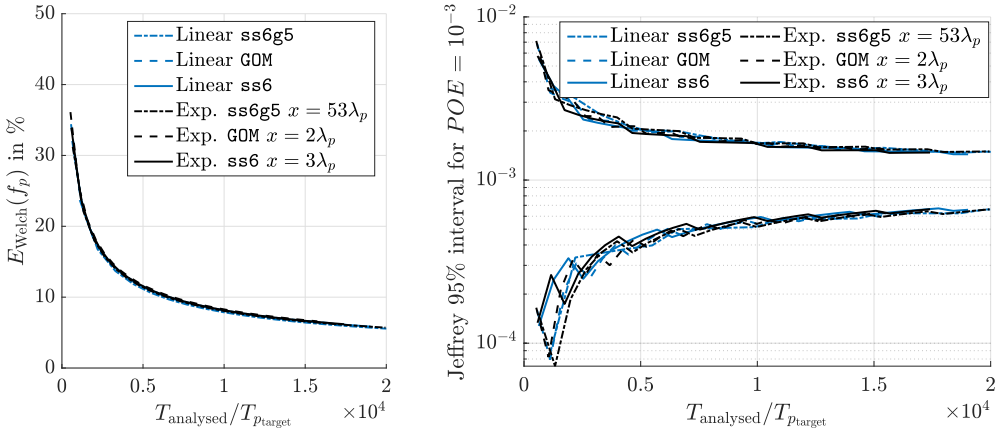

(a) $E_{\text{Welch}}(f_p)$ **(b)** Jeffrey intervals

Figure 1.12 – Prediction of the sampling variability using confidence intervals

estimate the sampling variability error of the results presented in this thesis.

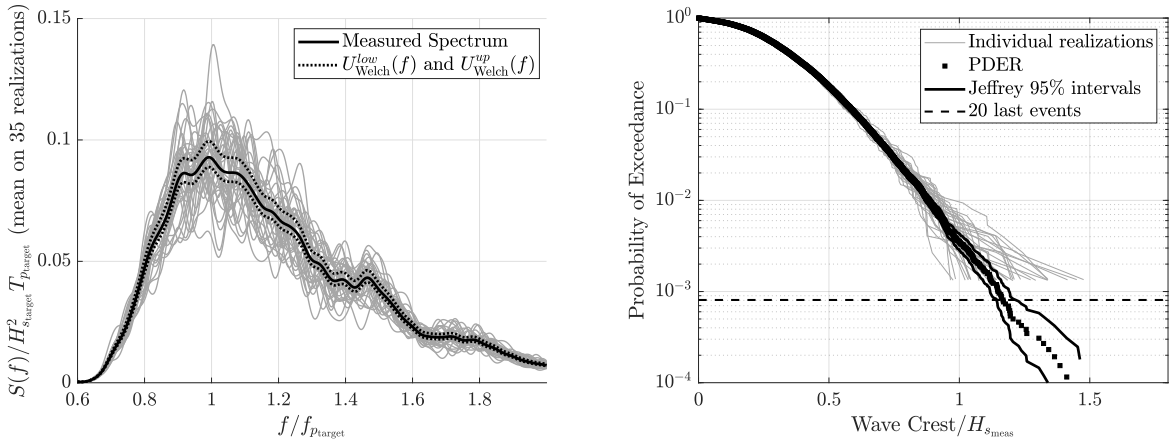

(a) Spectrum **(b)** Crest PDER

Figure 1.13 – Prediction of the sampling variability using confidence intervals, example with `ss6` sea states scale 40 at $x = 104m = 53\lambda_p$. Grey lines correspond to individual realizations, each of duration $\Delta T = 580T_{p_{\text{target}}}$

Example As an example, Figure 1.13 displays the entire intervals for a large dataset of `ss6` at scale 40 generated in the ECN O.E. tank and measured at $x = 3\lambda_p$. Thirty five $580T_{p_{\text{target}}}$-realizations

are analyzed, which leads to $T_{\text{analyzed}} = 20000T_{p_{\text{target}}}$. The corresponding $E_{\text{Welch}}(f_p)$ is slightly lower than 6%. For both the spectrum and crest distribution, the individual realization curves show strong deviations from one another. One realization corresponds to $T_{\text{analyzed}} = 580T_{p_{\text{target}}}$ (20 min at model scale and 2 hours at full scale). This is not enough to compute meaningful stochastic quantities.

Computing the mean spectrum and the crest PDER, displaying their confidence intervals, and ensuring $T_{\text{analyzed}} > 10000T_{p_{\text{target}}}$ seems to be a relevant procedure to limit and quantify the sampling variability. Furthermore, when analyzing the crest distributions, we set an uncertainty threshold at the probability level of the 20^{th} most extreme event due to excessive errors at smaller probabilities.

1.3.4 Sensibility to filters

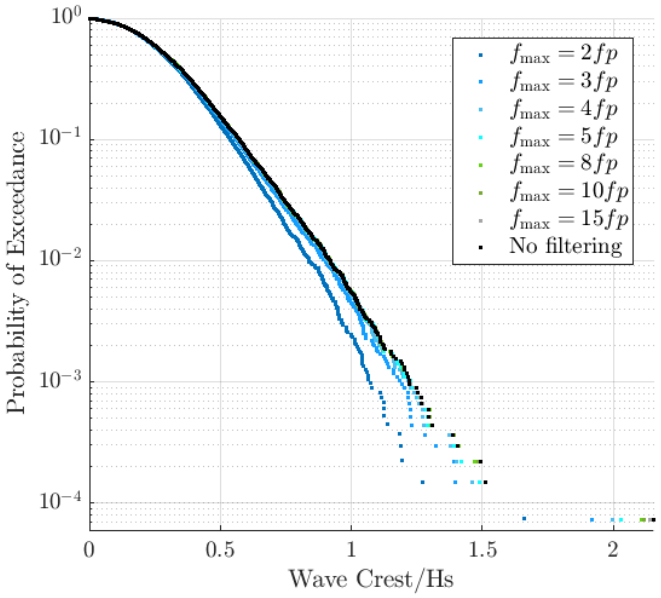

Figure 1.14 – Influence on the high frequency cut off on the crest distribution, `ss6g5` sea states scale 120 ECN towing tank measurements at $x = 53\lambda_p$, $f_{\text{sample}} = 200$ Hz

To remove noise in the experimental data (for example due to unexpected vibrations of the wave gauges) high frequencies are filtered. To data presented in this thesis are filtered with a frequency cut-off $f_{\max}$ set to $15f_p$. To ensure that this process does not affect the quantities of interest, we will briefly evaluate its influence on the crest distribution. The latter is expected

to be the more affected quantity. It is known to be closely related to the spectrum tail, which is partially cut when high frequencies are filtered.

Figure 1.14 presents an extreme crest distribution, computed from `ss6g5` sea state data (measured at $x = 53\lambda_p$ in the Towing tank), for several $f_{\max}$ values. Note that the absence of filtering corresponds to a $f_{\text{sample}}/2$ cut-off according to the Shannon criteria (f_{sample} being the sampling frequency of the measured signal). For the present case, $f_{\text{sample}} = 200$ Hz$= 220 f_p >> f_p$. The $f_{\text{sample}}/2$ cut off has therefore no influence on the crest distribution.

We observe that for $f_{\max} > 10 f_p$ the filtering has almost no effect on the crest PDER, even for the very extreme events with probabilities below 10^{-4}. However, for smaller $f_{\max}$, the severity of these events decreases at the same probability level. The extreme crests are lower. The effect is more pronounced for $f_p < 2 f_p$, as we enter the significant energy content of the spectrum. The adopted $f_{\max} = 15 f_p$ appears to be a relevant cut-off.

1.3.5 Deterministic comparisons

Besides the analysis of the stochastic quantities, it is also of major importance to characterize and compare time domains deterministic signals.

To this aim, we introduce a comparison method based on the Pearson correlation coefficient. For two free surface elevation series $\eta_1(t)$ and $\eta_2(t)$ having the same length and time resolution, we express the Pearson correlation coefficient as

$$r(\eta_1, \eta_2) = \frac{\sum_{j=1}^{N} \eta_{1_i} \eta_{2_i}}{\sqrt{\sum_{j=1}^{N} {\eta_{1_i}}^2} \sqrt{\sum_{j=1}^{N} {\eta_{2_i}}^2}} \tag{1.54}$$

with $\eta_{1_i} = \eta_1(t_i)$ and $\eta_{2_i} = \eta_2(t_i)$, (t_i) being the time vector.

The deterministic comparison method follows. For a set of free surface elevation sequences $\eta_n(t)$, $n \in [1 : N_{\text{run}}]$, either we select an arbitrary reference run, or we compute the two-by-two Pearson correlation coefficients and select the run that exhibits the largest coefficients. Then, the runs are segmented into N_{Tp} T_p windows. In this thesis, we use $N_{\text{Tp}} = 5$. For each run, we compute, segment by segment, i) the time shift δt from the reference run (maximizing the correlation) and ii) the Pearson correlation coefficient between the unshifted segment and the corresponding segment of the reference run. This gives a deterministic error as a function of time. Examples of such comparisons will be provided throughout the manuscript.

CHAPTER 2

THEORETICAL PROPAGATION OF AN IRREGULAR SEA STATE IN A WAVE TANK ENVIRONMENT

The current thesis focuses on investigating unidirectional irregular wave fields propagating in deep-water wave tank environments. The problem involves numerous physical phenomena, and the research field has been significantly active in recent decades (as discussed in Introduction). This chapter provides a brief overview of the theoretical tools drawn from existing literature, that have been used in the present manuscript to interpret the results.

2.1 From linear to nonlinear sea states

2.1.1 Nonlinear physics in tanks

Figure 2.1 summarizes the phenomena influencing the evolution of the wave fields along the tank. The input wave sequences sent to the wave maker are linear (i.e. superpositions of frequency components with amplitudes following an input spectrum and random phases, see Sec. 1.2.2). However, the wave propagation equations are nonlinear (see Massel (1996) and Mei et al. (2005) books). The linear theory framework is only applicable to very low steepness sea states ($\varepsilon_p < 1\%$) and small distances/durations of propagation (because some nonlinear effects are cumulative). It is not suitable for the wave conditions studied in this thesis.

When accounting for second-order nonlinear terms, it is found that the self-interactions of each component lead to bound waves that do not obey the dispersion relation (Eq. 1) but affect the shape of the wave profiles. Indeed, they make the troughs flatter and the crests sharper (see the sketch at the top right-hand corner of Fig. 2.1). This occurs all along the domain. More

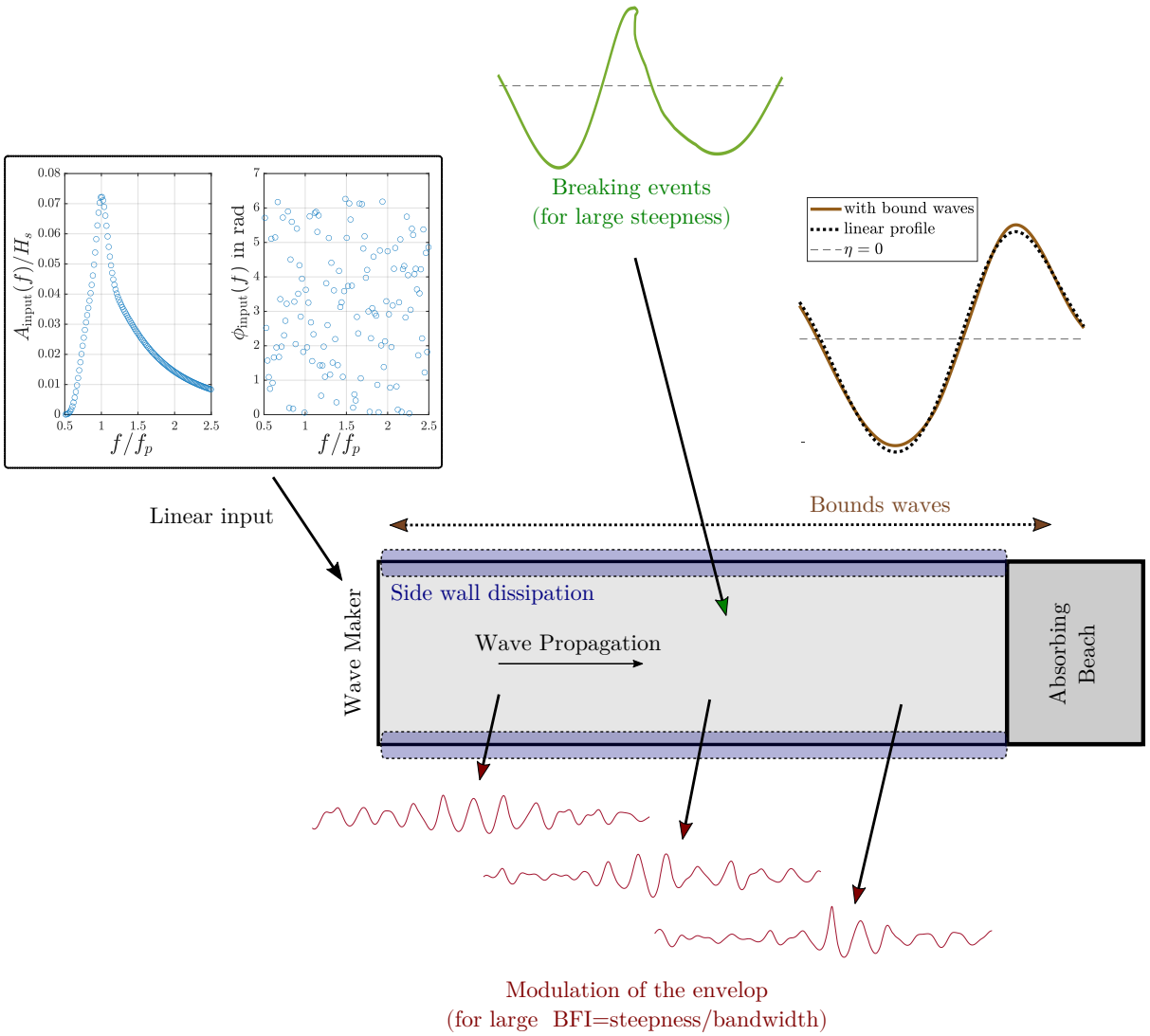

Figure 2.1 – Waves physics in a tank environment.

generally, as detailed in Forristall (2000) each second-order interaction of type

$$(f_1^{\text{interact}} = f_1\ , \quad f_2^{\text{interact}} = f_2\ , \quad f_3^{\text{interact}} = f_1 + f_2) \tag{2.1}$$

contributes to "the sharpening of the crests and flattening of the troughs ". In addition, second-order interactions of type

$$(f_1^{\text{interact}} = f_1\ , \quad f_2^{\text{interact}} = f_2\ , \quad f_3^{\text{interact}} = f_1 - f_2) \tag{2.2}$$

also occur. They lead to low-frequency bound waves that induce a "setdown of the water level under wave groups" (Forristall, 2000).

Besides, for steep and narrow spectra the third-order nonlinear terms lead to the modulation of the wave envelope (see the sketch at the bottom of Fig. 2.1), due to the "Benjamin Feir instabilities" (Benjamin and Feir, 1967). The disposition of the sea states to develop such instabilities can be quantified by the Benjamin Feir Index (BFI), the ratio between the steepness and the nondimensional spectral width, introduced in Janssen (2003). The definition used in the present thesis was suggested in Serio et al. (2005):

$$\mathrm{BFI} = \varepsilon_1 \sqrt{2} / \nu_w \tag{2.3}$$

with $\varepsilon_1 = k_1 \sigma_\eta$ the mean steepness and ν_w the nondimensional spectral width defined with the peakedness method (see Eq. 1.22). This definition of the BFI leads to smaller values than the one used in the famous Onorato et al. (2009) and Onorato et al. (2006) studies, the spectral width being defined in these papers using the half width at the half maximum.

Additionally, waves are also affected by dissipation mechanisms. In long and narrow wave tanks, the side walls friction dissipates the energy of the waves. In intermediate water depth conditions ($d/\lambda \in [1/20, 1/2]$), the bottom of the tank also contributes to the dissipation. An analytical model of these phenomenon will be provided in Sec. 2.3. Moreover, for large-steepness sea states ($\varepsilon_p > 3\%$), breaking events appear, reducing the amplitude of the most extreme crests and dissipating the spectrum.

2.1.2 Consequences of the nonlinear behavior for the quantities of interest

Now that the main phenomena have been introduced, we focus on their impact on the quantities of interest (spectrum and wave statistics).

Evolution of the wave spectrum Contrary to linear theory predictions, the wave spectrum evolves along the tank. For deep-water unidirectional nonlinear conditions, third-order wave interactions (including the previously mentioned Benjamin Feir instabilities) tend to modify the spectrum shape. To quantify this phenomenon Janssen (2003) carried out theoretical studies relying on the Zakharov equations as well as the NonLinear Schrödinger equations for water waves. The theory mostly predicts a broadening of the wave spectrum along the domain and a downshift of the peak. Additionally, breaking events tend to dissipate the energy of the spectrum, especially in the high-frequency domain ($f > f_p$). These phenomena have been

observed in a large number of experimental studies, see for instance Onorato et al. (2006); Shemer et al. (2010); Fadaeiazar et al. (2020b).

Evolution of the wave height statistics Concomitantly, the spatial evolution of wave height statistics in a wave tank environment is an intricate phenomenon. The wave maker motion is built from a free surface elevation sequence which corresponds to the linear superposition of the wave field random components. Therefore, the wave height statistics of this input sequence are Gaussian (see for example a demonstration in Mei et al. (2005) book). However, the generated waves are affected by nonlinearities and as a consequence, the statistical properties of the wave field differ from the Gaussian input. First, the bound waves induce a vertical asymmetry of the free surface elevation series ($\lambda_3 > 0$). This influences the crest distribution, leading to an increase in crest height at a given probability level compared to the linear prediction. Second, higher-order nonlinear effects lead to deviations in the tail of the crest distribution that strongly depend on the sea state characteristics and the distance from the wave maker.

With a domain of typical size (propagation length below 60 wavelengths), experimental observations show that the statistical quantities of the wave field vary with the distance from the wave maker (Onorato et al., 2006; Shemer et al., 2010; Cherneva et al., 2009). More precisely, the probability of extreme events increases along the tank. This is especially observed for nonlinear narrow-banded spectra i. e. large BFI sea states.

Predictions of the evolution of wave statistics Some theoretical tools have been developed over the years to predict the spatial evolution of wave statistics and to quantify the emergence of extreme events, known as rogue waves, along the tank. One of the most relevant approaches uses the framework of the nonlinear Schrodinger equations (NLS) for water waves. Janssen (2003) established an analytical evolution of the wave statistics from a Gaussian to a nonlinear converged wave field. It considers the influence of i) the wave conditions, ii) the water depth, and iii) the directionality. The quantity studied is the kurtosis of the free surface elevation, λ_4. It is found that for unidirectional waves, λ_4 increases along the tank before reaching a converged value, after a transition area that can reach dozens of wavelengths. The theory has been established under the assumption of weakly-nonlinear deep-to-intermediate-depth waves and narrow-banded wave spectra. A complete description can be found in Fedele (2015) and Fedele et al. (2016). Here follows a brief presentation of the main results.

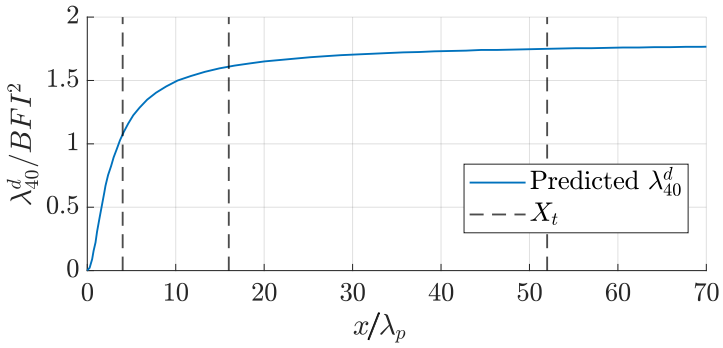

Figure 2.2 – Predicted Excess Kurtosis of the free surface elevation along the tank

The kurtosis of the free surface elevation can be decomposed into 3 terms,

$$\lambda_4 = 3 + \lambda_{40}^b + \lambda_{40}^d \tag{2.4}$$

with 3 the Gaussian prediction, λ_{40}^b the bound (Stokes) harmonic contribution and λ_{40}^d the dynamic component enhanced by nonlinear quasi-resonant wave-wave interactions. We can also define the excess kurtosis $\lambda_{40} = \lambda_4 - 3$

λ_{40}^b can be directly linked with the vertical asymmetry of the wave field, which is characterized by the skewness of the free surface elevation $\lambda_3 = \sqrt{\lambda_{40}^b/2}$. The evolution of λ_3 and λ_{40}^b depends on the wave steepness. Their asymptotic value can be predicted as $\lambda_3 = 3\varepsilon_1$ or equivalently $\lambda_{40}^b = 18\varepsilon_1^2$.

The dynamic excess kurtosis λ_{40}^d characterizes the third order nonlinear effects. Its accurate prediction is as a crucial step for the tracking of extreme events. The theoretical framework presented in Janssen (2003); Fedele (2015); Fedele et al. (2016) includes an analytical formula. For unidirectional cases, starting from a Gaussian wave field at the position $x = 0$,

$$\lambda_{40}^d(x) = 6\,\mathrm{BFI}^2\,\Im\left(\int_0^{\nu_w^2\omega_1 x/c_g} \frac{1}{\sqrt{1-2i\alpha+3\alpha^2}}d\alpha\right) \tag{2.5}$$

with c_g the group velocity at mean frequency and $\omega_1 = 2\pi/T_1$. $\Im$ is the imaginary part operator.

As an example, Fig. 2.2 presents λ_{40}^d spatial evolution along the ECN towing tank computed for `ss6g5` sea state at scale 120 (see Table 1.2). The theoretical excess kurtosis increases monotonically towards an asymptotic value directly linked with the BFI of the wave

spectrum,

$$\lambda_{40,max}^{d} = \mathrm{BFI}^2 \frac{\pi}{\sqrt{3}} \tag{2.6}$$

In this thesis, the BFI in (eq. 2.6) will be computed with the definition introduced in (eq. 2.3).

2.2 Statistical distributions of reference

The crest distribution i. e. crest probability of exceedance is a quantity of great importance for the analysis of irregular waves fields (see Sec. 1.3.2d). Therefore, sets of benchmarks have been consecutively developed over the years. They account for the different orders of nonlinearity in wave propagation. The shape of these theoretical distributions is parametrized with the properties of the generated wave spectrum. They are mainly used to compare the measured crest PDER and qualify the wave fields. This section provides the analytical description of the distributions used throughout the present thesis.

2.2.1 Background knowledge

This first paragraph introduces the background knowledge needed to derive and interpret the theoretical distributions.

Definitions Let introduce X, a continuous random variable. We define:

— the density probability function f_X, such as $P(X \in [x;x+dx]) = f_X(x)dx$

— the repartition function F_X, such as $F_X(x) = \int_{-\infty}^{x} f_X(x)dx = P(X \leq x)$

— the probability of exceedance POE_X such as $POE_X(x) = 1 - F_X(x)$

— the k-order moment $E(X^k) = \int_{-\infty}^{+\infty} x^k f_X(x)dx$

with $E()$ the expected value operator.

Stationary and ergodic random process For our problem, the random variable is the free surface elevation time series $\eta(t)$, which is a function of time. With N_{run} realizations (each realization, $\eta_n(t)$, defined over a duration ΔT), we can introduce the vertical and horizontal α averages of $\eta(t)$, denoted as H_α and V_α, respectively. For a given time t_0,

$$V_\alpha(t_0) = 1/N_{\mathrm{run}} \sum_{n=1}^{N_{\mathrm{run}}} {\eta_n}^{\alpha}(t_0) \tag{2.7}$$

For a given realization n,

$$H_{\alpha,n}(\Delta T) = 1/\Delta T \int_0^{\Delta T} {\eta_n}^{\alpha}(t)dt \tag{2.8}$$

A stochastic process is stationary if V_α does not depend on t_0 and ergodic in time if $V_\alpha = H_{\alpha,n}$, whatever n, for sufficiently large ΔT and N_{run}.

Normal/Gaussian law A random variable X following the normal law is characterized by

$$f_X(x) = \frac{1}{\sigma_X\sqrt{2\pi}} \exp\left(-\frac{1}{2}\left(\frac{x-E(X)}{\sigma_X}\right)^2\right) \tag{2.9}$$

with σ_X the standard deviation and $E(X)$ the mean.

2.2.2 Linear distributions

First, theoretical density probability functions and distributions were derived, within the frame of linear irregular wave fields.

a) $\eta(t)$, a stationary and ergodic Gaussian process

As a reminder, using a linear model, the free surface elevation at a given location can be expressed as

$$\eta(t) = \sum_{j=1}^{N_{\text{harmo}}} A(f_j) cos(2\pi f_j t + \phi(f_j)) \tag{2.10}$$

Relying on the assumptions below, it can be demonstrated (see for instance Massel (1996)) that $\eta(t)$ is a Gaussian process, stationary and ergodic in time, which follows the normal law of zero-mean and variance $m_0 = \sum_{j=1}^{N_{\text{harmo}}} S(f_j)\delta f_j$:

(i) N_{harmo} tend to ∞

(ii) the f_n frequencies are distinct, and equally distributed with a resolution δf

(iii) the amplitudes are deterministic and defined through:

$$A(f_j)^2 = 2S(f_j)\delta f \tag{2.11}$$

with $S(f)$ the wave spectrum.

(iv) the phases $\phi(f_j)$ are independent random variable following the uniform law $2\pi U_{[0;1[}$

b) Extension to the wave height distribution

As detailed in Sec.1.3.2d), $\eta(t)$ series are decomposed into lists of individual zero-crossing waves, each characterized by a crest height H_c and crest-to-trough height H. POE distribution of H and H_c are then computed.

Even when assuming a linear framework, deriving theoretical shapes for these distributions is not straightforward. The main difficulty is to analytically include the influence of the spectrum width. In Tayfun and Fedele (2007) paper, the authors gathers the most known theoretical wave height (H) distributions, derived over the past decades. They follow the same shape. For a given threshold h, the probability to find a zero-crossing wave of height $H > \sigma_\eta h$ is expressed as:

$$POE_H(h) = P(H/\sigma_\eta > h) = c_0 \exp\left(-c_1 h^2\right) = 1 - F_H(h) \tag{2.12}$$

c_1 and c_0 are parameters that depend on the model. The most used reference is the Rayleigh distribution. It corresponds to $c_1 = 1/8$ and $c_0 = 1$. It was derived for narrow-banded sea states and is an upper bound for finite band spectra. It has the advantage to accurately predict the asymptotic behavior of the POE (tail of the distribution) whatever the spectrum width.

c) Extension to the crest height distribution

To obtain the zero crossing crest height (H_c) distribution, we use the symmetry of the linear wave field, introducing the wave crest threshold $c = h/2$. Then,

$$POE_{H_C}(c) = P(H_C/\sigma_\eta > c) = P(H/\sigma_\eta > 2c) = c_0 \exp\left(-c_1 (2c)^2\right) \tag{2.13}$$

Subsequently, the Rayleigh distribution ($c_1 = 1/8$ and $c_0 = 1$, assuming a narrow-band spectrum) gives,

$$POE_{H_C}(c) = P(H_C/\sigma_\eta > c) = \exp\left(-c^2/2\right) \tag{2.14}$$

See for instance Longuet-Higgins (1952) for more details.

2.2.3 Consideration of 2^{nd}-order effects

Nonetheless, the bound waves emerging from second-order nonlinearities are known to break the vertical symmetry of the waves, making the troughs smaller and the crests larger. It has consequently significant effects on crest distributions. Note that the wave heigth POE is almost not affected (a small correction of the Rayleigh distribution can be done, see Tayfun

and Fedele (2007)). This paragraph focuses on the crest distributions accounting for the bound waves.

a) Tayfun Equation

First, theoretical works have been carried out by Tayfun (1990), leading to the Tayfun equation. The core of the theory is the use of the variable h_0 defined by

$$h = h_0 + \mu^* h_0^2/2 \tag{2.15}$$

that is to say,

$$h_0 = \frac{-1+\sqrt{1+2\mu^* h}}{\mu^*} \tag{2.16}$$

The steepness parameter μ^* is computed as

$$\mu^* = 3\varepsilon_1 \tag{2.17}$$

Replacing h per h_0 in the linear distributions of type (Eq. 2.13) models the bound waves influence. The formula has been extensively validated (see for instance Tayfun and Fedele (2007))

b) Forristall

Complementary, the Foristall semi-empirical distribution was also developed to consider the second order effects (Forristall, 2000). It is built with a large number of simulation results considering only 2^{nd}-order interactions in a given irregular wave filed. It is generally given as a reference by classification societies for ocean engineering studies, see *e.g.* Det Norske Veritas (2010). The mathematical definition is given below: for a given threshold c,

$$POE_{H_C}(c) = P(H_C > \sigma_\eta c) = \exp\left(-\left[\frac{\sigma_\eta c}{\alpha_r H_s}\right]^\beta\right) \tag{2.18}$$

For long-crested waves (i. e. unidirectional fields), $\alpha_r = 0.3536 + 0.2892 S_1 + 0.106 U_r$ and $\beta = 2 - 2.1597 S_1 + 0.0956 U_r^2$. The Ursell number and the integral steepness are defined as $U_r = \frac{H_s}{k_1^2 d^3}$ and $S_1 = \frac{2\pi}{g}\frac{H_s}{T_1^2}$.

2.2.4 Consideration of higher-order effects i.e. modulational instabilities

The theoretical distributions mentioned above assume an oceanic environment that is ergodic in time and stationary. However, some high-order nonlinear effects cumulative. Consequently, in addressing a pure wave propagation problem with nonlinear wave conditions, the oceanic environment becomes non-stationary, causing the statistics at a position x to evolve over time. Similarly, in a tank environment, high-order nonlinear effects increase with the distance from the wave maker, leading to a spatial evolution of the statistics.

As a consequence, several consecutive studies in wave tank environments found that with highly nonlinear wave conditions, the second-order references fail to predict the tail of the distributions when the distance from the wave maker increases (Onorato et al., 2006, 2009; Buchner et al., 2011; Latheef and Swan, 2013; Shemer et al., 2010). With no or limited breaking phenomena, the third-order nonlinearities appear to modulate the wave envelop and strongly increase the number of extreme events, as a result of nonlinear processes such as modulational instabilities / third-order near-resonant interactions. The effects of directionality have also been explored, revealing the limitations of high-order effects for short-crested waves. Note that the conclusions were established under the assumption of deep water waves, which is the framework of the present thesis. As a matter of completeness, a reduced water depth is associated with smaller departure from second-order references due to third-order effects (Tang and Adcock, 2021).

a) Modified Tayfun distribution accounting for the excess kurtosis

To account for these high-order effects, Tayfun and Fedele (2007) presents the theoretical NBGC (Narrow Band Gram-Charlier) model, also detailed in Tayfun and Fedele (2007) and Fedele et al. (2011)). It predicts the following crest height POE:

$$POE_{H_C}(c) = P(H_c/\sigma_\eta > c) = \exp(-c_0^2/2)(1+\Lambda/64c^2(c^2-4)) \tag{2.19}$$

with,

$$\Lambda = 8\lambda_{40}/3 \tag{2.20}$$

The model uses as parameter the excess kurtosis λ_{40}, to tune the shape of the distribution. λ_{40} can be directly computed from the free surface elevation series. As a reminder, it can also be predicted as a function of the distance from the wave maker (see Sec. 2.2). In this thesis, both NBGC distribution computed using the theoretical and the measured λ_{40} will be displayed

(fully-predictive and semi-predictive models respectively).

b) Semi-empirical Huang distribution

Eventually, Huang and Guo (2017); Huang and Zhang (2018) provide a set of semi-empirical crest height benchmark distributions including PDER and PDSR upper and lower bounds. These are assumed to be a realistic statistical description of nonlinear deep-water long-crested wave fields. The model was built with numerical data, generated by nonlinear potential-flow wave solvers and CFD solvers, covering a wide range of wave conditions. The distribution is based on a Weibull formulation. The exact definition can be found in Huang and Zhang (2018). This distribution is used as a reference by some industrial actors (NWT Preparation Workgroup, 2019).

However, it was built assuming time and spatial ergodicity, which is not ensured in a wave tank environment. Its use consequently presents some limitations associated to the spatial evolution of statistical properties.

2.3 Side wall dissipation

Furthermore, during the wave propagation in a tank, even for non-breaking sea states, the wave spectrum is modified by dissipation mechanisms. Different sources can be identified (Henderson et al., 2015; Deike et al., 2012). They are due to the effect of viscosity in the: i) fluid bulk, ii) bottom boundary layer, iii) side wall boundary layer, and iv) free surface. When using a configuration of a deep water towing tank (case of all the experiments performed with the ECN Towing) and non breaking wave conditions (for instance `ss6` and `ss6g5` sea states), the observed dissipation is dominated by viscous phenomena acting on the lateral side walls of the towing tank. A theoretical framework, considering the energy losses of non breaking progressive waves along a tank is described in Kit and Shemer (1989) and Henderson et al. (2015). It takes into account, the bottom and side walls friction and the air interface assuming a clean surface. Each η Fourier component $A(f,x)$ of the wave field at position x is expressed as

$$A(f,x) = A(f,0)\exp\left(-\frac{x}{L_{dissip}(f)}\right) \tag{2.21}$$

with f the frequency of the Fourier component, $A(f,0)$ the initial Fourier amplitude at frequency f, and L_{dissip} the dissipation length, dependent on wave frequency. The latter is defined as,

$$1/L_{dissip}(f) = \sqrt{\frac{\nu}{2\omega}}\frac{2k}{L_y}\frac{\sinh(2kd)+kL_y}{\sinh(2kd)+2kd} + \frac{4\nu k^3}{\omega} \tag{2.22}$$

$4\nu k^3/\omega$ is the contribution of the water air interface. ν is the kinematic water viscosity ($\nu = 1.10^{-6}\mathrm{m}^2.\mathrm{s}^{-1}$) and L_y is the wave tank width. Computing the exponential dissipation for all the frequency components, the theoretical wave spectrum $S(f,x)$ at position x is then:

$$S(f,x) = 0.5A(f,x)^2/\delta f \tag{2.23}$$

with δf the frequency resolution. The associated significant wave height $H_s(x)$ at position x can be deduced with the spectrum integration over the entire frequency range. Note that these predictions were established under the assumption of a linear wave field with deep or intermediate water depth.

CHAPTER 3

EXPERIMENTAL UNCERTAINTIES: QUANTIFICATION AND PROCEDURES

The studies presented in this thesis rely mainly on the analysis of stochastic quantities, computed from experimental free surface elevation series. As for any experiments, uncertainties affect the data. In the field of ocean engineering, the leading references for deriving uncertainty ranges are the International Towing Tank Conference (ITTC) guidelines and procedures [1].

Specifically, ITTC (2017a) addresses the topic of wave-structure interaction experiments. It underlines the significant role of wave quality. Two key aspects are considered: i) the uncertainties affecting the measurement and the reproducibility of the wave data and derived parameters, and ii) the deviations between measured wave field properties (e.g., spectrum, statistics) and target values, due to wave propagation from the wave maker to the target position. The latter aspect is also covered in ITTC (2021) and is the core of the second part of this thesis. In this chapter, we concentrate on the measurement uncertainties and the reproducibility concerns.

ITTC (2017a) mentions three sources of uncertainties in the wave analysis: the measurement system, the wave generator, and the reflected waves. Relying on the general ISO/IEC (2008) approach, it recommends estimating uncertainty ranges through statistical analysis of repeated wave sequences ("Type A" assessment) and evaluating each uncertainty source using quoted or assumed values ("Type B" assessment). More detailed explanations of "Type A" and "Type B" methods are provided in Sec. 3.1.

In practice, estimating the uncertainty of a result is very complicated. The ITTC guidelines give a general procedure to follow. However, a significant proportion of uncertainties depend on error factors specific to the experimental set-up and the protocols followed by the experimentalist. Furthermore setting up dedicated tests to estimate uncertainties is often impractical. The experimentalist must therefore make well-considered but arbitrary choices in order to set error bars on his results.

Based on the recommendations and approaches proposed by the ITTC, the aim of this

1. https://ittc.info/

chapter is to identify the main sources of error, and to estimate the influence of each one on the quality of the presented results. For each quantity of interest, we will propose uncertainty bars that best represent the uncertainties. This study does not claim to be exhaustive. The idea is to verify that the experimental results and analyses presented in the rest of the thesis make sense, and to provide an estimation of the experimental uncertainties.

Before tackling our problem, section 3.1 outlines the uncertainty assessment procedures proposed by the ITTC. Mathematical modeling of uncertainties is also discussed. Next, Section 3.2.1 focuses on our problem: the stochastic generation of unidirectional irregular deep-water waves in tanks. We will start by identifying the sources of uncertainty, and build a strategy to follow, based as closely as possible on the procedures presented in Sec. 3.1. The remainder of the chapter will then be devoted to the implementation of this approach and a point-by-point study of the identified sources of uncertainty.

The conclusions drawn from this analysis will apply to all the analyzed experimental data. The list of the experiments carried out for this thesis can be found in Appendix A. It includes the experimental campaigns features and the positions of the probes.

3.1 Standard guidelines to estimate uncertainty ranges

Based on the ITTC (2017a), ITTC (2008), and ISO/IEC (2008), this section outlines the uncertainty assessment procedures proposed by the ITTC. Background knowledge in mathematical modeling of uncertainties is also provided.

Problem definition Let's define a quantity X which is measured (for example the free surface elevation at a given time and position $\eta(t_0, x_0)$). Quantifying the uncertainty of X involves answering the question, 'To what extent is the value of X that I have measured representative of the true value of X that I want to measure?'".

Type A and Type B uncertainties For each quantity X measured, the standard procedures recommend estimating the uncertainties in two different ways.

The first uncertainty to be assessed is Type A uncertainty. The method consists in building a statistical distribution of X based on several realizations of the same test repeated multiple times. For N measurements of X we note X_{mean} the mean value and σ_X the standard

deviation. The Type A uncertainty is

$$u_A(X) = \sigma_X/\sqrt{N} \tag{3.1}$$

It is the standard deviation that represents the dispersion of X_{mean}.

In addition, the ITTC procedures recommend assessing uncertainty using a Type B method. This method involves estimating the uncertainty of X without relying on a statistical approach. Instead, it treats X as a random variable and makes assumptions about its probability distribution 'based on judgment from all relevant information available' (ITTC (2008)).

In practice, the Type B procedure is as follows. The experimentalist needs to estimate the various sources of uncertainty (S_i) affecting the quantity X. For each source S_i, an uncertainty $u_{B_i}(X)$ is estimated, either through a statistical study carried out beforehand (i. e. Type A estimation dedicated to the source S_i) or by assuming a uniform law and specifying a maximum error $E_{\max}$, either provided by the sensor manufacturer or estimated by the experimentalist. For the latter case, the Type B uncertainty of the source S_i is:

$$u_{B_i}(X) = E_{\max}/\sqrt{3} \tag{3.2}$$

The Type B uncertainty of the measured quantity X, $u_B(X)$, taking into account the sources of uncertainty (S_i), is then obtained by the formula

$$u_B(X) = \sqrt{\sum_i u_{B_i}(X)^2} \tag{3.3}$$

Standard uncertainty Type A uncertainty quantifies the dispersion of measurements of X when repeating the experiment. The statistical study on which it is based comes from a repeatability test carried out multiple times without changing the study parameters (same measurement system, same experimental set-up). Therefore, Type A uncertainty does not incorporate systematic biases. For example, let's take the case where the measured value is $\eta(t_0, x_0)$ when generating a specific realization of a particular sea state, e.g. `ss6g5`. If the Type A uncertainty is evaluated by performing several times the run, with the same measurement system and the same basin, the associated Type A uncertainty does not take into account possible systematic errors in wave sensor gain or wave maker transfer function, as these errors do not change from one repeatability test to another.

This is why standard procedures call for Type A uncertainty to be combined with Type B uncertainty. The latter, which includes the intrinsic errors of each source of uncertainty, takes

measurement bias into account. To return to our example, the Type B uncertainty of $\eta(t_0, x_0)$ is obtained by combining the uncertainty of the wave probe and the transfer function of the wave maker, and therefore includes the possible biases that may result.

Therefore the standard uncertainty, $u_s(X)$ that is used to derive uncertainty ranges, is obtained by combining Type A and Type B uncertainties:

$$u_s(X) = \sqrt{u_A(X)^2 + u_B(X)^2} \tag{3.4}$$

Propagation law If the quantity under analysis is the result of a chain of measurements, i.e. is a value calculated from several measured quantities, then its uncertainty is obtained from a propagation law.

For the case of a quantity $Y = f(X_1, X_2, ..., X_n)$ which is a function of n measured independent variables (X_i), the standard uncertainty is computed as:

$$u_s(Y) = \sqrt{\left(\frac{\partial f}{\partial X_1}\right)^2 u_s(X_1)^2 + \left(\frac{\partial f}{\partial X_2}\right)^2 u_s(X_2)^2 + ... + \left(\frac{\partial f}{\partial X_n}\right)^2 u_s(X_n)^2} \tag{3.5}$$

Expanded uncertainty Instead of characterizing the uncertainty by a standard deviation (standard uncertainty denoted as $u_s(Y)$), we can also compute intervals that ensure, at a given level of confidence, the coverage of the true value of Y (expanded uncertainty denoted as $U(Y)$). Assuming a normal distribution, the expanded uncertainty at a 95% confidence level satisfies

$$U(Y) = 2u_s(Y) \tag{3.6}$$

ITTC guidelines for wave experiment In practice, the systematic computation of Type A and Type B uncertainties is not always possible, and the experimentalist must make compromises. ITTC (2017a) proposes an approach to evaluate the uncertainties affecting the study sea states generated in tanks. The aim is to determine the uncertainty of the parameters of interest (H_s, spectrum, statistics).

For each quantity, Type A and B uncertainties need to be estimated. As the quantities analyzed are stochastic, they require several realizations. Evaluating a Type A uncertainty for each wave condition and setup is therefore prohibitively long and expensive. To overcome this difficulty, 'it is recommended that only a few selected representative test conditions should be repeated to obtain some understanding of the type A uncertainty' ITTC (2017a).

In parallel, to assess Type B uncertainty, the ITTC procedure identifies the following sources: i) 'limitations of wave generators', ii) 'reflections from beach devices', and iii) 'uncertainty due to measuring and processing errors'. It recommends disregarding the first two (too difficult to estimate) and concentrating on the 'Type B uncertainty established from properties of measuring device and data process'. In our case, this involves estimating the η time-series Type B uncertainty associated with the resistive wave probes and propagating it to the quantities of interest.

3.2 Application to our problem

Based on the guidelines recommended by the ITTC and detailed in the previous section, we will now build an approach adapted to the experiments carried out for this thesis.

3.2.1 Sources of uncertainty

The experiments analyzed in this thesis are stochastic generations of sea states, conducted in the ECN tank facilities. As detailed in Section 1.2.2, for each sea state, several realizations with random phases are generated. The free surface elevation is measured by resistive wave gauges at several positions. The recorded time signals are then used to compute statistical or spectral quantities (Section 1.3.2). It is these quantities that we aim to associate with uncertainty ranges.

Following ITTC guidelines, we will estimate the Type A and Type B uncertainties for each quantity as far as possible. Firstly, to better understand the problem and to prepare the estimation of the Type B uncertainty, we will list the different sources of uncertainty that affect the results.

Figure 3.1 identifies and classifies the sources of error. The factors affecting the quality of the results are divided into three families: (i) the *measurement uncertainty* i.e. the differences between the recorded data and the occurring waves ; (ii) the *generation uncertainty* i.e. the differences between the expected waves assuming a perfect environment (perfectly controlled wave maker, calm water at $t = 0$, no spurious waves) and the generated waves; and (iii) the *sampling variability* i. e. the differences between the statistically converged quantities and the one computed with limited data size. Note that the latter topic is not specific to experiments and is related to the data analysis procedures. It was treated in the previous chapter, see Sec. 1.3.3. (i) affects the veracity of the results while (ii) brings reproducibility concerns and confusions in the interpretation (identification of the physical phenomena at stake).

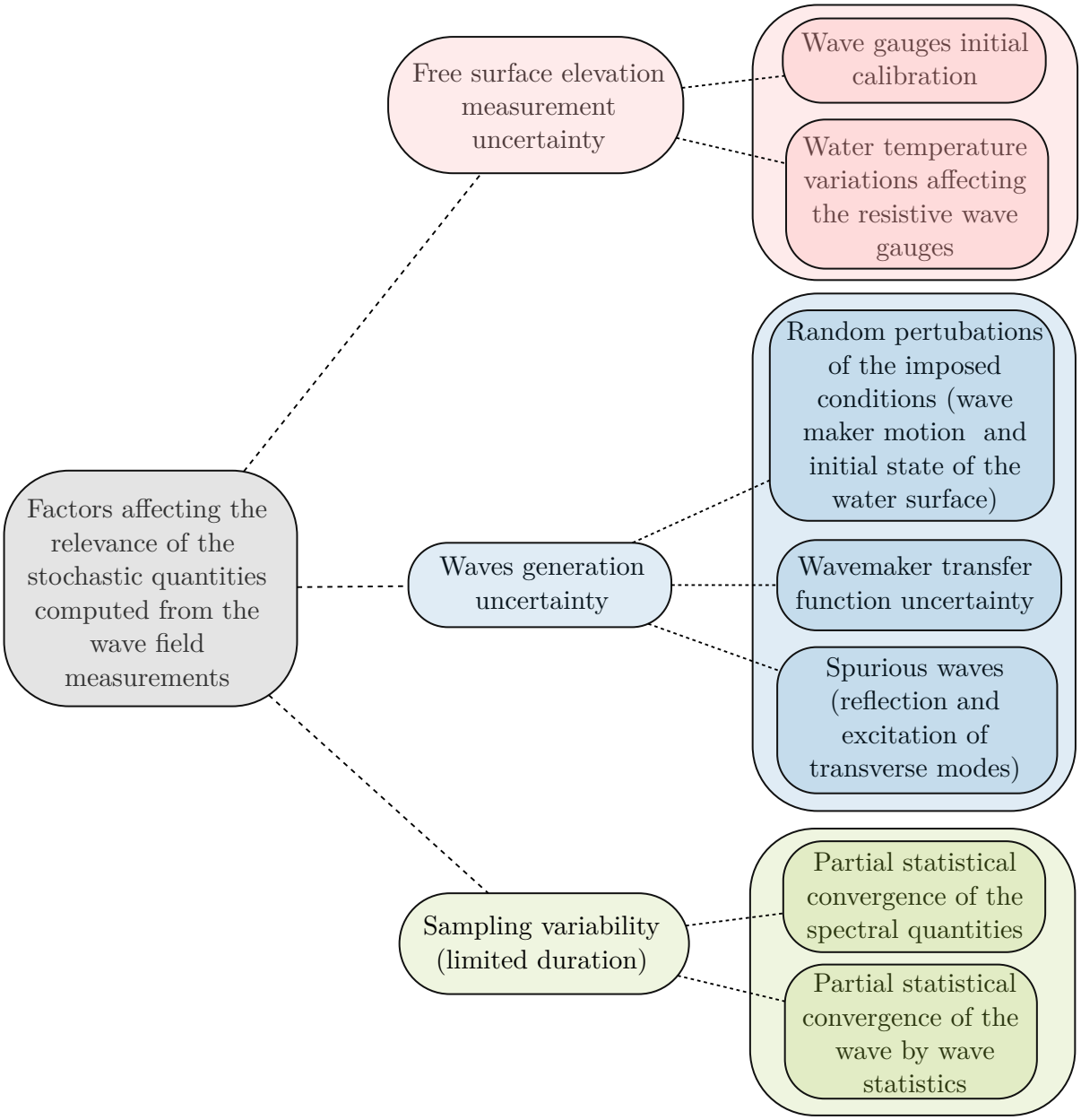

Figure 3.1 – Classification of the uncertainty sources

3.2.2 Needs depending on the type of study

The same set of realizations can be analyzed for different purposes, and depending on the type of analysis, the uncertainty to be estimated differs. We will distinguish two types of analyses.

The first analysis is the *fully-stochastic analysis*. This is the case where we want to

study the properties of a generated sea state and generalize the results for any phase set and any test basin. Uncertainty bars must then include all the sources of error detailed in Figure 3.1: the uncertainty of the measurement system (measurement uncertainty), the variability of results from one set of realizations to another (sampling variability), and from one basin/setup to another (generation uncertainty).

The second analysis is the *semi-stochastic analysis*. This is the case where we want to study a specific set of realizations, without sampling variability concerns. The aim is not to extend the results to another set of random phases. Uncertainty bars must then only include the measurement and generation uncertainties.

To give a practical example, in Chapter 4 we analyze 30 realizations of `ss6g5` generated in the Towing tank. The aim is to characterize the spatial evolution of spectral and statistical quantities along the domain. This is a fully-stochastic analysis. On the other hand, in Chapter 8, we investigate the differences between several versions of these 30 realizations, generated using different wave generation procedures, but with the same random phases. This is a semi-stochastic analysis.

3.2.3 Strategy adopted

The aim is to compute for each quantity of interest the Type A and Type B uncertainties. As indicated in the ITTC guidelines, calculating the Type A uncertainty for each experiment is not possible. We will therefore estimate the order of magnitude of the Type A uncertainty by means of a repeatability study of a specific realization. This will include the influence of the "random perturbations of the imposed conditions", which are part of the uncertainty of generation. This study will be carried out in Section 3.6.

In addition, Type B uncertainty will be evaluated by studying the influence of the sources listed in Figure 3.1. Measurement uncertainty, generation uncertainty and sampling variability (taken into account or not, depending on the type of analysis) will therefore be considered as three sources of uncertainty to be combined.

The chapter is organized as follows. Section 3.3 explores the accuracy of the wave gauges and quantifies the Type B measurement uncertainty. The propagation law (eq. 3.5) is used to propagate the uncertainty in the free surface elevation to the quantities of interest. Then, Sec. 3.4 and 3.5 investigate the influence of the spurious transverse modes and reflected waves (topics related to the wave generation uncertainty). Next, Section 3.6 gives an estimate of the Type A uncertainty, through the study of a repeatability dataset. Finally, the conclusion (Sec. 3.7) takes into account the findings of the previous sections and defines the uncertainty ranges

that will be included in the results presented throughout Chapters 4 to 8.

3.3 Measurement uncertainty

3.3.1 Measurement system

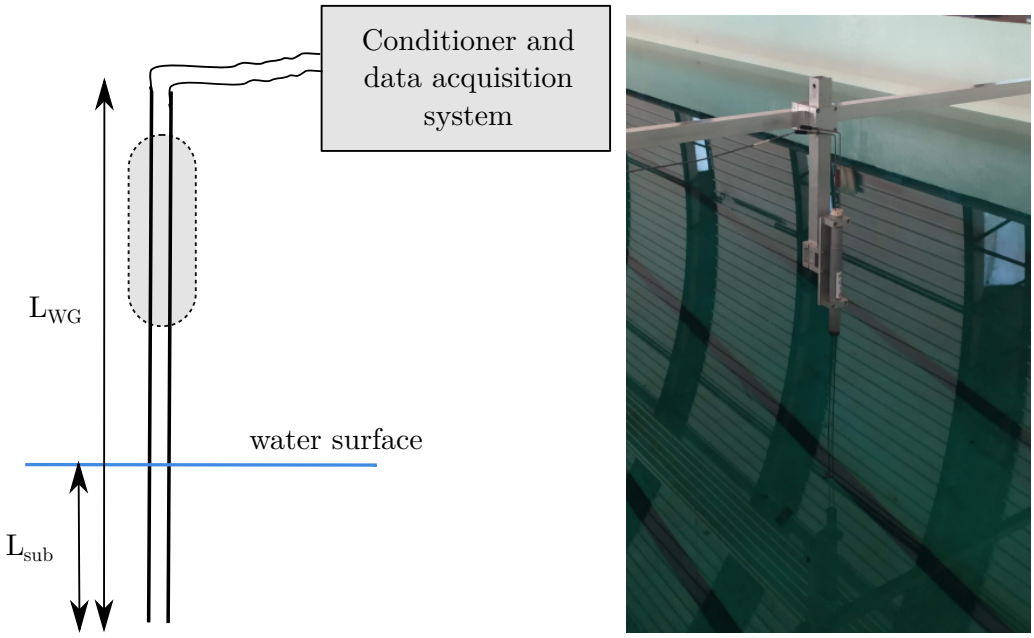

(a) sketch of the sensor **(b)** Photo in ECN Towing Tank

Figure 3.2 – Resistive wave gauge

All the experimental results provided in this document come from resistive wave gauge (WG) measurements. These sensors rely on the water conductivity. They consist of two vertical metal rods centered at the mean water level (see Fig 3.2). As part of the measurement electrical network, including amplifiers and a data acquisition system, the tension measured between the two rods is directly proportional to the free surface elevation at the probe position. The calibration coefficient differs from one gauge to another, depending on the geometry and the amplifier channel. It is measured before installation using a dedicated wave gauge calibration bench. This system equipped with a position sensor and a data acquisition system carries up and down the probes, measuring the latter position as a function of the measured tension. This method is usually assumed to be enough to accurately calibrate the gauges.

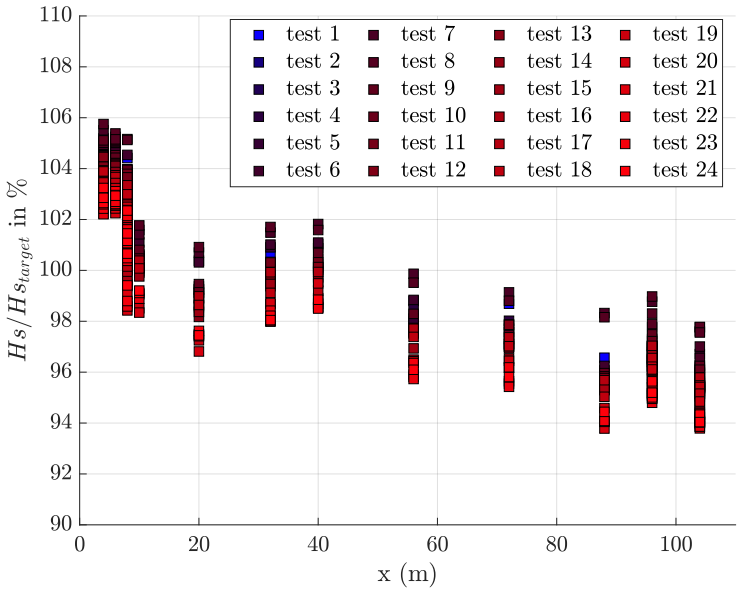

Figure 3.3 – Significant wave height computed from the repeatability tests of Campaign D

3.3.2 Correction of the calibration factor

The reliability of the resistive wave gauges was explored throughout the several experimental campaigns. As the sensors rely on water conductivity, they are very sensitive to the water temperature. For short experiments (duration of a couple of days), it is assumed that the inertia of the large volume of water limits temperature variations. However, the stochastic generation of sea states needs several weeks (tens of realizations are run). For such long-duration campaigns, the water temperature is likely to change, which induces a time evolution of the calibration factors.

To track the variations, repeatability tests were performed at least once a day. These dedicated experiments were used to adapt the calibration factors of the wave gauges daily. The calibration bench was also used to re-calibrate the gauges in the event of strong variations. A detailed analysis of a repeatability test is provided in Sec. 3.6. As an example, Figure 3.3 presents the evolution of the significant wave height computed from the repeatability tests of the campaign D (see Appendix A). The dataset includes 24 runs generated each day before other experiments, starting with a calm water surface. The repeated sequence is a realization of `ss6` sea state at scale 40 (i. e. $H_{s_{\text{target}}} = 0.15$ m $T_{p_{\text{target}}} = 1.9$ s). We observe that H_s values vary from one day to another within a range of approximately $4\%H_{s_{\text{target}}}$. The same trend is

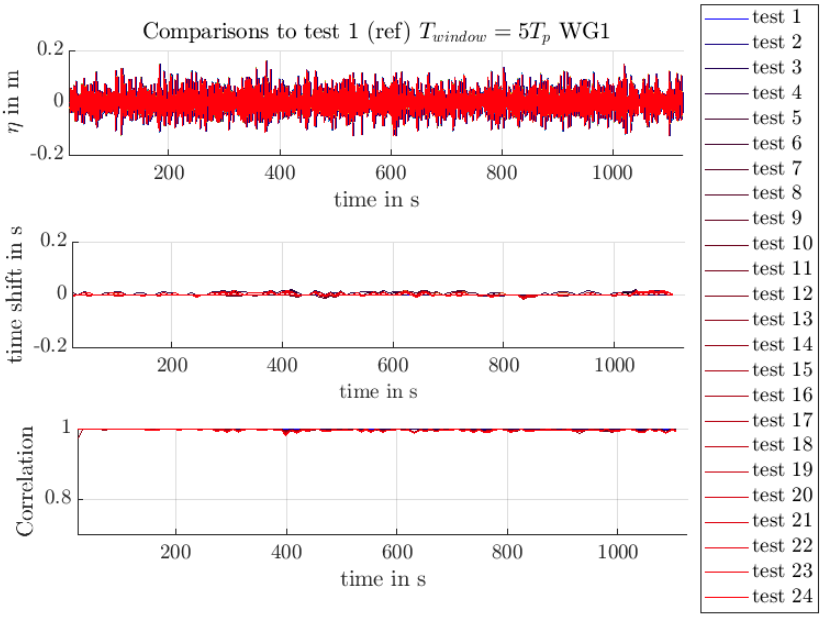

Figure 3.4 – Deterministic comparison of campaign D repeatability tests; WG1 measurements ($x = 4$ m$= 0.7\lambda_{p_{\text{target}}}$)

observed for each wave gauge. In addition, Fig. 3.4, following the procedure of Sec. 1.3.5, provides the deterministic comparison of the data for a wave gauge located at $x = 4$ m (WG1). The time series are perfectly correlated (correlation coefficient defined in (eq. 1.54) larger than 0.99 during the entire run duration). The only differences are variations in amplitude. This is indicative of water temperature fluctuations that result in incorrect calibration factors. As discussed in Section 3.6, at a larger distance from the wave maker, the correlation between the runs decreases due to repeatability issues. To deal with the probes involved, we assume that the significant wave height accurately tracks the calibration factor variations (i.e. the repeatability noise does not change H_s).

Based on these findings, for each gauge j and day i, the correction coefficient is defined as:

$$C_{R_{(i,j)}} = \frac{H_{s_{(0,j)}}}{H_{s_{(i,j)}}} \tag{3.7}$$

where $H_{s_{(0,j)}}$ represents the significant wave height of the first repeatability test, conducted immediately after calibration using the bench system (that uses the water pumped from the wave tank the same day). $H_{s_{(i,j)}}$ represents the significant wave height of the repeatability test

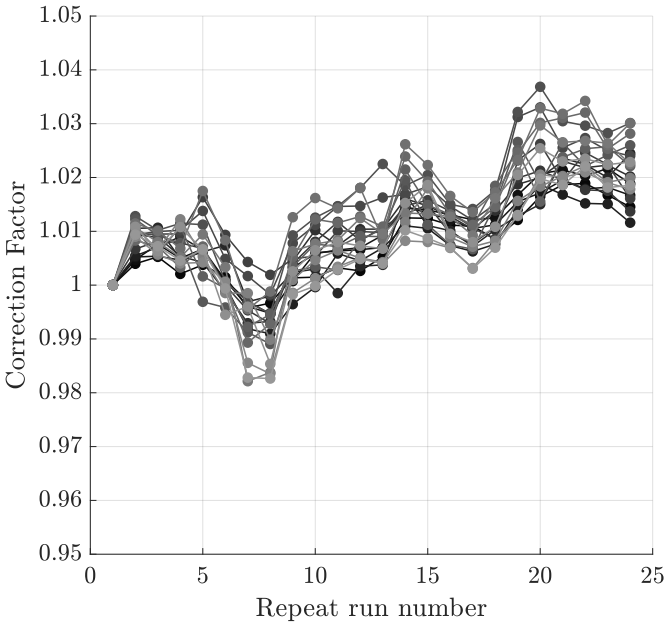

Figure 3.5 – Calibration factors computed for campaign D; each line corresponds to a wave gauge, the darker ones are closer to the wave maker

conducted on the morning of day i.

Figure 3.5 presents the calibration factors of Campaign D. The values are consistent with the range of deviations observed in Figure 3.3. We see that all the gauges follow the same trend, which further confirms the impact of water temperature changes (assumed to be uniform throughout the tank).

3.3.3 Quantification of the uncertainties

Now that the measurement process has been detailed, the objective is to compute the Type B measurement uncertainty. The ranges will first be obtained for the free surface elevation and then propagated to the quantities of interest.

Calibration Factor obtained from the Calibration Bench For each wave gauge, we distinguish between $\eta_B(t)$ obtained with the gain estimated with the calibration bench and $\eta(t)$ corrected with the coefficient C_R obtained with the daily repeatability test.

$$\eta(t) = C_R\,\eta_B(t) \tag{3.8}$$

First, we look at the uncertainty of η_B. The influence of correction will be seen in the next paragraph. η_B comes from the linear relation

$$\eta_\mathrm{B}(t) = V(t)\, G^B_\mathrm{WG} \tag{3.9}$$

$V(t)$ is the voltage given by the measurement acquisition system in Volt, and G^B_WG is the calibration factor obtained from the calibration bench in meters per Volt. Several sources of uncertainty can be identified:

— u_calib, the uncertainty of the calibration bench process. The calculation of G^B_WG is influenced by uncertainties associated with the calibration bench's motor and ruler. Furthermore, the wave gauge behavior slightly deviates from the linear model (eq. 3.9).

— u_acq, the uncertainty of the voltage measurement acquisition system. This error is very low (below $0.1\%V(t)$) and, consequently, it can be neglected regarding u_calib.

— $u_\mathrm{installation}$, the uncertainty due to the installation of the probes from the calibration bench to their position in the tank. Indeed, it is assumed that when they are set up, the probes remain undamaged. However, this cannot be ensured. Even minor bendings of the metal rods can alter the calibration factor, which is dependent on the gauge's geometry. This error is difficult to estimate. It is therefore disregarded. On the other hand, probes with identifiably odd behavior immediately after installation are removed from the tank.

— u_stat2dyn, the uncertainty associated with the fact that when calibrated with the bench, the probes are in a static environment. The water does not move. In the tank, however, waves exert a force on the probes. This can cause them to bend slightly, which can affect the measurement.

— $u_\mathrm{temperature}$, the uncertainty due to temperature variations. Three scales of variation time must be considered: variations over several days (due to weather changes around the facility), variations within a single day (due to atmospheric temperature fluctuations during day-night cycles), and variations during the test duration (the water temperature is known to stratify in the z direction, and the runs can induce water circulation that may break the temperature field patterns, and consequently modify the wave gauge behavior). Several-day variations are corrected through the correction factor C_R, and the influence of single-day variations will be estimated with $u_s(C_R)$ in the next paragraph. $u_\mathrm{temperature}$ is therefore not treated as part of $u_s(\eta_\mathrm{B}(t))$. Test-duration variations will be neglected, as large waves are usually generated before the runs to break the water stratification that occurs during the inactivity periods (night, week-end, ect).

As a result, the measurement uncertainty in η_B follows as

$$u_s^{\text{meas}}(\eta_{\text{B}}(t)) = \sqrt{u_{\text{calib}}^2 + u_{\text{acq}}^2 + u_{\text{installation}}^2 + u_{\text{stat2dyn}}^2} = u_{\text{calib}} \tag{3.10}$$

We now need to estimate u_{calib}. For each wave gauge, G_{WG}^B is estimated from a set of N calibration points provided by the bench (η_i, V_i). More precisely, we calculate the linear regression of the points (η_i, V_i) to recover the relationship (eq. 3.9). G_{WG}^B is the slope of the linear regression. ITTC (2017b) guidelines provide formulas for quantifying the uncertainty of a quantity obtained through regression analyses. We apply these formulas to our problem.

The standard uncertainty is modeled by the standardized error of estimate

$$u_{\text{calib}} = SEE = \sqrt{SS_R/(N-2)} \tag{3.11}$$

SS_R is the sum square of the residuals

$$SS_R = \sum_i (\eta_i - G_{\text{WG}}^B V_i)^2 \tag{3.12}$$

The uncertainty of the calibration factor (slope of the regression) is expressed as

$$u_s(G_{\text{WG}}^B) = SEE/s_{xx} \tag{3.13}$$

with

$$s_{xx} = \sum_i (V_i - V_{\text{mean}})^2 \tag{3.14}$$

As it will be shown in Figure 3.7, this leads to $u_s^{\text{meas}}(\eta_{\text{B}}(t))$ values ranging from 0.5 mm to 2.5 mm, and $u_s(G_{\text{WG}}^B)/G_{\text{WG}}^B$ values ranging from 0.5% to 1.5%.

Uncertainties related to the correction of the calibration factor Estimating $u_s(C_R)$ is less straightforward due to technical and practical issues, primarily difficulties in accurately measuring the water temperature. First, we assume the first run (serving as a reference for repeatability tests) to be of perfect quality. This assumption appears reasonable as it is generated immediately after using the calibration bench. The latter is coupled with the experiment's acquisition system and utilizes water from the tank. Then, neglecting uncertainties associated with the first run, the estimation of $u_s(C_R)$ only requires accounting for water temperature variations that occur within a single day.

Building on this approach, to evaluate $u_s(C_R)$, the repeatability test (still the same `ss6`

scale-40 realization) was generated 8 times on the same day in the ECN Towing tank, within the scope of Campaign E. Figure 3.6 presents the resulting H_s measured along the tank, together with a deterministic comparison (see Sec. 1.3.5) of the measured signals at $x = 4$ m$= 0.7\lambda_{p_{\text{target}}}$ (first wave gauge). Across the entire domain, we observe deviations in H_s within a range of

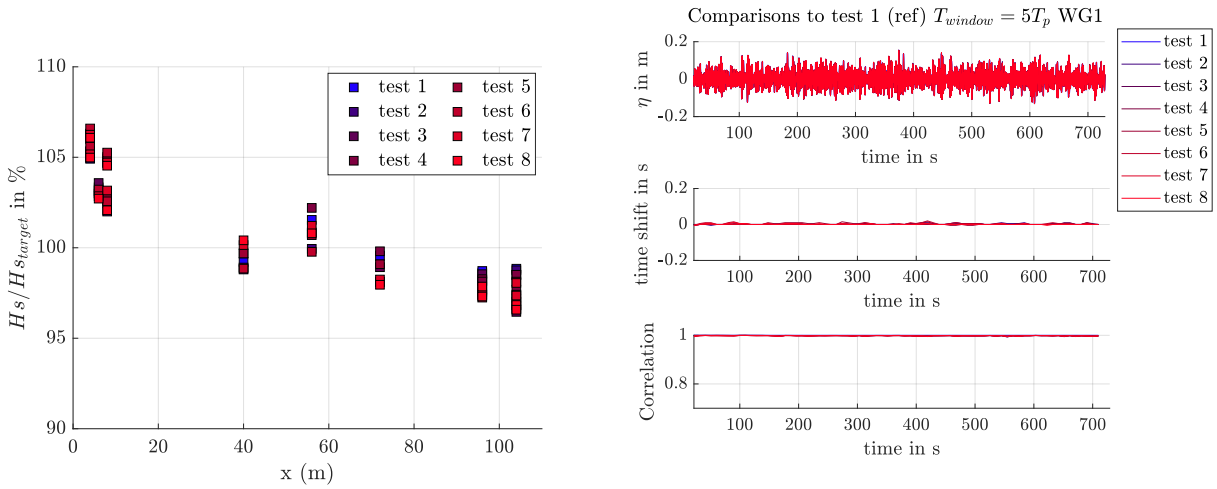

(a) H_s along the tank

(b) Deterministic comparison at $x = 4$m

Figure 3.6 – Campaign E repeatability tests run the same day, H_s along the tank and deterministic comparison at the first probe ($x = 4$ m$= 0.7\lambda_{p_{\text{target}}}$)

$\pm 0.75\%$. Furthermore, the deterministic comparison shows that at the very beginning of the tank, although there are slight variations in H_s depending on the run, the signals are perfectly correlated. Therefore, these differences are amplitude variations. We can extrapolate the H_s variations to estimate the uncertainties in the correction factors: $u_s(C_R)/C_R \approx 0.75\%$. We assume that this value does significantly vary from one setup (tank, gauge network) to another. $u_s(C_R)/C_R \approx 0.75\%$ will therefore be used for all the experimental campaigns.

$\eta(t)$ uncertainty formula Based on the propagation law (eq 3.5) and the definition of $\eta(t)$ (eq. 3.9), the $u_s^{\text{meas}}(\eta(t))$ measurement uncertainty is derived as

$$u_s^{\text{meas}}(\eta(t))/\eta(t) = \sqrt{\left(\frac{u_s^{\text{meas}}(\eta_{\text{B}}(t))}{\eta_{\text{B}}(t)}\right)^2 + \left(\frac{u_s(C_R)}{C_R}\right)^2} \tag{3.15}$$

Using (eq. 3.10), this leads to

$$u_s^{\text{meas}}(\eta(t))/\eta(t) = \sqrt{\left(\frac{u_{\text{calib}}}{\eta_{\text{B}}(t)}\right)^2 + \left(\frac{u_s(C_R)}{C_R}\right)^2} \tag{3.16}$$

which can be written as,

$$u_s^{\text{meas}}(\eta(t)) = \sqrt{(C_R u_{\text{calib}})^2 + \left(\eta(t)\frac{u_s(C_R)}{C_R}\right)^2} \tag{3.17}$$

To propagate the uncertainty of the free surface elevation to the quantities of interest, it will be useful to define the corrected calibration factor

$$G_{\text{WG}} = G_{\text{WG}}^B C_R \tag{3.18}$$

Based on the propagation law, its uncertainty follows as

$$\frac{u_s(G_{\text{WG}})}{G_{\text{WG}}} = \sqrt{\left(\frac{u_s(G_{\text{WG}}^B)}{G_{\text{WG}}^B}\right)^2 + \left(\frac{u_s(C_R)}{C_R}\right)^2} \tag{3.19}$$

Example: wave gauges uncertainty in Campaign D As a concrete example, Figure 3.7 provides an overview of the uncertainty ranges computed for the 19 wave gauges settled for Campaign D. Regarding $\eta_B(t)$, the uncertainty ranges from 0.5 to 2.5 mm, with a mean value of 1.5 mm. For the relative gain uncertainty, the largest source of error is $u_s(G_{\text{WG}}^B)/G_{\text{WG}}^B$, which reaches up to 1.8% for two wave gauges. The mean $u_s(G_{\text{WG}})/G_{\text{WG}}$ is approximately 1.2%. The trends of $G_{\text{WG}}^B)/G_{\text{WG}}^B$ and $u_s^{\text{meas}}(\eta_B(t))$ are similar. By construction, these errors include the same uncertainty in wave gauge behavior.

Additionally, Figure 3.8 presents the uncertainty ranges for a typical free surface time trace (Campaign D, WG1 measurements of scale 120 `ss6g5` sea state). The ranges correspond to the standard uncertainty $u_s^{\text{meas}}(\eta)$ (eq. 3.17). The main dynamics of the free surface elevation are well-captured, but due to $u_s(C_R)$ influence, the error is slightly larger near the crests.

Since the same procedures and wave gauges were employed across all experimental campaigns, the order of magnitude of the uncertainty ranges is the same for all the experimental data, regardless of the wave condition or the tank facility.

The ranges correspond to the standard uncertainty. To obtain the 95% expanded uncertainty, you can multiply the ranges by two (see Section 3.1).

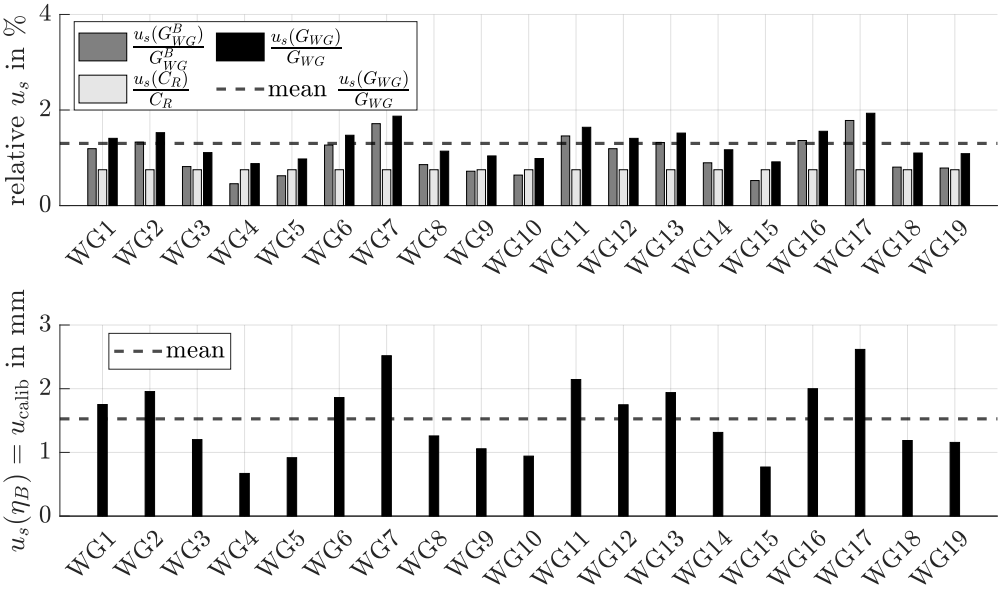

Figure 3.7 – Campaign D wave gauges uncertainties

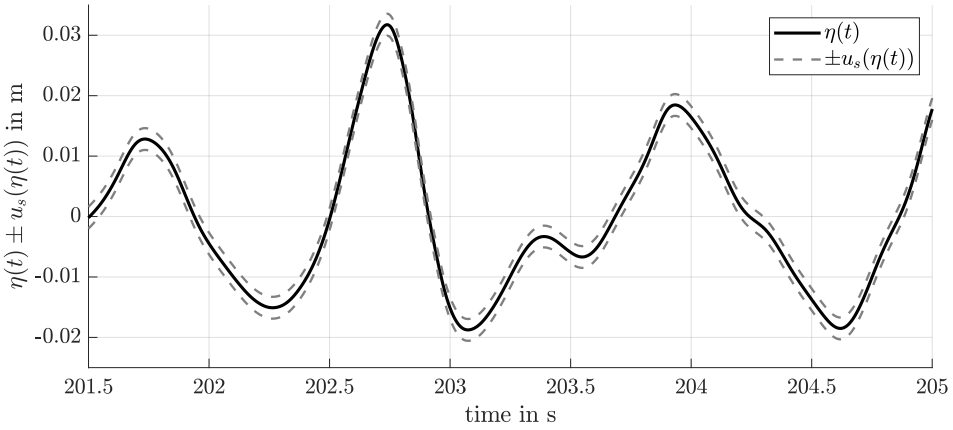

Figure 3.8 – Campaign D WG1 η measurements displayed with measurement uncertainty ranges (`ss6g5` sea state at scale 120)

Case of several probes at the same distance from the wave maker As shown in Appendix A, the probe networks often include one or several lines of WG perpendicular to the propagation direction. Since the generated waves are unidirectional, these probes, which are settled at the same distance x from the wave maker, should measure the exact same signals. As discussed in

Sec. 3.4, the time series measured at the same distance x are averaged and the resulting $\eta_{\text{mean}}(t)$ signal is used for analysis. To estimate $\eta_{\text{mean}}(t)$ uncertainty, it was chosen to compute the mean $u_s(G_{WG})/G_{WG}$ and $u_s^{\text{meas}}(\eta(t))$.

3.3.4 Extension to the quantities of interest

This subsection addresses the propagation of the $\eta(t)$ and G_{WG} uncertainty ranges expressed in (Eq. 3.17) and (Eq. 3.19) to the stochastic quantities of interest (spectrum, statistical moments, and crest distribution). It relies on the uncertainty propagation law (Eq. 3.5). As a reminder, we address here the measurement uncertainty only. The other Type-B uncertainties (wave generation uncertainty, sampling variability) and the Type-A uncertainties will be estimated in the upcoming sections (except for sampling variability which has been treated in Sec. 1.3.3). The final uncertainty ranges to be displayed will be defined in Sec. 3.7.

a) Wave spectrum

To derive measurement uncertainty ranges for the wave spectrum, $u_s^{\text{meas}}(\eta(t))$ needs to be propagated to the measured Fourier amplitudes $A(f)$. For this specific case, to simplify the calculations, we assume that the wave gauges have a perfectly linear behavior. This implies that the uncertainty in the measured free surface elevation only comes from an error in the calibration factor, which is a systematic error introducing the same relative deviation at each time or frequency. Consequently, based on the expression of $u_s(G_{\text{WG}})/G_{\text{WG}}$ (Eq. 3.19), the uncertainty in the measured Fourier amplitudes can be determined as follows:

$$u_s^{\text{meas}}(A(f)) = A(f)\sqrt{\left(\frac{u_s(G_{\text{WG}}^B)}{G_{\text{WG}}^B}\right)^2 + \left(\frac{u_s(C_R)}{C_R}\right)^2} \tag{3.20}$$

Therefore, relying on the spectrum definition (Eq. 1.17) and using the uncertainty propagation law (Eq. 3.5),

$$\frac{u_s^{\text{meas}}(S(f))}{S(f)} = 2\frac{u_s^{\text{meas}}(A(f))}{A(f)} \tag{3.21}$$

which is equivalent to

$$u_s^{\text{meas}}(S(f)) = 2S(f)\sqrt{\left(\frac{u_s(G_{\text{WG}}^B)}{G_{\text{WG}}^B}\right)^2 + \left(\frac{u_s(C_R)}{C_R}\right)^2} \tag{3.22}$$

b) Moments of the $\eta(t)$ distribution

We now turn our attention to the moments of the $\eta(t)$ distribution, namely the variance (related to H_s), skewness, and kurtosis. To model their measurement uncertainty, we have several options. Firstly, we can directly propagate $u_s^{\text{meas}}(\eta)$ using the propagation law and moment definitions. However, the calculation is not straightforward and does not allow us to use the systematic nature of the calibration coefficient errors.

We will, therefore, adopt an alternative strategy. Here, we distinguish between two types of measurement errors: (i) an error in the calibration factor, which is a systematic error inducing the same relative deviation at each time, and (ii) an error resulting from the non-perfectly linear behavior of the probe. Both (i) and (ii) are encompassed within the term $u_s^{\text{meas}}(\eta)$. We make this distinction because they have different effects on the statistical moments.

As the calibration factor remains constant during a run, the calibration error, of magnitude $\frac{u_s(G_{\text{WG}})}{G_{\text{WG}}}$, induces a constant amplification (or a reduction) of the measured series. As a result, for the significant wave height, it introduces an error within the range of $\frac{u_s(G_{\text{WG}})}{G_{\text{WG}}}$, while for the skewness and kurtosis, which are normalized quantities, it has no effect.

The estimation of nonlinear errors (ii) is less straightforward. To address this problem, we will handle these errors separately by considering a discrete free surface elevation time series (η_k) of N points, with no calibration factor uncertainty. We assume that each point η_k is affected by an independent error of range $u_{\text{nonlinear}}$.

The variance is defined as

$$var_t(\eta) = \frac{1}{N}\sum_{k=1}^{N}\eta_k^2 \tag{3.23}$$

Then, as we consider each η_k as a measured quantity having an independent uncertainty, we can use the propagation law (Eq. 3.5),

$$u_s(var_t(\eta)) = \sqrt{\left(\frac{\partial \frac{1}{N}\sum_{k=1}^{N}\eta_k^2}{\partial \eta_1}\right)^2 (u_s(\eta_1))^2 + ... + \left(\frac{\partial \frac{1}{N}\sum_{k=1}^{N}\eta_k^2}{\partial \eta_N}\right)^2 (u_s(\eta_N))^2} \tag{3.24}$$

with $u_s(\eta_1) = u_s(\eta_2) = ... = u_s(\eta_N) = u_{\text{nonlinear}}$ and $\frac{\partial \frac{1}{N}\sum_{k=1}^{N}\eta_k^2}{\partial \eta_1} = \frac{2}{N}\eta_1$. This leads to

$$u_s(var_t(\eta)) = \frac{2u_{\text{nonlinear}}}{\sqrt{N}}\sqrt{\frac{1}{N}\sum_{k=1}^{N}\eta_k^2} = \frac{2u_{\text{nonlinear}}}{\sqrt{N}}\sigma_\eta \tag{3.25}$$

Using (Eq. 3.5) it follows that

$$u_s(\sigma_\eta) = \frac{u_{\text{nonlinear}}}{\sqrt{N}} \tag{3.26}$$

This implies that the influence of nonlinear errors on the variance and standard deviation of the η time series approaches zero as the duration of the series increases. In this thesis, the series consist of hundreds of waves captured with a sampling frequency $f_{\text{sample}} > 40 f_p$. Consequently, $u_s(var_t(\eta))$ and $u_s(\sigma_\eta) = u_s(H_s)/4$ can be disregarded. A similar analysis can be conducted for the skewness and kurtosis, also indicating that the nonlinear errors have no impact.

To summarize, the measurement uncertainty in the significant wave height is modeled as

$$u_s^{\text{meas}}(H_s) = \frac{u_s(G_{\text{WG}})}{G_{\text{WG}}} \tag{3.27}$$

and is neglected for the skewness and kurtosis.

c) Crest distribution

The crest probability of exceedance is the distribution of a list of crest heights. The latter are the zero-crossing maxima of $\eta(t)$ sequences. Therefore, their uncertainty is the same as that of $\eta(t)$. The crest POE is usually normalized by the measured significant wave height $H_{s_{\text{meas}}}$ of the analyzed series. Therefore, it is not affected by $u_s(C_R)$. In (eq. 3.17), only $u_s(\eta_B)$ needs to be accounted. We will then consider the following ranges

$$u_s^{\text{meas}}(H_c/H_{s_{\text{meas}}}) = C_R\, u_s^{\text{meas}}(\eta_B)/H_{s_{\text{meas}}} \tag{3.28}$$

3.3.5 Conclusion

In this section, we have have estimated the Type-B measurement uncertainty in the free surface elevation time series, the spectrum, the moments of the free surface elevation distribution, and the crest distribution. Ranges have been derived. In Sec. 3.7 they will be incorporated in the final uncertainty ranges displayed throughout this thesis when analyzing experimental results. Note that, with our estimation methods, the measurement uncertainty does not affect the skewness and kurtosis.

3.4 Wave generation uncertainty: spurious Transverse Modes

The strategy implemented to estimate the uncertainty of experimental results (see Section 3.2.3) includes the following steps: quantification of Type B uncertainty related to sampling variability (Section 1.3.3 in Chapter 1), quantification of Type B uncertainty related to measurements (Section 3.3), quantification of Type B uncertainty related to wave generation (differences between the expected waves assuming a perfect environment and the generated waves), and analysis of Type A uncertainty (Section 3.6).

Type B uncertainty related to wave generation results from several phenomena listed in Figure 3.2.1. In this context, we will focus in this section on the influence of spurious transverse modes, which interfere with the wave field.

Within the scope of this thesis, only unidirectional sea states were generated and studied. However, transverse disturbances were visually observed during the experiments in both the Towing and the Ocean Engineering tanks. These can be seen in Figure 3.9 that presents pictures of partially breaking crests and Figure 3.10, which shows high-frequency standing transverse waves localized near the wave maker in the Towing tank.

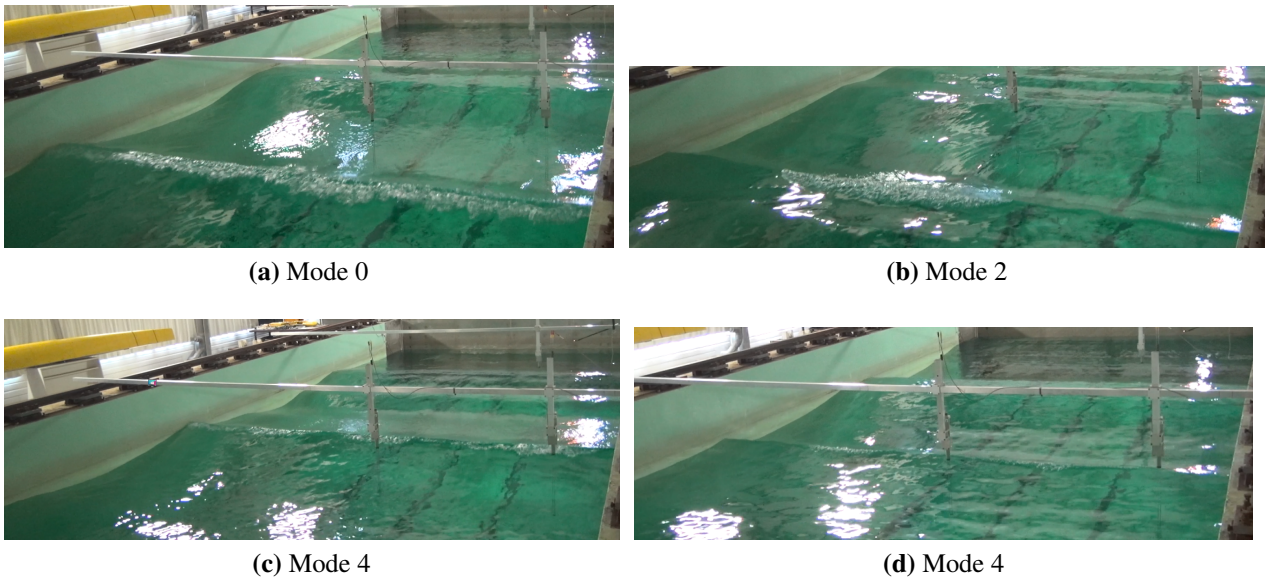

(a) Mode 0 **(b)** Mode 2

(c) Mode 4 **(d)** Mode 4

Figure 3.9 – Identification of transverse modes on breaking crests (GOM sea state at scale 94 in the Towing tank at $x = 8$ m)

Several phenomena can explain the origin of the transverse excitations. Firstly, gaps between the walls and the wave maker (or between the different paddles of the wave maker)

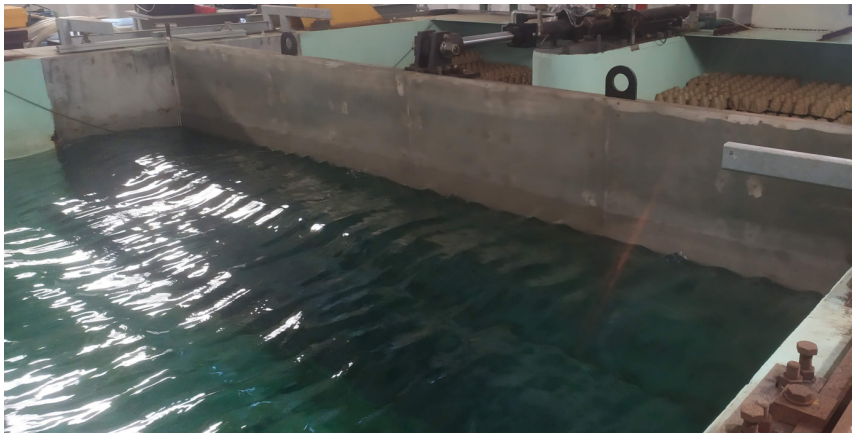

Figure 3.10 – Spurious high-frequency transverse waves near the Towing tank wave maker (`ss6g5` sea state at scale 120)

produce small water jets. The spurious waves generated by these jets excite the standing transverse eigenmodes of the tank (in the y direction). This energy transfer occurs when the wavelength of the generated waves is close to the wavelength of a transverse eigenmode (the latter being defined by the tank width and a mode number).

Furthermore, cross waves are naturally generated at the wave maker's position as a result of the nonlinear excitation of the paddle movement. Their frequency is twice that of the longitudinally propagating waves. This phenomenon has been studied in detail in Garrett (1970). Also note that fourth-order solutions can lead to crests having a crescent shape, disturbing the unidirectionality of the flow. However, this mainly occurs for large steepness regular waves (Fuhrman et al., 2004).

The resulting y-axis standing waves interact with the longitudinal (x-axis) waves and propagate along the tank (see Figure 3.9, where transverse eigenmodes 2 and 4 are observed at $x = 8$ m in the ECN Towing tank while generating the `GOM` sea state at a model scale of 94). In the context of the present study, we assume that the leading factor explaining the generation of spurious modes is the transverse excitations resulting from the gaps between the wave maker paddles. This assumption is based on the fact that crescent waves are unlikely to occur in irregular seas (Fuhrman et al., 2004), and the high-frequency cross waves are primarily concentrated near the wave maker without significant interaction with the propagating wave field. The objective here is to develop an analysis procedure to: i) identify the signatures of transverse modes along the tank, ii) quantify their influence on the measured stochastic wave properties, and iii) remove it when feasible.

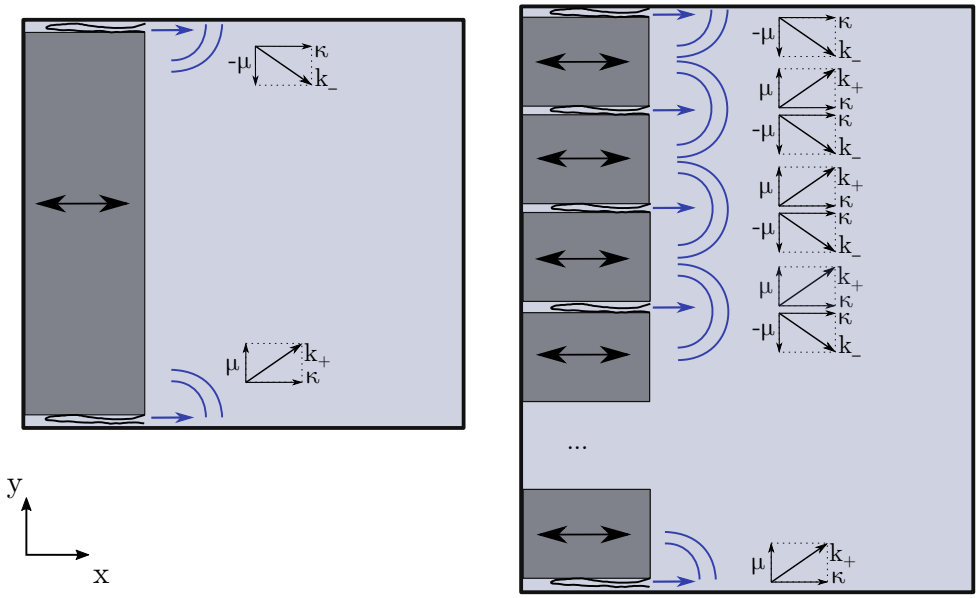

Figure 3.11 – Generation of spurious transverse-propagating modes; Top view of the Towing tank (left) and Ocean Engineering tank (right)

3.4.1 Analytical description

This first subsection provides a brief analytical description of the transverse disturbances generation and propagation, introducing the notion of transverse-propagating modes. It draws upon on the formalism provided in Bonnefoy (2005). The objective is to establish guidelines for predicting, from given wave condition and tank, the characteristics of the spurious transverse modes that are excited. The problem is first addressed for regular waves and then for the configurations studied in this thesis. In the remainder of the section, the theoretical predictions will be applied to track the transverse modes in the experimental data and assess their influence on the stochastic quantities of interest.

a) Regular wave

Before addressing the generation of sea states of interest, we will begin with a monochromatic wave case (regular wave). The idea is to introduce the analysis formalism for this simple case before applying it to the wave conditions generated in this thesis.

Linear regular wave model Let's consider a regular wave run, generated with the sinusoidal wave maker input $\eta_{\text{input}}(t) = A\cos(\omega t)$. To simplify, we neglect nonlinear effects ($kA << 1$)

and assume deep water conditions ($kd >> 1$), with the wavenumber k defined through the linear dispersion relation $\omega^2 = gk$. Then, in the case of a purely unidirectional flow, the 1D free surface elevation at the distance x from the wave maker is expressed as

$$\eta_{1D}(x,t) = A\cos(\omega t - kx) \tag{3.29}$$

Our objective is to incorporate the effects of transverse excitations occurring at the wave maker position into this analytical description.

Spurious waves generated by water jets at the wave maker interstices Transverse disturbances arise due to water jets induced by the gaps between the paddles of the wave maker. This mechanism is illustrated in Figure 3.11. It is similar for both the Towing tank configuration (with two gaps between the wall and the single wave maker paddle) and the Ocean Engineering tank configuration (which features several gaps between numerous wave maker paddles). We model the spurious waves resulting from these jets as a superposition of waves oscillating at the frequency of the wave maker motion ω and at its associated harmonics (2ω, 3ω, etc.). From now on, n_{harmo} will refer to the harmonic number (to not be confused with n which will refer to the transverse eigen mode number). These disturbances propagate in both the x and y directions. We denote their wavenumbers along the x and y axes as μ and κ, respectively.

Mathematical formulation of the jet-induced perturbations Let's denote $\eta_{n_{\text{harmo}}}(x,y,t)$ the free surface elevation of jet-induced disturbances, and associated with the n_{harmo} harmonic of the wave maker motion frequency. As sketched in Figure 3.11, it is a sum of waves going in the directions ($x > 0$,$y < 0$) and ($x > 0$,$y < 0$). Analytically, noting $A_{n_{\text{harmo}}}$ the amplitude of the perturbations, this gives:

$$\eta_{n_{\text{harmo}}}(x,y,t) = A_{n_{\text{harmo}}}\cos(n_{\text{harmo}}\omega t - \kappa_{n_{\text{harmo}}}x + \mu y) + A_{n_{\text{harmo}}}\cos(n_{\text{harmo}}\omega t + \kappa_{n_{\text{harmo}}}x + \mu y) \tag{3.30}$$

yet,

$$\eta_{n_{\text{harmo}}}(x,y,t) = 2A_{n_{\text{harmo}}}\cos(\mu y)\cos(n_{\text{harmo}}\omega t - \kappa_{n_{\text{harmo}}}x) \tag{3.31}$$

The wave number vector $\overrightarrow{k_{n_{\text{harmo}}}}$ can be written as

$$\overrightarrow{k_{n_{\text{harmo}}}} = \kappa_{n_{\text{harmo}}}\overrightarrow{x} \pm \mu\overrightarrow{y} \tag{3.32}$$

which induces,

$$k_{n_{\text{harmo}}}^2 = \kappa_{n_{\text{harmo}}}^2 + \mu^2 \tag{3.33}$$

with $k_{n_{\text{harmo}}}$ which obeys the dispersion relation:

$$(n_{\text{harmo}}\omega)^2 = g k_{n_{\text{harmo}}} \tag{3.34}$$

Since the domain is restricted by the side walls of the basin, the y component of $\eta_{n_{\text{harmo}}}$ is stationary and the transverse wavenumber is restricted to solutions of the form:

$$\mu = \mu_n = n\pi/L_y \tag{3.35}$$

Each n corresponds to a transverse eigenmode of the tank. The discretization of the possible values of μ also affects the possible values of the wave number of the x component ($\kappa_{n_{harmo}}$ becomes $\kappa_{n,n_{harmo}}$). Indeed, for each harmonic n_{harmo} and mode n, the longitudinal and transverse wavenumbers verify:

$$k_{n_{\text{harmo}}}^2 = \kappa_{n,n_{\text{harmo}}}^2 + \mu_n^2 \tag{3.36}$$

In this way, for each n_{harmo} harmonic, we can isolate the free surface elevation related to the mode n:

$$\eta_{n,n_{\text{harmo}}}(x,y,t) = 2A_{n,n_{\text{harmo}}} \cos(\mu_n y)\cos(n_{\text{harmo}}\omega t - \kappa_{n,n_{harmo}} x) \tag{3.37}$$

The free surface elevation resulting from the disturbance is therefore a sum of components of the form (eq. 3.37). These modes are linearly propagating waves modulated in the y direction. Henceforth, they will be referred to as transverse-propagating modes ($n_{\text{harmo}}\omega$, n).

Characteristics of the spurious modes Only the modes that satisfy $\mu_n^2 < k_{n_{harmo}}^2$ can propagate (i.e. $n\pi/L_y < n_{harmo}^2\omega^2/g$). The modes with $\mu_n^2 > k_{n_{harmo}}^2$ are transverse standing waves that decay in the x direction, primarily located near the excitation source, namely the wave maker. The characteristic dissipation length of these x-evanescent modes is given by:

$$\delta_{n,n_{harmo}} = 1/\sqrt{|k_{n_{harmo}}^2 - \mu_n^2|} \tag{3.38}$$

When the wave maker frequency or one of its harmonic $n_{harmo}\omega$ reaches a natural transverse mode frequency $\sqrt{g\mu_n} = \sqrt{gn\pi/L_y}$, the dissipation length tends toward the infinite. This means that associated waves are transverse stationary modes oscillating in the y direction, and remaining uniform in the x direction. The energy provided by the jets is completely transferred to the

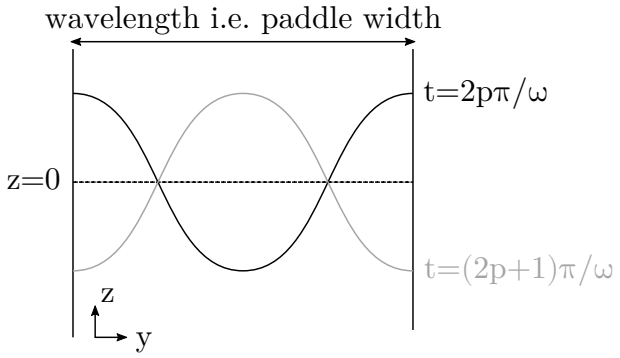

Figure 3.12 – Sketch of modes $2N_{paddle}$

transverse direction.

For each paddle, the first excited modes are even (i.e., symmetric modes). Figure 3.12 illustrates this mechanism. Each paddle-side jet simultaneously exerts forces at anti-nodes. Consequently, the y-axis wavelength of these modes is equal to the width of the paddle. The excited transverse mode number is given by $2N_{\text{paddle}}$, where N_{paddle} is the number of paddles. This is why the expected modes are even. However, odd modes were experimentally observed in cases where ω matches the natural transverse frequency of an odd mode.

Summary In conclusion, at a sufficiently large distance from the wave maker ($x > \max(\delta_{n,n_{harmo}})$), the generated wave field contains (i) the target unidirectional progressive wave, (ii) the sum of the excited transverse-propagating modes verifying $\mu_n^2 < k_{n_{harmo}}^2$, and (iii) the purely stationary transverse modes, excited if one of the harmonics of the target wave ω matches a natural transverse frequency of the tank. Note that the waves (i) and (ii) propagate at slightly different velocities, which can lead to beat phenomena in the x direction.

Therefore, to predict the potential excitation of transverse modes when generating a regular wave with a target wavelength λ, one should calculate the nature of the possible spurious modes (transverse/propagating or evanescent), at least for the first harmonics.

Example Figure 3.13 provides an example using the Towing tank configuration ($L_y = 5$ m) and a wave frequency of $f = 0.89$ Hz ($\lambda = 2$ m). This corresponds to the peak frequency of several reference sea states generated for this thesis (i.e., `ss6g5` and `GOM` sea states at scales 120 and 188, respectively). The target and mode 5 wavelengths are nearly equal. As a result, the latter eigenmode is likely to be generated as a strictly transverse standing wave. Additionally, the wavelength of mode 4 is slightly shorter than λ, which can lead to a transverse propagative

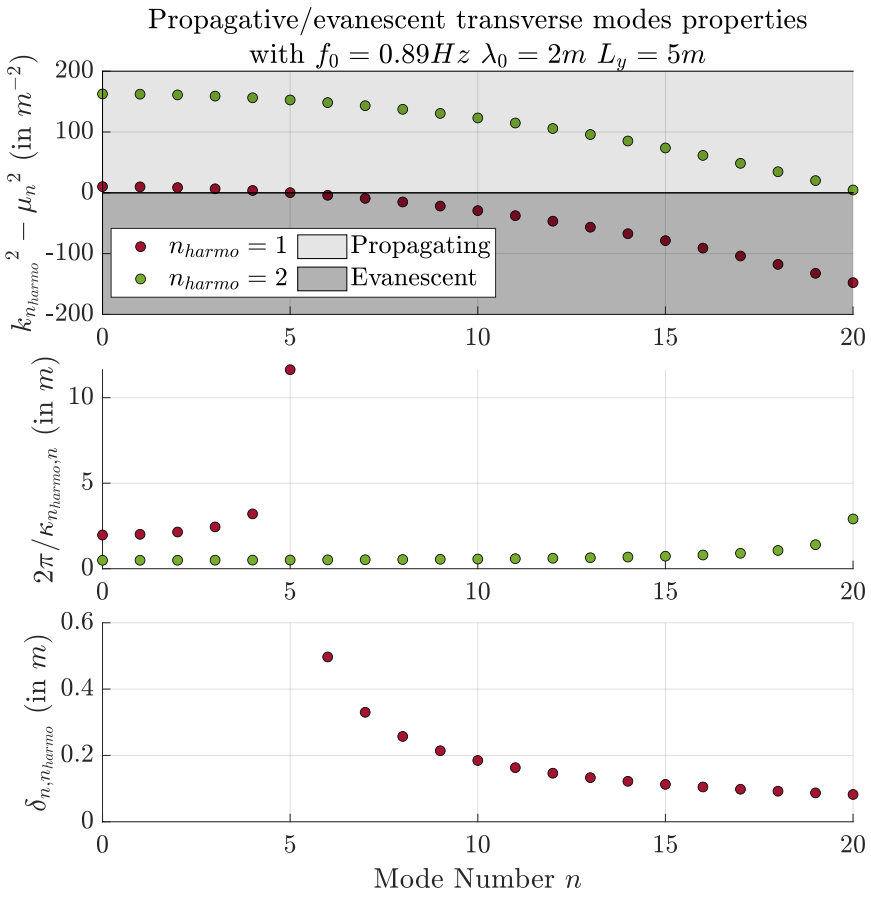

Figure 3.13 – Transverse modes nature, wavenumber, and evanescent dissipation length for a regular wave of frequency $f = 0.89$ Hz in a tank of width $L_y = 5$ m

mode with a wavelength of $0.65L_y = 3.25$ m in the x direction. The higher modes ($n > 5$) cannot be generated by the first harmonic, allowing them only an evanescent nature. Nonetheless, the second harmonic can generate spurious modes up to $n = 19$.

b) Extension to the irregular sea states

In the previous section, we established an analytical formalism to determine the nature of the jet-induced disturbances in the case of monochromatic wave conditions. These disturbances can manifest as transverse-propagating modes, purely-transverse standing modes, or x-axis evanescent modes depending on the frequency of the wave maker motion and the tank width. Now, the objective is to expand this analysis to the irregular wave conditions studied in this

Table 3.1 – Configurations to study

	$\lambda_p = 2$ m $f_p = 0.89$ Hz	$\lambda_p = 4$ m $f_p = 0.63$ Hz	$\lambda_p = 5.85$ m $f_p = 0.52$ Hz	$\lambda_p = 7.50$ m $f_p = 0.46$ Hz
Towing Tank $L_y = 5$ m	`ss6g5` Scale 120 `GOM` Scale 188	`ss6g5` Scale 60 `GOM` Scale 94	`ss6` Scale 40	/
O.E. Tank $L_y = 29.74$ m	/	`ss6g5` Scale 60 `GOM` Scale 94	`ss6` Scale 40	`GOM` Scale 50

thesis. This expansion will help establish, for each experiment conducted, the list of the possible spurious modes that could impact the results.

In the context of irregular sea states (numerous propagating frequencies), the total wave field, including the water jet disturbances consist of:

— the input x-axis propagating spectrum,

— the y-axis standing modes excited if the input frequencies and harmonics match the eigenmode frequencies of the tank,

— the allowable transverse-propagating modes excited by the input frequencies and their harmonics.

As a result, providing an accurate description of the wave field is a complex task. It will not be done in this thesis. To tackle the problem, our adopted strategy follows two steps. First, for each conducted experiment, we predict the transverse modes which are likely to be generated. Then, we track them in the experimental data. This subsection is dedicated to the first step.

Table 3.2 – Transverse eigenfrequencies of the ECN Towing tank

Mode n	0	1	2	3	4	5	6	7	8
Frequency f_n (Hz)	0	0.38	0.56	0.68	0.79	0.88	0.97	1.05	1.12

Table 3.3 – Transverse eigenfrequencies of the O. E. tank

Mode n	10	11	12	13	14	15	16	17	18	19	20
Frequency f_n (Hz)	0.49	0.51	0.54	0.56	0.58	0.61	0.63	0.65	0.67	0.69	0.71

Table A.2 in Appendix A provides a list of all the experiments conducted for this thesis. From this list, Table 3.1 identifies 6 configurations. In this context, a 'configuration' refers to a combination of tank width (defining the eigenmode wavelength) and peak wavelength

(characterizing the frequencies of the perturbations). Complementary, Table 3.2 and 3.3 provide the natural transverse mode frequencies specific to the ECN Towing and O.E. tanks respectively. We can already deduce that the configuration $f_p = 0.89$ Hz, generated in the Towing tank, is very likely to excite the transverse mode 5 which has an eigenfrequency of 0.88 Hz.

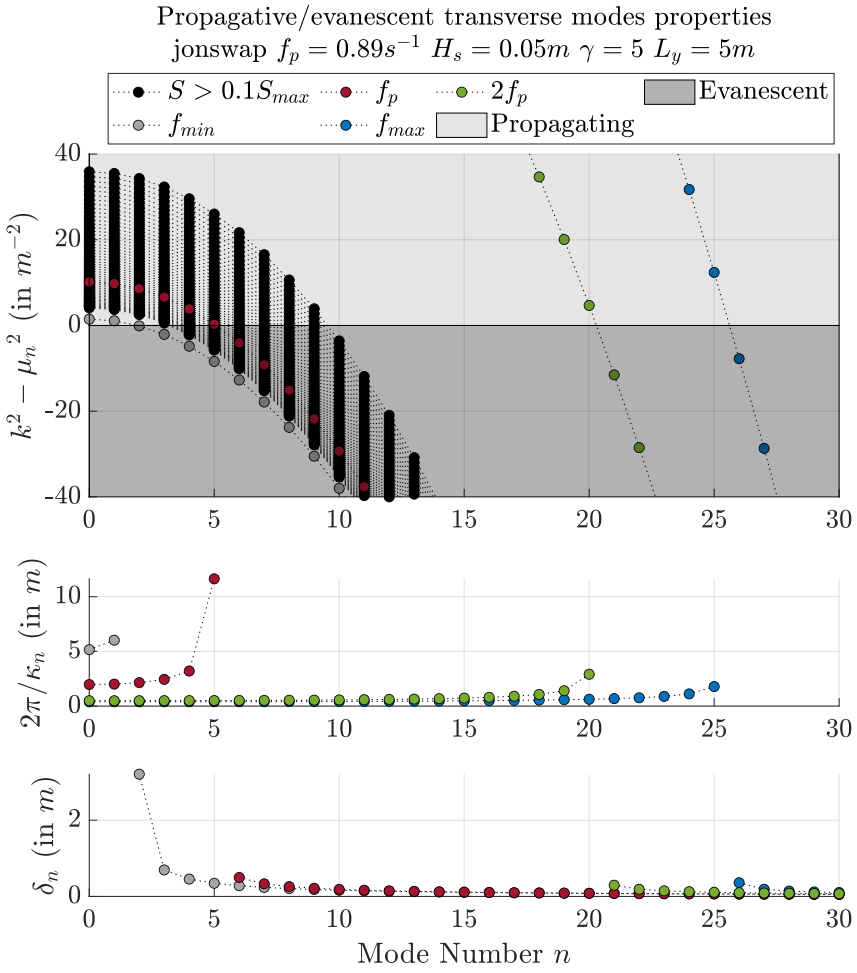

Figure 3.14 – Transverse modes nature, wavenumber and evanescent dissipation length for `ss6g5` sea state at scale 120 in the ECN Towing tank

Example: study of the configuration (Towing tank, $f_p = 0.88$ Hz) To provide an example, Figure 3.14 illustrates the modes that can be excited by the `ss6g5` scale 120 sea state generated in the Towing tank.

Each line with circular markers corresponds to a frequency component of the spectrum.

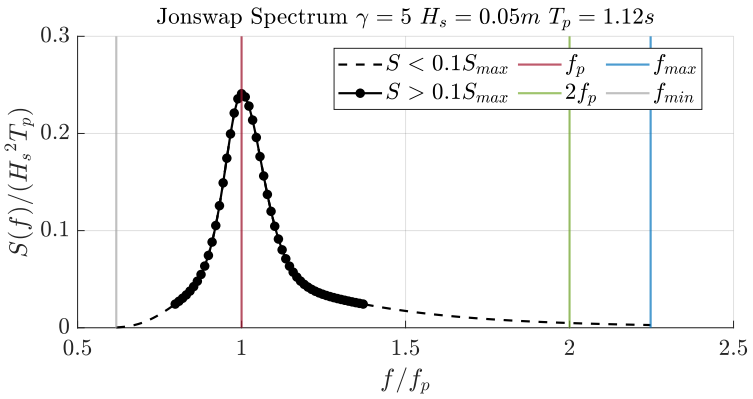

Figure 3.15 – `ss6g5` scale 120, frequencies used in Figure 3.14

For each component, the three plots display: the value of $\kappa_n^2 = k^2 - \mu_n^2$ for each mode number n (which allows identification of the mode's nature), the x-axis wavelength $2\pi/\kappa_n$ for the propagating modes, and the dissipation length δ_n for the evanescent modes.

Since the irregular wave field consists of hundreds of components, only the relevant frequencies are plotted, including the energetic frequencies (those verifying $S(f) > 0.1\max(S(f))$), the peak frequency f_p, the second harmonic of the peak frequency $2f_p$, the minimum frequency f_{min}, and the maximum frequency f_{max}. For further clarification, Figure 3.15 presents these frequencies on the `ss6g5` spectrum shape.

We observe that f_p closely matches the natural frequency of mode 5, leading to the generation of a long-wavelength transverse propagating mode likely to influence the results throughout the tank. Moreover, pure transverse modes 4 to 9 can also be excited by the most energetic frequencies. More generally, transverse propagating modes below 9 may be generated while higher-order modes are evanescent. Also, note that the second harmonic of the peak frequency can excite mode 20.

Prediction of the transverse disturbance for the 6 configurations under study Similar analyses were conducted for all the configurations listed in Table 3.1. The primary findings are gathered in Table 3.4. Some configurations include multiple sea states with different γ factors (i.e., different frequency widths). For the sake of brevity, only the γ values displayed in Table 3.4 were considered to establish the list of frequency components for study. Note that it can slightly affect the number of allowable transverse modes. Table 3.4 predictions will be utilized in the next subsection to effectively track the transverse disturbances in the experimental data.

Table 3.4 – Prediction of the transverse modes for the different wave conditions and tanks

	$\lambda_p = 2$ m Towing $\gamma = 5$	$\lambda_p = 4$ m Towing $\gamma = 2.6$	$\lambda_p = 4$ m O.E. $\gamma = 2.6$	$\lambda_p = 5.9$ m Towing $\gamma = 1$	$\lambda_p = 5.9$ m O. E. $\gamma = 1$	$\lambda_p = 7.5$ m O. E. $\gamma = 2.6$
Pure transverse modes near f_p	5	2 and 3	15	2	10	8
Other pure transverse modes	3 to 10 +20	2 to 6 +10	8 to 38 + 58	1 to 7	5 to 41	4 to 20
Transverse propagating modes	<10	<6	<38	<6	<41	<20

3.4.2 Tracking of the transverse modes in the experimental data

In the previous paragraphs, with the help of theoretical considerations, we have listed the transverse modes that could be generated for each configuration. We will now try to identify them in the experimental data and assess their influence on the quantities of interest (spectrum, statistics). If possible, strategies will be implemented to remove these transverse disturbances from the analyzed data.

As observed in Table 3.3 and 3.2, the predicted transverse mode numbers and frequencies significantly differ between the Ocean Engineering and the Towing tank. As a result, the approach adopted to address the problem will also differ. This subsection provides a dedicated study for each of the two tanks.

a) Towing tank data

This subsection is devoted solely to the analysis of transverse modes in the Towing tank. The result that will be presented come from Campaigns A and D.

Experimental setup strategy The Towing tank has a relatively small width of 5 meters, and wave gauges can be placed at any positions along the y-axis. This flexibility allows for the setup of lines of wave gauges perpendicular to the wave propagation direction. In these lines, the gauges share the same x-coordinate but have different y-coordinates. According to Table 3.4, the number of modes that can propagate is quite small (only the modes lower than 10).

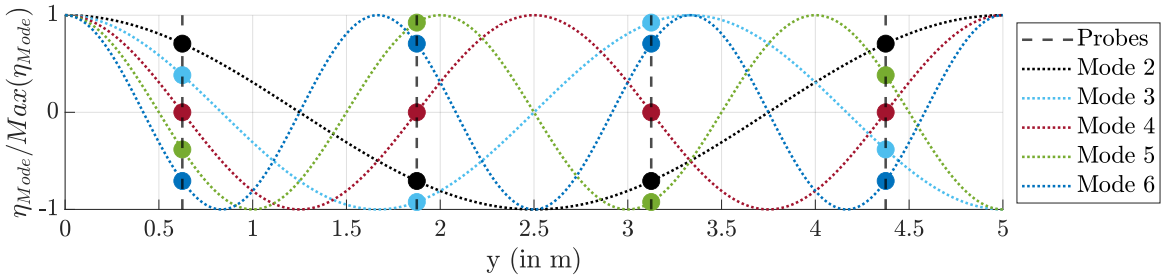

Figure 3.16 – Profile of the transverse modes along the $x = 8$ m measurement line setup in Campaigns A and D

Consequently, it is possible and relevant to strategically adjust the y-positions of the probes to mitigate the influence of a specific mode (using the symmetry of the modes, and the node positions).

Such a strategy was implemented in Campaigns A and D. At selected x-positions of interest, multiple gauges were installed to form lines of four probes. Figure 3.16 presents the shape of the transverse mode along with the probe locations along a line. The chosen positions of the probes correspond to the nodes of mode 4 ($y = 0.625$ m, $y = 1.875$ m, $y = 3.125$ m, and $y = 4.375$ m). With such a setup, the sum of the amplitudes of modes 2 to 6 vanished. Consequently, when averaging the data from the four free-surface elevation time series (computation of $\eta_{\text{mean}}(t) = (\eta_1(t) + \eta_2(t) + \eta_3(t) + \eta_4(t))/4$), the lateral symmetry of the flow erases the influence of modes 2 to 6. In addition, the symmetry of the probe positions also removes all the odd modes. The average series $\eta_{\text{mean}}(t)$ will then be considered free from transverse disturbances.

Signatures of the transverse modes for $\lambda_p = 4m$ and $\lambda_p = 5.9m$ configurations Table 3.1 identifies three peak wavelengths to analyze for the Towing tank: $\lambda_p = 5.85$ m, $\lambda_p = 4$ m and $\lambda_p = 2$ m. We first analyze $\lambda_p = 5.85$ m and $\lambda_p = 4$ m configurations.

To identify the transverse modes, for each transverse position y, we extract the difference $\eta(y,t) - \eta_{\text{mean}}(t)$. This quantity fully characterizes the transverse disturbances. Figures 3.17 and 3.18 present the $\eta(y,t) - \eta_{\text{mean}}(t)$ series and spectrum for `ss6` scale 40 and `GOM` scale 94 sea states ($\lambda_p = 5.85$ m and $\lambda_p = 4$ m, respectively). The data come from the transverse line at $x = 8$ m set up within the framework of Campaign D. As predicted in Table 3.4, for both wave conditions, the energy of the disturbances is localized near the mode 2 frequency (which in both cases slightly differs from the peak frequency). Looking at the spectral energy density of $\eta -$

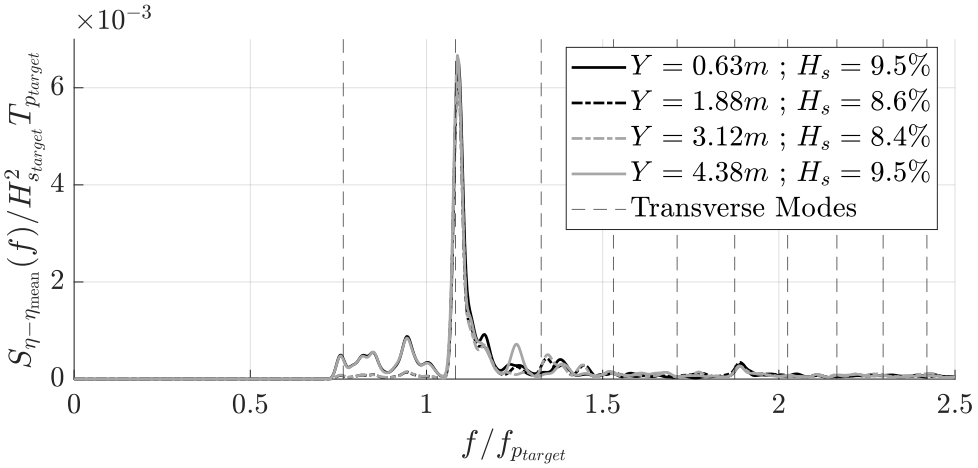

(a) Spectrum

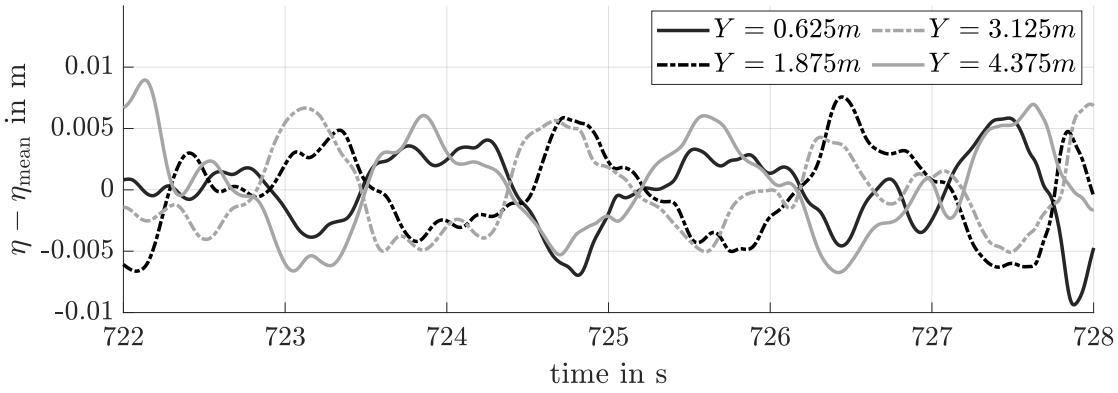

(b) Time series

Figure 3.17 – $\eta - \eta_{\text{mean}}$ analysis along the transverse line; `ss6` sea state at scale 40 ($\lambda_p = 5.85$ m); $x = 8$ m; ECN Towing tank Campaign D.

η_{mean}, it seems that the influence of the other modes can be neglected. Furthermore, the series of $\eta(y,t) - \eta_{\text{mean}}(t)$ show that the signals at $y = 0.625$ m and $y = 4.375$ m are similar and with opposite phase compared to the signals at $y = 1.875$ m and $y = 3.125$ m. The sketch provided in Figure 3.16 shows that this behavior is in agreement with the mode 2 shape. Therefore, it is established that for `ss6` scale 40 and `GOM` scale 94 sea states, transverse mode 2 is excited and is the leading mode. The $\eta(y,t) - \eta_{\text{mean}}$ spectra indicate that for both wave conditions, the significant wave height of the transverse disturbance reaches approximately 10% of the total H_s (computed from the mean signal and henceforth referred to as $H_{s_{\text{ref}}}$). The interpretation of this value will be discussed later in this section.

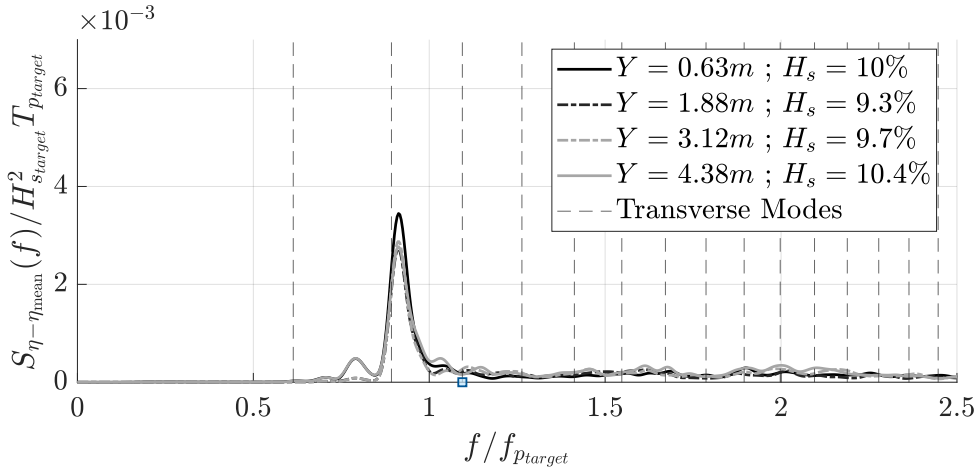

(a) Spectrum

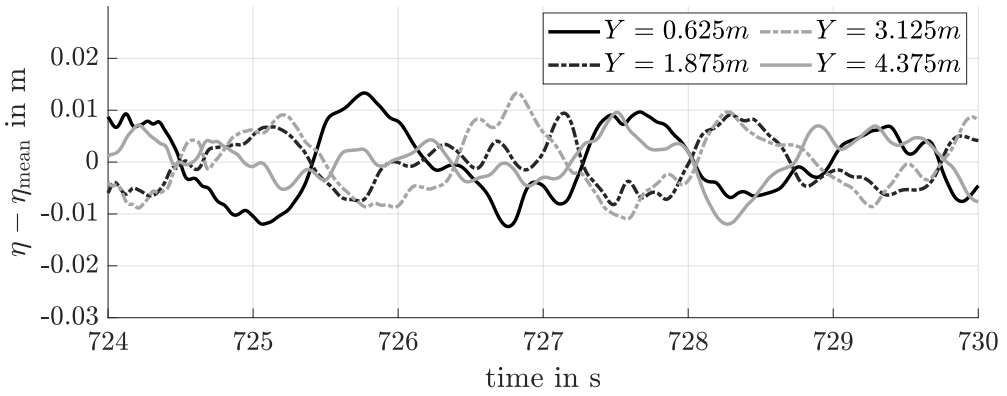

(b) Time series

Figure 3.18 – $\eta - \eta_{\text{mean}}$ analysis along the transverse line; `GOM` sea state at scale 94 ($\lambda_p = 4$ m); $x = 8$ m; ECN Towing tank Campaign D.

Signatures of the transverse modes for $\lambda_p = 2m$ configuration: $\eta(y,t) - \eta_{\text{mean}}$ analysis We now investigate the transverse modes for the $\lambda_p = 2$ m configuration. Figure 3.19 shows the $\eta(y,t) - \eta_{\text{mean}}$ spectral density for the `ss6g5` sea state at scale 120, still at $x = 8$ m (Campaign D). The results are somewhat challenging to interpret. There is no clear signature of transverse modes. In all four signals, the energy is concentrated around the mode 5 frequency, which coincides with the peak frequency of the sea state. As shown later in Figure 3.21, which presents artificial linear data, a small lack of parallelism between the transverse line and the wave maker can introduce noise near f_p when examining the $\eta(y,t) - \eta_{\text{mean}}$ spectrum. In addition, inaccurate calibration factors also introduce noise. As a remainder, Table 3.7 indicates

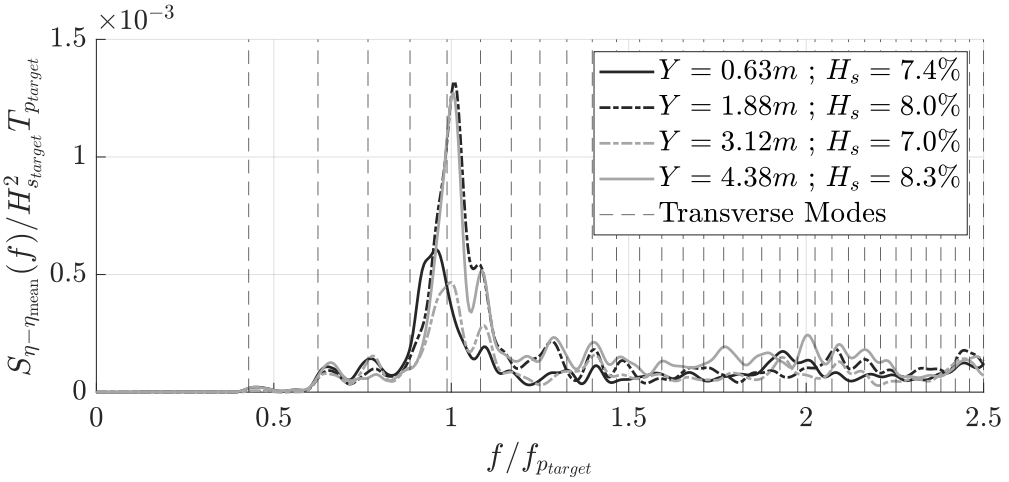

Figure 3.19 – $\eta - \eta_{\text{mean}}$ spectrum for the probes of the transverse line at $x = 8m$; `ss6g5` sea state at scale 120 ($\lambda_p = 2$ m); ECN Towing tank Campaign D

uncertainties of 0.75%, 1.4%, 1.8%, and 1% for the wave gauge factors at $y = 0.625$ m, $y = 1.875$ m, $y = 3.125$ m, and $y = 4.375$ m, respectively. This inevitably affects $\eta(y,t) - \eta_{\text{mean}}$ spectrum. Given these complexities, we will use an alternative strategy to identify the transverse modes for the $\lambda_p = 2m$ configuration.

Signatures of the transverse modes for $\lambda_p = 2m$ configuration: post-run noise analysis
After an experimental run, when the wave maker stops and the last generated waves reach the end of the tank, the water does not immediately return to a calm state. Residual waves persist. First, as the wave-absorbing system is not perfect, a part of the generated waves is reflected at the end of the tank and propagates in the $-\overrightarrow{x}$ direction. Next, they encounter the wave-maker paddles, which are reflective, causing them to propagate back in the $\overrightarrow{x}$ direction. These reflected waves gradually dissipate after a few crossings of the tank.

Additionally, the transverse modes also persist after the end of the run. Indeed, they only interact with the perfectly reflective side walls (no absorbing system on the sides of the domain). As a consequence, they take a considerable amount of time to dissipate completely (≈ 1 h).

Therefore, to identify and quantify the transverse modes, one can analyze the post-run data within a time window starting after the dissipation of the reflected waves and ending before the dissipation of the transverse modes. For the present work, we consider that the reflected waves are totally dissipated after two crossings of the tank (i.e. after the second reflection at the

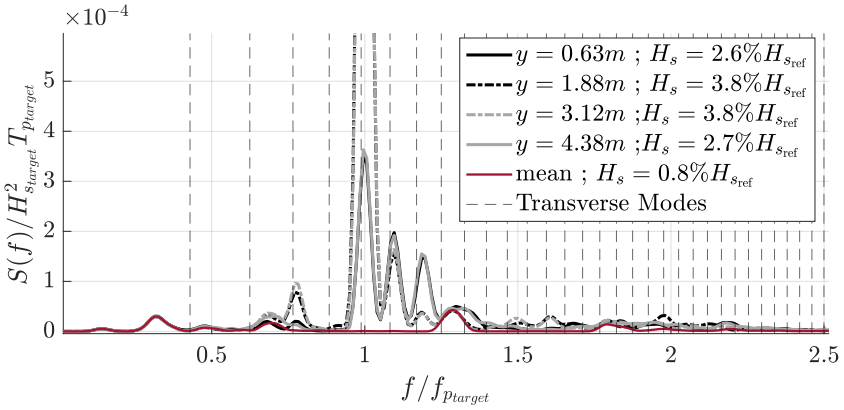

(a) Spectrum

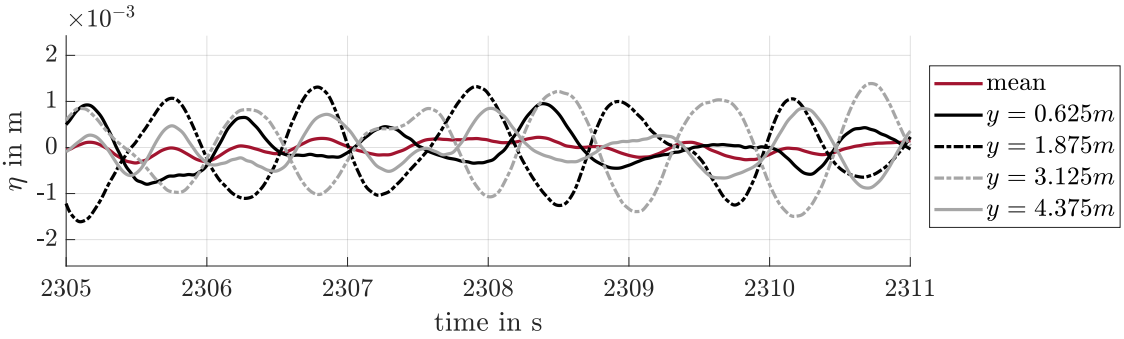

(b) Time series

Figure 3.20 – Post run analysis for the probes of the transverse line at $x = 8m$, without reflection i. e. $t > (T_{\text{WVMK}} + (2L+x)/c_g(f_p))$; `ss6g5` sea state at scale 120 ($\lambda_p = 2$ m); ECN Towing tank Campaign D

beach). This leads to a time window analysis of type:

$$t_{\text{beg}} = T_{\text{WVMK}} + (2L_x + x)/c_g(f_p) \tag{3.39}$$

and

$$t_{\text{end}} = t_{\text{beg}} + 300T_p \tag{3.40}$$

with T_{WVMK} the time at which the wave maker stops running. The value of t_{end} specified here is arbitrary and depends on the duration of the recorded data. It is set to be as large as possible, while ensuring that it does not include the decay of the noise.

Following this strategy, Figure 3.20 analyzes the post-run data, free from reflection, recorded along the $x = 8$ m transverse line, after a run of `ss6g5` at scale 120. For each probe, it

displays the time series of the signals and the spectrum. For information, $T_{\text{WVMK}} = 1610s$ and $(2L+x)/cg(f_p) = 330s$.

Upon examining the spectrum, we notice that the energy is focused around transverse mode frequencies. Mode 5 is the most energetic but modes 3, 6, and 7 are also clearly observable. Since all the probes are positioned at the mode 4 nodes, mode 4 is not measured. We also observe that the wave gauges at $y = 1.875$ m and $y = 3.125$ m are more affected by mode 5. This aligns with expectations from Figure 3.16, which provides the theoretical shape of the modes along the transverse line.

Furthermore, in the time series comparisons, we observe that the signals at $y = 0.625$ m and $y = 3.125$ m have opposite phase compared to $y = 1.875$ m and $y = 4.375$ m signals, which is again indicative of mode 5. Lastly, the mean signal is almost zero, which validates the experimental method that involves averaging the signals from the four wave gauges to mitigate the influence of the transverse modes.

Limitations of the methods The use of the H_s values obtained from the $\eta - \eta_{\text{mean}}$ spectral density to assess transverse modes energy is not straightforward. As mentioned earlier, factors like transverse line alignment and errors in wave gauge calibration introduce residual noise. To better understand the amount of noise unrelated to transverse modes in the previous analyses (Figures 3.17, 3.18, and 3.19), Figure 3.21 presents an analysis of $\eta - \eta_{\text{mean}}$ spectra for artificial linear data modeled along a transverse line at y =0.625, 1.875, 3.125, 4.375 m. These data are affected either by i) a realistic small misalignment $\delta_x = 0.02$ m between $y = 0$ m and $y = L_y = 5$ m (Fig 3.21a), ii) realistic wave gauge calibration errors (Fig 3.21b), iii) or both $\delta_x = 0.02$ m and calibration errors (Fig. 3.21c).

The δ_x deviation introduces noise of up to $3.5\%H_{s_{\text{ref}}}$ for the gauges furthest from the center. The spectrum shape follows the η_{mean} spectrum, but there is a significant amount of energy for frequencies larger than f_p. On the other hand, wave gauge calibration errors lead to noise spectra ranging from 1 to $1.3\%H_{s_{\text{ref}}}$, which perfectly align with the η_{mean} spectrum. Combining both effects does not significantly amplify the errors.

Based on these results, we can conclude that the H_s values presented in Figures 3.17, 3.18, and 3.19 are likely to be affected by noise in the range of 2 to $4\%H_{s_{\text{ref}}}$. As a reminder, for all the studied wave conditions, the H_s values obtained from the $\eta - \eta_{\text{mean}}$ spectra are between 7 and 8% (see Figure 3.19). Therefore, the portion of the height attributed to the transverse modes is estimated to be between 3 and 6% of the significant wave height of the wave fields. This estimation is corroborated by the values derived from the post-run noise analysis (Fig.

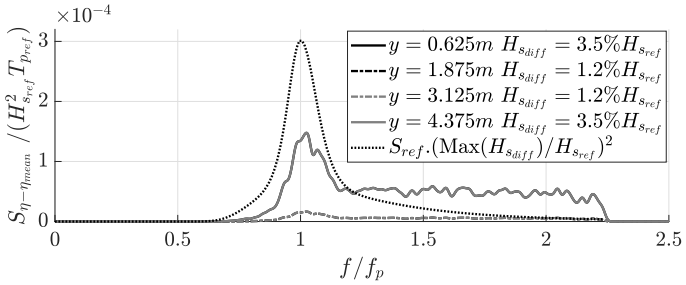

(a) $\delta_x = 0.02$ m; perfect WG calibration

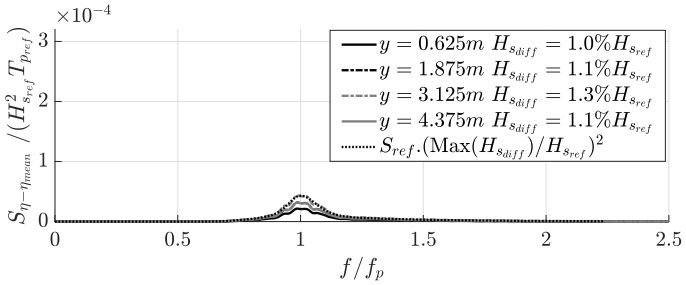

(b) $\delta_x = 0$ m; WG error of -1.1, +1, -1.5, and +1% for y =0.625, 1.875, 3.125, 4.375 m respectively

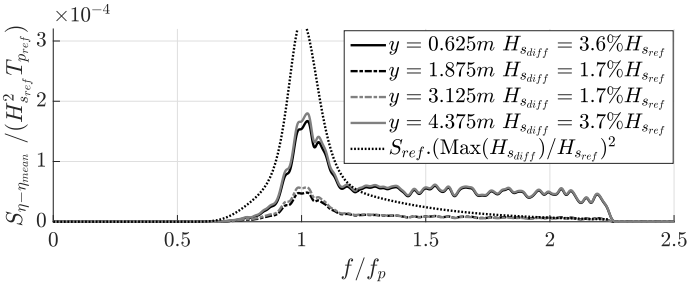

(c) $\delta_x = 0.02$ m; WG error of-1.1, +1, -1.5, and +1% for y =0.625, 1.875, 3.125, 4.375 m

Figure 3.21 – Artificial linear `ss6g5` at scale 120; $\eta - \eta_{\text{mean}}$ analysis: influence of δ_x and wave gauge calibration factor errors

3.20).

Transverse mode influence on the quantities of interest Now that the transverse modes have been identified and quantified, the next and final step is to study their influence on the quantities of interest. For the sake of brevity, this paragraph focuses on `ss6g5` sea state scale 120 wave conditions generated in the Towing tank as part of Campaign D. Specific analyses dedicated to other sea states will be provided throughout the manuscript when necessary. The influence of the transverse modes will not be included in the uncertainty bars.

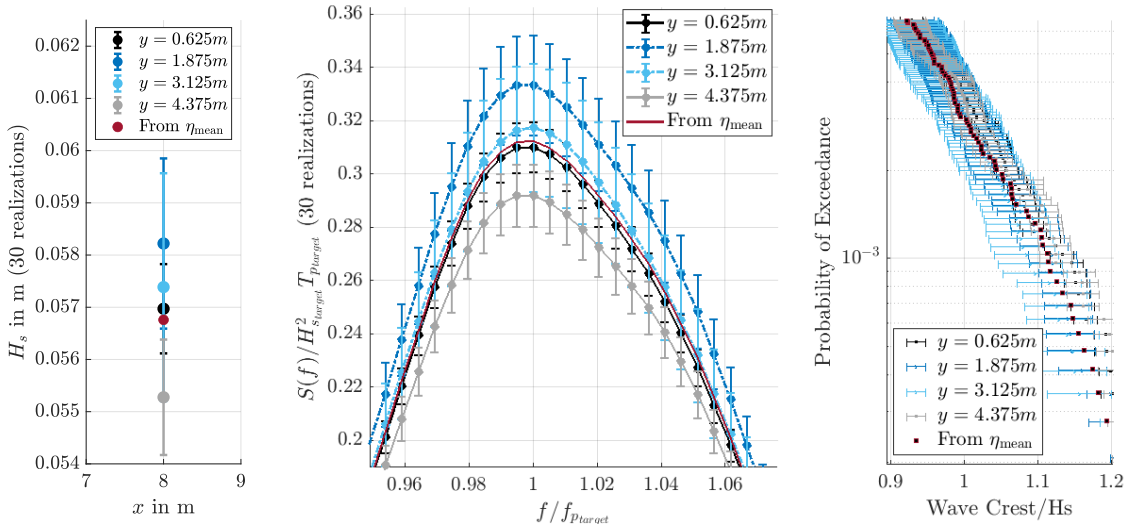

(a) H_s **(b)** Spectrum **(c)** Crest PDER

Figure 3.22 – Influence of transverse modes on the quantities of interest, `ss6g5` sea state at scale 120, Campaign D, probes at $x = 8$ m

In this context, Figure 3.22 presents the measured significant wave height, spectrum, and crest PDER for the four wave gauges along the transverse line at $x = 8$ m, as well as their mean η_{mean}. The data include 30 realizations, each of approximately 400 T_p in duration. The displayed uncertainty ranges correspond to the measurement standard uncertainty (see Section 3.3.4).

As described in previous paragraphs, the wave fields are affected by transverse mode 5, which has a frequency nearly-equal to f_p and predominantly influences the probes located at $y = 1.875$ m and $y = 3.125$ m. This influence is evident in the H_s and wave spectrum data, where the curves for $y = 1.875$ m and $y = 3.125$ m consistently appear above the others, even considering the uncertainty ranges.

However, there is also a clear effect of wave gauge calibration error. The signal at $y = 1.875$ m appears unrealistically more energetic than at $y = 3.125$ m across the displayed frequency range centered around f_p. This discrepancy cannot be explained solely by transverse mode effects since mode 5 symmetrically affects the energy at $y = 1.875$ m and $y = 3.125$ m. The incorrect calibration factor for $y = 1.875$ m also explains why the η_{mean} spectrum does not fall below all the others, as it should, being free from transverse modes and their associated energy. Lastly, the normalized crest PDER variations from one gauge to another are too small

to be interpreted when compared to the uncertainty associated with the wave gauges.

In conclusion, transverse modes have an influence on the significant wave height and spectrum of an order of magnitude similar to the calibration factor uncertainty but do not significantly change the normalized crest heights.

b) O.E. tank data

Strategy The cases analyzed in the previous subsection come from Towing tank runs. Now, we need to investigate the data from the Ocean Engineering tank. This facility has a considerably larger width ($L_y = 29.74$ m). Consequently, it is more likely to excite high-frequency transverse modes (as indicated in Table 3.4). The difference in frequency between these modes is very small, and a significant number of modes may be excited. Furthermore, their wavelengths are short. These factors make it challenging to place probes at specific nodes and antinodes, as was done for the Towing tank experiments.

Therefore, in the Ocean Engineering tank data, we analyze the presence of transverse modes by examining the post-run noise, similar to the approach used for $\lambda_p = 2$ m sea states in the Towing tank (see previous subsection). As with the Towing tank, we ensure that the analysis time windows are selected to avoid the reflected waves, using the criterion: $t_{\text{beg}} > T_{\text{WVMK}} + (2L + x)/cg(f_p)$.

Results Figure 3.23 displays the spectra obtained from data recorded after the runs along the transverse lines of probes for the three configurations analyzed in the Ocean Engineering tank (as listed in Table 3.1). Several observations can be made from these spectra.

First, for each case, the measured significant wave height is approximately 6% of the $H_{s_{\text{target}}}$ of the previously generated wave field. This is slightly larger than the value observed in the Towing tank. The remaining energy is clearly concentrated around the frequencies of the transverse modes, confirming that these modes are responsible for the noise. The excited modes are predominantly located near the peak frequency f_p, which aligns with the predictions presented in Table 3.4.

However, for each sea state, we also observe the presence of transverse mode 96, along with other high-frequency modes. This occurrence is a result of the 48 paddles in the Ocean Engineering tank, which naturally excite mode numbers up to $2N_{\text{paddle}}$ (as shown in Figure 3.12).

The influence of these transverse modes on stochastic quantities of interest will be addressed as needed for each specific configuration when analyzing the experimental data from

the Ocean Engineering tank.

3.4.3 Conclusion

In this section, we have studied the transverse spurious modes, appearing while generating unidirectional sea states. In our global approach for estimating the experimental uncertainties, these transverse disturbances are part of Type-B wave generation uncertainty.

For both Towing tank and O.E. tank experiments, we have found that the significant wave height of the transverse modes ranges from 3 to $6\%H_{s_{\text{target}}}$. For the Towing tank experiments, a strategy based on specific probe networks has been successfully implemented to remove the influence of the transverse modes. For the O.E. tank experiments, this strategy can not be easily implemented. Therefore, the influence of the transverse modes on stochastic quantities of interest will be addressed as needed for each specific O.E. tank configuration. It will not be included in the uncertainty bars.

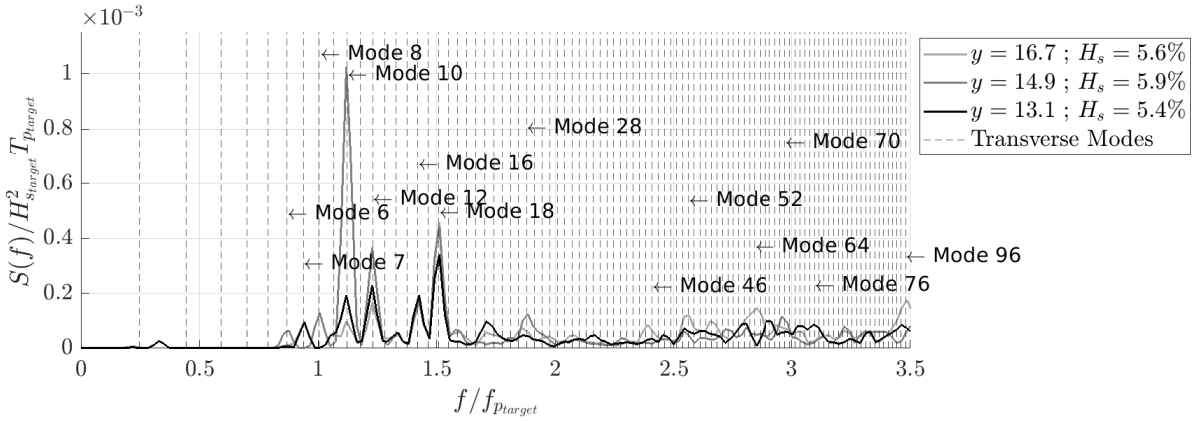

(a) GOM scale 50 Campaign B $x = 15$ m

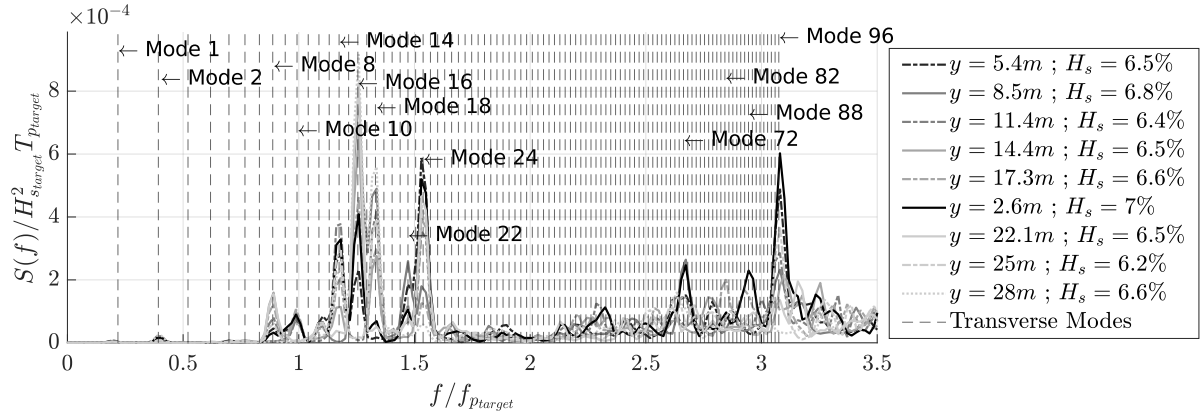

(b) ss6 scale 40 Campaign C $x = 20.3$m

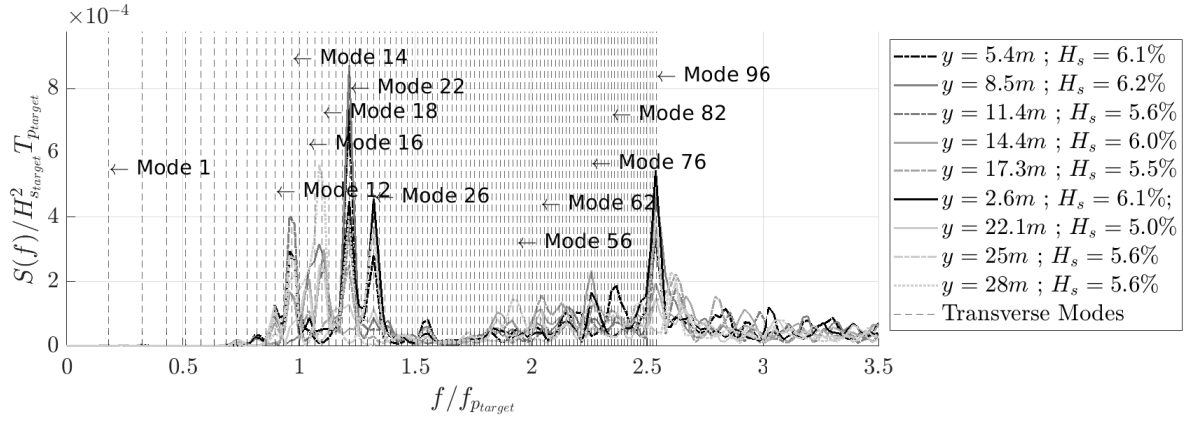

(c) GOM scale 94 Campaign C $x = 20.3$m

Figure 3.23 – Analysis of the remaining after the runs in the O.E. tank to identify the excited transverse modes

3.5 Generation uncertainty: reflection

The strategy implemented to estimate the uncertainty of experimental results (see Section 3.2.3) includes the following steps: quantification of Type B uncertainty related to sampling variability (Section 1.3.3 in Chapter 1), quantification of Type B uncertainty related to measurements (Section 3.3), quantification of Type B uncertainty related to wave generation (differences between the expected waves assuming a perfect environment and the generated waves), and analysis of Type A uncertainty (Section 3.6).

Type B uncertainty related to wave generation results from several phenomena listed in Figure 3.2.1. In the previous section, we studied the influence of spurious transverse modes. In this section, we will focus on the reflected waves.

The absorbing beaches at the end of the Towing and Ocean Engineering tanks are not perfect. They allow some waves to reflect and propagate back towards the wave maker, where they reflect again toward the beach. This back-and-forth process continues until the waves are totally dissipated. This can be visually observed during experiments, especially when generating short regular wave sequences. The objective of this section is to quantify the reflected waves for the generated irregular sea states and estimate their influence on the quantities of interest.

3.5.1 Quantification of the reflection

Several methods exist to characterize the efficiency of absorbing beaches. For a detailed list, refer to Bonnefoy (2005), which studied the ECN O.E. tank absorbing system. Typically, reflection is quantified for each frequency using a reflection coefficient, which is defined as the ratio between the Fourier amplitude of the reflected waves and the incident ones. This coefficient depends on the wave's frequency and steepness. Various internal studies conducted by the LHEEA laboratory have measured reflection coefficients ranging from 5% to 10% within the applicable range of the two ECN tanks. To verify this order of magnitude, we will quantify the reflection for `ss6g5` sea state generated at scale 120 in the Towing tank, which is a representative wave condition frequently used in this thesis.

To conduct this assessment, similar to the identification of transverse modes, we will examine the residual waves that still propagate after the end of the run (i. e. post-run data). However, in this case, we adapt the analysis time window to track the reflected waves.

The time window is illustrated in Figure 3.24. For each wave gauge located at a position x, it begins after the passage of the last wave of the incident wave field (indicated by the white diamond in Fig. 3.24). It ends when this last wave reaches the gauge position again, after

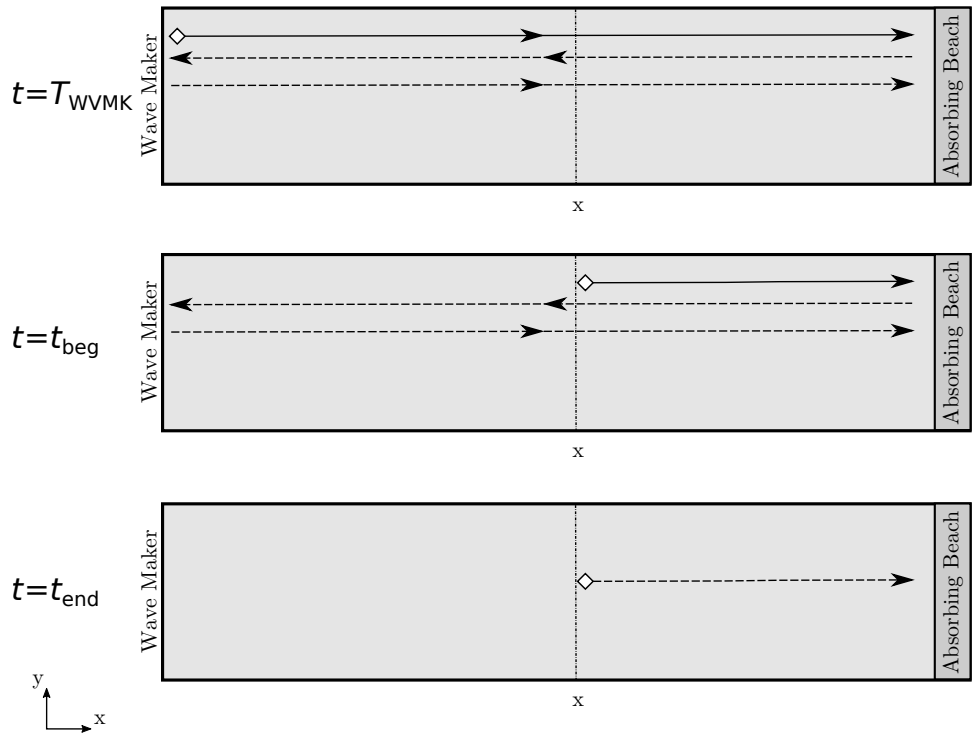

Figure 3.24 – Sketch presenting the time window analysis adopted to isolate the reflected waves at the end of the run; the continuous lines represent the incident wave field generated by the wave maker and the dotted line represents the reflected wave field; the white diamond indicates the last generated wave

partially reflecting at the beach, traveling from the beach to the wave maker, and returning to the gauge position. Specifically, the time window for analysis is defined as follows:

$$t_{\text{beg}} = T_{\text{WVMK}} + x/c_g(f_p) \tag{3.41}$$

and

$$t_{\text{end}} = T_{\text{WVMK}} + (2L+x)/c_g(f_p) \tag{3.42}$$

Within this time window, we examine the reflected waves but also the transverse modes that persist after the run (see previous section).

Figure 3.25 presents the spectra of post-run data measured at the 4 wave gauges located at $x = 8$ m within the framework of Campaign D. The run is the same as the one previously analyzed in Figure 3.20a for the identification of the transverse modes. Theoretically, the mean signal over the 4 probes is free from transverse mode influences.

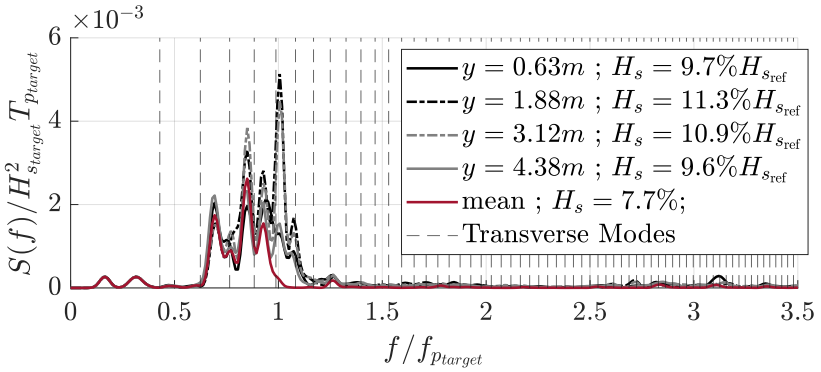

Figure 3.25 – Post run analysis including reflection and transverse noise; spectrum for the probes of the transverse line $x = 8m$; `ss6g5` sea state at scale 120 ($\lambda_p = 2$ m), ECN Towing tank Campaign D

When comparing Figure 3.25 (which contains the reflected waves and the transverse modes) to Figure 3.20a (where we isolated the influence of the transverse modes) we observe that the η_{mean} spectrum (in red) which is almost zero in Figure 3.20a, has energy in Figure 3.25. This energy likely represents the reflected waves. It is mainly localized around $[0.6f_p; 1f_p]$. The beach seems to be more efficient for the high frequencies. The displayed H_s percentages are relative to the measured significant wave height computed before the end of the run, using the mean signal of the 4 probes ($H_{s_{\text{ref}}}$).

For this irregular wave case, we will quantify the reflection with the ratio:

$$R_{H_s} = \frac{H_{s_{\text{reflect}}}}{H_{s_{\text{ref}}}} \tag{3.43}$$

with $H_{s_{\text{reflect}}}$ the significant wave height of the reflected waves only.

In our case, to estimate $H_{s_{\text{reflect}}}$, we use the $H_s(\eta_{\text{mean}})$ value shown in Figure 3.25. We obtain a R_{H_s} value of 7.7%. The order of magnitude aligns with our expectations.

3.5.2 Influence on the stochastic quantities of interest

The objective now is to assess the impact of reflected waves on the stochastic quantities of interest.

To this aim, we rely on a numerical study conducted using the HOS-NWT solver. The code description is provided in Chapter 5. In HOS-NWT simulations, reflection is controlled through an absorbing zone located at the end of the domain (see Ducrozet et al. (2012)). For a

zone size of several wavelengths, reflected waves are entirely absorbed. However, with smaller zones, some numerical waves can be reflected. For the present study we will use `HOS-NWT` as a model which enables to vary the reflection rate and therefore quantify its influence on the quantities of interest (spectrum, crest distribution).

To evaluate the impact of reflected waves, we will analyze the same HOS simulation conducted with various sizes of absorbing zones. The generated wave condition is `ss6g5` sea state at scale 120, and the domain is based on the characteristics of the ECN O.E. tank. The spatial discretization is configured as $k_{\text{max}}^{\text{HOS}} = 25k_p$, the nonlinearity order is set at 5, and the Tian breaking model is employed for robustness. You can find further details and a comprehensive interpretation of the numerical setup in Section 5.2.1, which specifically addresses the numerical generation of non-breaking sea states.

For each simulation employing a different size of the absorbing zone, we extract the reflected waves by subtracting, in the time domain, the free surface elevation $\eta_{\text{noreflect}}$ obtained when employing a large-size numerical beach (with no reflection):

$$\eta_{\text{reflect}}(t) = \eta_{\text{ref}}(t) - \eta_{\text{noreflect}}(t) \tag{3.44}$$

η_{ref} correspond to the total wave fields measured with the numerical probes. Next, by calculating the significant wave height of η_{reflect} and η_{ref}, we can compute $R_{H_s} = H_{s_{\text{reflect}}}/H_{s_{\text{ref}}}$.

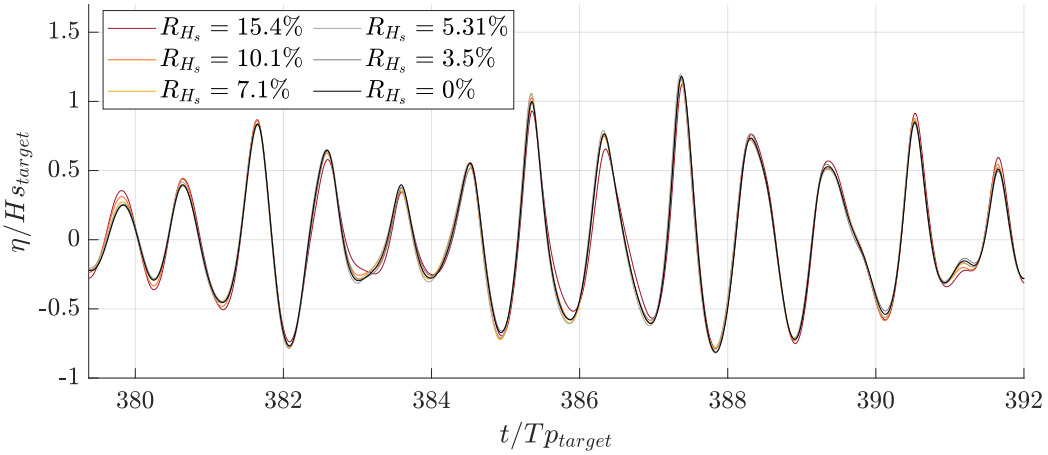

Figure 3.26 – Effects of reflected waves on the free surface elevation measured signal (HOS-NWT simulations, `ss6g5` sea state scale 120, Campaign D twin).

Figure 3.26 displays the obtained time series for different R_{H_s} values. As a reminder,

experimentally, R_{H_s} falls in the range of $[7,8]\%$. For this range of reflection coefficients, no significant differences can be observed in the time domain.

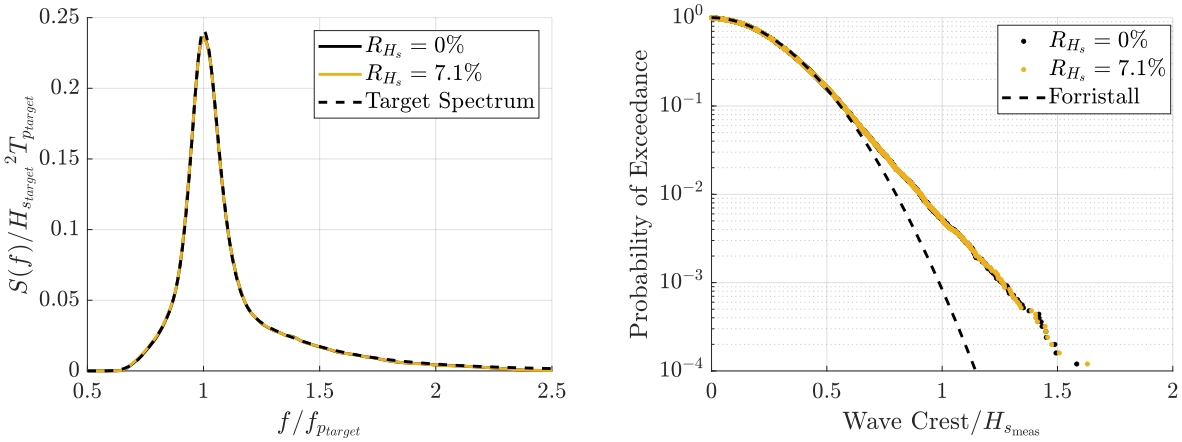

(a) Correlation and time shift

(b) Zoom on 12 periods

Figure 3.27 – Effects of reflected waves on the spectrum and crest distribution: $R_{H_s} = 7.1\%$ compared with $R_{H_s} = 0\%$ (35 seeds, HOS-NWT simulations, `ss6g5` sea state scale 60, $x = 52\lambda_p$)

In addition, in Figure 3.27, we compare the spectrum and crest distribution computed from two datasets, each consisting of 35 realizations ($T_{\text{analyzed}} \approx 22000 T_{p_{\text{target}}}$). One dataset was generated with a zone ensuring $R_{H_s} = 7.1\%$ (reflection rate measured in experiments) while the other was generated with $R_{H_s} = 0\%$ (no reflection). Here again, there are no significant differences. The reflection rate observed in the tanks has no impact on the quantities analyzed. We will therefore neglect the influence of reflection.

3.6 Type A study: repeatability

In the previous sections, we estimated the type B uncertainty linked to measurement errors (u_s^{meas}) and wave generation uncertainties (spurious transverse modes and reflection). Following the ITTC (2017a) guidelines, we are now going to estimate the order of magnitude of type A uncertainties affecting the quantities of interest, using a repeatability study of representative cases.

We will investigate variations in time series $\eta(t)$ and stochastic quantities (spectrum, crest distribution) from one repeatability run to another. Such deviations can come from residual

waves and currents (van Essen and Lafeber, 2017) that persist at the beginning of the runs (i), unavoidable perturbations in the measurement acquisition system (ii), and small defaults in the control of the wave maker's motion (iii). Phenomena (i) and (iii) are part of the wave generation uncertainty (see Figure 3.1).

It is important to note that all the results presented in this section were obtained after correcting the wave gauge calibration factors (using the first repeatability test as a reference, see Sec. 3.3.2). By construction there are no H_s differences between the runs.

3.6.1 Deterministic limits of repeatability

First, we focus on the deterministic repeatability of a given free surface elevation time sequence. The study relies on several repeatability datasets generated in the ECN Towing tank during campaigns D and E. As the domain is long (150 m), the influence of the distance from the wave maker can be studied.

a) Study on the Campaign D repeatability data set

As part of Campaign D, a specific realization of `ss6` scale 40 was conducted each morning for 24 days in the ECN Towing tank.

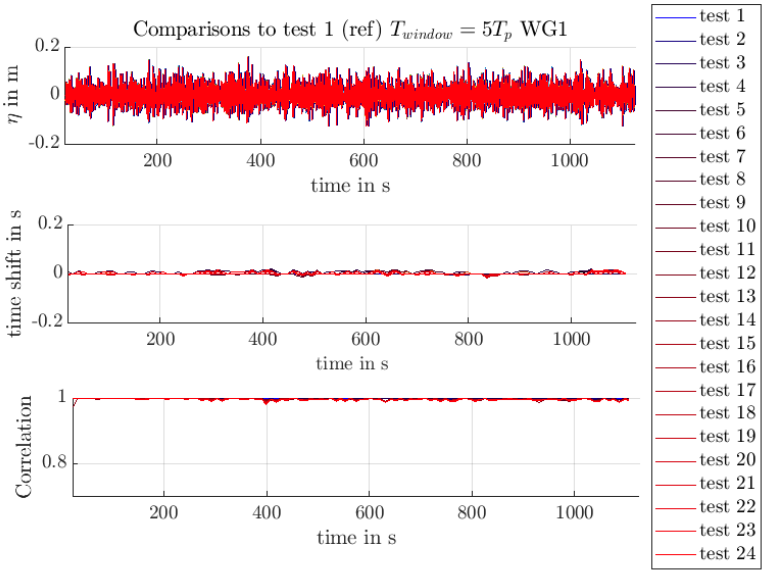

Figure 3.28 – Deterministic comparison of campaign D repeatability tests; WG1 measurements ($x = 4$ m$= 0.7\lambda_{p_{\text{target}}}$)

As a reminder, in Sec. 3.3, Figure 3.4 provided the deterministic comparison of the runs for WG 1 (located at $x = 4$ m). Figure 3.28 displays again the results. It is observed that the time series from the 24 runs perfectly match each other.

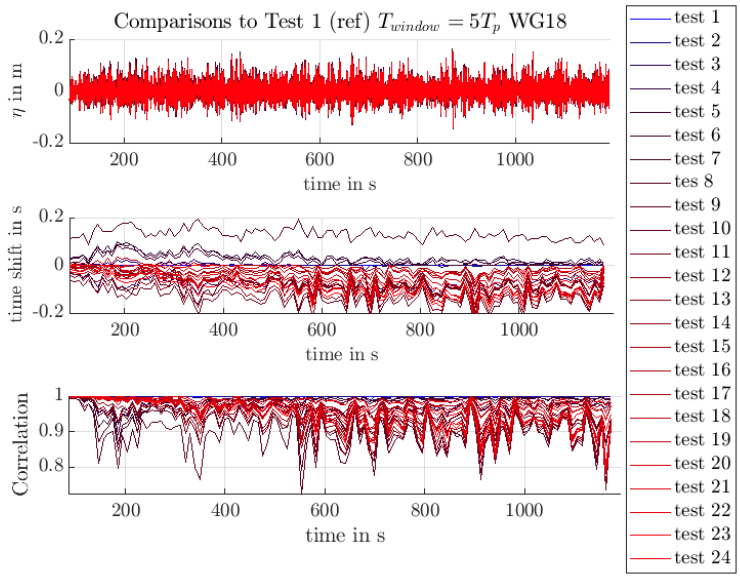

(a) Correlation and time shift

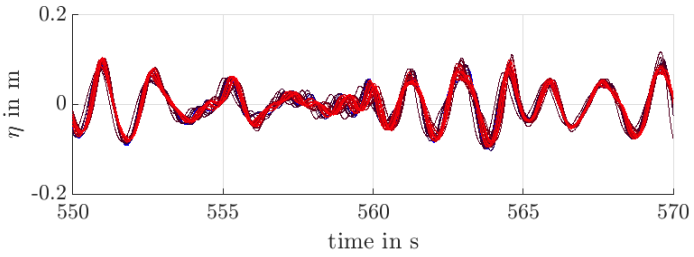

(b) Zoom on 12 periods

Figure 3.29 – Campaign D repeatability tests; deterministic comparison at WG18 ($x = 104$ m$= 18\lambda_{p_{\text{target}}}$)

In addition, Figure 3.29 presents the deterministic comparison of the data measured with WG 18, which is positioned at the end of the tank ($x = 104$ m). Unlike what occurred at $x = 4$ m, significant variations are observed between the repeated runs at this location. The Pearson correlation coefficients range between 0.75 and 1 (compared to greater than 0.99 at $x = 4$ m), and the measured time shifts between the signals range from 0.1 s to 0.2 s (approximately 5% of T_p). The zoomed-in view shown in Fig. 3.29b gives a better idea of the order of magnitude of the deterministic differences observed from one repeated run to another.

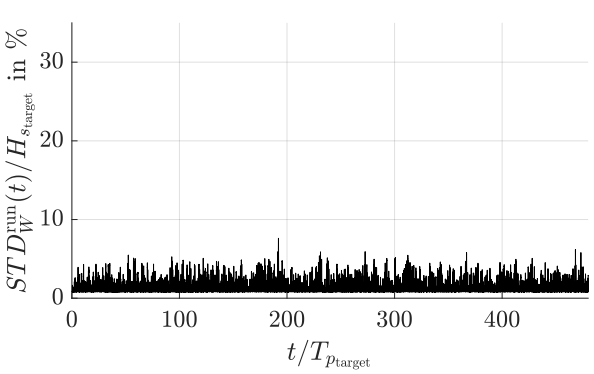

(a) wave maker motion at $z = 0$

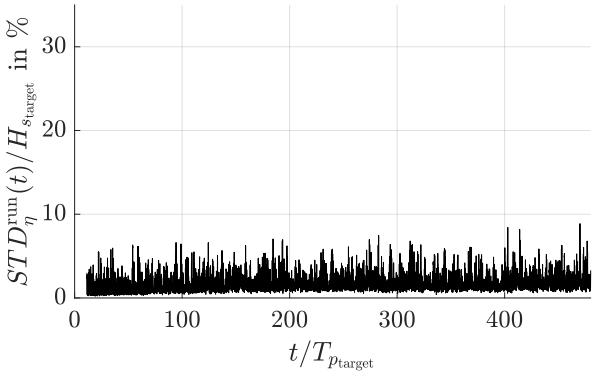

(b) WG1 $x = 4$ m$= 0.7\lambda_{p_{\mathrm{target}}}$

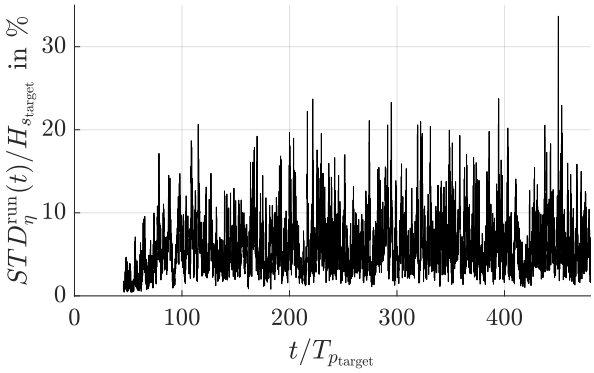

(c) WG18 $x = 104$ m$= 18\lambda_{p_{\mathrm{target}}}$

Figure 3.30 – Campaign D repeatability tests; standard deviation among the runs for each time step

To better characterize the loss of accuracy and investigate the role of the distance from the wave maker, Figure 3.30 displays the standard deviation among the 24 runs for each time step throughout the run duration. This quantity will be referred to as $STD_\eta^{\mathrm{run}}(t)$, to not be confused with σ_η which refers to the standard deviation of a given $\eta(t)$ time series.

The results are presented for the wave maker motion time series records $W(t)$ (Fig. 3.30a), WG 1 located at $x = 4$ m (Fig. 3.30b), and WG 18 located at $x = 104$ m (Fig. 3.30c). We observe that the wave maker motion time series slightly differs from one run to another, with a standard deviation below 2% of $4\sigma_W$. This is the limitation of accuracy of the wave maker control system. Besides, the repeated free surface elevation time traces measured at $x = 4$ m are affected by a standard deviation of approximately 2%. However, at $x = 104$ m, these values increase, ranging from 3 to 20%. Within the adopted analysis time window, no significant

evolution in time are observed.

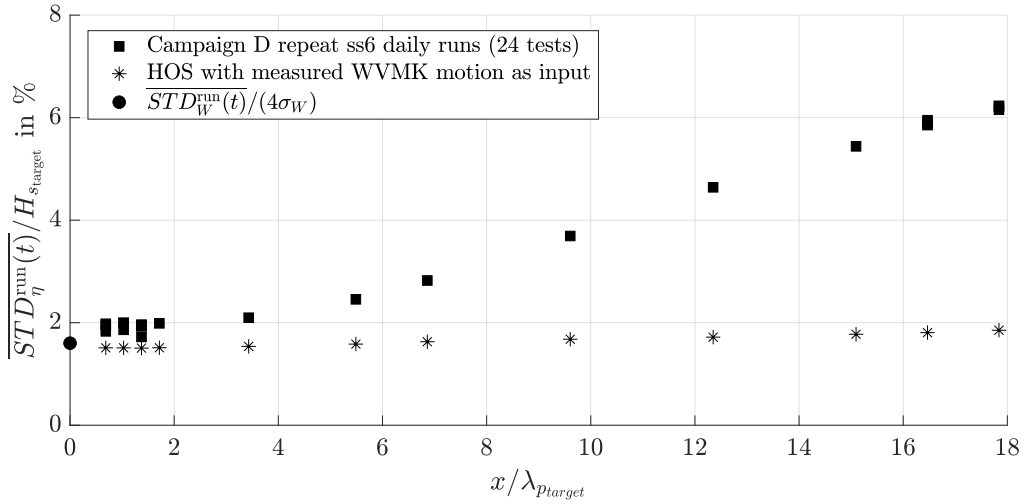

Figure 3.31 – Campaign D repeatability tests; standard deviation among the runs for each time step, mean over the run duration; influence of the wave maker motion deviations

To have a clearer view of the influence of the distance from the wave maker, Fig. 3.31 provides the mean standard deviation over the run duration $\overline{STD_\eta^{\mathrm{run}}(t)}$, for all the available wave gauges. Moreover, the figure displays numerical results coming from `HOS-NWT` simulations (see Chapter 5 for more details about the code and the setup adopted), using as input the measured wave maker motion of Campaign D repeated tests. We observe that the variations among the repeated runs increase along the tank for the experimental data and stand still for the numerical data.

From all these observations, we can deduce several mechanisms. First, the wave maker motion time sequences are not perfectly controlled, which leads to differences from one run to another. The `HOS-NWT` simulations model a perfect environment (no uncertainties, no spurious waves, no residual waves and currents before the runs). The only source of discrepancies among the numerical repeated tests are the variations in the input wave maker motions (measured motions of Campaign D repeatability dataset). It is consequently expected that the differences from one `HOS-NWT` repeated run to another have the same order of magnitude as the wave maker deviations. However, what is not immediately clear is why these deviations do not increase along the tank, as it observed in experiments.

In experiments, we observe a growth in deviations with increasing distance from the wave maker. This is a signature of the "chaotic" behavior of the wave propagation (i.e. small

perturbations in the initial conditions yield significantly diverging free surface elevation series as the waves propagate). Therefore, since the HOS−NWT data does not capture this chaotic behavior, it suggests that wave maker motion deviations alone cannot induce it. Other sources of variation should be examined

b) Influence of noise before the run

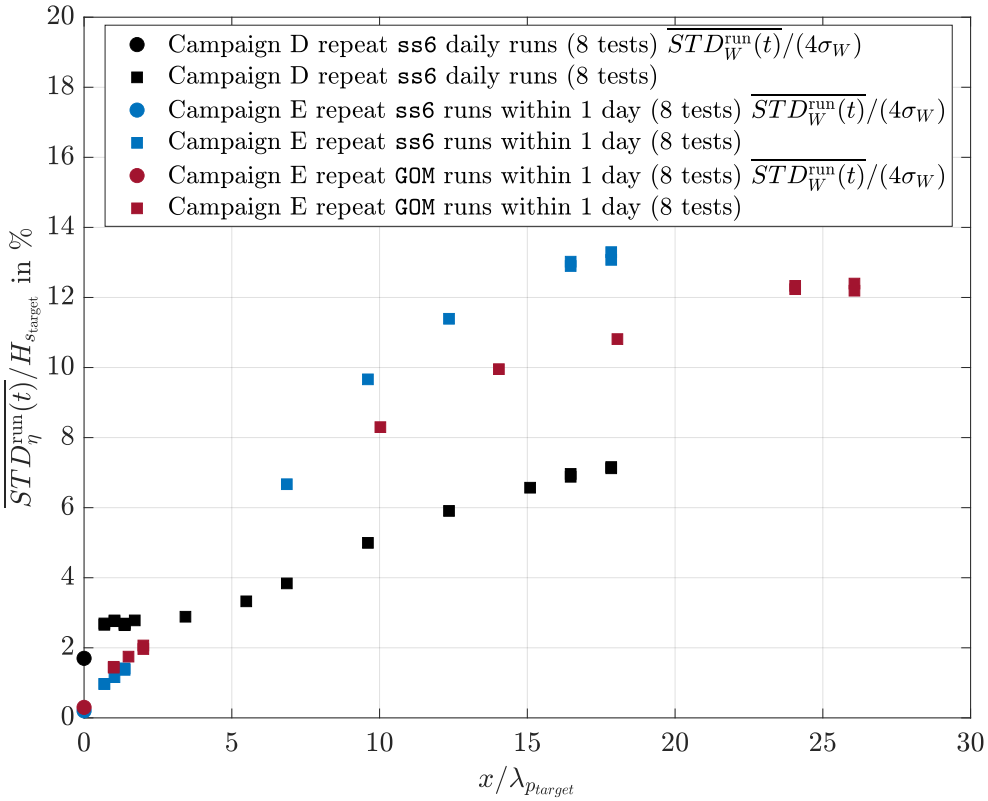

Figure 3.32 – Campaign D and E repeatability tests ; standard deviation among the runs for each time step, mean over the run duration; influence of noise before the runs

Likely candidates responsible for the growth of the deviations along the tank are the residual waves and currents that persist before the runs (see van Essen and Lafeber (2017)). We will investigate their influence in this paragraph. To do so, within the framework of Campaign E, eight repeated runs were conducted consecutively with 20-minute breaks between each run. As a reminder, the 24 repeated runs analyzed in the previous paragraphs were carried out daily (i.e., one repeated test every day) for one month. They corresponded to the first run of the day, which ensured relatively calm water conditions before wave generation (the significant wave height of

the noise just before the run, $H_{s_{\text{noise}}}$, was less than $1\% H_{s_{\text{target}}}$). In contrast, for the new Campaign E datasets, the noise reached 5% of $H_{s_{\text{target}}}$. Two repeated conditions were generated: the `ss6` scale 40 repeated run already studied in Campaign D (non-breaking condition, $\lambda_p = 5.85$ m), and a `GOM` scale 94 realization (breaking condition, $\lambda_p = 4$ m).

Figure 3.32 presents, for each of these datasets, the computed mean standard deviation among the repeated runs as a function of the distance from the wave maker. To ensure consistent comparisons, only eight runs from the Campaign D dataset were randomly selected. This limited number of runs restricts the generalization of the analysis. Only trends and orders of magnitude should be considered.

Firstly, it is observed that the wave maker motion deviations are lower for datasets generated within a single day. This suggests that the wave maker behavior remains relatively stable over a day but exhibits slight changes over the course of a month. These changes are probably due to long-duration mechanical stress.

Secondly, it can be seen that the mean standard deviation increases more significantly for datasets generated within one day, which were affected by a 5% initial noise in $H_{s_{\text{target}}}$. It can be concluded that the residual waves and currents before the runs affect the repeatability of the wave propagation and participate in chaotic behavior. Note that the computed error (time-averaged standard deviation among the repeated runs) is sensitive to time shifts between the time series (which exist, as observed in Figure 3.29a). Therefore, it leads to large values (up to $13\% H_{s_{\text{target}}}$ for the datasets generated within one day).

3.6.2 Propagation to the quantities of interest

To evaluate the consequences of the repeatability issues for the computed stochastic quantities of interest, Figure 3.33 provides the results for each repeated run of the Campaign D dataset (24 runs of an `ss6` scale 40 realization). It focuses on the spectrum (Fig 3.33a and 3.33b) and the crest distribution (Fig 3.33c and 3.33d). To account for the effect of the distance from the wave maker, the results are presented at $x = 8$ m and $x = 104$ m. As expected it is observed that close to the wave maker the stochastic quantities are almost identical from one run to another. At the end of the tank ($x = 104$ m), where the repeatability of the time series has been identified as not accurate (8% of mean standard deviation observed in Figure 3.31), the tail of the crest PDER is affected by significant deviations but the spectra are almost identical.

From this analysis, we conclude that the repeatability of a given free surface elevation time series loses accuracy as the distance from the wave maker increases. The phenomenon is boosted by the presence of residual noise before the runs, and can not be explained by the lack of

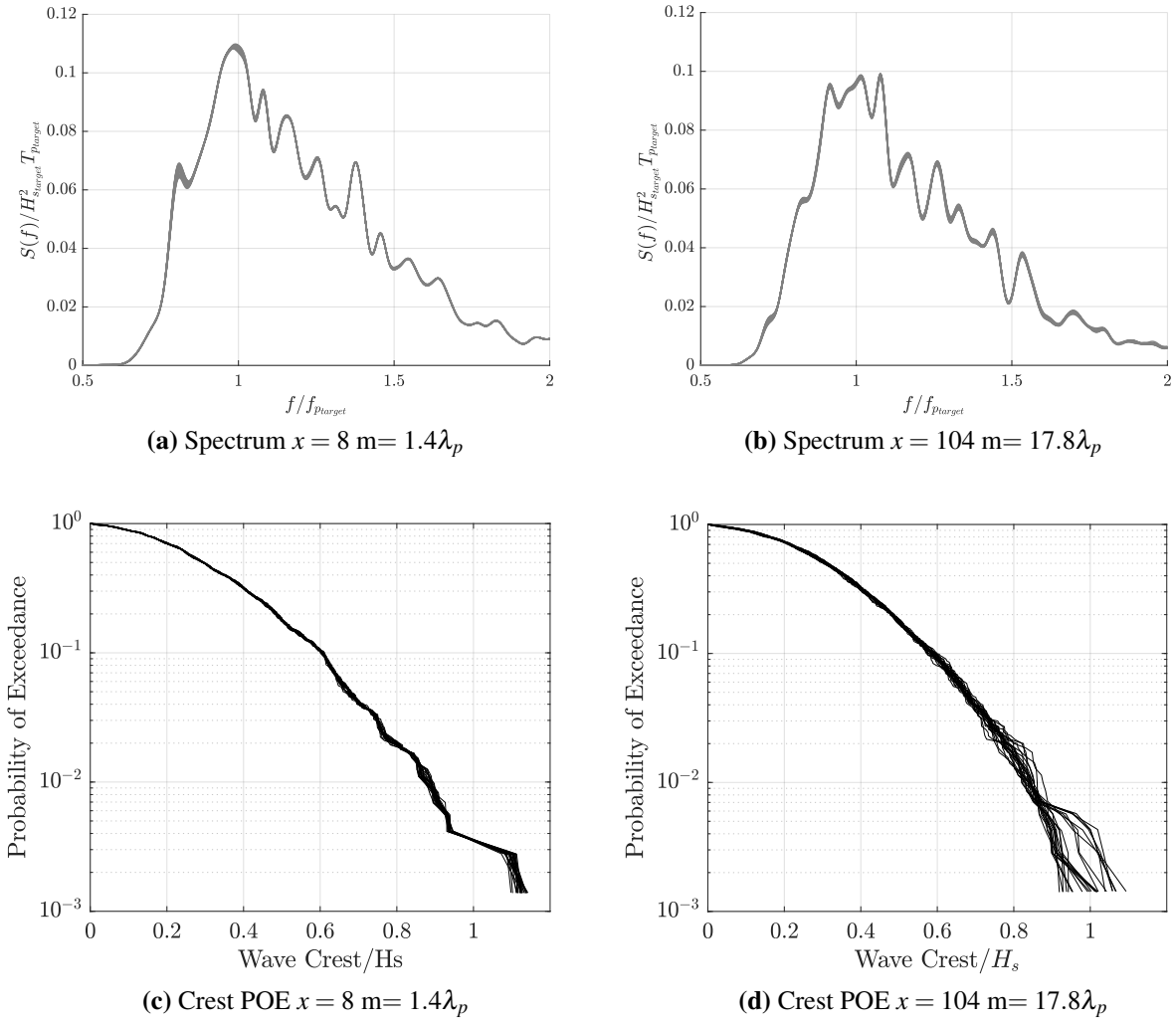

(a) Spectrum $x = 8$ m$= 1.4\lambda_p$

(b) Spectrum $x = 104$ m$= 17.8\lambda_p$

(c) Crest POE $x = 8$ m$= 1.4\lambda_p$

(d) Crest POE $x = 104$ m$= 17.8\lambda_p$

Figure 3.33 – Campaign D repeatability tests; spectrum and crest distribution for each individual repeated test, at $x = 8$ m and $x = 104$ m

accuracy of the wave maker motion. The resulting repeatability error does not affect the spectral quantities. However, it induces discrepancies in the tail of the crest distribution. One should note that we analyze here a repeatability run whose duration is approximately $500T_p$. The crest distributions usually analyzed within the scope of the present thesis are ensemble distributions considering tens of realizations (the total duration is larger than $10000T_p$). Besides, only the part of the distributions that is statistically converged (see Sec. 1.3.3) will be considered in the analyses. In this part of the distribution, if considering the repeatability discrepancies as random, their influence is likely to be erased. The accurate quantification of the error was not carried out

within the frame of the present PhD thesis. Future investigations and dedicated experiments should be considered to complete and improve the conclusions of this section.

Therefore, the Type A uncertainty will not be incorporated into the ranges displayed in the remainder of this thesis. It will be disregarded for stochastic quantities, and when analyzing time traces of free surface elevation, we will recall the order of magnitude of variations obtained in this section and take them into account in the analysis.

3.7 Conclusion

Following the strategy introduced in Section 3.2.3, which is based on ITTC recommendations, we have studied the various sources of uncertainty that impact the experimental results analyzed in this thesis. Figure 3.34 illustrates the approach and provides the key conclusions.

The steps are summarized below:

— Quantification of uncertainty related to sampling variability (Section 1.3.3 in Chapter 1), treated as a Type B uncertainty and denoted as $u_s^{\text{samp}}(X)$ (with X the quantity analyzed). The methods used to estimate $u_s^{\text{samp}}(X)$ vary from one quantity to another. In Section 1.3.3, Figure 1.11 provides for H_s, skewness and kurtosis a statistical convergence error as a function of T_{analyzed}. These errors will model $u_s^{\text{samp}}(X)$. In addition, for the spectrum we use the 95% Welch confidence intervals $U_{\text{Welch}}^{low}(f)$ and $U_{\text{Welch}}^{up}(f)$, averaged over the realizations and divided by $\sqrt{N_{\text{run}}}$. And, for the crest PDER, we use the 95% Jeffrey confidence intervals. For all these cases, it should be emphasized that we do not model $u_s^{\text{samp}}(X)$ by standard uncertainty ranges (ranges representing a standard deviation). The interpretation of the ranges varies from one quantity to another. This will be recalled and taken into account when using $u_s^{\text{samp}}(X)$ to interpret the results.

— Quantification of Type B measurements uncertainty (Section 3.3). We derived ranges $u_s^{\text{meas}}(X)$ for the primary quantities of interest.

— Estimation of Type B generation uncertainty (differences between the expected waves assuming a perfect environment and the generated waves). This source of uncertainty arises from several phenomena detailed in Figure 3.2.1. Among these, we investigated the influence of spurious transverse modes and reflected waves. The influence of reflected waves was found to be negligible, but this is not the case for transverse modes. Transverse modes affect the energy content of the wave field. They impact the significant wave height and the spectrum. Their influence is highly case-dependent and will not be included in

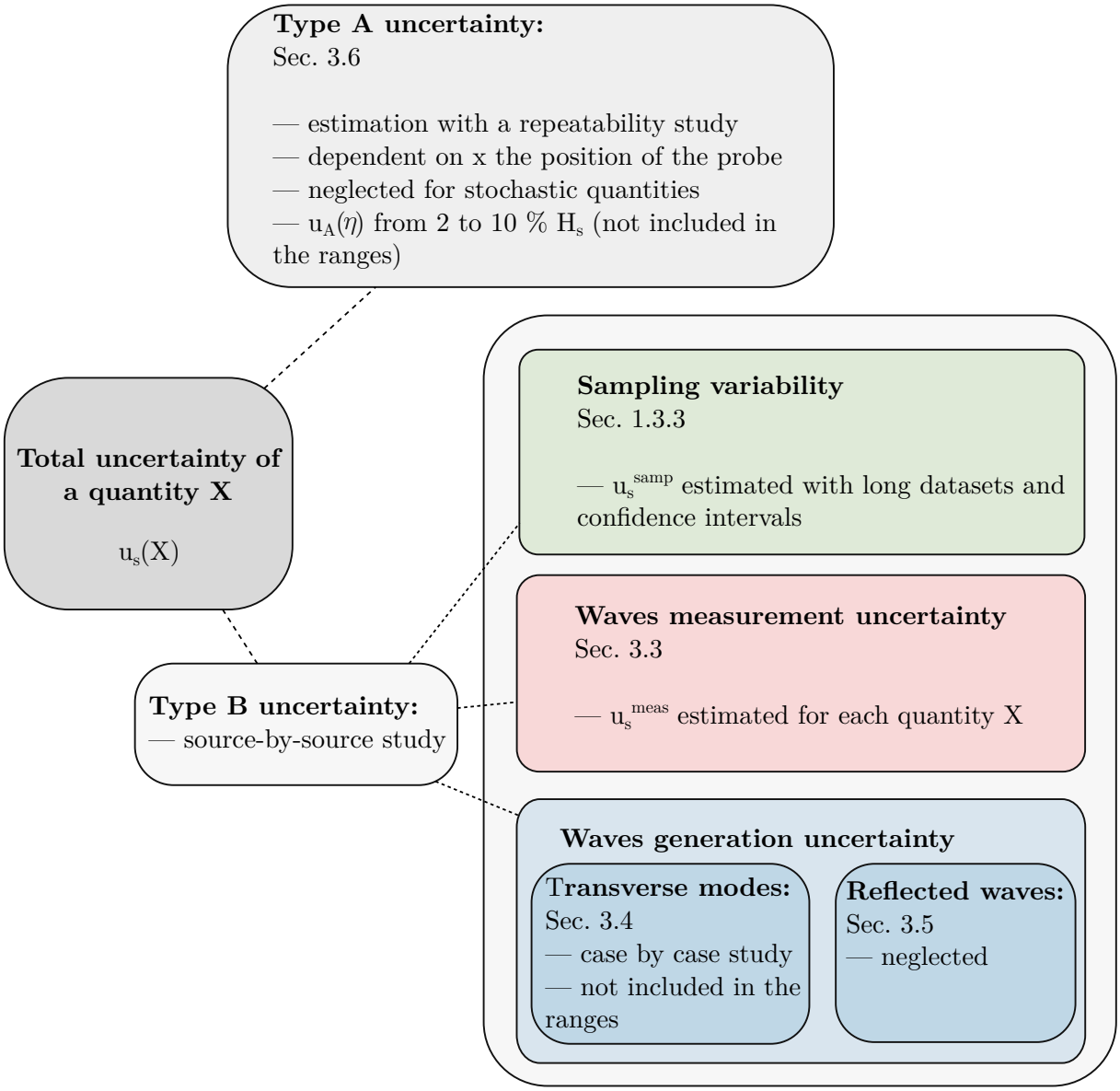

Figure 3.34 – Strategy implemented to estimate the uncertainty in the experimental results

the ranges. But Section 3.4.2 provides further details regarding their influence for each studied configuration.

— Estimation of Type A uncertainty through repeatability studies (Section 3.6). It was observed that as the distance from the wave maker increases, the repeatability error also increases, resulting in mean standard deviations among the repeat runs $\overline{STD_\eta^{\text{run}}(t)}/H_s$ in the range of 10%. However, due to difficulties in deriving a relevant range and its relatively small

impact on the spectrum and the crest distribution, Type A uncertainty is not included in the final ranges. However, when analyzing time traces of free surface elevation, we will recall the order of magnitude of repeatability variations obtained in Section 3.6.

Based on the above findings, we will plot the uncertainty ranges for each quantity X using the following equation:

$$u_s(X) = \sqrt{u_s^{\text{meas}}(X)^2 + u_s^{\text{samp}}(X)^2} \tag{3.45}$$

As explained in Section 3.2.2, $u_s^{\text{samp}}(X)$ is necessary only for fully-stochastic analysis. For semi-stochastic analysis, it is omitted from $u_s(X)$, and we will only plot $u_s(X) = u_s^{\text{meas}}(X)$.

In practice, the wave gauge uncertainties $u_s^{\text{meas}}(X)$ will always be represented solely with error bars. Besides, for fully stochastic analysis, the total $u_s(X)$ ranges, which include the sampling variability intervals (Equation 3.45), will be shown using dedicated shaded colored areas. Note that the crest POE is an exception because the wave gauge uncertainty affects the horizontal axis, while the sampling variability (estimated by Jeffrey intervals) impact the vertical axis. Therefore, the ranges are not combined but displayed in their respective axis.

For the sake of clarity, when comparing several wave series (sets of realizations), the uncertainty bounds may not always be provided. Example ranges are presented in Chapter 4 (Sec. 4.1 and 4.2) for the study of `ss6g5` sea state generated at scale 120 in the Towing tank. The ranges are similar across the different wave conditions and setups. So, when they are not displayed, please refer to Chapter 4 plots to get an order of magnitude of $u_s(X)$.

CHAPTER 4

PROPAGATION OF A UNIDIRECTIONAL NARROW-BAND SEA STATE IN A LONG EXPERIMENTAL WATER TANK

This thesis aims to improve the control of wave fields generated for offshore engineering studies in wave tank environments (in experiments and numerical simulations). We are particularly interested in controlling the spectrum and crest height distribution at given positions in the domain. More specifically we need to understand the probability of occurrence of extreme events (rogue waves), which can be critical for ocean engineering studies.

In the second part of the thesis, we will set up specific procedures for generating and qualifying sea states. However, before tackling this problem, it is important to study the propagation characteristics of design sea states in "wave tank environments". This chapter addresses this topic from an experimental point of view. Numerical modeling of sea states will be the subject of Chapter 5.

The experimental study of stochastic sea states generated in wave tanks is not a new topic. As discussed in Introduction, numerous works have been published in recent years, both in the context of wave physics and offshore engineering research. Numerous subjects have been addressed, including the influence of depth (Karmpadakis et al., 2019; Tang and Adcock, 2021), directionality (Onorato et al., 2009), distance from the wave maker (Onorato et al., 2006), steepness (Shemer et al., 2010), and breaking (Latheef and Swan, 2013).

In this chapter, we carry out an experimental study adapted to our problem. We will focus on the propagation of a unidirectional non-breaking narrow-band design spectrum in deep water, in the Towing Tank. In particular, we will be focusing on the statistical features and the tracking of extreme events, namely rogue waves. Specific nonlinear analysis tools such as groupiness factors (see section 1.3.2 e)) or tri-spectrum slices (see section 1.3.2 f)) will be used to characterize and quantify the effects of the nonlinear interactions among the frequency components of the wave field. The work relies on the data analysis procedures, the theoretical

predictions, and the uncertainty ranges introduced in Chapter 1, 2, and 3 respectively. The analyses and interpretations were carried out in close collaboration with Professor Francesco Fedele from the Georgia Institute of Technology [1], as part of the WASANO project [2].

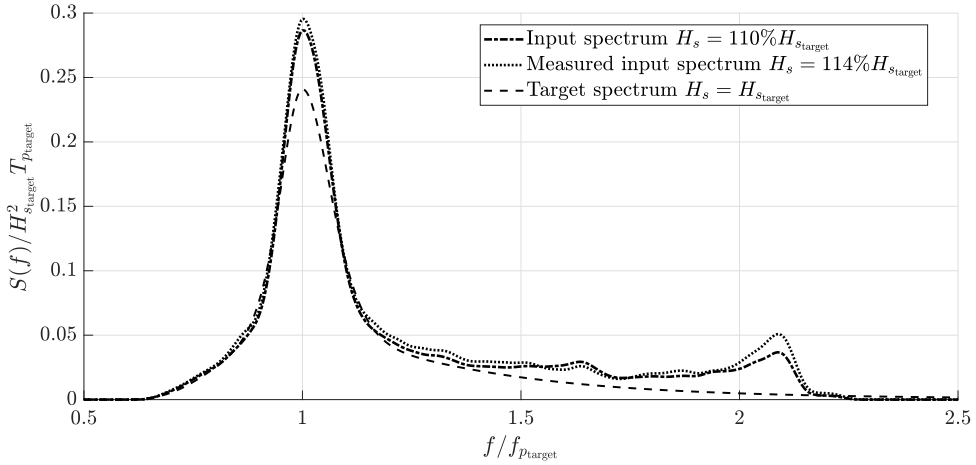

Figure 4.1 – Input spectrum for the generation of `ss6g5` sea state at $X_t = 53\lambda_p$ in the ECN Towing tank within the frame of Campaign D

The sea state under study is `ss6g5` at scale 120. Its detailed characteristics are provided in Sec. 1.2. Notably, $H_{s_{\text{target}}} = 0.05$ m, $T_{p_{\text{target}}} = 1.1183$ s (i. e. $\lambda_{p_{\text{target}}} = 1.95$ m), $\gamma = 5$, $\varepsilon_p = 2.5\%$ and $BFI = 0.51$ (computed with (eq.2.3)). `ss6g5` spectrum shape is provided in Figure 4.1 (curve labeled 'Target spectrum').

This chapter focuses on a dataset of 30 random-phases realizations, each realization lasting 15 minutes. These were generated in the Towing tank as part of Campaign D (refer to Appendix A for information about the probe positions). Considering the analysis time window (see Section 1.3.1), each realization contains 390 waves at peak period ($\Delta T/T_{p_{target}} = 390$), which leads to a dataset of total duration $T_{\text{analyzed}} = 11700 T_{p_{\text{target}}}$.

The spectrum used as input by the wave maker to generate the runs differs from the target `ss6g5` spectrum. Indeed, it was constructed using a spectrum control procedure introduced and validated in Chapter 7. Its shape is displayed in Figure 4.1 (curve labeled "Input spectrum"). In this modified input spectrum, energy was added around the peak frequency and in the high-frequency tail. The control procedure was set to generate the `ss6g5` shape at the target location $X_t =$

1. https://ce.gatech.edu/directory/person/francesco-fedele
2. https://lheea.ec-nantes.fr/research-groups/iihne-interfaces-interactions-in-numerical-experimental-hydrodynamics/wasano-project?l=1

$53\lambda_p = 104$ m from the wave maker. The additional energy serves to counterbalance the effects of side walls dissipation and nonlinear energy transfers. It is added for frequencies lower than $f_{\max}^{\text{wvmk}} = 2Hz \approx 2.2 f_{p_{\text{target}}}$ (maximum frequency that the wave maker can generate).

Furthermore, Figure 4.1 also includes a "measured input spectrum", which corresponds to the wave spectrum derived from the recorded motion sequences of the wave maker during the experiments. Note that the wave maker transfer function was applied to convert the motion spectrum into a wave spectrum. The measured input spectrum is slightly more energetic than the input spectrum initially set as a target for the wave maker. This implies that the wave maker produced larger waves than expected based on its theoretical transfer function. Consequently, the input spectrum to consider in the analysis (characterizing the generated wave field at $x = 0$ m) is the "measured input spectrum".

Details about the intermediate steps leading to the input spectrum are provided in Chapter 7, Sec. 7.2.1. The influence of the correction process on the evolution of the wave field properties is addressed in Sec. 7.3 (study based on Campaign A data which correspond to the same `ss6g5` scale-120 design sea state).

4.1 Spatial evolution of the wave spectrum

This first section is dedicated to the analysis of the wave spectrum and its associated parameters during its propagation. Next, Section 4.2 and 4.3 will focus on the statistical quantities and the characterization of the nonlinear interactions.

4.1.1 Significant wave height along the tank

First, Figure 4.2 presents the measured significant wave height along the tank. The error bars indicate the measurement uncertainty $u_s^{\text{meas}}(H_s)$ (see Section 3.3.4). Complementary, the shaded areas include the measurement uncertainty combined with the sampling variability, $u_s(H_s) = \sqrt{u_s^{\text{meas}}(H_s)^2 + u_s^{\text{samp}}(H_s)^2}$ (eq.3.45). The sampling variability was estimated with the statistical convergence error provided in Figure 1.11 (see Section 1.3.3). For the sake of clarity, at the location of y-axis lines of probes, the displayed area is the one of the mean signal η_{mean}. With the 30-realization data, the sampling variability errors are very small, which means that the significant wave height is statistically converged. The measurement uncertainty reaches up to $\pm 2\%$ of $H_{s_{\text{target}}}$. This explains the local increases in H_s that are not realistic, as the wave field energy is necessary decreasing along the tank.

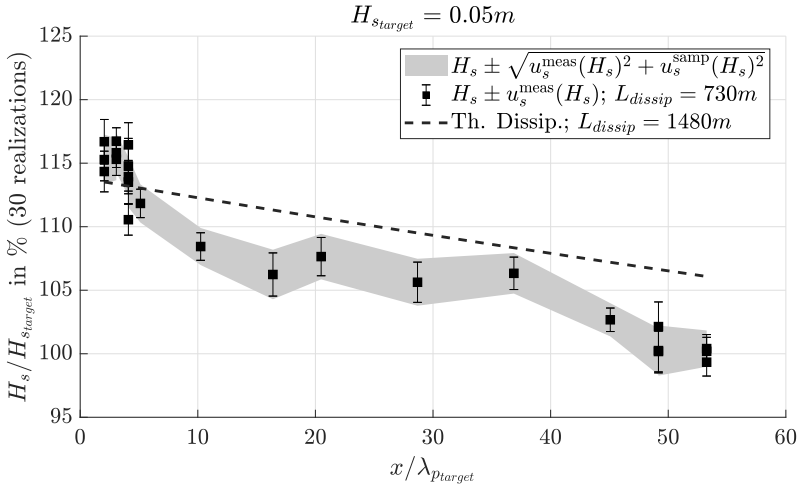

Figure 4.2 – `ss6g5` scale 120 targeted at $X_t = 53\lambda_p$ - Campaign D - H_s along the tank

As displayed in Figure 4.1, due to the spectrum correction procedure, the significant wave height of the measured input spectrum equals $114\%H_{s_{\text{target}}}$. This can also be observed when looking at the evolution along the tank. H_s reaches approximately $115\%H_{s_{\text{target}}}$ at $x = 4$, 6 and 8 m and then decreases down to $100\%H_{s_{\text{target}}}$ at the end of the tank (target location $X_t = 104m = 53\lambda_p$). The difference from the input $114\%H_{s_{\text{target}}}$ at the beginning of the tank can be explained either by the WG measurement uncertainty, or the presence of spurious transverse modes, see for instance Section 3.4.2 and Figure 3.22 for the interpretation of the discrepancies at $x = 8$ m.

The experimental results are compared to the predictions of the theory introduced in Section 2.3. The theory aims to model the side walls dissipation, bottom friction, and the stress at the water/air interface. As a reminder, `ss6g5` is a nonbreaking sea state. Indeed, no breaking events were observed during the experiments. Therefore, the energy losses are likely to be due to these mentioned phenomena. The H_s decrease is quantified through a dissipation length L_{dissip}, which corresponds to an exponential fit parameter (see also Sec. 2.3 for its definition). The theory under-predicts the dissipation ($L_{\text{dissip}} = 1480$ m versus 730 m for the experimental results). Even considering the uncertainty ranges, the theoretical curve is slightly above the experimental one. This might be because the theoretical framework was built for regular waves. The version used here generalizes its use by superposing linearly the frequency components of the irregular wave field. The nonlinear interactions are not taken into account. Moreover, the side walls are assumed to be perfectly smooth, which is not the case in the Towing tank. However, the order of magnitude of the dissipation is predicted. Therefore, it seems still reasonable to

interpret the energy decrease as the result of side walls friction.

4.1.2 Spectrum along the tank

Figure 4.3 presents the mean spectrum (over the 30 realizations) at $x = 2\lambda_p$ and $x = X_t = 53\lambda_p$. As previously mentioned above, the wave maker motions were adapted to generate the target spectrum at $X_t = 53\lambda_p$. Energy was added to the input spectrum to balance the effects of the side walls dissipation and nonlinear energy transfers. Consequently, as expected, the measured spectrum at $x = 2\lambda_p$ is close to the input spectrum, and at $X_t = 53\lambda_p$ it lies on the target shape (considering the WG uncertainty ranges). We observe that, around the peak, the sampling variability (modeled by the Welch 95% confidence intervals $U^{up}_{\text{Welch}}(f)$ and $U^{up}_{\text{Welch}}(f)$ introduced in Sec. 1.3.3) cannot be neglected. With this number of realizations (i.e. this number of waves analyzed), different choices of random phases may have produced larger or smaller spectrum peak ($E_{\text{Welch}}(f_p) \approx 8\%$).

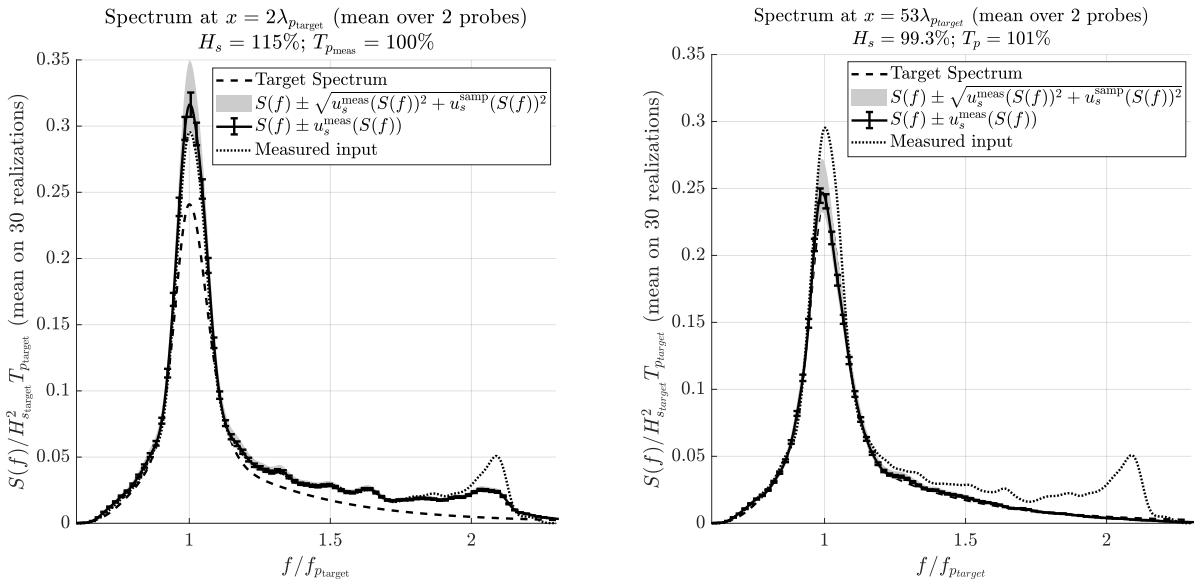

(a) $x = 4m = 2\lambda_p$ **(b)** $x = X_t = 104m = 53\lambda_p$

Figure 4.3 – `ss6g5` scale 120 targeted at $X_t = 53\lambda_p$ - Campaign D - Spectrum at $x = 4m = 2\lambda_p$ and $x = X_t = 104m = 53\lambda_p$

Further details regarding the evolution of the spectrum along the tank are provided in Figure 4.4. The energy 'plateau' between $1.5f_p$ and $2.2f_p$ gradually dissipates as the distance

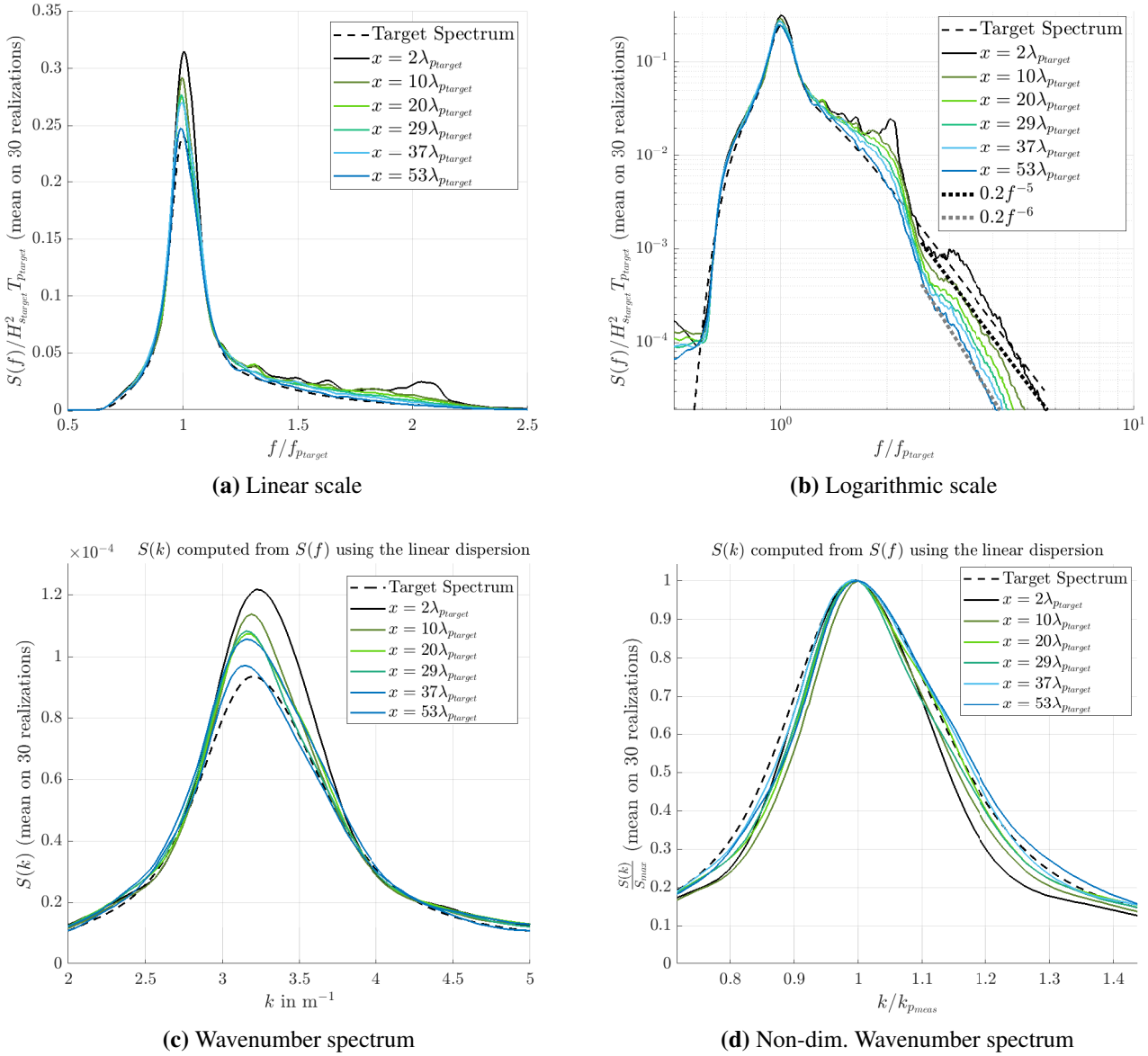

(a) Linear scale

(b) Logarithmic scale

(c) Wavenumber spectrum

(d) Non-dim. Wavenumber spectrum

Figure 4.4 – `ss6g5` scale 120 targeted at $X_t = 53\lambda_p$ - Campaign D - Spectrum along the tank

from the wave maker increases. In Fig. 4.4b, the spectra measured along the tank are presented in a logarithmic scale. This enables us to analyze the tail of the spectrum ($f > 2.2f_p = 2$ Hz). The tail is not generated by the wave maker, which is mechanically limited to $f_{\max}^{\text{wvmk}} = 2$ Hz. It is the result of an energy cascade toward high frequencies. The literature usually predicts f^{-7} to f^{-4} slopes, depending on the steepness, the dissipation processes, and the nature of the data

(In-Situ or laboratory waves), see Deike et al. (2015) for a review of the topic. In Figure 4.4b, the spectrum tail slope fits the f^{-5} curve close to the wave maker and progressively moves toward f^{-6} line as the distance from the wave maker increases. A similar trend was observed in Fedele et al. (2010), where "the spectrum tail slope behaves as f^{-5} closer to the wave maker and, eventually steepen to approximate a f^{-6} viscous range". There, the change of slope was interpreted as the result of viscous dissipation. This aligns with the present experiments in which the dissipation processes are strong.

The wavenumber spectra are also provided in Figure 4.4c and 4.4d. They are computed using the energy conservation $S(k)dk = S(f)df$ and the deep-water dispersion relation $(2\pi f)^2 = gk$ (valid for $k > 2$ m^{-1} and $d = 3$ m),

$$S(k) = S(f)/(8\pi^2 f/g) \tag{4.1}$$

This quantity results in broader shapes. It enhances our ability to visualize the evolution of the spectrum width along the tank. First, in Figure 4.4c, we observe a slight decrease in the peak wavenumber spectrum $k_{p_{meas}}$ (wavenumber corresponding to the maximum $S(k)$ value) along the tank. In addition, as the waves propagate, the spectrum width is reduced and the energy content around $k_{p_{meas}}$ dissipate. Figure 4.4d presents the wavenumber spectrum normalized by its maximum value, plotted as a function of the wavenumber normalized by $k_{p_{meas}}$. Consequently, it is unaffected by dissipation and the peak downshift. This normalized spectrum broadens along the tank (the spectral width increases around $k/k_{p_{meas}} = 1$). This behavior, along with the peak downshift, is known to be a consequence of high-order nonlinear interactions (Janssen, 2003; Fedele et al., 2010).

From these results, we can conclude that dissipation processes tend to dissipate the spectrum tail and decrease the spectral width. Concomitantly, nonlinear interactions slightly balance the width variations and induce a small peak downshift.

4.1.3 Spectrum width, peak period, and mean period along the tank

Eventually, Figure 4.5 presents the measured peak period T_p, the mean period T_1, and the non-dimensional spectral width ν_w along the domain. Note that ν_w is defined in Section 2.1.1 (eq. 1.22). As the computation of the mean period and ν_w relies on the spectrum moments, these two quantities are highly sensitive to the high-frequency energy 'plateau' (between $1.5f_p$ and $2.2f_p$), added by the control procedure to balance dissipation effects at $X_t = 53\lambda_p$. To remove the influence of this high-frequency energy 'plateau' and to focus on the most energetic part of the spectrum, we also display T_1 and ν_w computed from the spectrum truncated at $f = 1.5f_{p_{\text{target}}}$. The values computed from the truncated target `ss6g5` spectrum are plotted with dotted lines ($T_{1_{\text{target}}}^{\text{trunc}}$ and $\nu_{w_{\text{target}}}^{\text{trunc}}$).

Sampling variability is estimated with the standard deviation over the realizations, divided by $\sqrt{N_{\text{run}}}$. The resulting ranges are very small. For this large dataset ($T_{\text{analyzed}} = 11700T_{p_{\text{target}}}$), the periods and spectrum width are statistically converged. Measurement uncertainty ranges are not plotted. Indeed, the accuracy in T_p is directly dependent on the frequency resolution of the spectrum (see next paragraph). Besides, in Chapter 3, to derive $u_s^{\text{meas}}(S(f))$, we considered that the wave gauges have a linear behavior. With this assumption, propagating the wave calibration factor uncertainty to T_1 and ν_w leads to $u_s^{\text{meas}}(T_1) = 0$ and $u_s^{\text{meas}}(\nu_w) = 0$.

The results corroborate the findings from the study of spectrum shape evolution. Firstly, the peak period T_p remains relatively constant along the tank. Nonetheless, it is important to note that T_p was computed by tracking the index of the maximum spectrum value. Consequently, the resolution of T_p is directly dependent on the frequency spectrum resolution. This leads to a resolution of approximately $0.5\%T_{p_{\text{target}}}$. This is too large to accurately capture the small peak downshift observed in the wavenumber spectrum (Fig. 4.4c).

Next, the mean period computed using the full spectrum is significantly increasing along the tank. This is mainly due to the progressive dissipation of the high-frequency plateau. When truncating the spectrum tail at $1.5f_p$, the increase in T_1 almost disappears. However, in Figure 4.5c, which presents a zoomed view of the truncated-spectrum T_1 evolution, we can still observe a slight evolution along the tank. This is likely to correspond to the peak downshift observed in the wavenumber spectrum.

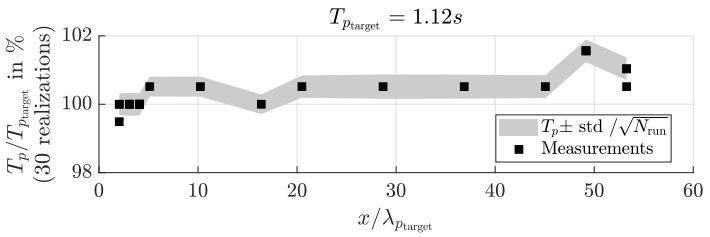

(a) Peak period

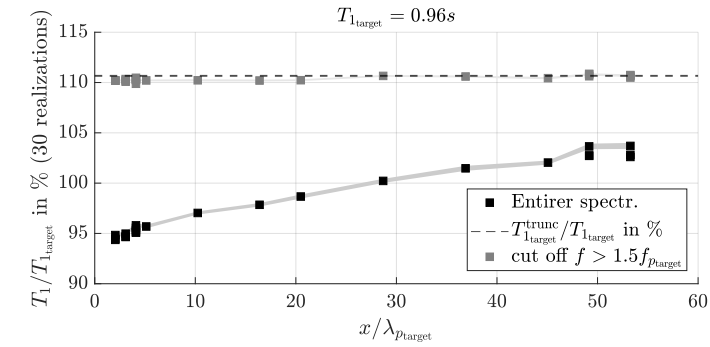

(b) Mean period

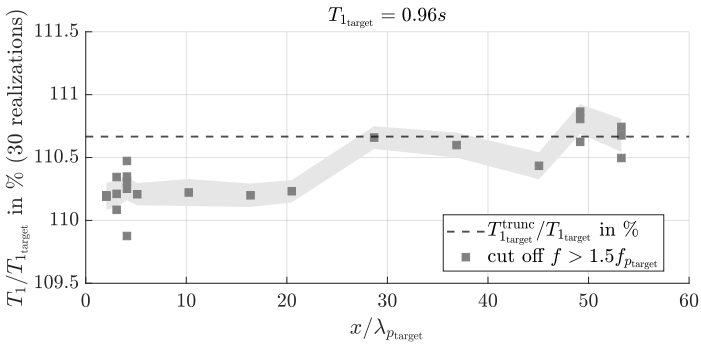

(c) Mean period zoom

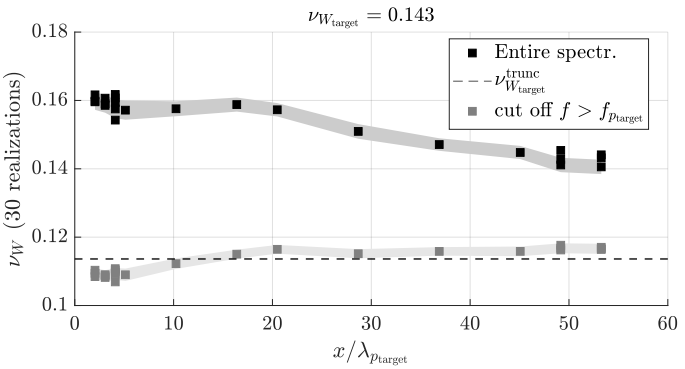

(d) Normalized spectrum width

Figure 4.5 – `ss6g5` scale 120 targeted at $X_t = 53\lambda_p$ - Campaign D - peak period, mean period and normalized spectrum width along the tank - the shaded areas correspond to the sampling variability computed as the standard deviation over the realizations divided by $\sqrt{N_{\text{run}}}$

Furthermore, ν_w decreases along the tank. This trend was also observed in Fedele et al. (2010) and was interpreted as the effect of 'viscous damping of high-frequency components.' In the present set of experiments, this corresponds to the dissipation of the high-frequency plateau along the tank. Conversely, ν_w computed from the truncated spectrum increases along the tank. The spectrum, free from its tail, broadens as the distance from the wave maker increases. This is can be attributed to high-order nonlinear interactions. A similar trend was observed in Shemer and Sergeeva (2009). In the latter study, the dissipation process was less active (the observed significant wave height was not decreasing), and the authors did not need to cut off the tail of the spectrum to observe the ν_w increase.

4.2 Evolution of the wave statistics

After investigating the spectral properties of the wave fields (energy content in the frequency domain), this section now focuses on the statistical quantities that characterize the occurrence and severity of wave events.

4.2.1 Skewness and kurtosis

First, Figure 4.6 presents the spatial evolution of the third and fourth moments of the free surface elevation distribution, namely the skewness and the kurtosis (see Sec. 1.3.2 c) for their definition and interpretation). The theoretical predictions detailed in Sec. 2.1.2 are also plotted. As a reminder, these were established for narrow-band spectra, using the framework of the nonlinear Schrodinger equations (NLS) for water waves. The displayed uncertainties correspond to the sampling variability. We neglect the wave gauge errors for the skewness and kurtosis (see Sec. 3.3.4). The quantification of the sampling variability was based on Section 1.3.3 study, providing convergence errors. As 11700 waves at peak period are analyzed, the ranges are very small for the skewness.

The skewness remains constant along the tank. As detailed in Sec. 1.3.2 c) it characterized the vertical asymmetry of the wave profile, induced by the bound waves mainly resulting from second-order nonlinear interactions. It is then strongly associated with the steepness of the wave spectrum (which is a measure of wave nonlinearities). The measured data approximately lies on the narrow-band theoretical prediction. It is not affected by the distance from the wave maker i. e. bound waves develop immediately and their normalized amplitude does not evolve in space. The decrease in H_s and the evolution of the spectrum shape do not influence λ_3.

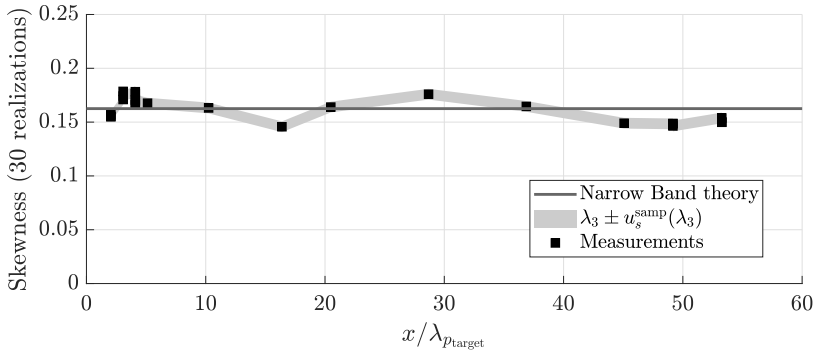

(a) skewness

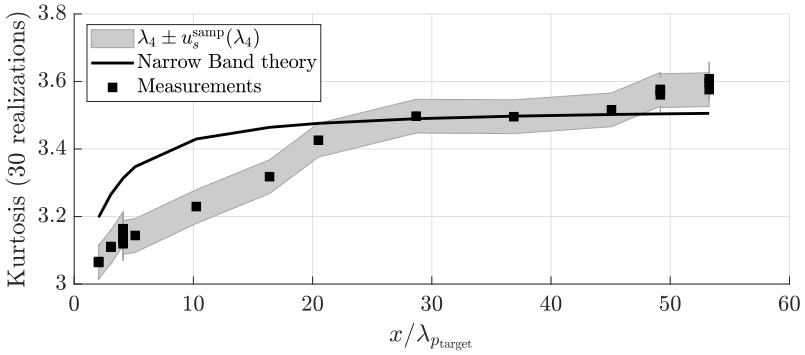

(b) kurtosis

Figure 4.6 – `ss6g5` scale 120 targeted at $X_t = 53\lambda_p$ - Campaign D - skewness and kurtosis along the tank - the shaded area corresponds to the sampling variability

It was demonstrated in several theoretical (Janssen (2003); Fedele (2015)), and experimental (Onorato et al. (2006); Shemer et al. (2010); Cherneva et al. (2009)) works that, when generating unidirectional waves, the probability of the extreme events increases along the tank, due to the development of modulational instabilities. The disposition of the sea states to develop such instabilities can be quantified by the Benjamin Feir Index (BFI), defined in this thesis by (eq. 2.3). `ss6g5` exhibits an intermediate $BFI = 0.51$. Consequently, we observe a spatial evolution of the statistics. The measured kurtosis monotonically increases along the domain before converging after $x > 30\lambda_p$. Note that from $x = 0$ to $x = 30\lambda_p$, the narrow-band theory over-predicts the kurtosis. However, further in the tank, the experimental and theoretical values are similar. It is worth noting that, from an ocean engineering point of view, `ss6g5` spectrum, defined with $\gamma = 5$, is narrow. However, the narrow-band theory detailed in Sec. 2.1.2 assumes that $\nu_w << 1$. In this context, `ss6g5` spectrum ($\nu_w \approx 0.15$) is not narrow.

4.2.2 Ensemble crest distribution

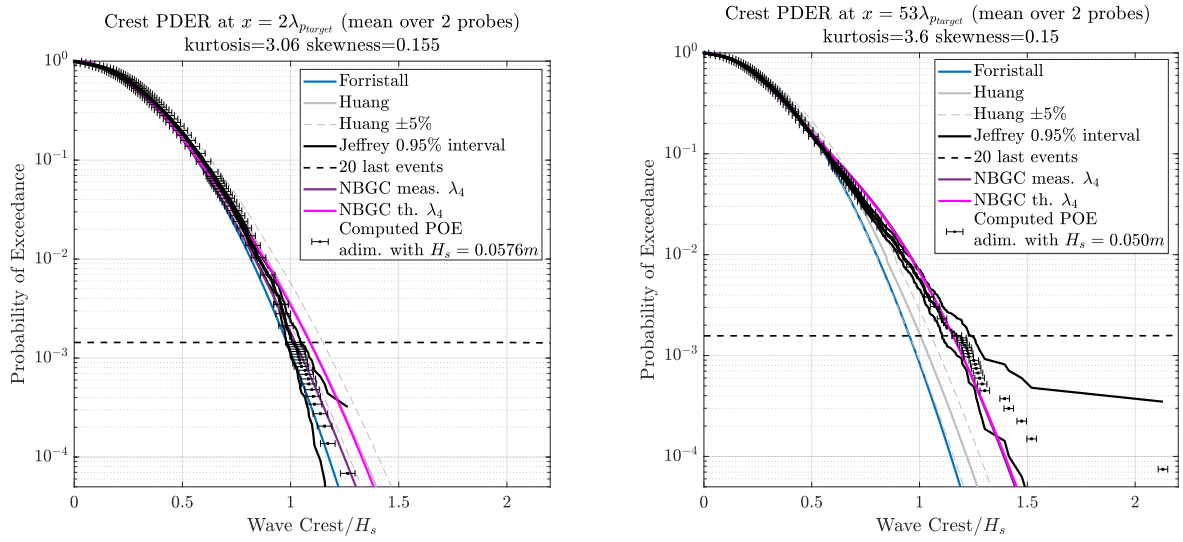

(a) $x = 4m = 2\lambda_p$ **(b)** $x = X_t = 104m = 53\lambda_p$

Figure 4.7 – `ss6g5` scale 120 targeted at $X_t = 53\lambda_p$ - Campaign D - Crest PDER at $x = 4m = 2\lambda_p$ and $x = X_t = 104m = 53\lambda_p$, normalized by the measured significant wave height

Figure 4.7 presents the ensemble crest distribution (considering the 30 realizations) at $x = 2\lambda_p$ and $x = X_t = 53\lambda_p$. As mentioned in the Introduction, the PDER is a crucial quantity, typically used in industry as the statistical quantity of interest for wave qualification procedures (see Det Norske Veritas (2010); ITTC (2021)). Its study allows for a fine analysis of the occurrence of extreme events. The kurtosis, characterizing the whole tail of the PDER, is less accurate in this context. Four references are plotted, their definition is provided in Sec. 2.2. The first one is the semi-empirical Forristall distribution (Forristall, 2000) built with a large number of simulation results considering nonlinearities up to second order. It is usually used as a benchmark for both wave-structure interaction studies, and analyses of in-situ deep-water ocean waves. Next, two other references are based on the Tayfun NBGC theoretical formula, see (eq. 2.19) in Sec. 2.2.4. The model labeled "NBGC meas. λ_4" uses the parameters (kurtosis, skewness) of the measured wave field. The other model, "NBGC th. λ_4", is built using the skewness and the kurtosis predicted by Fedele (2015) theory (see Sec. 2.1.2). Lastly, the semi-empirical Huang distribution is also plotted. This reference was built to consider up to 3^{rd} order effects. However, it assumes a wave field ergodic in space (no spatial variations), which is not the case for wave tank environments.

As expected from the kurtosis evolution, the distribution at $x = 4$ m ($2\lambda_p$) strongly differs from the one at $x = X_t = 104$ m ($53\lambda_p$). For probabilities below 0.06, the occurrence of extreme events increases with x. Table 4.1 compares, at different POE levels, the normalized crest height H_c/H_s provided by the distributions. For instance, the same probability level $POE = 10^{-3}$ is associated with $H_c/H_s = 1.04$ and 1.23 for $x = 2\lambda_p$, and $53\lambda_p$ respectively. Note that the definition of rogue waves proposed in Haver (2001) corresponds to $H_c/H_s > 1.25$, which is associated far from the wave maker with $POE = 8.9\ 10^{-4}$. This probability is close the usual probabilities of design used for ocean engineering studies, $P_{\text{design}} \approx 10^{-3}$ (ITTC, 2021; Fouques et al., 2021).

Table 4.1 – Comparison of the crest height for given POE levels, $x = 2\lambda_{p_{\text{target}}}$ versus $x = X_t = 53\lambda_{p_{\text{target}}}$ - `ss6g5` sea state - Campaign D

	$x = 2\lambda_{p_{\text{target}}}$	$x = X_t = 53\lambda_{p_{\text{target}}}$
$POE = 10^{-1}$	$H_c/H_s = 0.59$	$H_c/H_s = 0.57$
$POE = 10^{-2}$	$H_c/H_s = 0.85$	$H_c/H_s = 0.92$
$POE = 10^{-3}$	$H_c/H_s = 1.04$	$H_c/H_s = 1.23$
Rogue wave POE i.e. $POE(H_c/H_s = 1.25)$	$6.8\ 10^{-5}$	$8.9\ 10^{-4}$

Moreover, for this sea state exhibiting intermediate $BFI = 0.51$, the Forristall distribution is already slightly underestimated the extreme events at $x = 2\lambda_p$, which is an area very close to the wave maker. Consequently, the Forristall distribution is not relevant in almost all of the domain. The Huang distribution also fails to predict the tail of the distribution for $x > 2\lambda_p$. As mentioned in Sec. 2.2.4, it is because it was built without considering the influence of the distance from the wave maker. When generating long-crested sea states in a wave tank facility, both these reference distributions can significantly underestimate the largest waves appearing in a sea state. This has a possible significant impact on the design of model tests in ocean engineering.

On the contrary, the trend of the NBGC model built with the measured λ_3 and λ_4 consistently aligns with the experimental data. However, it loses accuracy for probabilities between 4.10^{-2} and 10^{-3}. Note that this model is not fully predictive since it requires the knowledge of the kurtosis. Therefore, its utility is limited, as the most common requirement in the context of ocean engineering experiments is to predict the crest PDER only from the target spectrum and the distance from the wave maker. In this regard, the fully predictive "NBGC th. λ_4" model is more interesting. In Figure 4.7, we observe that it lies on the "NBGC

meas. λ_4" model at $X_t = 53\lambda_p$. However, as the predicted kurtosis at $x = 2\lambda_p$ is too large (as shown in Figure 4.6), at the same probability level, the height of the events is overestimated by "NBGC th. λ_4". Lastly, it should be emphasized that the NBGC models were developed for narrow band spectra. Therefore, they may be less effective for wider spectra. Nevertheless, they remain valuable tools for providing rough predictions of extreme distributions not captured by semi-empirical references.

4.2.3 Height and period distribution

Complementary to Fig. 4.7 presenting the crest height PDER, Fig 4.8 presents the zero-crossing wave height and period ensemble distributions. See Section 1.3.2 d) for the definition of these quantities. The height distribution is normalized by the measured significant wave height and the period distribution is normalized by the mean zero-up-crossing period estimated with $T_{2_{\text{meas}}} = \sqrt{m_0/m_2}$.

As expected, the shape of the wave height PDER depends on the location. For the more extreme events ($POE < 10^{-2}$), at a given probability level the height of the zero crossing waves increases with x. As an example, the probability of exceedance $POE = 10^{-3}$ is associated with the normalized wave height $H/H_{s_{\text{meas}}} = 1.7$ and 2.1 for $x = 2\lambda_p$ and $53\lambda_p$ respectively. Note that one of the usual definitions of a rogue wave is $H/H_{s_{\text{meas}}} > 2$ (see Onorato et al. (2013)), a threshold which is reached at $X_t = 53\lambda_p$ at $POE = 1.7\ 10^{-3}$. This corroborates the analysis of the crest height PDER.

In contrast, the position x only has a slight effect on the wave period PDER. This difference is likely attributable to the normalization using $T_{2_{\text{meas}}}$, which is influenced by the spectrum shape. The period of the extreme events does not depend on the distance from the wave maker, even if their crest and wave height increase.

To complete the analysis, Fig. 4.9 presents the joint probability density function of wave heights and periods at $x = 2\lambda_p$ and $53\lambda_p$. First, we observe that regardless of the location, the most probable events are located around the point ($H = 0.7H_{s_{\text{meas}}}$, $T = 1.2T_{2_{\text{meas}}}$). This is in agreement with the PDER presented in Fig 4.8, in which only the tail of the wave and crest height distributions are affected by x. Then, the events characterized by $H > 1.1H_{s_{\text{meas}}}$, exhibiting different probabilities of exceedance in Fig. 4.8, are all located in Fig. 4.9 between $T/T_{2_{\text{meas}}} = 0.8$ and $T/T_{2_{\text{meas}}} = 1.4$. Their probability of occurrence increases with x (spreading of the probability density function towards larger wave heights).

The extreme events are characterized by large wave heights with similar wave periods whatever the propagating distance. In other words, the periods of the extreme events are not

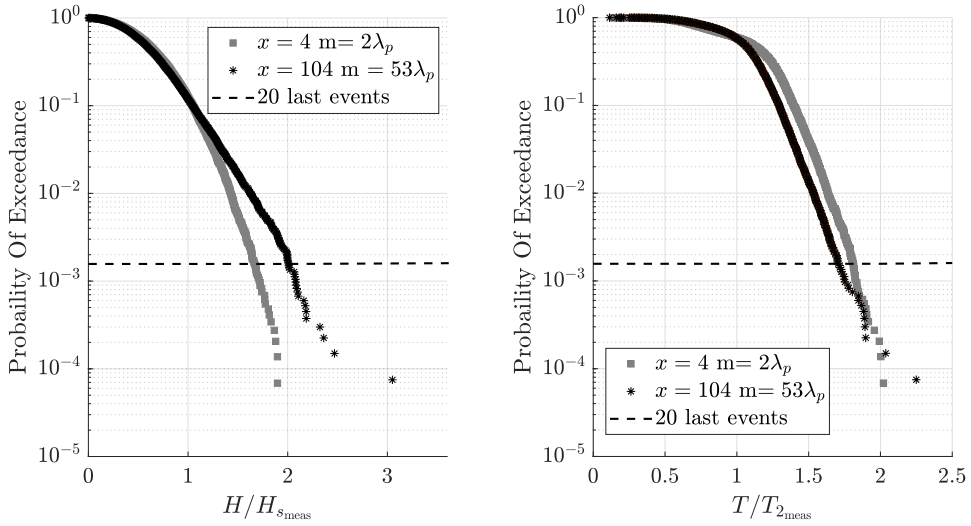

(a) Height POE **(b)** Period POE

Figure 4.8 – `ss6g5` scale 120 targeted at $X_t = 53\lambda_p$ - Campaign D - zero-crossing wave height and period PDER at $x = 4$ m$= 2\lambda_p$ and $x = X_t = 104$ m$= 53\lambda_p$, normalized by the measured significant wave height and mean period

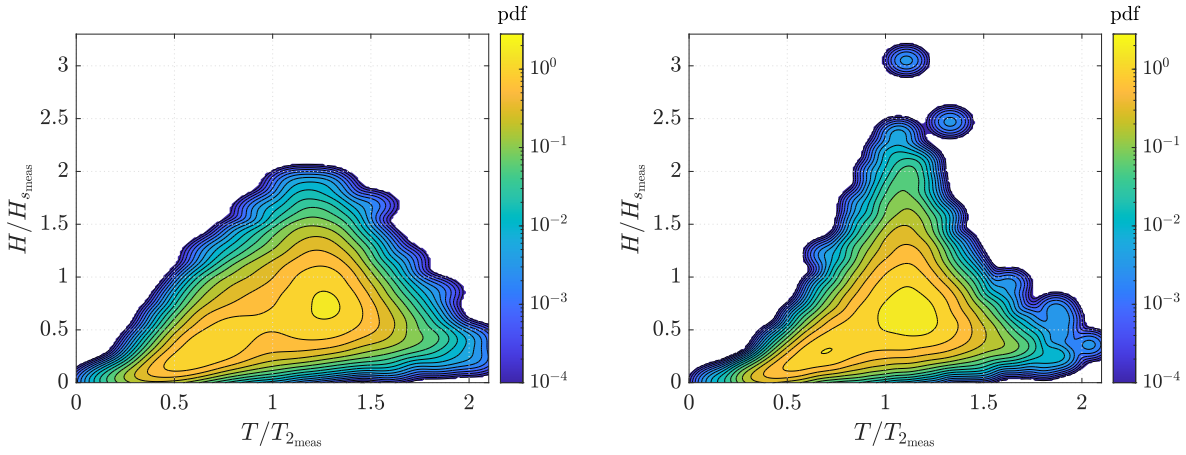

(a) $x = 4$ m **(b)** $x = X_t = 104$ m

Figure 4.9 – Joint distribution of zero crossing wave height and period at $x = 4$ m$= 2\lambda_p$ and $x = X_t = 104$ m$= 53\lambda_p$

extreme. They remain close to $T_{2_{\text{meas}}}$, which corresponds to the mean zero-up-crossing period. Only the height of the extreme events increases with x. This increase is again a consequence of

the nonlinear effects described in Sec. 2.1.1 and already identified in the spectrum, kurtosis, and crest distribution analysis. It cannot be predicted with a linear approach (see Forristall (2017)). In a wave tank environment, an accurate representation of the joint wave height and period statistics should account for the distance from the wave maker, even if the period distribution does not depend on x.

4.3 Characterization of the nonlinear phenomena at the origin of the extreme statistics

In the preceding two sections, we conducted a detailed analysis of the wave spectrum, the statistical moments of free surface elevation, and the zero-crossing wave distributions. These quantities are the standard quantities of interest, used to describe and qualify the wave conditions in ocean engineering experiments. Within the scope of this typical study, we observed spatial evolutions that are commonly explained by the development of high-order nonlinear interactions. Specifically, these include the broadening of the spectrum, the downshift of its peak, and the increase in probability of the extreme events (the so-called rogue waves) with the propagating distance. The increase in probability of the extreme events is a phenomenon of great importance to the ocean engineering community. It leads to extreme zero-crossing wave height and crest distributions which are not predicted by the usual references. In practice, for a sea-keeping test, it means that the number of critical events varies with the position of the structure and cannot be easily predicted.

To enhance our ability to generate and qualify wave fields accurately, we need to develop procedures that account for the spatial evolution of these statistics. This will be the core of the second part of this thesis. However, before addressing this topic, it seems also important to better understand the physical mechanisms at stake. This is the objective of this section that is dedicated to further investigations of the nonlinear phenomena at the origin of the extreme statistics.

Theoretically, the evolution of the statistics is explained by quasi-resonant four-wave interactions which modulate the envelope, leading to what is known as "modulational instabilities" (see Janssen (2003); Onorato et al. (2009)). Consequently, the present study will initially focus on characterizing and quantifying envelope modulations, using the concept of 'groupiness.' Subsequently, we will directly examine nonlinear interactions through the utilization of the trispectrum (quantity introduced in 1.3.2f)).

4.3.1 Groupiness

The concept of 'groupiness' is introduced in Section 1.3.2 e). It is a characteristic of the wave field that describes the modulations in the free surface elevation envelope. A strongly modulated envelope implies that the wave packets are well-defined and distinct. To quantify the groupiness, the factors GF and $\mathrm{GF}_{\mathrm{SIWEH}}$ are defined in the Section 1.3.2 e). They are derived from the standard deviation of the envelope and account for the number and the severity of the wave groups. They were computed for each realization and each wave gauge of the dataset (still the 30 realizations of `ss6g5` targeted at $X_t = 53\lambda_p$ during Campaign D).

Figure 4.10 presents the evolution of the two groupiness factors along the tank. The displayed quantities are the means across all realizations. The shaded area corresponds to the standard deviations over the realizations divided by $\sqrt{N_{\mathrm{real}}}$. It models the sampling variability.

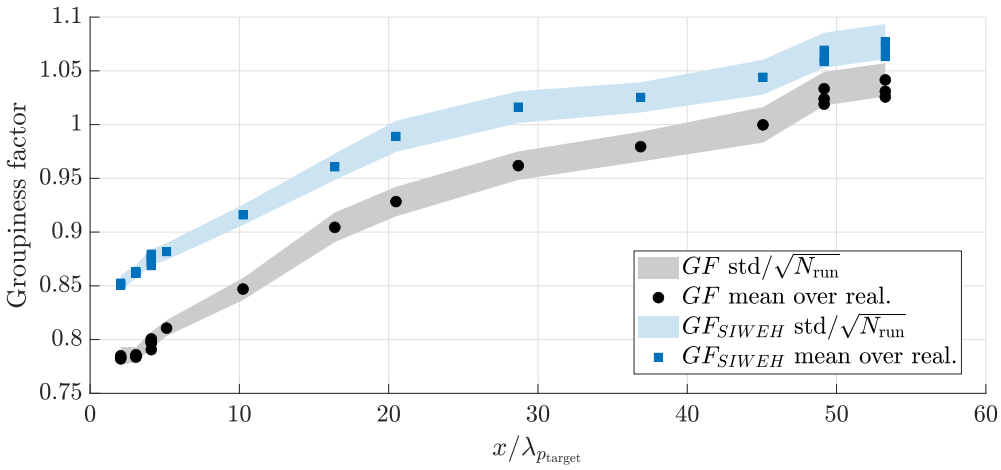

Figure 4.10 – `ss6g5` scale 120 targeted at $X_t = 53\lambda_p$ - Campaign D - Groupiness factors along the tank

The two groupiness factors lead to similar results, even if the values of $\mathrm{GF}_{\mathrm{SIWEH}}$ are slightly larger than GF values. The groupiness increases along the tank. It means that large and clear-cut wave groups appear as the waves propagate. This increase can be directly correlated with the kurtosis evolution (see Fig. 4.6). The enhanced occurrence of extreme waves with propagating distance is associated with the increased existence of wave groups. Note that these results should be compared with another experimental study carried out in the ECN towing tank (see Michel et al. (2020)). In the latter, the evolution of regular waves slowly modulated in amplitude and phase was associated with the emergence of coherent structures (Peregrine solitons) during the propagation, as a direct result of near-resonant wave interactions (self-focusing).

This phenomenon appears to be strongly related to the spatial kurtosis evolution and is likely to be connected to the GF increase measured in the present study.

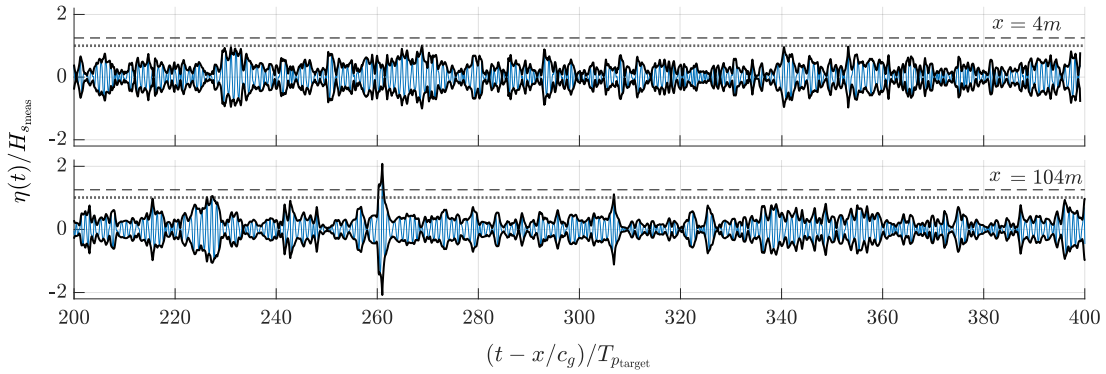

Figure 4.11 – `ss6g5` scale 120 targeted at $X_t = 53\lambda_p$ - Campaign D - Typical time series at $x = 2\lambda_p$ and $53\lambda_p$ - the envelope is displayed with the black full lines - the dashed line corresponds to $\eta/H_{s_{\text{meas}}} = 1.25$ and the dotted line to $\eta/H_{s_{\text{meas}}} = 1$

To provide a concrete illustration of what the increase in groupiness implies, Figure 4.11 presents typical free surface elevation time series at $x = 2\lambda_p$ and $x = X_t = 53\lambda_p$. To mitigate the influence of dissipation, the elevation is normalized by the significant wave height of the series, $H_{s_{\text{meas}}}$. Additionally, the envelope, computed using the Hilbert transform (see eq.1.33), is also displayed (black lines surrounding the free surface elevation).

Visually, the wave groups are more clear-cut at $X_t = 53\lambda_p$. Concomitantly, it results in a larger number of extreme events. Indeed, the time series measured at $X_t = 53\lambda_p$ exhibit 3 events verifying $H_c/H_s > 1$ (at 225, 260 and $310T_{p_{\text{target}}}$) while for the displayed data at $x = 2\lambda_p$, only one crest is higher than the significant wave height (around $270T_{p_{\text{target}}}$). Note that for this small time window (duration of $200T_p$), only one rogue wave (defined as $H_c/H_s > 1.25$) is observed. The latter event occurring at $X_t = 53\lambda_p$ at $t - x/c_g = 260T_{p_{\text{target}}}$ is impressively large, H_c reaches more than $2H_s$. It is the highest crest of the 30 realizations dataset.

To further investigate the development of this extreme wave, Figure 4.12 presents the available free surface elevation series measured behind $X_t = 104$ m. As in Figure 4.11, $x/c_g(f_p)$ is subtracted to the time axis to study the evolution of the wave groups at the same relative time within the total wave sequence. We can observe the envelope modulation, which gradually leads to the formation of a self-focusing wave packet. The envelope height increases with the propagating distance, giving rise to the rogue wave event. We have here an example where the

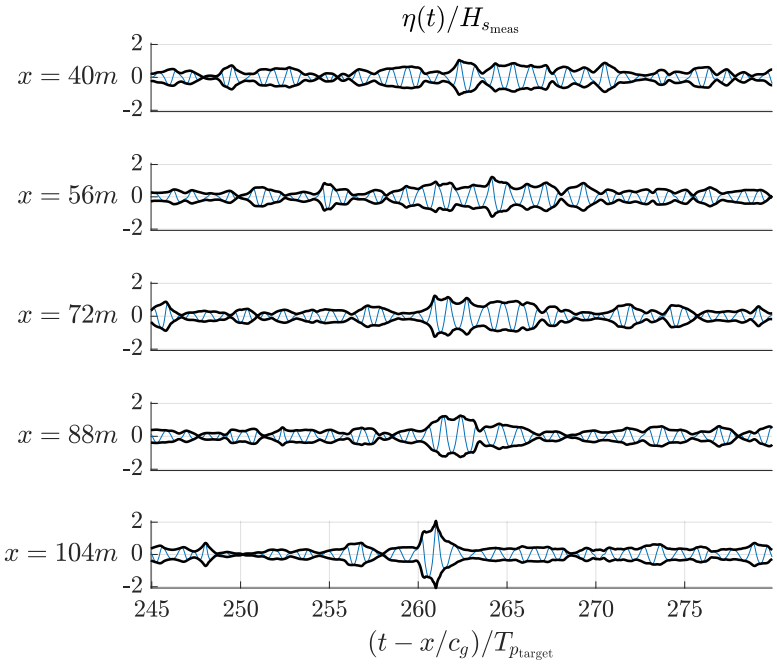

Figure 4.12 – `ss6g5` scale 120 targeted at $X_t = 53\lambda_p$ - Campaign D - envelope modulation generating a rogue wave event - the black lines correspond to the wave envelope

increase in groupiness leads to the occurrence of an extreme event. It enlightens once again the role of envelope modulation in the development of extreme statistics.

4.3.2 High-order spectral analysis

In the previous subsection, we correlated the extreme statistics with a time-domain rearrangement of the free surface elevation i e. envelope modulations. The objective now is to investigate the physical mechanisms responsible for this phenomenon: the high-order nonlinear wave interactions.

a) Nonlinear waves interactions

As the wave propagate, the frequency components of the wave field interact with each other (including with themselves), giving birth to new frequency components. Depending on the frequency multiplet, the nature of the interaction changes. If the new wave obeys the dispersion relation, it is referred to as a free wave, and the interaction is qualified as resonant. Otherwise,

the interaction is non-resonant and the new wave is what we call a 'bound wave', which only affects the shape of the first existing linear waves.

The second order of linearity (i.e. 3-wave interaction) cannot be resonant and only leads to bound waves. As an example, we consider a deep-water linear Airy wave of frequency f (and wavenumber $k = (2\pi f)^2/g$) interacting with itself. The wave propagation equations predict that the resulting new wave has a frequency $f_{\text{new}} = 2f$ and a wavenumber $k_{\text{new}} = 2k$ (see Mei et al. (2005) book). Therefore, $(2\pi f_{\text{new}})^2 \neq g k_{\text{new}}$, the dispersion relation is not satisfied. What happens is that the new wave follows the phase of the initial Airy wave, making its crest larger and its troughs flatter.

However, the third order of nonlinearity (i.e. 4-wave interactions) can lead to resonant interactions. This requires the following symmetry conditions,

$$\overrightarrow{k_1^{\text{interact}}} + \overrightarrow{k_2^{\text{interact}}} = \overrightarrow{k_3^{\text{interact}}} + \overrightarrow{k_4^{\text{interact}}} \tag{4.2}$$

and

$$f_1^{\text{interact}} + f_2^{\text{interact}} = f_3^{\text{interact}} + f_4^{\text{interact}} \tag{4.3}$$

with f_i^{interact} the frequencies and $\overrightarrow{k_i^{\text{interact}}}$ the wavenumber vectors (including the direction in the $x\,y$ plane) of the four-wave field components involved in the interaction. If these conditions are not satisfied, the interaction is non-resonant. For unidirectional waves, this is very restrictive. It requires that $k_1^{\text{interact}} = k_3^{\text{interact}}$ and $k_2^{\text{interact}} = k_4^{\text{interact}}$, or $k_1^{\text{interact}} = k_4^{\text{interact}}$ and $k_2^{\text{interact}} = k_3^{\text{interact}}$ (see Janssen (2003)).

For highly-nonlinear wave fields, near-resonant interactions can also occur. This concept is introduced for instance in Annenkov and Shrira (2006). To summarize, the idea is to allow small random deviations from the resonant conditions. This can be modeled by

$$\overrightarrow{K_1^{\text{interact}}} + \overrightarrow{K_2^{\text{interact}}} = \overrightarrow{K_3^{\text{interact}}} + \overrightarrow{K_4^{\text{interact}}} \tag{4.4}$$

and

$$F_1^{\text{interact}} + F_2^{\text{interact}} = F_3^{\text{interact}} + F_4^{\text{interact}} + \Delta F \tag{4.5}$$

with $|\overrightarrow{K_i^{\text{interact}}}| = |\overrightarrow{k_i^{\text{interact}}}| + \delta_i^k$, δ_i^k being a random error bounded by a chosen threshold, and F_i^{interact} the frequencies computed with the dispersion relation from $|\overrightarrow{K_i^{\text{interact}}}|$. ΔF is a frequency mismatch.

One of the most known four-wave interactions is the Benjamin Feir instability. The phenomenon was intensively studied in Benjamin and Feir (1967). In the latter work, it was

theoretically proven that a regular wave-train is not stable to close side band perturbations (i. e. perturbations in frequencies that almost equal the carrier wave frequency f_0). The envelope of the wave train modulates. And the theoretical growth of this modulational instability is exponential (in fact it is limited by breaking or multidirectional energy spreading). The concept was generalized for irregular narrow-band unidirectional sea state in Alber (1978). For a given leading frequency f_0, affected by a given side-band perturbations $f_0 \pm \delta_{\mathrm{BF}}$, the frequency quartet at stake is:

$$(f_1^{\mathrm{interact}} = f_0 - \delta_{\mathrm{BF}}\,, \quad f_2^{\mathrm{interact}} = f_0 + \delta_{\mathrm{BF}}\,, \quad f_3^{\mathrm{interact}} = f_0\,, \quad f_4^{\mathrm{interact}} = f_0) \tag{4.6}$$

The Benjamin–Feir instability is non-resonant. It is an example of a near-resonant four-wave interaction "in which the carrier wave is phase-locked with the sidebands" (extract of Janssen (2003)). This interaction is likely to be responsible for the envelope modulations and the extreme statistics observed in Sec. 4.3.1 and 4.2. For the irregular sea states studied in this thesis, we expect that the most prominent Benjamin Feir interactions occur for $f_0 = f_p$.

Based on the Non Linear Schrödinger equations and including the near-resonant interactions, Janssen (2003) derived a theoretical wave propagation model accounting for the envelope modulation. Fedele (2015) used the latter framework to develop the kurtosis theoretical predictions, introduced in the section 2.1.2 and providing a coherent description of the experimental data in Fig. 4.6.

The objective of this section is to track the direct signatures of the nonlinear interactions in the experimental data, and especially to enlighten the Benjamin Feir instabilities. To this aim, the next paragraph b) will present tri-spectrum slices computed from the `ss6g5` dataset studied throughout this chapter. The trispectrum definition was introduced in the paragraph 1.3.2f). It allows to enlighten the phase coherence between multiplets of the wave field components and quantifies the strength of their nonlinear interaction. It does not discriminate between resonant and non-resonant interactions. It discriminates frequencies resulting from nonlinear interactions from frequencies initially present in the linear input wave field.

The trispectrum can also be interpreted as the identification of the contribution of each triplet of the wave field components to the kurtosis of the η distribution, λ_4. Its integration over its 3D frequency domain equals λ_4. Consequently, the spatial evolution of the kurtosis observed in Figure 4.6 should be found by analyzing the trispectrum.

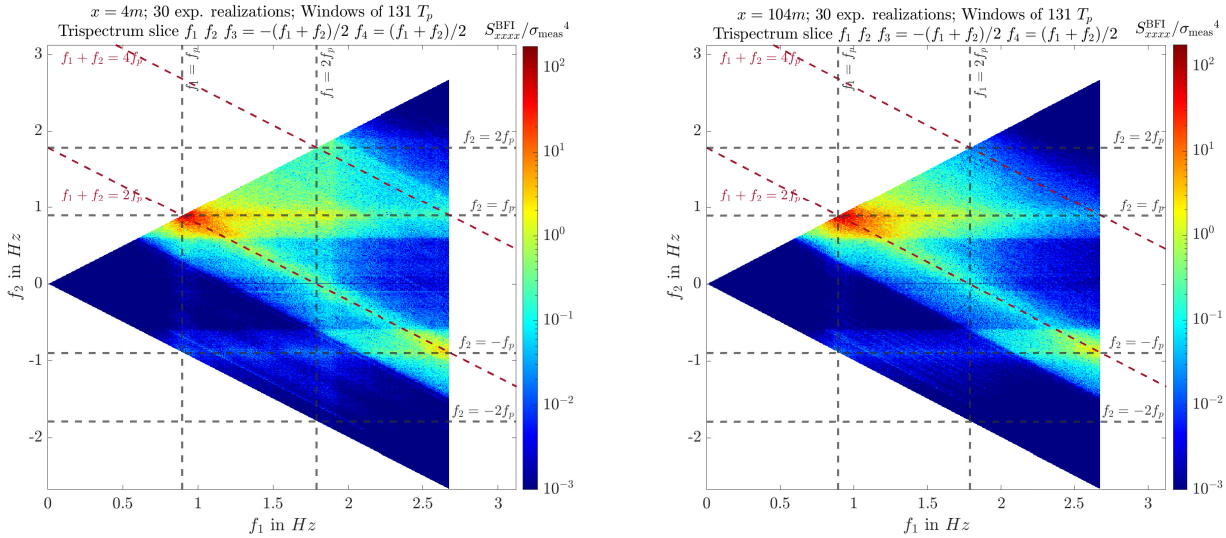

(a) $x = 4$ m **(b)** $x = X_t = 104$ m

Figure 4.13 – S^{BFI}_{xxxx} computed from $x = 4$ m and $x = X_t = 104$ m measurements

b) Trispectrum

As discussed in paragraph 1.3.2f), the trispectrum is a 3D quantity and is not easy to visualize. Since the aim of this subsection is to examine Benjamin Feir instabilities, we will study a trispectrum slice that highlights them. To this end, in paragraph 1.3.2f), we defined:

$$S^{BFI}_{xxxx}(f_1, f_2) = S_{xxxx}(f_1, f_2, -\frac{f_1+f_2}{2}) \tag{4.7}$$

tracking the interactions of type

$$(f_1^{\text{interact}} = f_1\,, \quad f_2^{\text{interact}} = f_2\,, \quad f_3^{\text{interact}} = (f_1+f_2)/2\,, \quad f_4^{\text{interact}} = (f_1+f_2)/2) \tag{4.8}$$

By denoting $f_0 = (f_1+f_2)/2$ and $\delta_{\mathrm{BF}} = |f_2 - f_1|/2$, we find the Benjamin Feir instability quartet (eq. 4.6).

The distinction between frequencies resulting from nonlinear interactions and those initially present in the linear input wave field is achieved through the averaging operation $E\{\}$ applied to the quantity $\mathscr{F}_\eta^{\Delta T}(f_1)\mathscr{F}_\eta^{\Delta T}(f_2)\mathscr{F}_\eta^{\Delta T}(-(f_1+f_2)/2)\mathscr{F}_\eta^{\Delta T *}((f_1+f_2)/2)$, across several time windows of the analyzed dataset (see eq. 1.40). For further explanations, please refer to Paragraph 1.3.2f).

The number of windows should be sufficient to ensure that the averaging process effectively removes the independent-phase waves from the waves resulting from nonlinear interactions. Furthermore, the size of the window defines the frequency resolution of the trispectrum: $\delta f = 1/\Delta T$.

To strike a good balance, from our experimental dataset of 30 realizations, each with a duration of $390T_p$, we created a set of windows, each with a size of $130T_p$, leading to a frequency resolution of $1/130f_p = 0.009$ Hz. To smooth S^{BFI}_{xxxx}, as advised in the literature (Collis et al., 1998; Ewans et al., 2021), we used a 50% overlap between the windows. As a result, the total number of windows is 180. The windows are rectangular. Tests were also conducted with Hanning shapes (Welch, 1967b), but no significant changes were observed.

Figure 4.13 displays S^{BFI}_{xxxx} computed from $x = 4$ m and $X_t = 104$ m measurements. The S^{BFI}_{xxxx} values are normalized by σ^4_{meas} to remove the influence of H_s value in the comparison. To facilitate analysis, lines of interest are displayed. These are interactions involving the peak frequency f_p. In particular, the line $f_1 + f_2 = 2f_p$ corresponds to the interaction

$$(f_1^{\text{interact}} = f_p + \delta_{\text{BF}}\,, \quad f_2^{\text{interact}} = f_p - \delta_{\text{BF}}\,, \quad f_3^{\text{interact}} = f_p\,, \quad f_4^{\text{interact}} = f_p) \tag{4.9}$$

The further away from the point ($f_1 = f_p$,$f_2 = f_p$), the greater the δ_{BF}. At both $x = 4$ m and $x = X_t = 104$ m, we can observe a concentration of significant trispectrum values around the point (f_p,f_p). The exact (f_p,f_p) point is a never-zero trivial point, since by definition, $S^{BFI}_{xxxx}(f_p, f_p) = S(f_p)^4$. However, the surrounding zone is composed of non-trivial points. It is the area where the Benjamin Feir instabilities are likely to happen: f_0 is close to f_p and δ_{BF} is nearly zero. When comparing S^{BFI}_{xxxx} at $x = 4$ m and $x = X_t = 104$ m in this area, we visually observe that the values are larger at $x = X_t = 104$ m. This could be a signature of more prominent Benjamin Feir instabilities at this large distance from the wave maker.

Influence of the spectrum shape on S^{BFI}_{xxxx} The number of windows required to completely remove the influence of the frequency components not resulting from interactions is known to be huge (Collis et al., 1998; Ewans et al., 2021). In Figure 4.13, we observe non-zero S^{BFI}_{xxxx} values in a large area (basically between the lines $f_1 + f_2 = 1.5f_p$ and $f_1 + f_2 = 4f_p$). Moreover, near the $f_1 + f_2 = 4f_p$ line, the values are larger at $x = 4$ m. This would imply that Benjamin Feir interactions occur for $f_0 \approx 2f_p$, and that these interactions are more pronounced close to the wave maker. However, the Benjamin Feir instabilities require space to develop (see Benjamin and Feir (1967); Janssen (2003)). Therefore, they are unlikely to be stronger at the beginning of the tank. Then, one should recall the shape of the wave spectra at both locations (see Fig. 4.3).

Due to the side walls dissipation, energy content was significantly larger at $2f_p$ for $x = 2\lambda_p$ compared to $x = 53\lambda_p$. The most reasonable interpretation is that the wave spectrum shape influences the trispectrum values (which should not have happened if the number of windows used to compute S^{BFI}_{xxxx} had been large enough).

As a result, to interpret the differences observed between $x = 4$ m$= 2\lambda_p$ and $x = X_t = 104$ m$= 53\lambda_p$, we first need to accurately determine the influence of the spectrum shape.

To determine the influence of the spectrum shape, we will compare our experimental results with semi-artificial signals. These were created by taking the Fourier amplitudes measured experimentally at $x = 4$ m $(2\lambda_p)$ and $x = X_t = 104$ m $(53\lambda_p)$ and adding random phases. For a set of measurements at x, denoted here for convenience as η_{expe}, we construct a set of semi-artificial realizations, η_{rd}, in the Fourier domain using the following equation:

$$\mathscr{F}^d_{\eta_{\text{rd}}}(f) = |\mathscr{F}^d_{\eta_{\text{expe}}}(f)| \exp(-i\Phi_{\text{rd}}) \tag{4.10}$$

with $\Phi_{\text{rd}} = 2\pi U_{[0;1]}$. These signals have random phases, so for an infinite number of windows, the associated trispectrum tends towards 0 for each non-trivial frequency multiplet.

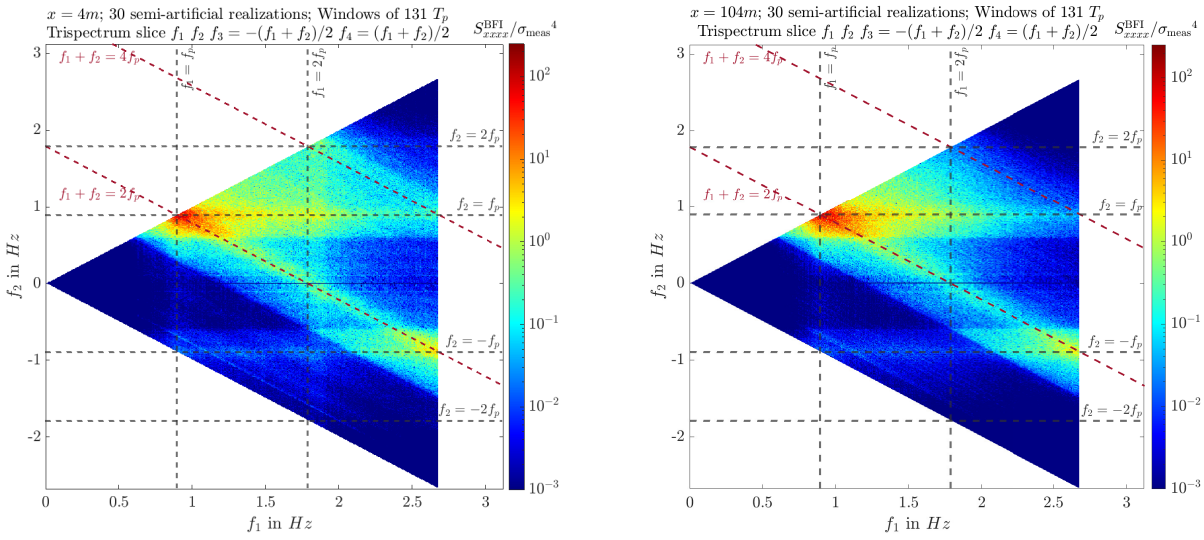

(a) $x = 4$ m **(b)** $x = X_t = 104$ m

Figure 4.14 – S^{BFI}_{xxxx} computed from $x = 4$ m and $x = X_t = 104$ m semi-artificial signals

Figure 4.14 displays S^{BFI}_{xxxx} computed from $x = 4$ m and $x = X_t = 104$ m semi-artificial signals. Several observations can be made. First, the main S^{BFI}_{xxxx} patterns are the same as those

observed with the experimental data. The differences around $f_1 + f_2 = 4f_p$ are still present, but the differences around (f_p, f_p) are slightly less pronounced. These S^{BFI}_{xxxx} computed from the semi-artificial signals only contain the influence of the spectrum shape, which is present because we analyze a finite number of waves. This means that the main patterns and the differences in high-frequency areas observed in Fig. 4.13 are only an effect of the spectrum shape and do not quantify any nonlinear interaction. However, from visual observation alone, it is challenging to draw a definitive conclusion regarding whether the differences around (f_p, f_p) in Fig. 4.13 are indeed indicative of more prominent Benjamin Feir instabilities at $x = X_t = 104$ m.

Quantification of the comparison between $x = 4$ m and $x = X_t = 104$ m To draw a conclusion and quantify the observed S^{BFI}_{xxxx} values, Figure 4.15 provides the probability of exceedance of the S^{BFI}_{xxxx} points displayed in Fig. 4.13 and 4.14. It includes the experimental and semi-artificial S^{BFI}_{xxxx} distributions at $x = 4$ m and $x = X_t = 104$ m. The figure displays, for each S^{BFI}_{xxxx} value, the probability of finding a larger value in the entire (f_1,f_2) domain. We observe that at $x = 4$ m, there are almost no differences between the experimental and the semi-artificial data. This implies that there are almost no nonlinear interactions. In contrast, at $x = X_t = 104$ m, we observe noticeable differences. The S^{BFI}_{xxxx} values of the experimental dataset are significantly larger for low probabilities. The order of magnitude of the values in this area (tail of the distribution) corresponds to the one of the values observed near (f_p,f_p) in Figure 4.13. Thanks to this analysis, we can conclude that the Benjamin Feir instabilities are more prominent at $x = X_t = 104$ m, and this is not an artifact of the spectrum shape. Therefore, we have correlated the emergence of extreme crest distributions, the modulation of the envelope, and the presence of Benjamin Feir instabilities at the end of the tank.

4.4 Conclusions

In this chapter, we have examined the propagation of `ss6g5` sea state in the Towing tank. `ss6g5` is a typical design sea state inspired by the reference wave conditions studied in the ocean engineering community (see NWT Preparation Workgroup (2019) and Fouques et al. (2021)). The spectrum is relatively narrow ($\nu_w = 0.14$), and the steepness is limited to $\varepsilon_p = 2.5\%$ (non-breaking case), resulting in an intermediate BFI value of 0.5.

For this non-extreme design sea state, we have observed strong spatial dynamics. Firstly, the tank's side walls introduce dissipation phenomena that impact the spectrum. Moreover, the statistical characteristics vary significantly across space. Beyond $x > 20\lambda_p$, the kurtosis values

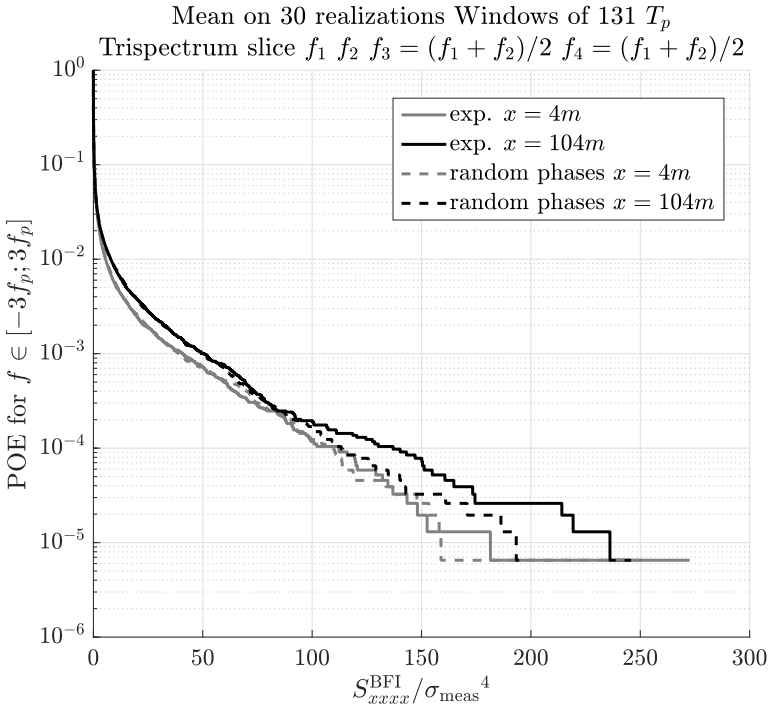

Figure 4.15 – Probability of exceedance of the trispectrum slice values

are large (above 3.4), and at the end of the tank, the crest distribution becomes extreme, no longer aligning with the industry benchmarks, such as Foristall and Huang distributions. This evolution of the statistics has been correlated with envelope modulations, which were measured using groupiness factors, and with the intensification of Benjamin Feir interactions, detected through the S^{BFI}_{xxxx} trispectrum slices.

The appearance of extreme distributions at the end of the basin raises several questions concerning the wave-structure interaction tests carried out in wave tank environments. It enlightens the presence of a significant number of extreme events that are likely to strongly affect the response of the tested structure. Considering those extreme wave fields as wave conditions for ocean engineering studies is still under question. Indeed, the crest PDER departure from reference distributions is significantly limited for breaking and directional sea states (Onorato et al., 2009), which represent more realistically extreme environmental conditions. However, accounting for the existence of those extreme wave fields in the procedures is a crucial step toward more relevant wave generation and qualification methods.

This study has provided us with a detailed understanding of how the quantities of interest evolve over long distances. The findings will be essential in the next part of this thesis. We

will use them to build wave generation procedures adapted to complex wave propagation. More specifically, Chapter 7 will address spectrum control at any distance (counterbalancing dissipation and nonlinear phenomena) and Chapter 8 will present a procedure for generating the extreme wave fields observed at the end of the tank, at any new location in the basin. Before, Chapter 5 addresses the numerical generation and propagation of sea states.

CHAPTER 5

NUMERICAL WAVE TANKS

The two previous chapters have focused on experimental wave propagation. Chapter 3 addresses experimental uncertainty and Chapter 4 provides a detailed study of an experimental dataset generated in the Towing tank. In addition, Chapter 4 provides insights into how sea states propagate in wave tank environments. However, as discussed in the Introduction, ocean engineering studies can be conducted in both experimental and numerical wave tanks (NWT). In the case of NWT, standard CFD codes are not suitable for simulating waves over long distances (more than a couple of wavelengths, see Choi et al., 2020). Instead, small-domain CFD simulations, solving wave-structure interaction problems, can be fed with numerical waves, generated with a dedicated wave solver mimicking a wave tank. Such a type of solver will be denoted as a "wave-NWT-solver". These solvers can also be used before experiments to calibrate the wave-maker inputs.

The understanding of wave-NWT-solvers' features and limitations is a crucial step towards developing relevant wave generation procedures. To this aim, this chapter is dedicated to the implementation of an efficient and realistic wave-NWT-solver, adapted for the generation of the wave conditions of interest (`ss6`, `ss6g5` and `GOM` sea states) in domains twinning the ECN experimental facilities (O.E. and Towing tanks). The model will be used in the second part of this thesis to build and improve wave generation procedures for ocean engineering studies (whether they are experimental or numerical).

The solver used in this thesis is `HOS-NWT` Ducrozet et al. (2012). The first section introduces the code, giving a general overview with a special focus on breaking modeling. The second section presents setups adapted to our problem, and evaluates their accuracy for both non-breaking and breaking conditions.

5.1 Description of the HOS−NWT solver

5.1.1 High-Order Spectral - Numerical Wave Tank

HOS−NWT solver is a fully nonlinear wave propagation code, relying on the potential flow theory and using the high-order spectral method to solve the free surface boundary conditions. The code is developed by the LHEEA laboratory, ECN, and is released open-source [1]. A complete description of the solver can be found in Ducrozet et al. (2012) or Ducrozet (2007). Here follows a brief summary for the unidirectional version of the code (scope of this thesis).

We consider a 2D rectangular numerical wave tank with horizontal dimension L_x and d the water depth. A wave maker is located on $x = 0$. The walls stand perfectly reflective and a numerical absorbing beach is implemented at the end of the domain. The latter is designed so that no reflection is expected to occur in the simulations. The fluid is assumed homogeneous, incompressible and inviscid. A velocity potential $\Phi(x,z,t)$ is introduced verifying the Laplace equation in the entire domain, $\Delta\Phi(x,z,t) = 0$. Dynamic and kinematic free surface conditions are expressed introducing the surface velocity potential $\widetilde{\Phi}(x,t) = \Phi(x,z = \eta(x,t),t)$, with $z = \eta(x,t)$ describing the free surface elevation. These two conditions read, on $z = \eta(x,t)$

$$\frac{\partial \eta}{\partial t} = \left(1 + \left(\frac{\partial \eta}{\partial x}\right)^2\right)\frac{\partial \Phi}{\partial z} - \frac{\partial \widetilde{\Phi}}{\partial x}\frac{\partial \eta}{\partial x} \tag{5.1}$$

$$\frac{\partial \widetilde{\Phi}}{\partial t} = -g\eta - \frac{1}{2}\left(\frac{\partial \widetilde{\Phi}}{\partial x}\right)^2 + \frac{1}{2}\left(1 + \left(\frac{\partial \eta}{\partial x}\right)^2\right)\left(\frac{\partial \Phi}{\partial z}\right)^2 \tag{5.2}$$

η and $\widetilde{\Phi}$ are the two quantities of interest. Time stepping is achieved solving Eqs. (5.1) and (5.2). The only unknown is the vertical velocity on the free surface $\frac{\partial \Phi}{\partial z}(x,z = \eta(x,t),t)$. This quantity is computed with the High-Order Spectral (HOS) method, using Taylor expansions and power series developments (Dommermuth and Yue, 1987; West et al., 1987). Those are computed keeping a given number of terms consistent with the so-called order of nonlinearity M. It can be specified arbitrarily. Spatial discretization is performed through spectral decomposition, using

1. https://github.com/LHEEA/HOS-NWT

wave-tank modes.

$$\eta(x,t) = \sum_j A_j^{\eta}(t)\cos(k_j^x x) \tag{5.3}$$

$$\widetilde{\Phi}(x,t) = \sum_j A_j^{\widetilde{\Phi}}(t)\cos(k_j^x x) \tag{5.4}$$

with $A_j^{\eta}(t)$ and $A_j^{\widetilde{\Phi}}(t)$ the modes amplitudes associated to the wavenumber $k_j^x = \frac{j\pi}{L}$. The number of mode N_x controls the spatial discretization and the maximum simulated wavenumber is defined by

$$k_{\max}^{\mathrm{HOS}} = N_x\pi/L \tag{5.5}$$

To allow for an accurate wave propagation of irregular sea states with a peak period T_p (and peak wavenumber k_p), N_x should be chosen so that at least $k_{\max}^{\mathrm{HOS}} > 15k_p$ (see for instance convergence studies in Ducrozet et al. (2012)). The numerical time step is adjusted during the course of the simulation thanks to the use of an adaptative Runge-Kutta scheme, specifying a tolerance value.

The original HOS model was dedicated to the propagation of a prescribed initial free surface elevation $\eta(x,t=0)$ with periodic boundary conditions (Ducrozet et al., 2016). The present NWT starts from rest and the waves are generated thanks to a wave maker with a prescribed motion. An additional potential accounting for wave maker motions is added, resulting in forcing terms modifying the free surface conditions.

$$\Phi = \Phi_{\mathrm{spec}} + \Phi_{\mathrm{add}} \tag{5.6}$$

Φ_{add} and Φ_{spec} verifying respectively the wave maker and the free surface boundary conditions. Please, refer to Ducrozet et al. (2012) for more details about the HOS−NWT model.

5.1.2 Breaking model

The previous HOS−NWT model is based on nonlinear potential flow formalism, which means it neglects air entrapment, vorticity and viscous phenomena. This enables an efficient and accurate wave propagation model. However, these assumptions limit the use of such models in the case of breaking waves (e.g. GOM sea state). To address this limitation, methodologies have been recently implemented in HOS−NWT for handling breaking events. One of these methodologies will be described in this section and used in this thesis. It is important to note that the breaking model does not directly solve breaking events but simulates their effects on wave propagation.

Since no dissipation is included in the standard `HOS-NWT` code, without any breaking model, the steepest waves induce strong energy transfer to high-frequency modes. This leads to numerical instabilities that cannot be resolved and stop the computation.

In general, a relevant breaking model for `HOS-NWT` should be stable (same model/parameters for all `HOS-NWT` setups and wave conditions), robust (solving of all the breaking events, preventing numerical instabilities) and realistic (allowing for an accurate reproduction of experimental wave propagation).

a) Tian-Barthelemy model

The breaking model used in this thesis is the Tian-Barthelemey model, introduced and validated in Seiffert et al. (2017); Seiffert and Ducrozet (2018). It is based on the definition of a breaking onset criterion, that detects the individual breaking events, prior to the effective breaking. This criterion compares the free-surface water particle velocity at the top of the crest U_x^{crest} to the crest speed C_x^{crest}, following Barthelemy's approach (Barthelemy et al., 2018)

$$B_x = \frac{U_x^{\text{crest}}}{C_x^{\text{crest}}} = \frac{\frac{\partial \Phi}{\partial x}\left(x = x_{\text{crest}}, z = \eta(x_{\text{crest}}, t), t\right)}{C_x^{\text{crest}}} > threshold \tag{5.7}$$

with x_{crest} the position of the crest. C_x^{crest} is computed through a complex procedure using Hilbert transforms. The threshold value at use is 0.85, as advised in Barthelemy et al. (2018); Derakhti et al. (2020); Seiffert and Ducrozet (2018). This value was found to be consistent in several contexts (deep-water, shallow-water).

The criterion is computed for each time step in the entire domain. Once it is verified a dissipative term is added to the free surface (Eqs. (5.2) and (5.1)), following the Tian model (Tian et al., 2012)

$$\frac{\partial \eta}{\partial t} = \left(1 + \left(\frac{\partial \eta}{\partial x}\right)^2\right)\frac{\partial \Phi}{\partial z} - \frac{\partial \widetilde{\Phi}}{\partial x}\frac{\partial \eta}{\partial x} + 2\nu_{\text{eddy}}\frac{\partial^2 \eta}{\partial x^2} \tag{5.8}$$

$$\frac{\partial \widetilde{\Phi}}{\partial t} = -g\eta - \frac{1}{2}\left(\frac{\partial \widetilde{\Phi}}{\partial x}\right)^2 + \frac{1}{2}\left(1 + \left(\frac{\partial \eta}{\partial x}\right)^2\right)\left(\frac{\partial \Phi}{\partial z}\right)^2 + 2\nu_{\text{eddy}}\frac{\partial^2 \widetilde{\Phi}}{\partial x^2} \tag{5.9}$$

The eddy viscosity ν_{eddy} is defined as $\nu_{\text{eddy}} = \alpha \frac{H_{BR} L_{BR}}{T_{BR}}$ with H_{BR}, T_{BR} and L_{BR} depending on the wave geometry profile just prior to breaking. Their definition can be found in Tian et al. (2012), and the recommended value for α is 0.02. ν_{eddy} is the same on the entire spatio-temporal

activation zone defined thanks to T_{BR} and L_{BR}. For more details, please refer to Seiffert et al. (2017); Seiffert and Ducrozet (2018).

b) Influence of the spatial discretization on the Tian model

Spatial discretization plays an important role in the HOS−NWT setup. It is related to the maximum resolved wavenumber, and therefore to the high-frequency content of the wave field. This same content is used to describe the steepest waves, and can be at the origin of numerical instabilities in the version of HOS−NWT that does not use a breaking model.

A breaking model implemented in HOS−NWT is therefore naturally influenced by the spatial discretization. And this influence needs to be studied in order to develop a setup that is adapted to the spatial discretizations used.

This subsection addresses the numerical propagation of GOM, which is a strongly breaking sea state, focusing on the influence of spatial discretization. The study provides insights into the stability and robustness of the Tian-Barthelemy model. It should be mentioned that the results were published at OMAE 2020 conference, Canard et al. (2020). Next, in Section 5.2.2, comparisons with experimental data assess the realistic aspect of the model.

Generation procedure and Numerical setup The simulations presented in this subsection were run at a model scale of 100 (Froude similitude). For each case, approximately 100 20-min realizations were run, which corresponds to $T_{\text{analyzed}} \approx 70,000 T_{p_{\text{target}}}$. For such large-size datasets, the sampling variability can be neglected. The wave maker inputs were adapted with the spectrum correction procedure presented in Sec. 7.1. It was applied for each case to ensure the generation of GOM shape at $x = 2\lambda_{p_{\text{target}}}$. More details about the generation procedure are provided in Chapter 7.

The dimensions of the numerical domain were those of the O. E. tank, length $L_x = 50$ m, depth $d = 5$ m. O. E. wave maker geometry was also reproduced and numerical probes were placed along the wave tank every meter. The order of nonlinearity M of the HOS method was fixed to 3. A convergence study showed that this ensures an accurate and efficient solution to the problem.

Generated cases Three cases were generated, varying the spatial discretization. $k_{\text{max}}^{\text{HOS}}$ values of 7, 10 and 15 $k_{p_{\text{target}}}$ were tested (with $k_{p_{\text{target}}}$ the peak wavenumber of the target spectrum, namely GOM). The finest spatial discretization, $k_{\text{max}}^{\text{HOS}} = 15 k_{p_{\text{target}}}$, is still relatively coarse. In this extreme condition context, the robustness of the breaking model is not perfect, preventing the

use of higher spatial discretizations. Indeed, as a consequence of the spectral method used in `HOS-NWT`, the high-frequency terms of Eqs. (5.1) and (5.2) are subject to numerical instabilities enhanced by i) the maximum wavenumber $k_{\max}^{\mathrm{HOS}}$ and ii) the nonlinearity of the wave field. The Tian-Barthelemy breaking model has been built to overcome this phenomenon. Nonetheless, a lack of robustness is observed using a fine spatial resolution together with strong breaking conditions. In practice, most of simulations stopped before ending when using $k_{\max}^{\mathrm{HOS}} > 15k_{p_{\mathrm{target}}}$.

The comparison to $k_{\max}^{\mathrm{HOS}} = 10k_{p_{\mathrm{target}}}$ and $k_{\max}^{\mathrm{HOS}} = 7k_{p_{\mathrm{target}}}$ cases aims to discriminate the influence of the discretization on the Tian model. Note that such discretizations are coarse and strongly decrease the quality of the simulated physics, the numerical solution not being converged.

Results Figure 5.1a presents the spatial evolution of the significant wave height, computed for the 3 cases. First, we observe that for $k_{\max}^{\mathrm{HOS}} = 15k_{p_{\mathrm{target}}}$, H_s strongly decreases along the wave tank. This evolution is expected. `GOM` is a strongly breaking sea state and breaking events dissipate the energy of the wave field.

In contrast, the degradation of the discretization appears to minimize the energy dissipation. With $k_{\max}^{\mathrm{HOS}}/k_{p_{\mathrm{target}}} = 7$ the phenomenon is quasi non-existent. The breaking onset is less activated than with finer discretizations and the Tian-Barthelemy breaking model action is clearly altered.

Indeed, the spatial discretization naturally filters wavenumbers larger than $k_{\max}^{\mathrm{HOS}}$. It modifies the physics of the solution. A significant part of the steepest events leading to breaking is then already erased due to the high energy cut-off. Tian-Barthelemy breaking model is consequently less active using coarse discretizations, preventing energy dissipation along the NWT. It is important to note that this is unrealistic. The quality of such a wave fields is strongly questioned.

In addition, Figure 5.1b presents the spatial evolution of the kurtosis of the free surface elevation along the wave tank. We can see that whatever the discretization, kurtosis increases with x. However, the increase intensifies with decreasing $k_{\max}^{\mathrm{HOS}}$.

Several phenomena can be distinguished to explain these observations. Firstly, higher-order nonlinear effects, studied in detail in Chapter 4 for `ss6g5` sea state, are also present for `GOM` wave condition. Near-resonant nonlinear interactions increase the probability of extreme events with distance from the wave maker. However, for this breaking sea state, this phenomenon is counterbalanced by the breaking of the most extreme events, modeled by the Tian model. This slows down the increase of kurtosis. But, for low spatial discretizations, the Tian model is less active, so the effect of breaking on statistics is not well reproduced.

Consequently, to model breaking sea states using the Tian model, one needs to find a

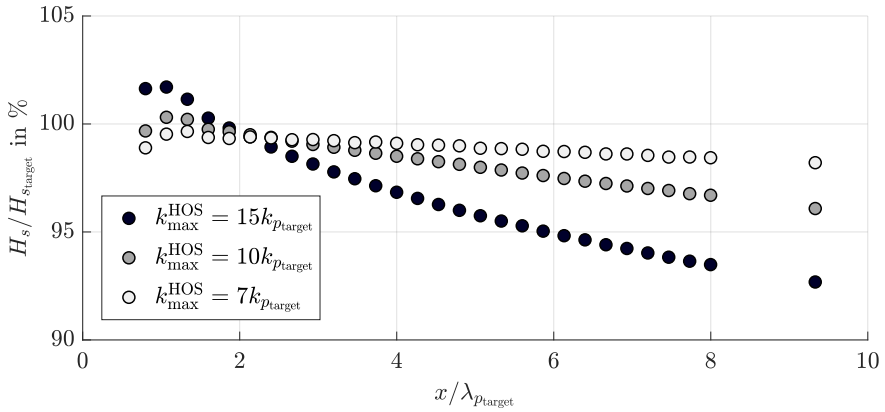

(a) H_s

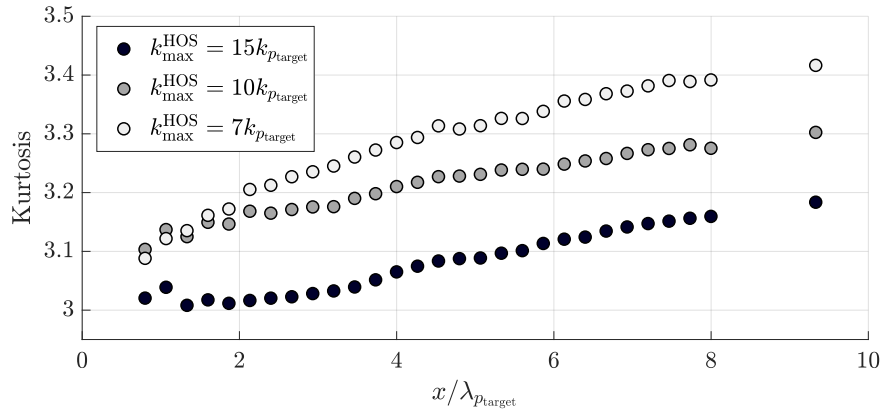

(b) Kurtosis

Figure 5.1 – Influence of the spatial discretization on `GOM` sea state, generated using `HOS-NWT` with the Tian-Barthelemy breaking model implemented.

spatial discretization that is sufficiently accurate to model breaking effects, but coarse enough to avoid numerical instabilities. A value of $15k_{p_{\text{target}}}$ seems appropriate and will be used in this thesis. Ongoing internal works at ECN are focused on the development of a new model, more robust and stable (topic of the ongoing Y. Wang PhD thesis). However, this manuscript does not address this topic.

5.2 Numerical twin of non-breaking and breaking sea states

In this section, we will now evaluate the ability of `HOS-NWT` to faithfully reproduce unidirectional sea state propagation in a basin. To this end, we will compare numerical wave

fields with experimental data. Both mild wave conditions and strongly-breaking conditions will be studied (`ss6` and `GOM` sea states respectively). The aim is also to define a suitable parametrization, independent of sea state and domain.

5.2.1 Non-breaking sea state

In this subsection, we will consider the case of non-breaking sea states, generated with an energy-preserving configuration. We are interested in cases where no dissipation phenomena affect wave propagation. Therefore, we do not model the phenomenon of dissipation due to side walls observed in Chapter 4.

a) Experiments

The reference experimental results to be reproduced with `HOS-NWT` come from the O.E. tank. They are `ss6` realizations generated at scale 40 as part of Campaign A (see the list and features of the experimental campaigns in Appendix A).

The experimental data contain 20 realizations of 20min each, corresponding to $T_{\text{analyzed}} \approx 11600 T_{p_{\text{target}}}$. Based on the studies presented in section 1.3.3, the number of waves considered in the analysis is sufficiently large for the effect of sampling variability to be negligible, whether for spectral or statistical quantities.

b) Numerical setup

To reproduce the experiments, `HOS-NWT` simulations were launched, using the same input wave maker motions as those of Campaign A realizations.

Table 5.1 – Numerical setups used for the reproduction of `ss6` Campaign A experiments

	`HOS-NWT` with Tian	`HOS-NWT` no brkg
M	3	3
$k_{\text{max}}^{\text{HOS}} / k_{p_{\text{target}}}$	25	25
Tolerance	10^{-4} s	10^{-4} s
Tian	Yes	No

Two numerical setups were tested. Their features are provided in Table 5.1. The order of nonlinearity was fixed to $M = 3$, the tolerance of the adaptive Runge-Kutta scheme to 10^{-4} s, and the spatial discretization was chosen such as $k_{\text{max}}^{\text{HOS}} = 25 k_{p_{\text{target}}}$. This ensured an accurate and efficient solution to the problem.

The difference between the two setups is the implementation or not of the Tian-Barthelemy breaking model. As a reminder, the `ss6` sea state to generate is not breaking. However, it was observed that, without breaking model, some `ss6` realizations stopped due to numerical instabilities. For this non-breaking case, theses instabilities are not due to breaking events, they are purely numerical. The large discretization $k_{\max}^{\mathrm{HOS}} = 25k_{p_{\mathrm{target}}}$ induces unstable high-frequency terms in Eqs. (5.1) and (5.2). In the literature, high-frequency filters are sometime used to face this issue. In this study, we use the Tian-Barthelemy breaking model. Indeed, numerical instabilities did not occur in the simulations with the Tian-Barthelemy model implemented.

For the comparison that will follow, the 20 experimental realizations reproduced correspond to runs where both the '`HOS-NWT` no brkg' and '`HOS-NWT` with Tian' models succeeded in simulating the 20min test without numerical instabilities.

c) Results

Deterministic comparison Firstly, Figure 5.5 compares deterministically the free surface elevation time traces of experimental and numerical results, at $x = 3\lambda_{p_{\mathrm{target}}}$. The displayed time window was arbitrary chosen, and is a hundred $T_{p_{\mathrm{target}}}$ long. The results are similar for the entire database.

Whatever the model, we can observe a strong similarity between experimental and numerical waves. The random phases specified in the input files are the same, which explains why the free surface elevation sequences are superimposed. Time shifts can be neglected, and the correlation oscillates between 0.9 and 1. As a reminder, what is displayed here is the Pearson correlation coefficient (eq. 1.54), computed for $5T_{p_{\mathrm{target}}}$-long time windows, see Sec. 1.3.5. To give an order of magnitude, the repeatability studies presented in Sec. 3.6 show that close to the wave maker (up to $x < 5\lambda_{p_{\mathrm{target}}}$) the correlation between two identical experimental tests remains above 0.95 and that further out in the basin ($x > 10\lambda_{p_{\mathrm{target}}}$), it decreases and oscillates between 0.8 and 0.95. In order of magnitude, the similarity between experimental and numerical waves is equivalent to that between two experimental repeatability tests, at a distance $x > 5\lambda_{p_{\mathrm{target}}}$. This is therefore enough to consider `HOS-NWT` as an accurate twin of the experimental wave tank.

The two `HOS-NWT` setups give almost the same results. The Tian-Barthelemy breaking model is hardly activated. Consequently, it does not modify wave dynamics.

Stochastic comparison In addition, Figure 5.3 compares the stochastic quantities of interest. As the available experimental probes are centered around $x = 3\lambda_{p_{\mathrm{target}}}$, it is at this position that spectra and crest height distributions are compared. For both quantities, whether the Tian model

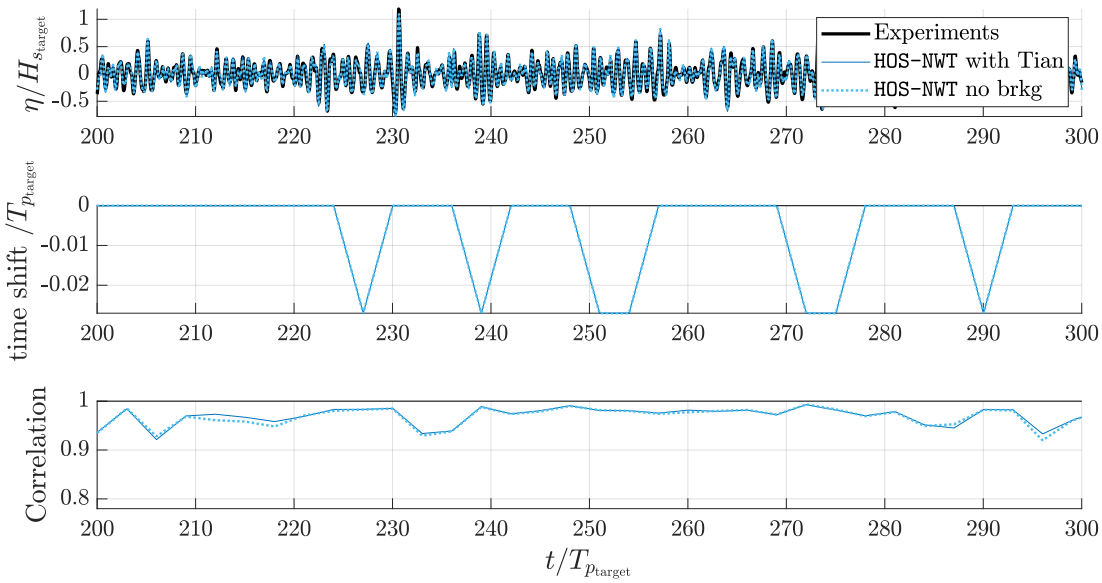

Figure 5.2 – Reproduction of `ss6` Campaign A experiments using `HOS-NWT`: Deterministic comparison $x = 3\lambda_{p_{\text{target}}}$

is implemented or not, the numerical reproduction matches the experimental results.

A few differences should be noted, however. Even considering the measurement uncertainties, the experimental spectrum slightly deviates from the two `HOS-NWT` spectra that align with the target `ss6` shape. The difference is likely to be due to the O.E. tank wave maker transfer function that slightly deviates from its theoretical implementation. Also, note that the spectrum overshoot around $f = 1.5f_p$ may be the result of transverse spurious modes. Indeed, the noise analysis after the runs for `ss6` scale 40 in the O.E. tank showed remaining transverse waves energy around $f = 1.5f_p$ (which corresponds to the mode 24), see Fig. 3.23b Sec. 3.4.2b). In addition, for probabilities below 10^{-3}, the Tian-Barthelemy breaking model slightly decreases the height of the extreme events (Fig. 5.3b).

For this low $BFI = 0.3$ sea state, the spatial evolution of the kurtosis is less pronounced than what was observed for `ss6g5` (BFI= 0.5) in Chapter 4. Figure 5.3d also displays a theoretical line. It corresponds to the prediction of the theory detailed in Sec 2.1.2. The latter was built for narrow-band spectra, which is not the case here. It is provided here for information only. It shows that the expected evolution of the kurtosis due to high-order nonlinear interaction is far less pronounced than the one predicted for `ss6g5` sea state.

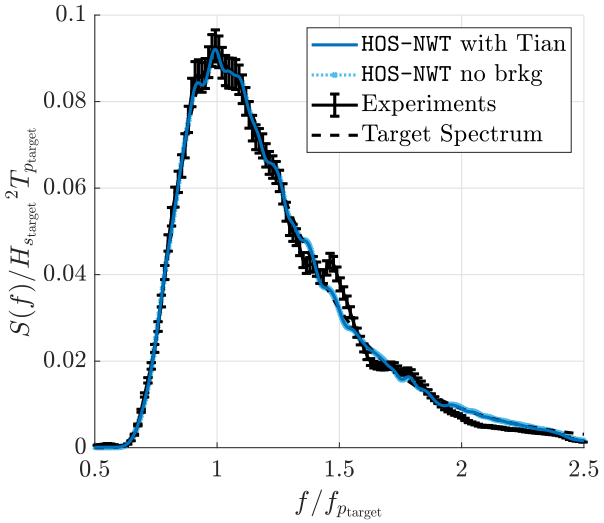

(a) Spectrum at $x = 3\lambda_{p_{\text{target}}}$

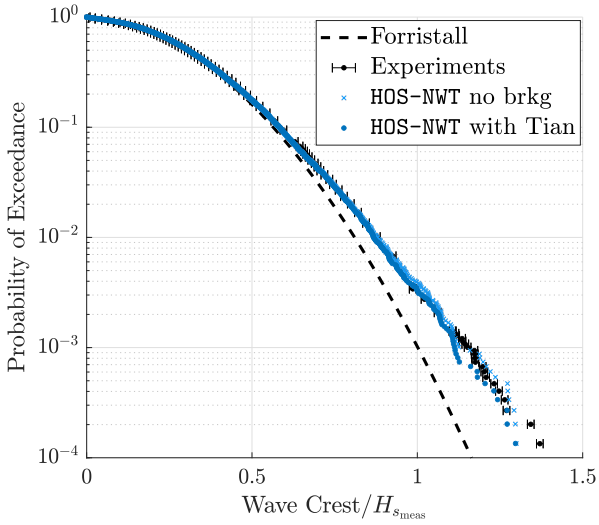

(b) Crest PDER at $x = 3\lambda_{p_{\text{target}}}$

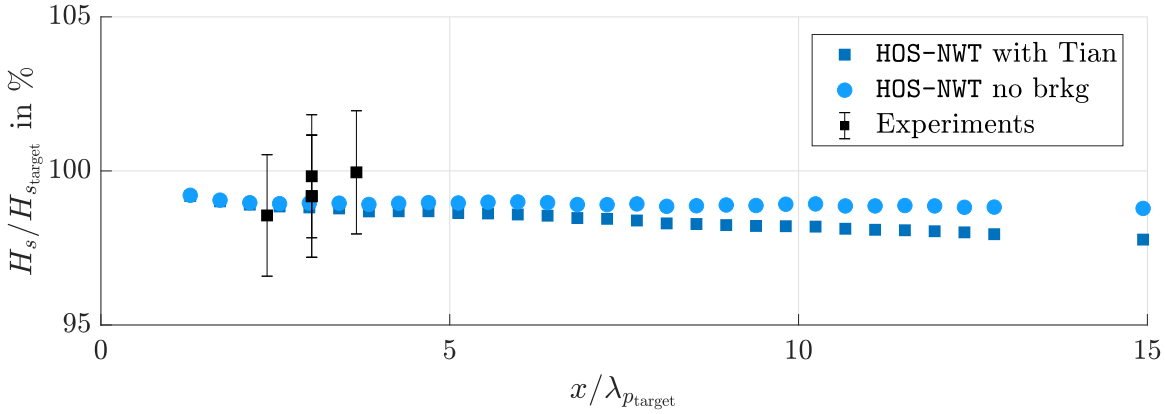

(c) H_s along the tank

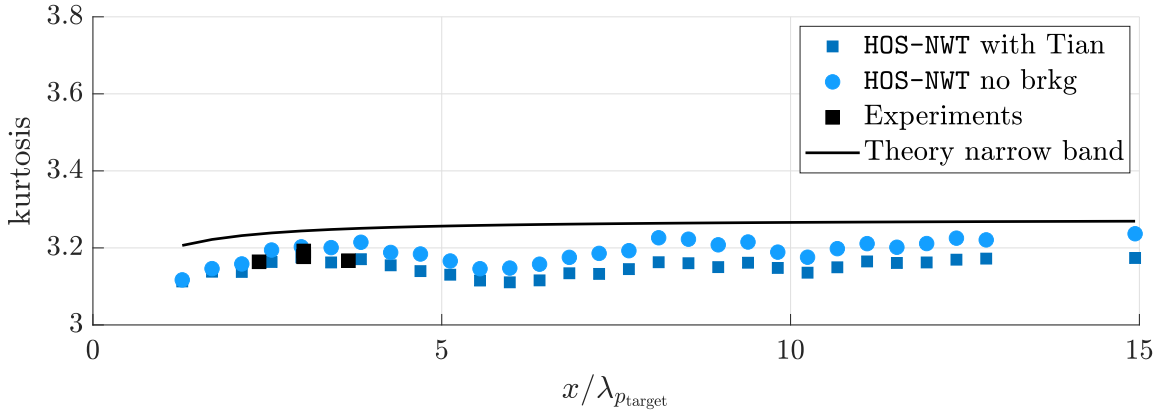

(d) Kurtosis along the tank

Figure 5.3 – Reproduction of `ss6` Campaign A experiments using `HOS-NWT`: stochastic analysis

However, even for this low BFI wave condition, the crest height distribution at $x = 3\lambda_{p_{\text{target}}}$ is more extreme than that predicted by Forristall (the reference used for ocean engineering studies). As will be discussed in more detail in the second part of this thesis, dedicated wave generation procedures are needed to better predict and control the statistics.

Observing the evolution of H_s and kurtosis along the domain, we can see that the two `HOS-NWT` setups start to differ from $x \approx 8\lambda_{p_{\text{target}}}$ for H_s and $x \approx 4\lambda_{p_{\text{target}}}$ for kurtosis. Tian's model slightly dissipates wave field energy and reduces the size of extreme events. This means that some events are interpreted as breaking by the model. However, during experimental tests, no breaking was observed. This raises the question of the accuracy of the predictions made by `HOS-NWT` with Tian setup at distances greater than $8\lambda_{p_{\text{target}}}$. However, for the significant wave height, the observed differences are negligible compared with the order of magnitude of the experimental uncertainties.

For this non-breaking case, 'HOS-NWT with Tian' setup is adapted to generate stochastic wave fields in a 'wave tank environment'. It is stable (no numerical instabilities) and accurately reproduces experiments.

5.2.2 Strongly-breaking sea state

In this subsection, we will assess the ability of the Tian-Barthelemy model to accurately generate and propagate breaking sea states. To this aim, experimental realizations of `GOM` will be compared to their numerical reproduction. Both deterministic and stochastic comparisons are provided.

a) Experiments

The experiments that were numerically reproduced consist of 27 realizations of `GOM` at scale 94 (that leads to $\lambda_{p_{\text{target}}} = 4$ m), run in the O.E. tank as part of Campaign F. Please refer to Appendix A to get the position of the probes, and to Sec. 1.2 to get the characteristics of `GOM` sea state.

Each realization lasted 20min. The total dataset features a T_{analyzed} larger than $17000T_{p_{\text{target}}}$.

b) Numerical setup

The experiments were reproduced numerically based on the setup described in Table 5.2. It is very similar to the 'HOS-NWT with Tian' setup used in Sec. 5.2.1 to simulate `ss6` sea state. The spatial discretization was decreased to $k_{\text{max}}^{\text{HOS}}/k_{p_{\text{target}}} = 15$ to prevent numerical

Table 5.2 – Numerical setups used for the reproduction of GOM Campaign F experiments

	HOS−NWT $15k_p$ with Tian
M	3
$k_{\max}^{\text{HOS}}/k_{p_{\text{target}}}$	15
Tolerance	10^{-4} s
Tian	Yes

instabilities (see the study presented in Sec. 5.1.2b). The generation scale is kept to 94, and the input random phases come from the experiment's input wave maker motion.

c) Results

Deterministic comparison Figure 5.4 compares time traces of free surface elevation over a time window of 100 $T_{p_{\text{target}}}$, at $x = 2\lambda_{p_{\text{target}}}$. Here again, the trend in the results is independent of the time window chosen. As in the non-breaking case (Sec. 5.2.1), the experimental and numerical waves align with each other. Indeed, the inputs are identical, and HOS−NWT accurately propagates the wave field.

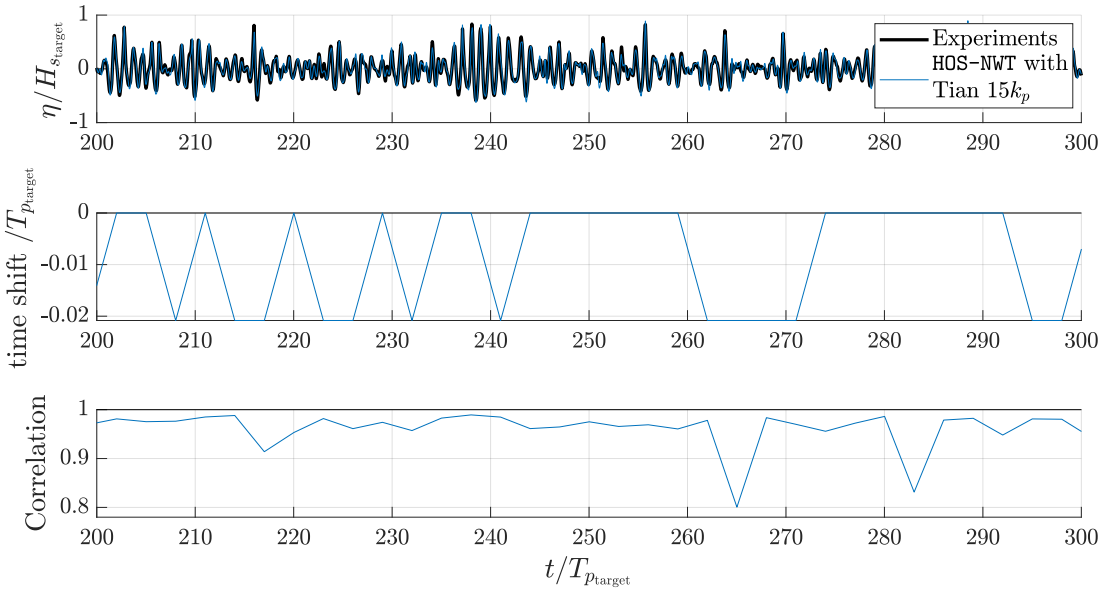

Figure 5.4 – Reproduction of GOM Campaign F experiments using HOS−NWT: Deterministic comparison at $x = 2\lambda_{p_{\text{target}}}$

Time shifts are negligible and the correlation ranges from 0.8 to 0.99. The numerical reproduction is slightly less accurate than for the non-breaking case (for which a correlation greater than 0.9 is observed). However, the correlation remains within the order of magnitude of what can be obtained by comparing two experimental repeatability tests. Experimental accuracy is therefore no greater than numerical accuracy.

Stochastic comparison Finally, Figure 5.5 presents the stochastic comparison between the experimental and numerical results. The comparison focuses on the position $x = 2\lambda_{p_{\text{target}}}$. This position will be used as a reference for several studies in the second part of this thesis.

In contrast to the non-breaking case, H_s decreases along the domain, from around $100\%H_{s_{\text{target}}}$ next to the wave maker to 95% at $x = 5\lambda_{p_{\text{target}}}$ (see Fig. 5.5c). Dissipation is due to breaking waves. This phenomenon is accurately reproduced by the '`HOS-NWT` $15k_p$ with Tian' model. The Tian model reproduces the dissipative effect of breaking.

The spectrum at $x = 2\lambda_{p_{\text{target}}}$ is also well generated by `HOS-NWT` (see Fig. 5.5a). It should be noted, however, that the experimental spectrum is affected by several spikes between $f = 1$ and $f = 1.5f_{p_{\text{target}}}$, which cannot be explained by experimental uncertainty. As with the non-breaking case studied in the previous section, several explanations are possible. The wave maker transfer function may slightly deviate from its theoretical behavior. And, transverse modes are present in the experimental wave field. In Figure 3.23c, Sec. b), we can see that for this configuration (`GOM` scale 94 in the Towing Tank), modes 12 to 26 are particularly excited. Their natural frequencies lie between $f = 0.8$ and $f = 1.4f_{p_{\text{target}}}$. This corresponds to the area affected by the spurious spikes in Figure 5.5a.

In addition, the evolution of the statistics is also reproduced by the '`HOS-NWT` with Tian $15k_p$' model. In Fig. 5.5d, for both numerical and experimental data, we observe a decrease in kurtosis between $x = 0.3\lambda_{p_{\text{target}}}$ and $x = 0.6\lambda_{p_{\text{target}}}$, and an increase for $x > 0.6\lambda_{p_{\text{target}}}$. Close to the wave maker, the decay can be explained by strong breaking, observed visually during the experimental runs, and inducing in Figure 5.5c a strong decay of H_s in the zone.

Close to the wave maker, the decay can be explained by strong breaking, which was visually observed during the experimental runs, and led to a significant reduction in H_s between $x = 0.3\lambda_{p_{\text{target}}}$ and $x = 0.6\lambda_{p_{\text{target}}}$ (in Figure 5.5c). `GOM` spectrum, generated at $x = 0\lambda_{p_{\text{target}}}$ is not stable and leads to breaking. At larger distances from the wave maker, the steepest events are already dissipated. Then, the number of breaking events decreases, the H_s is more stable and the kurtosis can increase.

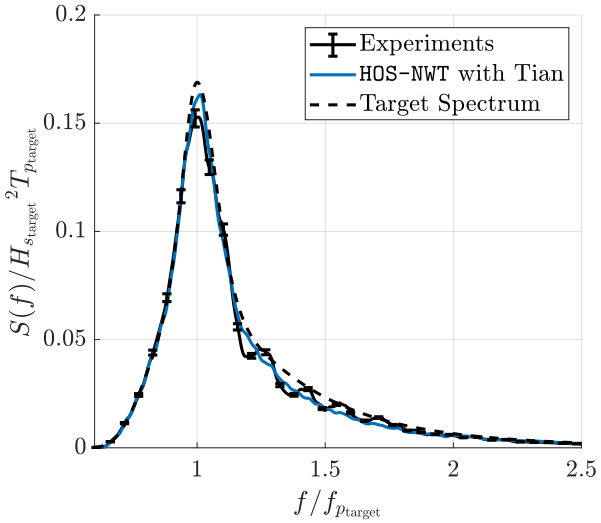

(a) Spectrum at $x = 2\lambda_{p_{\text{target}}}$

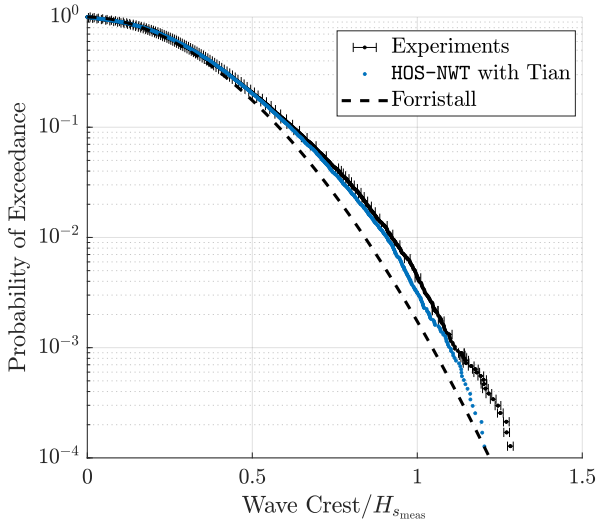

(b) Crest PDER at $x = 2\lambda_{p_{\text{target}}}$

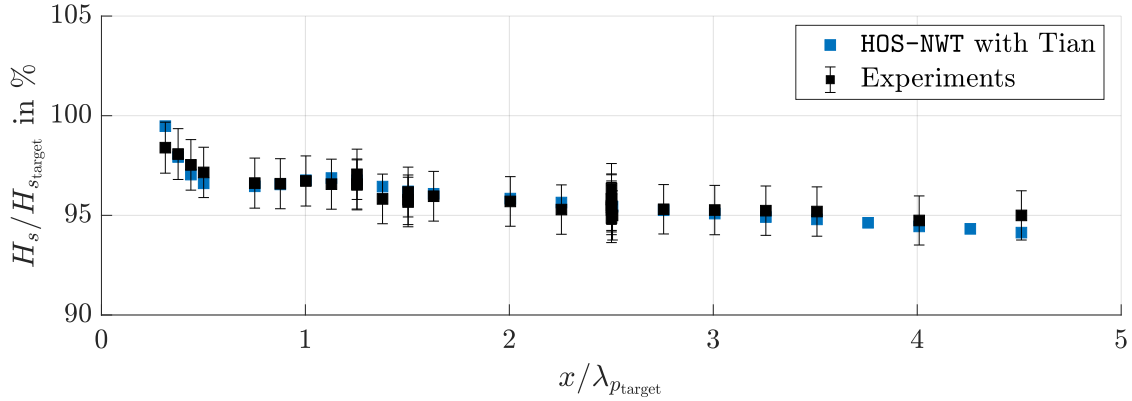

(c) H_s along the tank

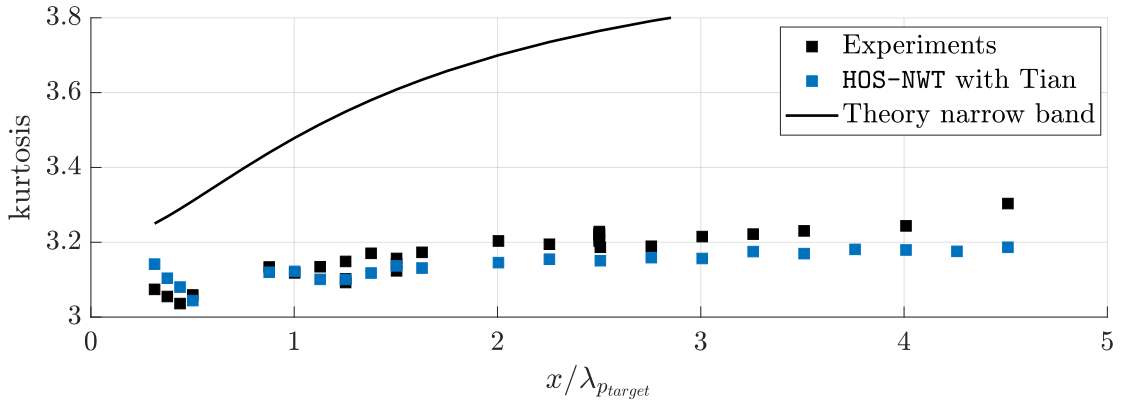

(d) Kurtosis along the tank

Figure 5.5 – Reproduction of GOM Campaign F experiments using HOS−NWT: stochastic analysis

It is also worth noting that when the flap wave maker generates the waves, evanescent modes are generated and localized in the area $x < \lambda_p$. These might help trigger the breaking events at the beginning of the domain.

Further out in the basin, the growth in kurtosis is due to the higher-order nonlinear interactions studied in Chapter 5. Indeed, the target `GOM` spectrum shape leads to a BFI value of 0.7, higher than the 0.5 BFI of `ss6` sea state. The phenomenon is therefore more pronounced than for `ss6` sea state. Here again, the theoretical evolution predicted by narrow-band theory is displayed. The predicted growth is extreme (kurtosis from 3.2 to 3.8 between $x = 0.2\lambda_{p_{\text{target}}}$ and $x = 3\lambda_{p_{\text{target}}}$). This is not observed in either the numerical or experimental results. This is because the theory does not take breaking into account. In the real world, the occurrence of extreme events is counterbalanced by breaking.

Breaking waves' effect is slightly overestimated by the '`HOS-NWT` with Tian $15k_p$' model. The kurtosis of `HOS-NWT` is slightly lower than that of the experimental data. This is reflected in the crest distribution tail at $x = 2\lambda_{p_{\text{target}}}$, displayed in Figure 5.5b. These differences cannot be explained by measurement uncertainty (the deviations are out of the uncertainty intervals in Fig. 5.5b), or by sampling variability (we are in the case of a semi-stochastic study, i.e. same set of random phases). However, the differences are only significant for probabilities below 10^{-3}, i.e. below the design probabilities used in ocean engineering studies (often limited to $P_{\text{design}} > 10^{-3}$).

The '`HOS-NWT` with Tian $15k_p$' model will therefore be used in this thesis to simulate strongly-breaking cases (`GOM` sea state).

5.3 Conclusion

We therefore have a '`HOS-NWT` with Tian' model that can simulate the propagation of non-breaking and strongly breaking sea states, without numerical instabilities (all realizations can be run without being stopped before ending). It should be noted that the spatial discretization must be slightly decreased for the strongly-breaking cases.

For the non-breaking case, `HOS-NWT` needs the Tian model to avoid numerical instabilities. However, this model has almost no effect on wave propagation. The evolution of statistical quantities is reproduced (kurtosis, crest distribution), although it should be noted that the probability of extreme events is slightly underestimated by the model.

For the breaking case, the model is accurate for the spectral quantities: breaking energy dissipation is well reproduced. The statistical nonlinear features are also well simulated (increase

in the kurtosis enhanced by nonlinear interactions but limited by breaking). However, the model slightly overestimates the effect of breaking for the most extreme events (the probability of extreme events is slightly underestimated). But the quality of the numerical results is sufficient for probabilities of occurrence greater than 10^{-3}.

'HOS−NWT with Tian' model will be used in the second part of the thesis to develop sea-state generation and qualification procedures for ocean engineering studies.

PART II

Improvement of irregular waves generation procedures for experimental and numerical wave tanks

---

In the first part of the thesis, tools and procedures have been introduced (Chapter 1). They allow for the generation and analysis of unidirectional irregular sea states in numerical and experimental wave tanks. The degree of accuracy that can be achieved has been assessed in detail, from an experimental point of view, with Chapter 3 dedicated to experimental uncertainties. Besides, Chapter 5 has introduced and validated `HOS-NWT` *models that can reproduce numerically the generation of non-breaking and breaking wave conditions. In addition, the phenomena involved in the propagation of sea states in basins have been studied (Chapter 2 and 4), providing keys to understanding and anticipating the evolution of the stochastic quantities of interest for ocean engineering studies (wave spectrum and crest distribution mainly).*

Based on the findings of the first part, this second part is now dedicated to the improvement of wave generation and qualification procedures in the context of ocean engineering studies. Specifically, we will focus on methods to better control the wave fields at any target position X_t in the domain. First, the existing methodologies used in the usual industrial ocean engineering studies will be presented and questioned (Chapter 6). Then, a procedure to generate a target design spectrum at any location of interest in the domain will be introduced and validated (Chapter 7). Its limitations will be accurately defined. Eventually, facing the strong dependence of the wave statistics on the target location X_t, a new procedure will be developed and tested to better control the statistical distributions independently of X_t.

CHAPTER 6

QUALIFICATION OF GENERATED SEA STATE FOR WAVE-STRUCTURE INTERACTION STUDIES

Wave tank experiments are often dedicated to wave-structure interaction studies that require specific wave conditions at a position of interest X_t (see ITTC (2021, 2017a); NWT Preparation Workgroup (2019)). As detailed in Introduction (page 25), different types of wave conditions exist (regular waves, design waves, and stochastic wave fields). The scope of this thesis is limited to stochastic wave fields. Several realizations are run, built from a design spectrum and random phases. The total duration is set to ensure the convergence of the statistical properties of the wave field at the design probability P_{design}. Refer to page 25 for more detailed explanations and Section 1.2.2 for the description of the standard wave generation procedure.

Wave-structure interaction studies are carried out either in experimental or numerical wave tanks. In the latter case, a dedicated nonlinear wave solver (for instance `HOS-NWT`) is used to model the wave propagation from the numerical wave maker to the position of interest X_t. These numerical waves are then used as input for a CFD solver that models the wave-structure interaction problem. See Introduction page 27 for more details.

For both experimental and numerical realizations, wave maker inputs are defined with input free surface elevation time-series at $x = 0$ specified in the Fourier space through a set of input harmonics (input spectrum S_{input} and associated phases ϕ_{input}, see Section 1.2.2). To consider the tests as relevant for the ocean engineering study, the generated waves at $x = 0$ must lead to a qualified design sea state at $x = X_t$. The qualification of a generated wave field varies from one study to another. The minimum requirement is usually the generation of a spectrum at X_t that matches S_{design}. Qualification criteria will be explored in detail in Sec 6.1.

The most basic generation procedure uses $S_{\text{input}} = S_{\text{design}}$ and uniformly distributed random phases (see Section 1.2.2). For nonlinear wave conditions (i. e. large-steepness and large-BFI sea states), this approach is not enough to generate S_{design} at X_t. It does not account

for the complex evolution of the nonlinear wave fields observed in Chapters 4 and 5. This thesis aims to explore and develop more complex generation procedures that allow for generating qualified sea states at any location X_t. Before tackling this issue, it is important to accurately define what a qualified sea state is.

Consequently, this short chapter provides the standard wave qualification requirements. They are introduced in Sec. 6.1 and questioned in Sect. 6.2, putting into perspective the ocean engineering needs and the experimental and numerical limitations explored in Chapters 3 and 5.

6.1 Existing criteria

Normalized procedures and established criteria accounting for nonlinear wave propagation and assessing the quality of generated sea states are still missing, especially in very harsh conditions.

ITTC guidelines The International Towing Tank Conference (ITTC) guidelines and procedures address the topic of wave qualification. ITTC (2021) report provides the outlines. It points out several quantities of interest that need to be qualified: the spectrum at X_t, the crest distribution at X_t and the groupiness factors at X_t. It advises to check the groupiness because the shape of the wave group affects the response of the structure. To qualify the crest distribution, ITTC guidelines recommend comparing it with Forristall (Forristall, 2000) and Huang (Huang and Zhang, 2018) references (see their definition in Sec. 2.2.4). In addition, it advises to calibrate the spectrum at X_t by iterating on the wave maker inputs. However, it does not provide accurate criteria for the spectrum, crest distribution, or groupiness.

JIP guidelines From a numerical point of view, the need for standardized wave input for CFD solvers is also grounded in a more general effort to normalize the entire CFD modeling process for offshore applications. This was the main objective of the Joint Industry Project (JIP) 'Reproducible CFD Modeling Practice for Offshore Applications' (see NWT Preparation Workgroup (2019); Fouques et al. (2021)). Within this frame, a set of wave qualification criteria was developed. It gathers the usual industrial practices at use, the recommendations of the classification societies (Det Norske Veritas, 2010), and ITTC guidelines. The resulting procedure can be extended for experimental studies. Here is a summary.

The strategy adopted focuses on the quality of the wave spectrum. The latter is first

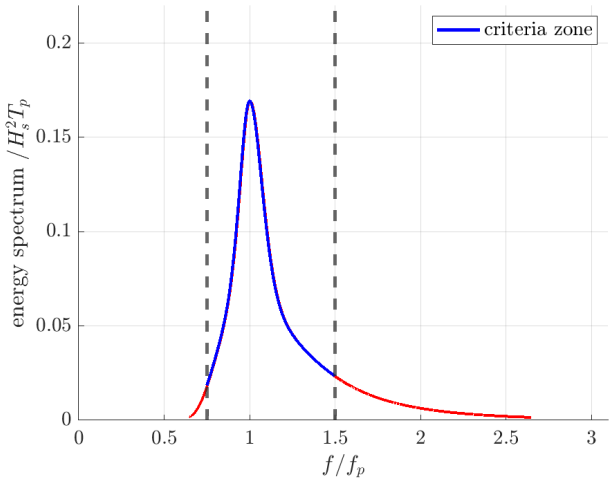

Figure 6.1 – Illustration of the spectrum qualification criteria.

generated and qualified at $x = X_t$. Then, zero-crossing wave statistics are compared with reference distributions. The spectrum to be qualified is the mean across the realizations, measured at $x = X_t$. It will be denoted as $S(f, X_t)$. Its quality is assessed through a criterion that concerns its difference from the design spectrum S_{design}, i. e. the relative spectrum error:

$$E_S(f) = (S(f, X_t) - S_{\text{design}}(f))/S_{\text{design}}(f) < C \tag{6.1}$$

The deviation must be within $C = 5\%$ for frequencies in the range $f \in \left[\frac{3}{4}f_p; \frac{3}{2}f_p\right]$. This frequency range covers the most energetic part of the spectrum. It has been arbitrarily chosen in the frame of the JIP. The criteria area is represented in Figure 6.1 between the 2 vertical dashed lines. The significant wave height is also used to qualify the wave field. Deviations below 2% are accepted.

Complementary, the crest height distributions are checked at the target location, relying on the Huang references (Huang and Zhang, 2018). The individual crest distributions (PDSR) should lie between the 99% lower and upper bounds of the Huang distribution while the PDER should agree with the Huang ensemble distribution within 5%. The spatial stability of the sea states is also evaluated close to the target location. In this region, the spatial variations in H_s, T_p, kurtosis, and skewness should be minimized.

6.2 Limitations of the criteria

The criteria listed above have some limitations. First, the spectrum qualification is arbitrary and can be too difficult to achieve, especially for experimental studies. Indeed, the qualification of a sea state at a target location is a fully stochastic analysis (see Sec. 3.2.2): one needs to account for the measurement uncertainty, the wave generation uncertainty (spurious transverse modes, Type A uncertainty), and the sampling variability. In Chapter 4, it has been shown that for a large dataset of 30 realizations the order of magnitude of the sampling variability around the spectrum peak (area of the criteria) reaches up to 5%. Moreover, the measurement uncertainty in the spectrum is approximately 3%. The combination of these uncertainties leads to errors larger than the criteria $C = 5\%$. Therefore, this value is only adapted for numerical studies (not affected by measurement uncertainty). $C \approx 10\%$ seems to be more adapted for experimental works.

Moreover, the $f \in \left[\frac{3}{4}f_p; \frac{3}{2}f_p\right]$ area of application is arbitrary. For example, the influence of spectrum tail is not taken into account. Specific analysis must be carried out to characterize the influence of the spectrum shape on the other quantities of interest (the crest distribution for instance). This topic will be addressed in Section 7.4.

One should also note that for numerical studies the wave qualification criteria must be accompanied by convergence studies to ensure the quality of the numerical solution.

In addition, the comparison to the Huang references can be questioned. As seen in the sections 2.2.4 and 4.2, the Huang distribution is not relevant when analyzing unidirectional wave fields measured at a large distance from the wave maker. Indeed, it was built assuming spatial ergodicity and does not take into account the kurtosis growth along the tank studied in Chapter 4. Spatial-dependent (or kurtosis-dependent) distributions such as the NBGC references (Tayfun and Fedele, 2007) (see Sec. 2.2.4) should be included in the criteria.

More generally the qualification process assumes the use of a wave generation procedure only focusing on the control of the spectrum at X_t. But is it enough to control or even predict the wave field statistics (crest distribution and kurtosis)? As a reminder, these quantities are of great importance, they are directly linked to the probability of extreme events, which can be critical when addressing wave-structure interaction problems.

In the Chapter 7, the strategy of the JIP guidelines will be adopted. A wave generation procedure will be implemented to control the spectrum at X_t and the crest distributions will be compared to references. The limitations will be clearly shown and the criteria will be adapted. Eventually, in Chapter 8, a new procedure allowing to better control the wave statistics will be

introduced.

CHAPTER 7

CONTROL OF THE WAVE ENERGY SPECTRUM

As detailed in the previous chapter, when generating large-duration wave fields in a wave tank environment for ocean engineering purposes, the usual wave qualification criteria focus on the quality of the measured wave spectrum at a target position X_t (referred to as $S(f,X_t)$). In this context, this chapter introduces and tests a wave generation procedure allowing to correct iteratively $S(f,X_t)$ to match the target design spectrum S_{design}. The efficiency and the limitations of the process will be explored, for both numerical and experimental configurations.

7.1 Presentation of the procedure

As detailed in Sec. 1.2.2, for each realization, the wave maker input is built in the Fourier space as a list of input harmonics amplitudes $A_{\text{input}}(f)$ and phases $\phi_{\text{input}}(f)$, that correspond to the linear decomposition of the targeted free surface elevation at $x = 0$. Then, to generate a design spectrum S_{design}, the most natural approach consists of using $A_{\text{input}}(f) = A_{\text{design}}(f)$ and random phases. However, as observed in the first part of this manuscript, this is usually not enough to observe the design spectrum at $x = X_t$. Indeed, the implemented wave maker transfer function might slightly differ from the actual behavior of the tank, which leads to deviations in the generated wave field harmonics at $x = 0$. And, nonlinear wave interactions and dissipation mechanisms cause the spectrum to evolve along the tank.

To control $S(f,X_t)$, a more accurate generation procedure must be used. ITTC (2021) and NWT Preparation Workgroup (2019) guidelines recommend iterative correction of wave generator inputs. The method is summarized in Figure 7.1. First series of runs (i.e. series of realizations varying the random phase input) are generated using $A^0_{\text{input}}(f) = A_{\text{design}}(f)$ (iteration 0). The iteration number is denoted with an upper script on the different quantities. Next, at $x = X_t$, the measured spectrum $S^0(f,X_t)$ smoothed and averaged over the realizations is used to compute the Fourier amplitudes $A^0(f,X_t)$. From theses amplitudes, a correction factor is

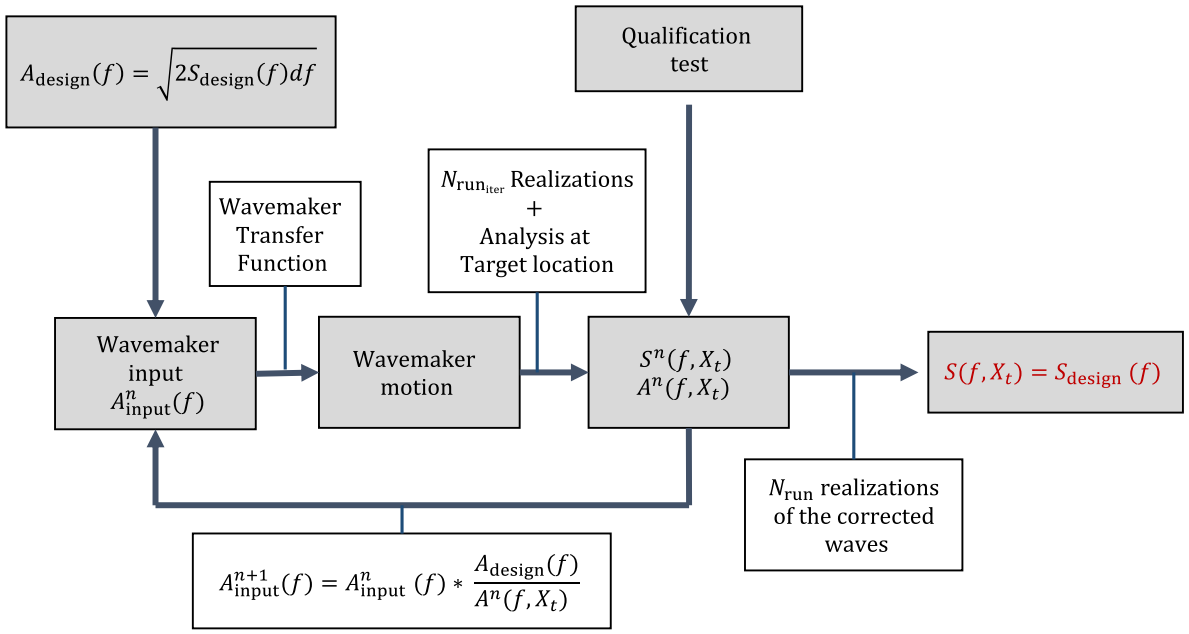

Figure 7.1 – Iterative procedure for the accurate generation of a design spectrum at a location of interest

derived and applied to build a new set of input amplitudes $A^1_{\text{input}}(f) = A^0_{\text{input}}(f)A_{\text{design}}/A^0(f,X_t)$ (iteration 1). The process is repeated iteratively until $S(f,X_t)$ lies on S_{design}. The qualification of $S(f,X_t)$ relies on the criterion described in the Chapter 6, i. e. the relative error $E_S(f) = (S_{\text{design}}(f) - S(f,X_t))/S_{\text{design}}(f)$ over the most energetic frequencies, $f \in [0.75f_{p_{\text{target}}}, 1.25f_{p_{\text{target}}}]$ (even if the spectrum is corrected over the entire frequency range covered by the wave maker).

Each iteration consists of $N_{\text{run}_{\text{iter}}}$ realizations, $N_{\text{run}_{\text{iter}}}$ being carefully chosen to ensure the statistical convergence of the wave spectrum. Once the spectrum is qualified, $N_{\text{run}} > N_{\text{run}_{\text{iter}}}$ realizations are generated to ensure the convergence of the crest PDER until the probability P_{design}.

This procedure can be used for numerical and experimental domains. Both frameworks will be tested. Moreover, we will also investigate the relevance of hybrid approaches (numerical correction using `HOS-NWT`, before experimental generation). Note that some of the results presented in this chapter have already been published in Canard et al. (2020, 2022a,b). Furthermore, the procedure has been numerically tested by several academic and industrial actors of the "JIP on reproducible CFD practices". The results are compared in Fouques et al. (2021).

7.2 Experimental and numerical validation

7.2.1 Mild conditions

Numerical correction of `ss6` sea state at $X_t = 3\lambda_{p_{\text{target}}}$ First, the procedure was tested to generate numerically `ss6` sea state at $X_t = 3\lambda_{p_{\text{target}}}$, with `HOS-NWT`. This corresponds to the mild case of the "JIP on reproducible CFD practices". The generation scale is 100 and the geometry of the numerical wave maker mimics the one of the O.E. tank. The adopted spatial discretization corresponds to $k_{\text{max}}^{\text{HOS}} = 25k_{p_{\text{target}}}$ and the Tian-Barthelemy breaking model is implemented. As the sea state is not breaking, only one or two numerical breaking events per realization occurred. They correspond to physical steep waves that may cause numerical instability without the model. The set up corresponds to the '`HOS-NWT` with Tian' model, introduced in Section 5.2.1.

Figure 7.2 presents iteration 0 (no correction) and iteration 1. $N_{\text{run}_{\text{iter}}} = 16$ was adopted and for each run a duration of $860T_{p_{\text{target}}}$ was analyzed, which means that each iteration includes 13700 waves at peak period (see Section 1.3.3 for the corresponding sampling variability estimate). The iteration 0 spectrum already lies approximately on the design (i. e. target) spectrum. Indeed, as the generation is numerical, the wave maker transfer function is exactly known and there are no measurement errors. Therefore, only nonlinear wave interactions can affects the spectrum shape at $x = X_t$. However, `ss6` has a low steepness and is broad. It is consequently a low-BFI sea state, indicating that few high-order nonlinear effects occur.

In Fig. 7.2c we observe small deviations out of the criteria limit $C = 5\%$ around $f = 1.4f_{p_{\text{target}}}$ and $f = 1.6f_{p_{\text{target}}}$ to $1.7f_{p_{\text{target}}}$. Even if these frequencies are beyond the range of the criteria application, corrective coefficients were computed and applied. They are plotted in Fig. 7.2b. After correction, the small deviations from the target shape decrease (Fig. 7.2d).

We can conclude that for the numerical generation of a mild sea state, without dissipation, the spectrum correction is almost unnecessary, and only one iteration is sufficient to achieve accuracy over a wide frequency range.

Note that the use of a $C = \pm 5\%$ criteria is questioned by the sampling variability intervals (Welch intervals) that also cover a $\pm 5\%$ range (even with a total analysis duration of $T_{\text{analyzed}} = 13700T_{p_{\text{target}}}$). A larger criteria limit may be considered to include the Welch intervals. Indeed, not being statistically converged means that small changes in the data sample (different number of realizations, different analysis time windows) can lead to significant deviations (quantified by the confidence intervals). Adding a $\pm 10\%$ limit to account for sampling variability might be relevant.

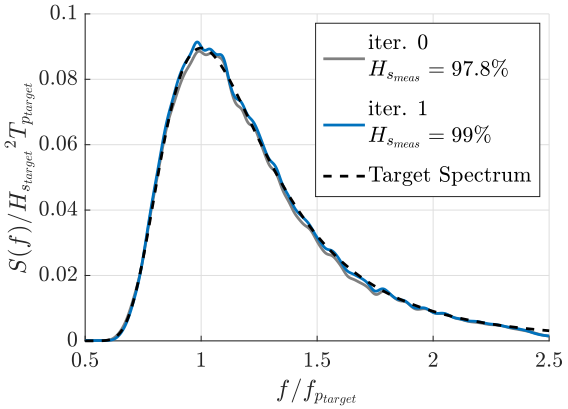

(a) spectrum at $X_t = 3\lambda_{p_{\text{target}}}$

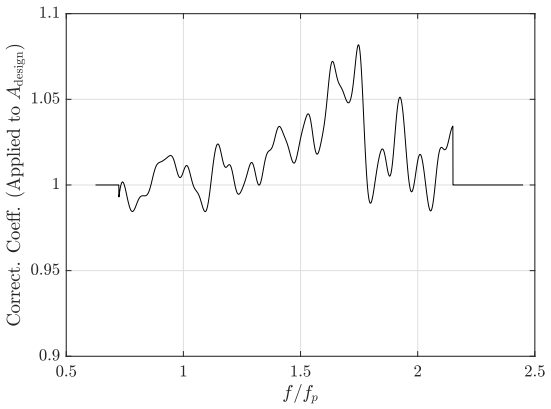

(b) Corrective coefficient from iter. 0

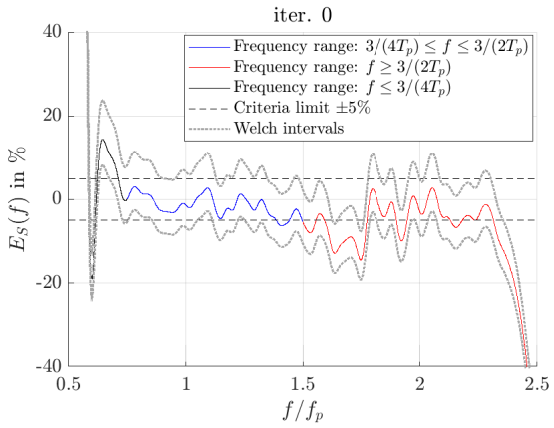

(c) Qualification of iter. 0 spectrum

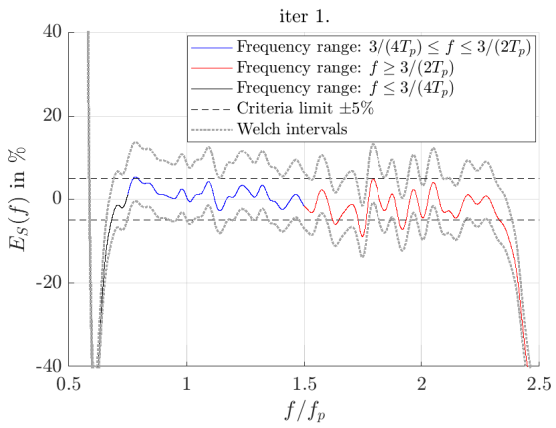

(d) Qualification of iter. 1 spectrum

Figure 7.2 – Correction of `ss6` sea state at $X_t = 3\lambda_{p_{\text{target}}}$, numerical generation with `HOS-NWT` (16 realizations i. e. of duration $860T_{p_{\text{target}}}$ 13700 waves at peak period).

Experimental reproduction of the corrected `HOS-NWT` realizations Then, the wave maker inputs of iteration 1 were experimentally generated in the O.E. tank at scale 40 within the frame of campaign B (see Appendix A). The experimental data, labeled "HOS iter.1 experiment", consists of 35 realizations of $580T_{p_{\text{target}}}$ i. e. $T_{\text{analyzed}} = 20,300T_{p_{\text{target}}}$. In Figure 7.3 these data are compared to the same 35 realizations of iteration 1 (i. e. same wave maker inputs) generated numerically with `HOS-NWT` (labeled "HOS iter.1 HOS"). The same analysis time window was adopted for both datasets so that the same events are analyzed. This means that the sampling variability can not explain the differences between numerical and experimental results.

The experimental spectrum slightly deviates from the HOS-qualified spectrum (Fig.

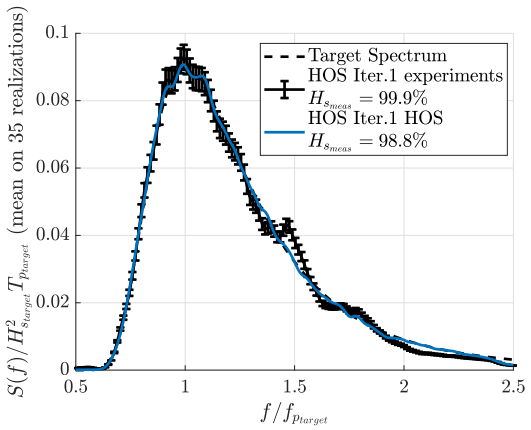

(a) spectrum at $X_t = 3\lambda_{p_{\text{target}}}$

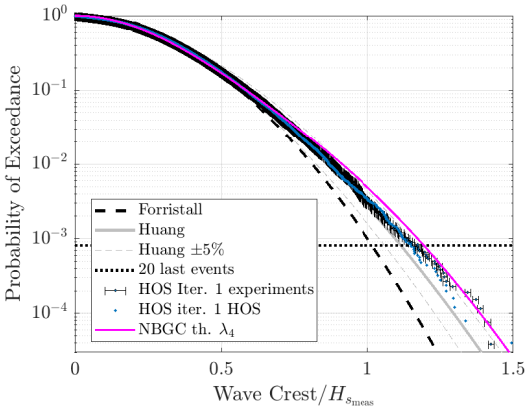

(b) Crest PDER at X_t

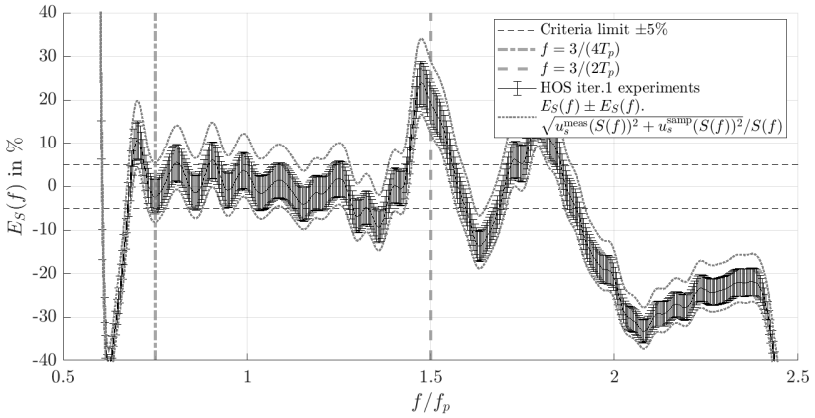

(c) Qualification of the experiments spectrum at X_t

Figure 7.3 – Correction of `ss6` sea state at $X_t = 3\lambda_{p_{\text{target}}}$, experimental reproduction based on the `HOS-NWT` correction (35 realizations of duration $580T_{p_{\text{target}}}$ i. e. $T_{\text{analyzed}} = 20,300T_{p_{\text{target}}}$), Campaign B - the error bars correspond to the measurement uncertainty u_s^{meas}

7.3a), even considering the measurement uncertainties. The difference is likely to be due to the O.E. tank wave maker transfer function that slightly deviates from its theoretical implementation. Also, note that the spectrum overshoot around $f = 1.5f_{p_{\text{target}}}$ may be the result of transverse spurious modes. Indeed, the noise analysis after the run for `ss6` scale 40 in the O.E. tank showed remaining transverse waves energy around $f = 1.5f_{p_{\text{target}}}$ (which corresponds to the mode 24), see Fig. 3.23b (Sec. 3.4.2b).

As a consequence, the experimental spectrum does not entirely satisfy the $C = \pm 5\%$ criteria limit (Fig. 7.3c). Thresholds of $C = \pm 10\%$ and $\pm 15\%$ seem more adapted to include respectively measurement uncertainty only and measurement uncertainty with sampling variability

(modeled by the Welch intervals).

Relevant values of C are therefore larger for experimental studies than for numerical studies. One may wonder whether this loss of accuracy has significant consequences for the quality of the wave fields or not. And in case of a wave-structure interaction test, one may ask whether it has a significant effect on the structure response or not. A comprehensive answer would require a dedicated study. However, what is sure is that it depends whether the spectrum changes within these large C values significantly affect the wave statistics. This specific question will be addressed in Section 7.4. As a first answer, in Fig. 7.3b, comparing the crest PDER for "HOS iter.1 experiments" and "HOS iter.1 HOS", we observe no differences between the distributions, even if the spectra are slightly different.

For this location relatively close to the wave maker, the Huang distribution seems to fit well the data. The Forristall reference underestimates the probability of extreme events, which means that high-order nonlinear effects affect wave propagation. However, their theoretical influence, modeled by the NBGC curve, is slightly overestimated. This was also the case for `ss6g5` sea state measured at a similar distance from the wave maker in the Towing tank (see Sec. 4.2). We also need to keep in mind that the NBGC model assumes a narrow-band spectrum, which is not the case for `ss6`.

7.2.2 Severe breaking conditions

In the previous subsection, we analyzed the efficiency of the spectrum correction procedure for `ss6` sea state. It corresponded to mild wave conditions, free from breaking events. We will now test the procedure for `GOM` sea state. Its peak steepness $\varepsilon_p = H_s/\lambda_p$ equals 4.5%. Strong and numerous breaking events are expected, meaning that the spectrum and the crest distribution are likely to be significantly altered at X_t.

a) Correction of the spectrum using `HOS-NWT` and reproduction in the O.E. tank

`HOS-NWT` iterations and reproduction of 10 corrected realizations in the O.E. tank First, the procedure was used to generate numerically `GOM` spectrum at $X_t = 1.9\lambda_{p_{\text{target}}}$, at a scale 100. This corresponds to the extreme case of the "JIP on Reproducible CFD practices". The adopted `HOS-NWT` setup is the "`HOS-NWT` with Tian $15k_p$" model introduced in Sec. 5.2.2. The spatial discretization is set to $k_{\text{max}}^{\text{HOS}} = 15k_{p_{\text{target}}}$ and breaking is taken into account by the Tian-Barthelemy model. The geometry of the numerical tank reproduces the O.E. tank. The number of realizations per iteration was fixed to $N_{\text{run}_{\text{iter}}} = 10$ and for each run the analysis

duration was set to $530T_{p_{\text{target}}}$. Within this frame, four iterations were needed to calibrate the spectrum at X_t. After these steps, 10 realizations of Iteration 4 were generated experimentally at a scale 50 in the O.E. tank. Figure 7.4 presents the results. As same sets of random phases and analysis time windows were adopted for "HOS iter.0 HOS", "HOS iter.4 HOS" and "HOS iter.4 experiments", the sampling variability does not affect the comparison.

In contrast to the case of `ss6` sea state, the spectrum at Iteration 0 (no correction) differs from the target shape (Fig. 7.4b and grey curve in Fig. 7.4a). Between $x = 0$ and $x = X_t = 1.9\lambda_{p_{\text{target}}}$ the Tian-Barthelemy breaking model dissipates the wave field energy, and especially the frequencies larger than $0.8f_{p_{\text{target}}}$. After four iterations of the correction process, the lack of energy is counterbalanced by the calibrated input spectrum and at $x = X_t$ the spectrum is qualified (the relative error being almost within the $\pm 5\%$ criteria limit), see Fig. 7.4c and Fig. 7.4a blue curve. As for the `ss6` study provided in the previous subsection, the experimental reproduction of the qualified numerical spectrum decreases the quality of $S(f, X_t)$. "HOS iter.4 experiments" spectrum is slightly more energetic than its numerical twin. This can be explained either by wave maker transfer function uncertainties or by a too-strong dissipation of the Tian-Barthelemy breaking model. However, the experimental spectrum error is still limited to $\pm 10\%$, including the wave gauge uncertainties. An experimental iterative correction of this spectrum will be presented in the next paragraph.

The procedure is validated for this extreme breaking sea state, at a target location relatively close to the wave maker. Also note that, as for `ss6` spectrum generation, the criteria limit $\pm 5\%$ does not account for both the sampling variability and the measurement uncertainties.

Correction of the experimental wave field and comparison with the numerical corrected wave field After the numerical correction of the spectrum at X_t, 35 realizations of "HOS iter.4 HOS" were run numerically. Moreover, the experimental wave field "HOS iter.4 experiments" was calibrated experimentally (two iterations in the O.E. tank) to correct the spectrum at $X_t = 1.9\lambda_{p_{\text{target}}}$. Then, 35 realizations of the resulting wave field, referred to as "HOS iter.4 exp. iter 2 exp.", were generated. Figure 7.5 compares those two numerical and experimental corrected sets of realizations. Note that the random phase seeds differ between "HOS iter.4 HOS" and "HOS iter.4 exp. iter 2 exp.". This means that the sampling variability can affect the comparison.

Fig. 7.5a and 7.4c present the qualification of the same wave field "HOS iter.4 HOS". The only difference is the number of realizations. $T_{\text{analyzed}} = 18375T_{p_{\text{target}}}$ in Fig. 7.5a and $T_{\text{analyzed}} = 5300T_{p_{\text{target}}}$ in Fig. 7.4c. Increasing database size reduces sampling variability confidence intervals: they are smaller in Fig. 7.5a. With this large T_{analyzed} value, the intervals remain within

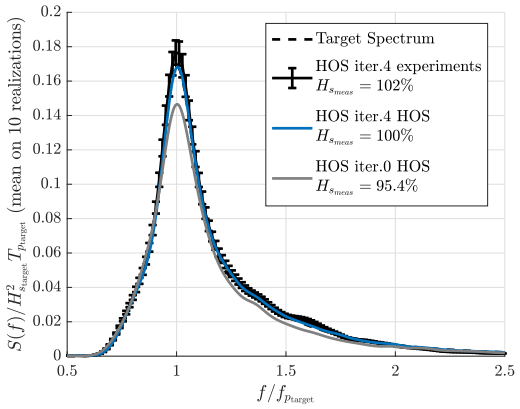

(a) spectrum at $X_t = 1.9\lambda_{p_{\text{target}}}$

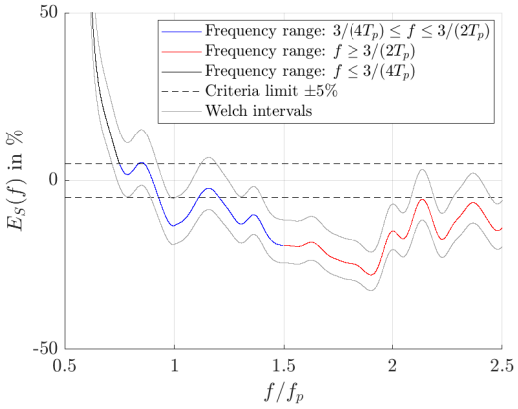

(b) Qualification of iter. 0 spectrum HOS

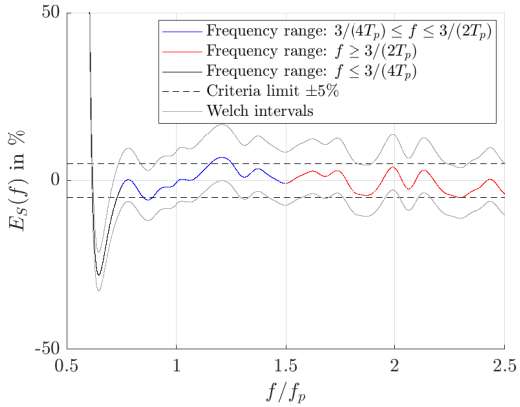

(c) Qualification of iter. 4 spectrum HOS

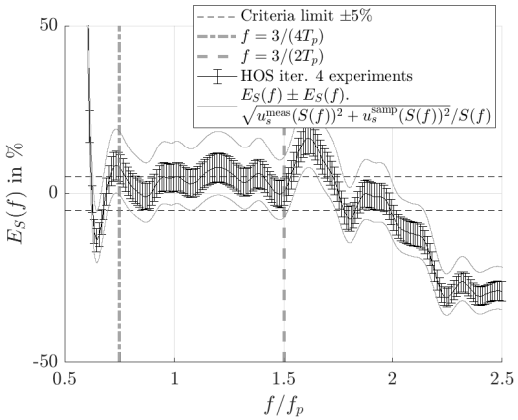

(d) Qualification of iter. 4 spectrum Experiments

Figure 7.4 – Correction of GOM sea state at $X_t = 1.9\lambda_{p_{\text{target}}}$, numerical generation with HOS−NWT (10 realizations of duration $530T_{p_{\text{target}}}$ i. e. 5300 waves at peak period), and experimental generation in the O.E. tank (Campaign B.) - the error bars correspond to the measurement uncertainty u_s^{meas}

the ±5% criteria limit.

After two iterations, the experimental reproduction of the numerical reference is almost qualified. "HOS iter.4 exp. iter 2 exp." spectrum (Fig. 7.5b) better matches the target shape than "HOS iter.4 exp." (Fig. 7.4d). The crest distribution is similar to the distribution of "HOS iter.4 HOS". For these strongly-breaking wave fields, the Forristall distribution seems to be the most relevant reference. Huang overestimates the probability of extreme events, and the NBGC theoretical distribution is unrealistic. NBGC model's behavior is explained by the large BFI value of GOM sea state (see Sec. 1.2) coming from its large steepness. The kurtosis-prediction

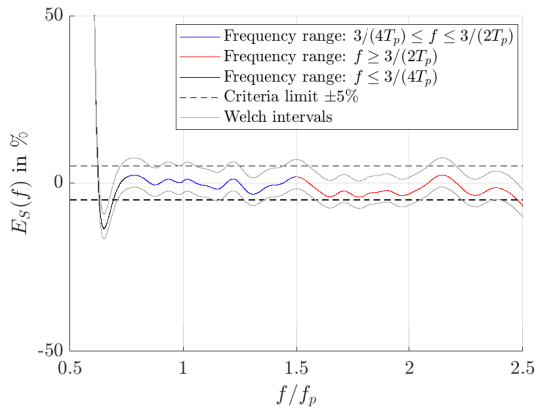

(a) Qualification of iter. 4 spectrum HOS

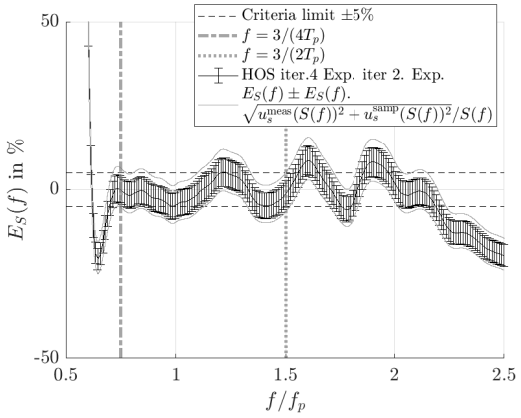

(b) Qualification of HOS iter. 4 exp. iter 2 spectrum exp.

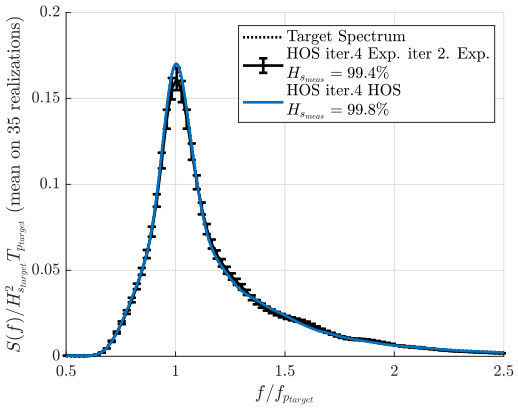

(c) spectrum at $X_t = 1.9\lambda_{p_{\text{target}}}$

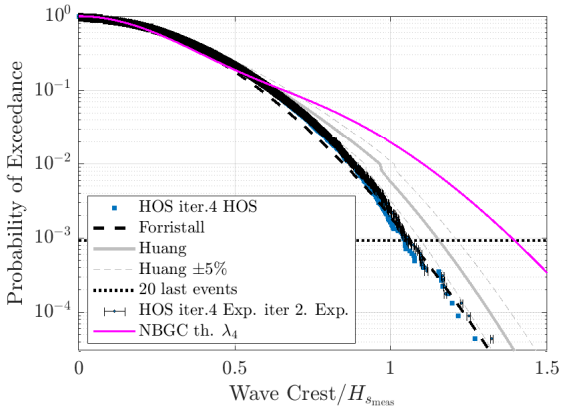

(d) Crest PDER at $X_t = 1.9\lambda_{p_{\text{target}}}$

Figure 7.5 – Calibrated GOM sea state at $X_t = 1.9\lambda_{p_{\text{target}}}$, numerical correction with HOS−NWT before experimental correction (35 realizations of duration $525T_{p_{\text{target}}}$ i. e. 18375 waves at peak period), Campaign B - the error bars correspond to the measurement uncertainty u_s^{meas}

theory which is the core of the "NBGC th. λ_4" model does not account for breaking and is therefore unrealistic for breaking sea states. Indeed, breaking events dissipate the extreme events that would have resulted from the Benjamin Feir instabilities predicted by the "NBGC th. λ_4" model.

b) Full experimental process

The spectrum correction procedure was also experimentally tested by iterating from scratch (without prior numerical calibration). These experiments were performed in the Towing

tank within the frame of Campaign D (see Appendix A). The target spectrum was GOM at scale 188 ($\lambda_{p_{\text{target}}} = 2$ m) and the target location was $X_t = 2\lambda_{p_{\text{target}}}$. The four first iterations (iterations 0 to 3) are presented in Fig. 7.6. A total duration of $2950T_{p_{\text{target}}}$ is analyzed for each iteration. For the sake of clarity, the wave gauge uncertainty ranges and the sampling variability intervals are not plotted. Estimations of the latter can be found in the section 1.3.3.

At iteration 0, the spectrum at $x = 2\lambda_{p_{\text{target}}}$ has missing energy in the area $f > 1.4f_{p_{\text{target}}}$, but its peak is almost not affected by breaking. In the previous subsection, HOS−NWT iteration 0 was a bit less energetic. The differences can be explained either by the Towing tank wave maker transfer function uncertainties or by a too-strong dissipation of the Tian-Barthelemy breaking model.

The relative error of the iteration-0 spectrum (generated in the Towing tank) is beyond the $\pm 5\%$ limit but it does not exceed $\pm 10\%$, within the criteria-application frequency domain. The iterations mainly improve the spectrum tail i. e. frequencies between $f = 1.5f_{p_{\text{target}}}$ and $2f_{p_{\text{target}}}$.

Therefore, for this extreme sea state, the fully-experimental procedure is also validated. However, it can not avoid some $\pm 10\%$ residual errors. The number of experimental iterations needed for a similar spectrum quality remains the same whether calibrating the input prior experiments with HOS−NWT or starting from scratch: 2 or 3 iterations (plus iteration 0).

c) Limitations for target locations larger than $5\lambda_{p_{\text{target}}}$

Within the frame of Campaigns C, the procedure was tested to calibrate GOM spectrum at $X_t = 6.6\lambda_{p_{\text{target}}}$. The experiments were performed at a scale of 94. Iterations 0 to 3 were generated. Figure 7.7 provides the results. Iteration 0 includes 4 realizations of duration $600T_{p_{\text{target}}}$, and Iteration 3 gathers 27 realizations of duration $520T_{p_{\text{target}}}$. For the sake of clarity, measurement uncertainty and sampling variability ranges have not been included in the plots. Please refer to Sec. 1.3.3 and the first figures of the present section to obtain an order of magnitude for the ranges.

Fig. 7.7c presents the evolution of the spectrum without any correction (Iteration 0). As for the Towing tank experiments provided in Fig. 7.6, the dissipation induced by the breaking events mainly affects the frequencies larger than $f = 1.4f_{p_{\text{target}}}$. However, the spectrum at X_t (blue curve Fig. 7.7c) is not qualified (see Fig. 7.7b black curve). Energy overshoots larger than 30% are observed around the peak frequency. These are likely to be the results of the combined effects of wave maker transfer function uncertainties and spurious transverse modes (the deviations are too strong to be only due to wave gauge errors (limited to 4% for the

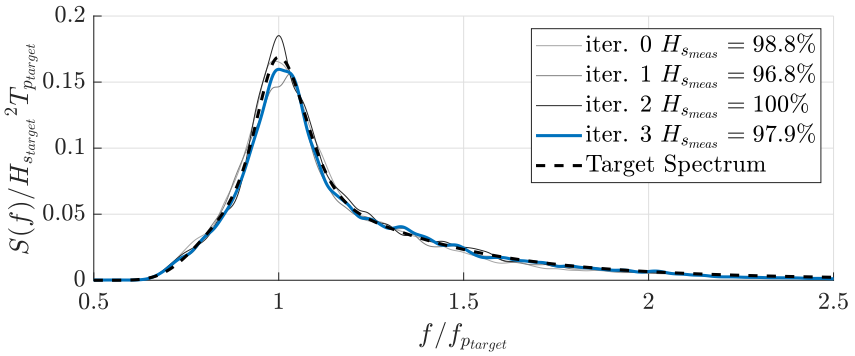

(a) spectrum at $X_t = 2\lambda_{p_{\text{target}}}$

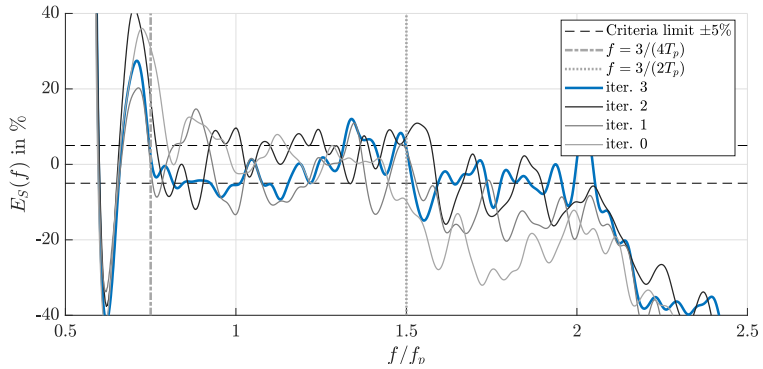

(b) Qualification at $X_t = 2\lambda_{p_{\text{target}}}$

Figure 7.6 – Correction of GOM sea state scale 188 at $X_t = 2\lambda_{p_{\text{target}}}$, Towing tank Campaign D; 5 realizations of $590T_{p_{\text{target}}}$ per iterations

spectrum) or sampling variability ($E_{\text{Welch}}(f_p) \approx 15\%$ for $T_{\text{analyzed}} = 2400T_{p_{\text{target}}}$)). Note that the noise analysis after the run for GOM scale 94 in the O.E. tank showed remaining transverse waves energy between $f = f_{p_{\text{target}}}$ and $f = 1.5f_{p_{\text{target}}}$ (which corresponds to the modes 14 to 26), see Fig. 3.23b Sec. 3.4.2b).

Therefore, the spectrum correction procedure was used to correct the spectrum at $X_t = 6.6\lambda_{p_{\text{target}}}$. Fig 7.7a presents the corrective coefficients applied to the inputs of Iteration 3. The factors are impressively large between $1.5f_{p_{\text{target}}}$ and $2f_{p_{\text{target}}}$. They aim to balance breaking dissipation. Iteration 3 spectra along the tank are provided in Figure 7.7d. The spectrum shape evolution is complex. Missing energy around $f = 1.3f_{p_{\text{target}}}$ at the beginning of the tank is progressively recovered while frequencies larger than $1.5f_{p_{\text{target}}}$ dissipate. This shows the presence of complex energy cascades. Even if the resulting spectrum partially matches the target shape, it is far from being qualified, even if we extend the criteria limit to $\pm 10\%$ (see Fig. 7.7b blue curve). No clear improvements are observed when compared to Iteration 0. For strongly-breaking

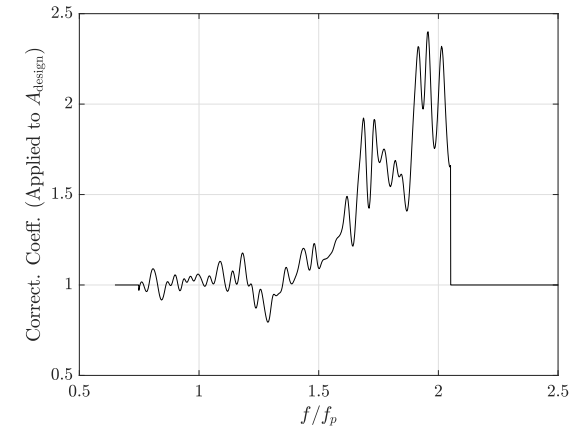

(a) Corrective coefficient applied for iter. 3

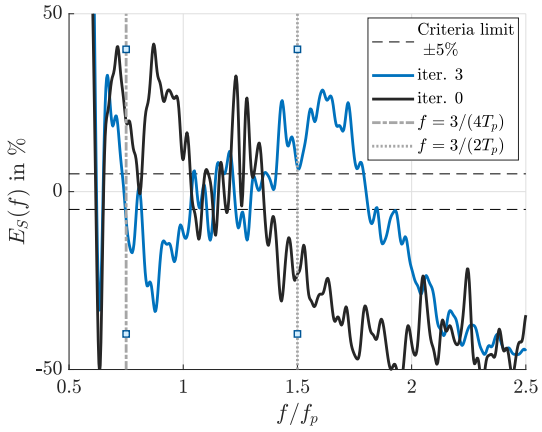

(b) Qualification at $X_t = 6.6\lambda_{p_{\text{target}}}$

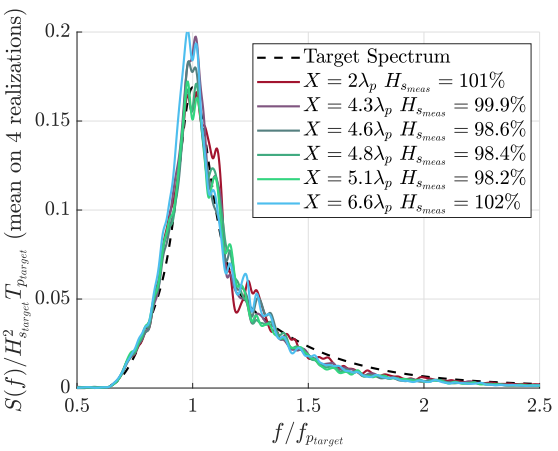

(c) Iter. 0 spectrum along the tank

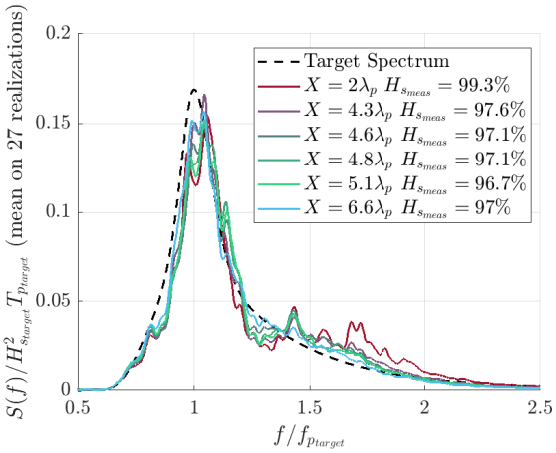

(d) Iter. 4 spectrum along the tank

Figure 7.7 – Calibration of GOM sea state scale 94 at $X_t = 6.6\lambda_{p_{\text{target}}}$, iteration 0 compared to iteration 3 - O.E. experimental results

sea states like GOM, the correction procedure can not correct the spectrum at distances larger than $5\lambda_{p_{\text{target}}}$ from the wave maker.

7.3 Influence of the distance from the wavemaker

In the previous section, the analysis was limited to positions relatively close to the wave maker ($X_t < 7\lambda_{p_{\text{target}}}$). Within this area the spectrum correction procedure was validated (except for breaking sea state targeted at $X_t > 5\lambda_{p_{\text{target}}}$) and the ensemble crest distribution of the

qualified waves matched either the Forristall or the Huang reference. However, as observed in Chapter 4, statistical features of non-breaking sea states are dependent on the distance from the wave maker. Indeed, for unidirectional wave fields, the probability of extreme events increases along the tank, due to the development of modulational instabilities. Thus, in Chapter 4, analyzing the evolution of `ss6g5` sea state at scale 120 in the Towing tank, we observed that the crest distribution strongly differs between $x = 2\lambda_{p_{\text{target}}}$ and $x = 53\lambda_{p_{\text{target}}}$. Especially, at $x = 53\lambda_{p_{\text{target}}}$ the distribution is extreme and is not captured by Huang and Forristall references (see Figure 4.8). In the latter study, the spectrum correction procedure was used to generate `ss6g5` target shape at $X_t = 53\lambda_{p_{\text{target}}}$. The spectrum was not qualified at $x = 2\lambda_{p_{\text{target}}}$, and one can still argue that the different statistical behaviors between $x = 2\lambda_{p_{\text{target}}}$ and $x = 53\lambda_{p_{\text{target}}}$ may result from the differences in the spectrum shape. To isolate the influence of the distance from the wave maker from the influence of the spectrum shape, this section compares wave fields that have the same qualified spectrum but are generated at significantly different target positions X_t. The study still focuses on `ss6g5` sea state at scale 120 generated in the Towing tank. The results were published in Canard et al. (2022b).

7.3.1 Generation of `ss6g5` sea state at 3 target postions

Experimental setup and wave conditions The study gathers results from Campaigns A and D. First, `ss6g5` sea state at scale 120 was generated in the Towing tank without spectrum correction (10 realizations of $\Delta T = 605T_{p_{\text{target}}}$). Then, using the iterative correction procedure, a qualified spectrum was consecutively generated at $X_t = 4\lambda_{p_{\text{target}}}$ (3 iterations including iteration 0), $X_t = 16\lambda_{p_{\text{target}}}$ (4 iterations including iteration 0), and $X_t = 53\lambda_{p_{\text{target}}}$ (5 iterations including iteration 0). The C quality threshold was set to 10%. This means that at the location of interest, the target spectrum was measured within an accuracy range of $C = 10\%$. The final iteration consisted of 25 realizations of $605T_{p_{\text{target}}}$ for the $X_t = 4\lambda_{p_{\text{target}}}$ series, 35 realizations of $605T_{p_{\text{target}}}$ for the $X_t = 16\lambda_{p_{\text{target}}}$ series, and 30 realizations of $390T_{p_{\text{target}}}$ for the $X_t = 53\lambda_{p_{\text{target}}}$ series. From now on, the term "converged series" will refer to a set of realizations generated with the corrective procedure. Each converged series is then associated with a target location X_t.

Significant wave height and spectrum Figure 7.8 presents the 10 not-corrected realizations and the three converged series. To avoid overloading the plots, Welch confidence intervals are not displayed. Based on Figure 1.12 Chapter 1, their amplitude can be estimated to $\pm 8\%$ for the converged series. Also note that the intervals are plotted in Figure 4.3, presenting $X_t = 53\lambda_{p_{\text{target}}}$ series.

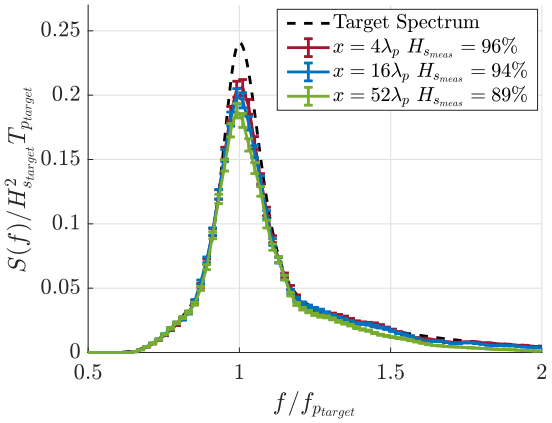

(a) Spectra at X_t without correction

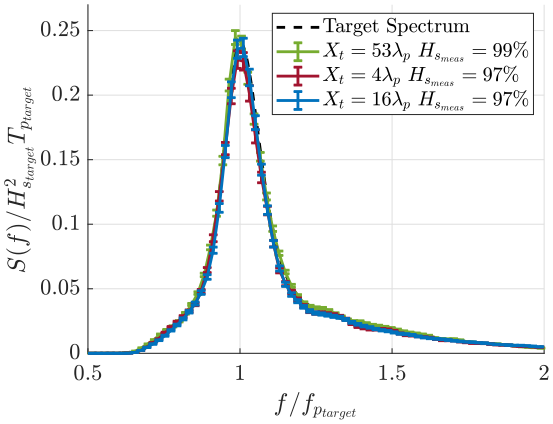

(b) Spectra at X_t after correction

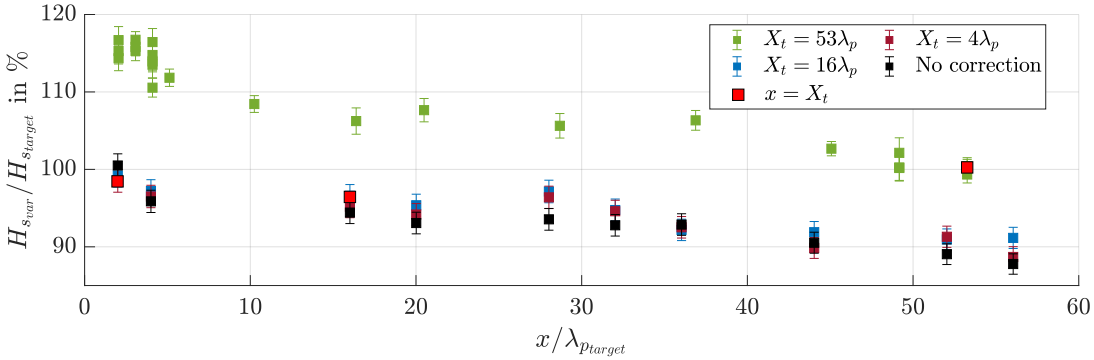

(c) H_s along the tank

Figure 7.8 – Generation of `ss6g5` scale 120 sea state at three target positions in the Towing tank (Campaigns A and D) - the error bars correspond to the measurement uncertainty u_s^{meas}

First, Figure 7.8c presents the evolution of the significant wave height for the 3 converged series and the 10 not-corrected realizations. As detailed in Chapter 4 the wave fields are affected by side walls dissipation. This leads to an H_s decrease of approximately 10% over the domain. This can be partially predicted by the theoretical model introduced in Sec. 2.3. For more details, please refer to Section 4.1 dedicated to the study of $X_t = 53\lambda_{p_{\text{target}}}$ series. As a consequence, without correction (black curve) the significant wave height is lower than its target value in most of the domain. This can be observed in Figure 7.8a which presents the spectrum at $x = 4$, 16, and $53\lambda_{p_{\text{target}}}$ for the not-corrected realizations, giving an overview of the spectrum evolution along the tank. As expected, close to the wave maker ($x = 4\lambda_{p_{\text{target}}}$) the spectrum lies approximately on the target shape. Then, as the distance from the wave maker increases, energy dissipation

significantly affects the peak and the tail of the spectrum (respectively $f/f_{p_{\text{target}}} \in [0.95; 1.05]$ and $f/f_{p_{\text{target}}} \geq 1.2$). The spectrum is not qualified in most parts of the tank. Considering the experimental accuracy limits explored in the previous section, for the present study, we tolerate H_s and spectrum shape deviations up to 5% and 10% respectively. This is not satisfied without correction for $x \geq 4\lambda_{p_{\text{target}}}$. Therefore, iterations are needed to ensure the generation of the target sea state.

Then, in Figure 7.8c we observe that, for the three converged series, the corrective procedure ensures the target H_s near the positions of interest (for each series the latter are marked in red). The correction compensates the energy losses with an increased energy level delivered by the wave maker, dependent on the target location. As the final result of the iterative procedure, Fig. 7.8b presents the converged spectrum at the three target locations. The deviations from the target sea state observed in Fig. 7.8a were corrected. The corrective procedure ensures the generation of a converged spectrum lying on the target shape with a 10% tolerance, considering the measurement uncertainty.

The corrective iterative procedure, already validated in the previous section for target locations relatively close to the wave maker (below to $6\lambda_{p_{\text{target}}}$) has been successfully extended to large target locations (up to $50\lambda_{p_{\text{target}}}$) for `ss6g5` sea state. This is likely to be generalized to any non-breaking sea state. From this point, it is of great importance to remember that for each converged series, the target spectrum is accurately controlled at its target location.

7.3.2 Comparisons of the 3 qualified wave fields

`ss6g5` was successfully generated in the Towing tank at consecutively $4\lambda_{p_{\text{target}}}$, $16\lambda_{p_{\text{target}}}$ and $53\lambda_{p_{\text{target}}}$ from the wave maker. This subsection presents the second step of the study which consists of comparing the statistical characteristics of the converged series depending on the target location.

Kurtosis along the tank First, Fig. 7.9 presents the evolution of the kurtosis λ_4 along the tank for the three converged series. This quantity is commonly used to easily estimate the probability of occurrence of extreme waves (see Sec. 1.3.2 for its definition and interpretation). The black line corresponds to the theoretical results predicted by the narrow-band theory (described in Sec. 2.1.2). As expected, for the three converged series the kurtosis is around 3 near the wave maker (signature of the imposed Gaussian wave field) before increasing along the tank. The observed order of magnitude corresponds to the theoretical prediction. As already studied in Sec. 4.2 the four-wave near-resonant interactions considered in the theory are likely to be at the

origin of the measured increase in kurtosis. No significant changes in behavior were observed when changing the target location X_t. Note that a larger X_t leads to slightly larger values of kurtosis at a given position. At the end of the domain ($x > 30\lambda_{p_{\text{target}}}$), the value of the kurtosis stabilizes in agreement with the theoretical predictions.

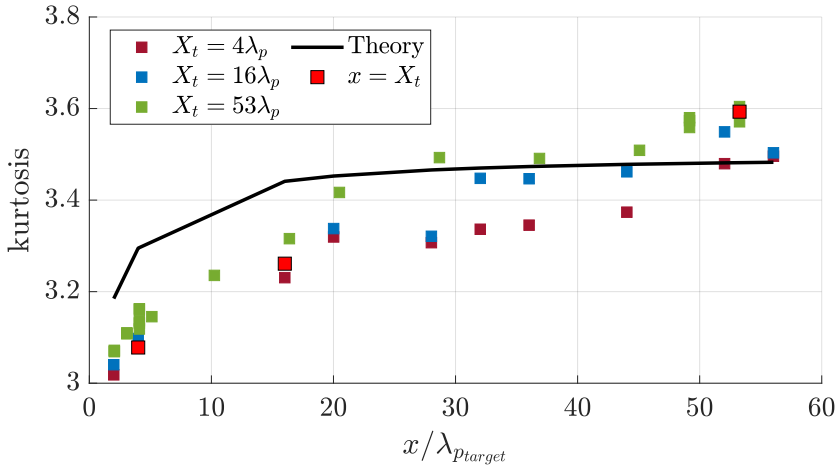

Figure 7.9 – Comparisons of `ss6g5` scale 120 sea state generated at three target positions in the Towing tank (Campaigns A and D) - Kurtosis along the tank after iterative corrections

The target locations are colored in red in Fig. 7.9. The same spectrum generated at $X_t = 4\lambda_{p_{\text{target}}}$, $16\lambda_{p_{\text{target}}}$ and $53\lambda_{p_{\text{target}}}$ is associated with kurtosis of 3.1, 3.3 and 3.6 respectively. The different kurtosis values observed at X_t depending on the converged series demonstrate that a single wave spectrum can be associated with various statistical behaviors. The influence of the spectrum corrective process is significant only for the spectrum shape and does not deeply interfere with the nonlinear mechanisms responsible for the kurtosis increase along the tank. Consequently, the target spectrum can be easily generated at a specified location but its associated kurtosis (or equivalently probability of occurrence of large waves) is strongly dependent on the distance from the wave maker. While the theory is an interesting framework to easily obtain a first estimate of the kurtosis dependence on X_t, these predictions assume narrow-banded weakly nonlinear waves and do not account for the spectrum evolution along the tank; which limits the scope of applications.

Crest distribution Additionally, the ensemble crest distribution considering all the realizations (PDER) is a crucial quantity, typically used in industry as the statistical quantity of interest for wave qualification procedures (see Chapter 6). The study of the PDER allows for a fine analysis

of the occurrence of extreme events. The kurtosis, characterizing the whole tail of the PDER, is less accurate in this context.

Figure 7.10 presents the crest PDER at $x = X_t$ for the three converged series. As a reminder, the associated wave spectra are qualified and nearly identical (see Fig. 7.8b). The Forristall and Huang references were built using the target spectral parameters. Each distribution is nondimensional and expressed with respect to the measured significant wave height. Note that with the number of waves used to build the distributions, the probabilities below 10^{-3} are not statistically converged and should not be analyzed (see section 1.3.3). Eventually, the "NBGC th. λ_4 $x = 53\lambda_{p_{\text{target}}}$" reference corresponds to the "NBGC th. λ_4" model (based on the theoretical kurtosis evolution, see Sec.2.2.4) computed for $x = 53\lambda_{p_{\text{target}}}$. It is therefore built to be compared with $X_t = 53\lambda_{p_{\text{target}}}$ series only.

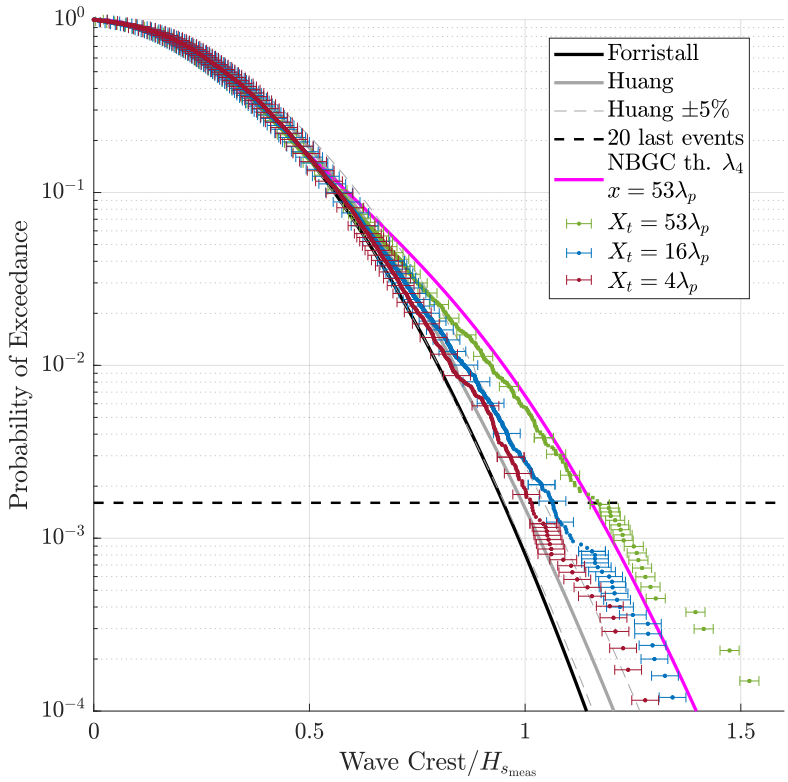

Figure 7.10 – Comparisons of `ss6g5` scale 120 sea state generated at three target positions in the Towing tank (Campaigns A and D) - PDER at X_t after correction - the error bars correspond to the measurement uncertainty u_s^{meas}

First, Fig. 7.10 should be related to the red markers in Fig. 7.9 which correspond to the

kurtosis at X_t for the three converged series. As we observed analyzing the kurtosis, the free surface elevation statistics evolve along the tank and this evolution is almost independent of the target location. As a consequence, the same spectrum was associated with various values of kurtosis, depending on X_t. The study of the PDER exhibits the same trend. For a single qualified spectrum, the target position strongly affects the tail of the crest PDER, the occurrence of extreme events increasing with X_t. As a result, the probability of exceedance $POE = 10^{-3}$ is associated with the normalized crest height $H_c/H_s = 1.06$, 1.13 and 1.23 for $X_t = 4\lambda_{p_{\text{target}}}$, $16\lambda_{p_{\text{target}}}$ and $53\lambda_{p_{\text{target}}}$ respectively.

Moreover, for this sea state exhibiting intermediate BFI=0.51, the Forristall distribution is not relevant, even in the areas close to the wave maker. The Huang distribution, built to capture the high-order nonlinear effects also fails to predict the tail of the distribution for $X_t > 4\lambda_{p_{\text{target}}}$. As studied in the Sec. 4.2, dedicated to the analysis of the distribution measured at $53\lambda_{p_{\text{target}}}$ for the $X_t = 53\lambda_{p_{\text{target}}}$ series, the "NBGC th. λ_4" distribution is more relevant for those extreme wave fields. Indeed, it accounts for the kurtosis increase along the tank.

Attention should therefore be paid to the wave qualification procedure recommended by the 'JIP on reproducible CFD' (see Chapter 6). The latter consists of targeting a wave spectrum at a given position and then comparing it with the benchmark distributions. Nonetheless, the data yielded by this study show that in the case of moderate BFI unidirectional sea states, the usual benchmark distributions (Forristall and Huang) are not relevant, and depending on the target location, the crest statistics are different even if the target spectrum is qualified.

Role of the component's'phase in the different statistical behaviors arising from the same qualified spectrum The same qualified spectrum can be associated with various wave-field statistics, depending on the distance from the wave maker. Two explanations can be suggested. First, the phases of the wave field components differ. Moreover, spectrum deviations remain, even if they are tolerated by the qualification criteria. The latter topic will be addressed in the next section.

In Sec 4.3, we concluded that the increase in the probability of the extreme events along the tank is correlated with a time-domain rearrangement of the free surface elevation i. e. envelope modulations. This rearrangement is driven by the phases of the wave field components that become coherent. To track this phenomenon, we used the groupiness factors defined in Sec. 1.3.2 e)).

The groupiness factor GF is provided in Figure 7.11 for the three converged series, at all the measured positions. For each case, GF increases along the tank which means that large and

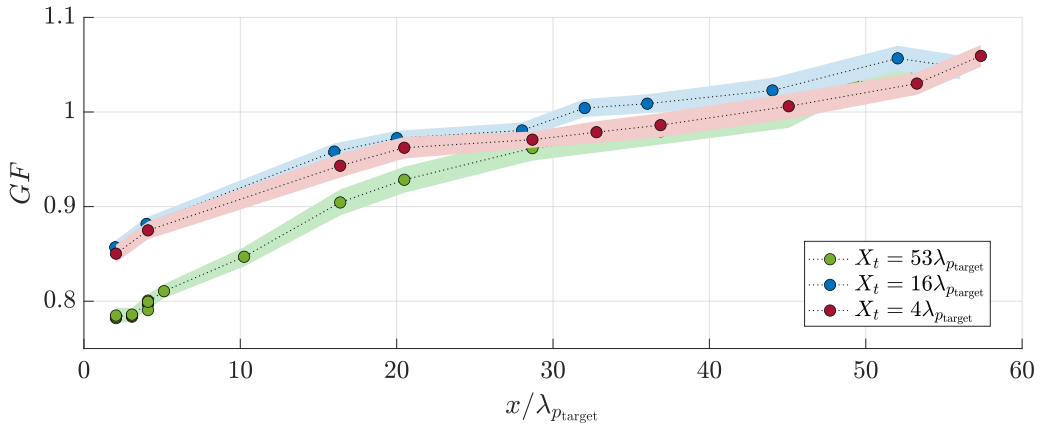

Figure 7.11 – Groupiness factor comparison of `ss6g5` scale 120 sea state generated at three target positions in the Towing tank (Campaigns A and D) - the shadded areas correspond to the sampling variability

clear-cut wave groups appear as the waves propagate. This increase can be directly correlated with the kurtosis evolution. The enhanced occurrence of extreme waves with propagating distance is associated with the increased existence of wave groups, and consequently the coherence of the phases of the wave field components.

The influence of the corrective process is limited. *GF* spatial evolution does not significantly depend on the input spectrum variations that correct the spectrum at the target location. However, it should be noted that the input spectrum used for $X_t = 53\lambda_{p_{\text{target}}}$ series decreased the groupiness values for $x < 20\lambda_{p_{\text{target}}}$. This input spectrum is displayed in Figure 4.1. To balance side wall dissipation, its tail contains far more energy than the one of $X_t = 16\lambda_{p_{\text{target}}}$ and $X_t = 4\lambda_{p_{\text{target}}}$ inputs. This affects *GF* at the beginning of the tank. Note that the results presented here slightly differ from Canard et al. (2022b) content. Indeed, for practical reasons and due to repairs on the Towing tank wave maker that affected its transfer function, in the present study, an additional corrective iteration was applied to generate the $X_t = 53\lambda_{p_{\text{target}}}$ series. As a result, the latter series slightly differs from the one presented in Canard et al. (2022b).

For each converged series, the groupiness factor is mainly dependent on the distance from the wave maker, the wave groups being more defined at the end of the tank. Hence, a single qualified wave spectrum can be associated with wave fields characterized by different groupiness, depending on the distance from the wave maker. This tends to demonstrate that the difference in the statistics between the qualified wave fields is mainly due to a rearrangement of the phases, as a results of nonlinear wave interactions. Even accurately controlling the wave

spectrum amplitudes would not enable to control the wave statistics.

7.4 Influence of the spectrum shape on wave height statistics

It has been demonstrated in the previous section that the same qualified spectrum can be associated with various wave-field statistics, depending on the distance from the wave maker. This questions the procedure that focuses on the qualification of the spectrum, assuming that the statistics will follow the benchmark distributions.

We observed that the behavior of the statistics is correlated to the rearrangement of the wave field component's phases. However, spectrum shape deviations might also affect the statistics, even if they are limited by the criterion tolerance.

The spectrum qualification process can be questioned. The criterion introduced within the scope of the "JIP on Reproducible CFD practices" (see Chapter 6) concerns the relative spectrum error at $x = X_t$, within the frequency range $f \in [0.75 f_{p_{\text{target}}}; 1.25 f_{p_{\text{target}}}]$. The allowed maximum relative error is 5%. In Sec. 7.2 this qualification criteria was tested, after the use of the correction spectrum procedure. The results showed that the $\pm 5\%$ accuracy can only be reached for numerical wave fields and that a 10% threshold is more adapted for the experimental data. As a consequence, the qualified spectra are affected by small deviations from their target shape, within and outside of the $f \in [0.75 f_{p_{\text{target}}}; 1.25 f_{p_{\text{target}}}]$ range. This can affect other properties of the wave field such as the crest distribution which also needs to be considered for the sea state qualification.

In this respect, this section is dedicated to the study of the spectrum deviations tolerated by the qualification criteria. Their consequences for the wave field statistics will be studied. Only same-X_t wave fields will be compared, to be free from the position influence and investigate the influence of the spectrum shape.

7.4.1 Influence of deviations below $f = 2 f_{p_{\text{target}}}$

Figure 7.12 provides the comparisons of two sets of 28 realizations of `ss6g5` scale 120. One is associated with a spectrum almost lying on the target shape (Series B). The other presents $\pm 15\%$ of error within the frequency range $f \in [0.75 f_{p_{\text{target}}}; 1.5 f_{p_{\text{target}}}]$ (Series A). The data come from the Towing tank (Campaign D). Both Series A and B were measured at $x = 8$ m$= 4\lambda_{p_{\text{target}}}$, which means that no spatial effects can affect the comparison. Series A was built using the "control stat." procedure that will be presented in the Sec. 8.1, using $X_{t_{\text{stat}}} = 53\lambda_{p_{\text{target}}}$

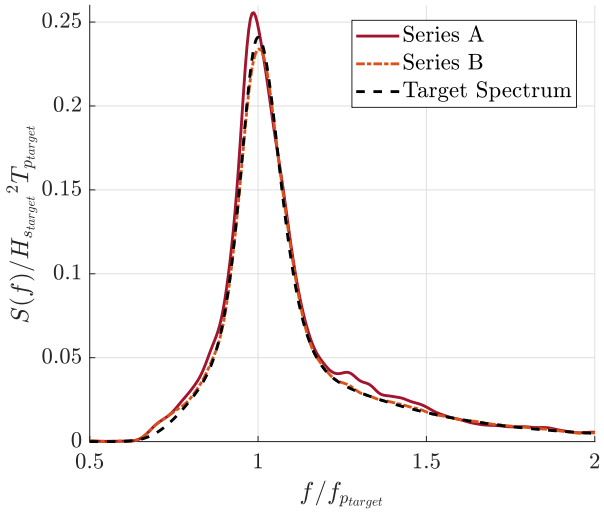

(a) spectrum

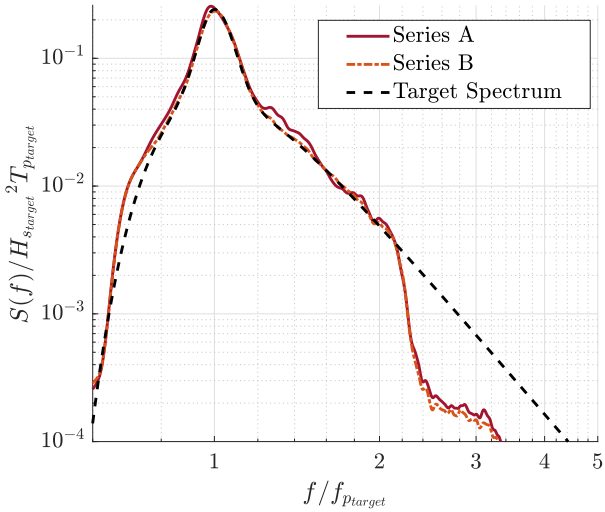

(b) spectrum log. scale

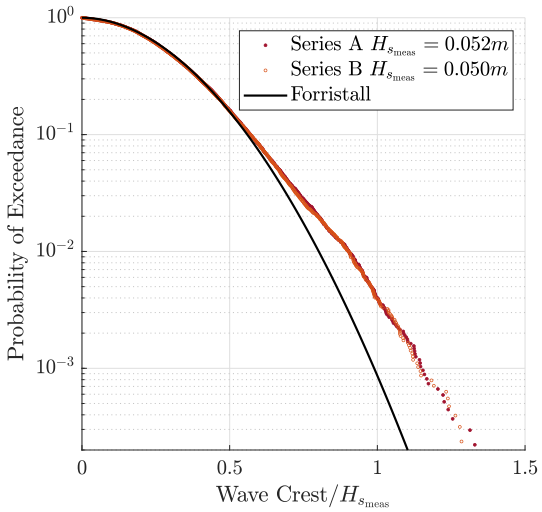

(c) crest PDER

Figure 7.12 – Comparisons of `ss6g5` scale 120 sea state generated in the Towing tank (Campaign D) using the control stat. method (see Sec. 8.1), Series A: reproduction of $X_t = 53\lambda_{p_{\text{target}}}$ reference at $x = 4\lambda_{p_{\text{target}}}$ iter. 0 ; Series B: reproduction of $X_t = 53\lambda_{p_{\text{target}}}$ reference at $x = 4\lambda_{p_{\text{target}}}$ iter. 1

and $X_t = 4\lambda_{p_{\text{target}}}$. Refer to the latter section for detailed explanations. Series B was generated iterating once on Series A spectrum using the correction procedure introduced in Sec. 7.1. Using a logarithmic scale (Fig. 7.12b) we observe that Series A and B have a very similar spectrum tail

($f > 2f_{p_{\text{target}}}$). The cut-off at $f = 2.2f_{p_{\text{target}}}$ comes from the mechanical limitation of the Towing tank wave maker which can not generate frequencies higher than $f_{\text{max}}^{\text{wvmk}} = 2$ Hz.

Then, Fig. 7.12c compare the crest PDER. The latter quantity is almost the same for series A and B. This means that for this non-breaking sea state, spectrum deviations of $\pm 15\%$ within $f \in [0.75f_{p_{\text{target}}}; 1.5f_{p_{\text{target}}}]$ do not affect the crest distributions. As a consequence, it seems reasonable to extend the spectrum qualification criteria to $\pm 10\%$ within $f \in [0.75f_{p_{\text{target}}}; 1.5f_{p_{\text{target}}}]$, as suggested in the Sec. 7.2.

7.4.2 Influence of high frequencies (spectrum tail)

In the previous subsection, the spectrum shape differences were localized in the $f \in [0.75f_{p_{\text{target}}}; 1.5f_{p_{\text{target}}}]$ frequency range. Here, we compare wave fields whose spectra mainly differ in the high-frequency domain ($f > 2f_{p_{\text{target}}}$).

Four datasets are included in the comparison. Each consists of 35 realizations of `ss6` sea state measured at $x = 3\lambda_{p_{\text{target}}}$. The difference arises from the presence or absence of a high-frequency cut-off in the input wave maker motions. The experimental data were generated within the frame of Campaign B and the numerical data with the "`HOS-NWT` with Tian" model described in Sec. 5.2.1. Here is a description of the datasets.

— "Experiments $f_{\text{max}}^{\text{input}} = 2.5f_p$ Exp. iter 0" dataset was generated in the O.E tank. It corresponds to the experimental data presented in Sec. 7.2.1. The inputs were built by calibrating the spectrum with `HOS-NWT` simulations at scale 100. This induced a high-frequency cut-off $f_{\text{max}}^{\text{input}} = 2.5f_{p_{\text{target}}}$.

— "Experiments $f_{\text{max}}^{\text{input}} = 3.2f_p$ Exp. iter 1" dataset was generated in the O.E. tank. It was built by applying correction coefficients to "Experiments $f_{\text{max}}^{\text{input}} = 2.5f_p$ Exp. iter 0" inputs, to correct the spectrum at $X_t = 3\lambda_{p_{\text{target}}}$, including the frequencies larger than $2.5f_{p_{\text{target}}}$. The generation scale is 40. The $f_{\text{max}}^{\text{wvmk}} = 2$ Hz limitation induced $f_{\text{max}}^{\text{input}} = 3.2f_{p_{\text{target}}}$.

— "`HOS-NWT` $f_{\text{max}}^{\text{input}} = 3.2f_p$ Exp. iter 1" corresponds to the numerical reproduction of "Experiments $f_{\text{max}}^{\text{input}} = 3.2f_p$ Exp. iter 1" experiments.

— "`HOS-NWT` $f_{\text{max}}^{\text{input}} = 2.5f_p$ Exp. iter 1" corresponds to the numerical reproduction of "Experiments $f_{\text{max}}^{\text{input}} = 3.2f_p$ Exp. iter 1" experiments, but with an imposed high-frequency cut-off $f_{\text{max}}^{\text{input}} = 2.5f_{p_{\text{target}}}$.

To summarize, experimental and numerical data were generated with nearly identical wave-maker inputs, with or without a cut-off at $f_{\text{max}}^{\text{input}} = 2.5f_{p_{\text{target}}}$.

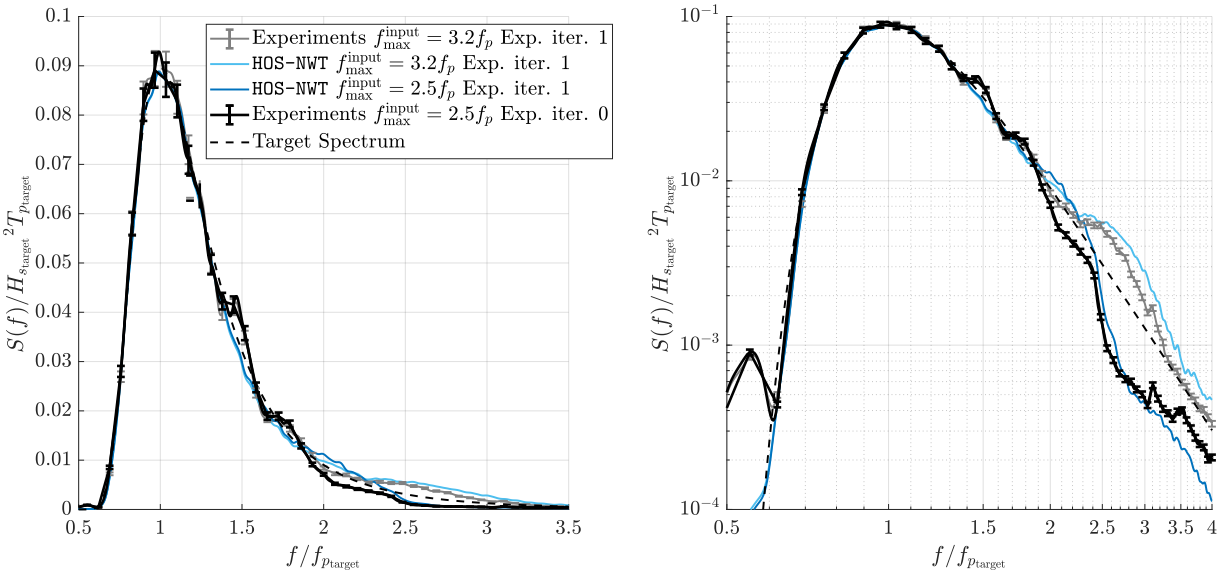

(a) Linear scale **(b)** Logarithmical scale

Figure 7.13 – `ss6` scale 40 and 100 sea state generated experimentally and numerically in the O.E. tank with varying $f_{\max}^{\text{input}}$ - spectrum at $X_t = 3\lambda_{p_{\text{target}}}$ - the error bars correspond to the measurement uncertainty u_s^{meas}

Figure 7.13 compares the spectra at $X_t = 3\lambda_{p_{\text{target}}}$, in linear and logarithmical scale. We observe that up to $f = 2.5 f_{p_{\text{target}}}$ the spectra of the four datasets are nearly identical (and even identical for the two `HOS-NWT` datasets). For larger frequencies, the datasets whose inputs were cut at $f = 2.5 f_{p_{\text{target}}}$ show significantly less energy.

Figure 7.14 compares the crest distributions at $X_t = 3\lambda_{p_{\text{target}}}$. The datasets whose inputs were cut at $f = 2.5 f_{p_{\text{target}}}$ show a departure from the two others. For the probabilities below 3.10^{-3}, removing the high frequencies from the inputs increases the height of the events. The difference is less pronounced than the one induced by the influence of the target location (see Sec. 7.3), but it must not be ignored.

In conclusion, based on our observations, spectrum deviations of $\pm 10\%$ within the range of $f \in [0.75 f_{p_{\text{target}}}; 1.5 f_{p_{\text{target}}}]$ do not affect the statistics. But, $f_{\max}^{\text{input}} = 2.5 f_{p_{\text{target}}}$ cut off in the inputs (leading to spectrum shape differences for $f > 2.5 f_{p_{\text{target}}}$) increases the probability of the extreme events. Dedicated investigations should be carried out to confirm these findings, and characterize more accurately the effect of the spectrum shape on wave statistics. Note that for directional cases, Tang et al. (2022) investigated numerically the effect of a high-frequency

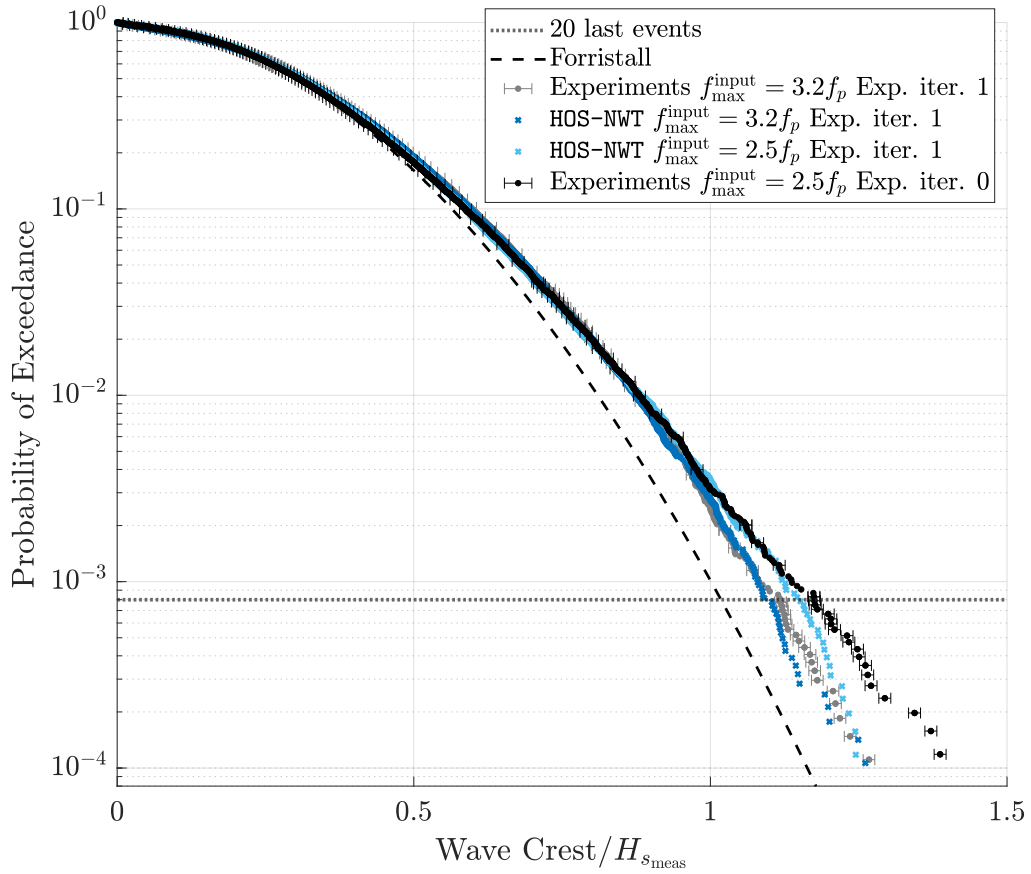

Figure 7.14 – `ss6` scale 40 and 100 sea state generated experimentally and numerically in the O.E. tank with varying $f_{\max}^{\text{input}}$ - crest PDER at $X_t = 3\lambda_{p_{\text{target}}}$ - the error bars correspond to the measurement uncertainty u_s^{meas}

cut-off in the initial conditions. The authors found that cutting the tail of the input spectrum increases the probability of extreme events. Detailed investigations should be performed to link the observations of this section with the phenomenon enlightened in Tang et al. (2022) for directional sea states.

Combined influence of the spectrum shape and the target location In Sec. 7.3 we compared three wave fields having the same qualified spectrum but different statistics. We attributed the difference in statistics to the phase rearrangement of the wave field components, induced by high-order nonlinear interactions. However, in the light of the study of this subsection, we can wonder whether this difference can be observed in the spectrum tail or not.

To investigate, Figure 7.15 compares the spectrum of the three converged series, in a logarithmical scale. We observe that the tail is similar for $X_t = 4\lambda_{p_{\text{target}}}$ and $X_t = 16\lambda_{p_{\text{target}}}$ series. However, $X_t = 53\lambda_{p_{\text{target}}}$ spectrum is slightly above the two others for $f \in [2.3f_{p_{\text{target}}}; 3f_{p_{\text{target}}}]$. This is likely to be a consequence of the nonlinear energy transfer induced by the nonlinear wave interactions (see Fedele et al. (2010)).

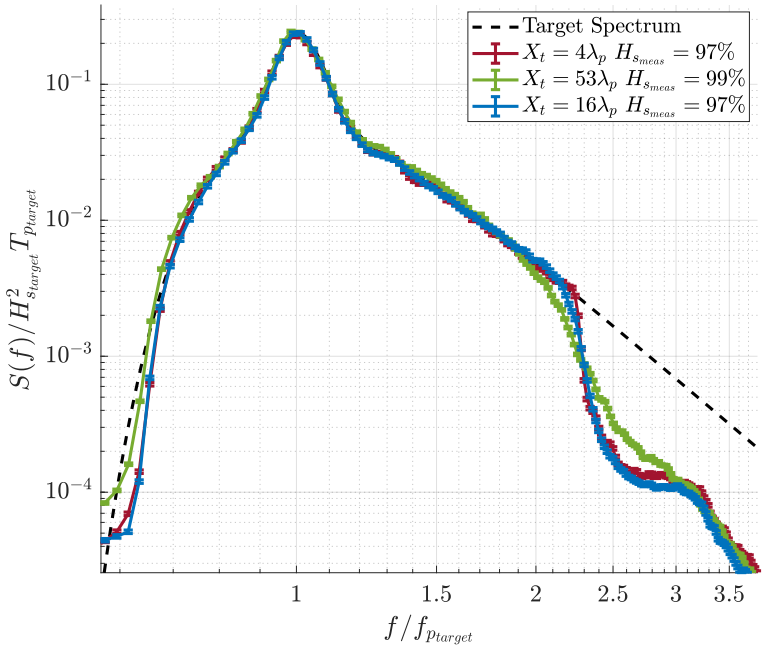

Figure 7.15 – Spectrum comparison of `ss6g5` scale 120 sea state generated at three target positions in the Towing tank (Campaigns A and D) - the error bars correspond to the measurement uncertainty u_s^{meas}

The results can not be corroborated with the behavior observed in Figure 7.14. In the study of this subsection, we concluded that larger spectrum tails lead to less extreme statistics. Here, we observe the opposite. Moreover, the order of magnitude of the spectrum tail deviations is not the same. In Figure 7.14, the deviations were more pronounced.

As a result, it seems reasonable to assert that the influence of the target location is predominant. And, at a same target location, a frequency cut-off in the inputs can modify the statistics.

7.5 Conclusion

The iterative spectrum correction procedure recommended by ITTC (2021) and NWT Preparation Workgroup (2019) guidelines was tested experimentally and numerically for various configurations: mild conditions, strongly-breaking conditions, and non-breaking conditions in a long tank where side walls induce dissipation. The findings are gathered in Table 7.1.

Table 7.1 – Conclusions of the studies testing the spectrum correction procedure.

Non/mild Breaking Sea States	**Strongly Breaking Sea States**
Control of $S(f,X_t)$ whatever X_t	Control of $S(f,X_t)$ for $X_t < 6\lambda_{p_{\text{target}}}$
1 to 4 iterations needed (including iteration 0) depending on X_t	At least 3 iterations needed (including iteration 0)
For a same qualified $S(f,X_t)$, the statistics are influenced by: i) X_t, ii) the spectrum tail	For a same qualified $S(f,X_t)$, the statistics are influenced by: i) X_t, ii) the spectrum tail, iii) the breaking model (for `HOS-NWT` data)
$E_S < \pm 10\%$ within $f \in [0.75f_{p_{\text{target}}}; 1.5f_{p_{\text{target}}}]$ is enough	$E_S < \pm 10\%$ within $f \in [0.75f_{p_{\text{target}}}; 1.5f_{p_{\text{target}}}]$ is enough

Efficiency and limitations of the spectrum correction For non-breaking sea states, not affected by side walls dissipation, one iteration is enough to qualify the spectrum at X_t. With side wall dissipation, depending on the target location, 4 iterations may be needed. X_t larger than $50\lambda_{p_{\text{target}}}$ can be achieved. For strongly-breaking sea states the number of iterations is around 4, and the procedure can not achieve the generation of the target spectrum at locations larger than $6\lambda_{p_{\text{target}}}$.

The procedure was validated numerically and experimentally. No significant difference in efficiency was observed. However, we found that the spectrum accuracy of $C = \pm 5\%$ within $f \in [0.75f_{p_{\text{target}}}; 1.5f_{p_{\text{target}}}]$ can only be reached for numerical wave fields. In experiments, because of measurement and generation uncertainties, $C = \pm 10\%$ is more realistic.

In addition, when generating experimentally a sea state, the number of experimental iterations needed remains almost the same whether calibrating the input prior experiments with `HOS-NWT` or starting from $S_{\text{input}} = S_{\text{design}}$ (we found that only one additional experimental iteration is needed when generating `GOM` at $X_{=}2\lambda_{p_{\text{target}}}$ without numerical calibration). For non-breaking conditions, this is mainly because in experiments the transfer function of the wave maker does not exactly follow its theoretical behavior. Therefore, the `HOS-NWT` spectrum

slightly differs from the experimental one, and experimental iterations are needed to correct the deviations. For strongly breaking conditions, the Tian-Barthelemy breaking model, which is not perfectly accurate, also induces differences between the calibrated spectrum in `HOS-NWT` and the same spectrum generated in experiments.

Qualified spectrum and wave statistics We observed that a single qualified spectrum can be associated with different statistical behavior, depending on i) the distance from the wave maker and ii) the spectrum tail content.

We concluded that, for non-breaking unidirectional sea states, due to the high-order nonlinear interactions studied in Sec. 4.3, the distance from the wave maker induces a rearrangement of the wave phases, modulating the envelope and increasing the probability of the extreme events, even when calibrating the spectrum with the iterative correction procedure. Accurately controlling the spectrum is therefore not enough to control the statistics.

In addition, we observed that, $\pm 10\%$ spectrum deviations within $[0.75 f_{p_{\text{target}}}; 1.5 f_{p_{\text{target}}}]$ do not affect the statistics, but a high-frequency cut-off in the inputs (leading to differences in the spectrum tail) increases the probability of the extreme events.

The influence of distance from the wave maker is the predominant factor influencing the statistics of a qualified wave field. This raises some issues. The wave statistics, including the crest distribution, are of major importance for ocean engineering studies. They need to be predicted and if possible controlled whatever X_t. To tackle the problem the next chapter introduces and validates a new wave generation procedure to better control the statistical distributions independently of X_t.

CHAPTER 8

CONTROL OF THE WAVE STATISTICS

The wave generation procedure studied in Chapter 7 enables the control of the mean spectrum at the position $x = X_t$. However, wave fields are also characterized by the crest height distribution. This quantity is important as it quantifies the severity and probability of occurrence of individual events. Such information is not included in the wave spectrum. As observed in Chapter 7 and especially in Section 7.3 the same qualified spectrum can correspond to varying crest height statistics depending on the distance from the wave maker to the target location.

Specifically, in Sec. 7.3 we observed that for a unidirectional non-breaking sea state with a moderate BFI (`ss6g5`), the distributions obtained at target locations far from the wave maker (i.e. more than $20\lambda_{p_{\text{target}}}$) show a strong departure from the usual reference distributions. This enlightens the presence of a significant number of extreme events. In the context of wave-structure interaction tests, these occurrences are likely to strongly affect the response of the tested structure. For $X_t > 30\lambda_{p_{\text{target}}}$, the crest PDER stops varying with X_t and stays favorable to extreme events.

Nonetheless, the usual target locations used in experimental wave tanks are relatively close to the wave maker (less than $10\lambda_{p_{\text{target}}}$). In this area, the probability of occurrence of extreme events is smaller. This means that the severity of critical design events (occurring at a probability $P = P_{\text{design}}$) is possibly significantly underestimated with the state-of-the-art procedures.

Considering these extreme wave fields for wave-structure interaction tests is still under question. Indeed, the crest PDER departure from reference distributions observed for large X_t is significantly limited for breaking and directional sea states (Onorato et al., 2009), which represent more realistically extreme environmental conditions. However, classification societies mainly require unidirectional wave conditions, so the question of which crest PDER to target is open. Regardless of the answer, the accurate control of the wave spectrum $S(f, X_t)$ and the crest PDER at any target location in the tank is a crucial step toward more relevant procedures.

In this context, the present chapter proposes a procedure that offers the possibility to generate closer to the wave maker the same distributions that are measured further in the tank with state-of-the-art procedures. The objective is to generate, at a typical X_t, a qualified spectrum

associated with wave statistics converged in space. The framework is limited to non-breaking unidirectional waves. The procedure will be tested both experimentally and numerically.

8.1 Procedure to generate extreme wave statistics at any target location

Figure 8.1 summarizes the process. It can be decomposed into two steps. First, the iterative spectrum correction procedure described in Sec. 7.1 is used to accurately generate N_{run} realizations of $S_{\text{design}}(f)$ at a target location $X_{t_{\text{stat}}}$, large enough to be associated with spatially converged statistics (Step 1). Note that the waves need to be measured at least at $x = X_{t_{\text{stat}}}$ and $x = X_{t_{\text{stat}}} - X_t$ (respectively green and grey locations in Figure 8.1). At the end of this first step, the wave field at $X_{t_{\text{stat}}}$ is characterized by a qualified spectrum $S(f, X_{t_{\text{stat}}})$ and a spatially converged crest PDER, possibly exhibiting a large occurrence of extreme events.

Then, the waves measured at $x = X_{t_{\text{stat}}} - X_t$ are used as input sequences for the wave maker, i. e. $\eta^{\text{step2}}_{\text{input}}(t) = \eta^{\text{step1}}(t, X_{t_{\text{stat}}} - X_t)$ (Step 2). The regeneration of recorded wave signals into wave maker motion is a well-known and controlled process, usually used to artificially increase an experimental domain (see *e.g.* Chabchoub et al. (2012)). For the present procedure, the idea is to reproduce between the wave maker and X_t, the wave propagation that occurred at Step 1 between $X_{t_{\text{stat}}} - X_t$ and $X_{t_{\text{stat}}}$. It is important to note that to build the wave maker motion we use the Fourier transforms of $\eta^{\text{step2}}_{\text{input}}(t)$ sequences. The complex nonlinear wave signals are converted into a linear sum of Fourier components. As a consequence, the measured bound waves are converted into free waves by the wave maker. A dedicated process will be tested to remove the bound waves from the wave maker input signals (see Sec. 8.2.4b)).

At the end of Step 2, the wave field at X_t (red in Figure 8.1) should exhibit i) the design spectrum (qualified $S(f, X_t)$) and ii) the spatially converged crest PDER naturally emerging at $X_{t_{\text{stat}}}$.

The remainder of this current chapter will be devoted to the numerical and experimental validation of the procedure.

8.2 Step 1: Generation of a qualified spectrum at $X_{t_{\text{stat}}}$

To test the procedure, we need to select i) a design spectrum and ii) a ($X_{t_{\text{stat}}}$, X_t) couple. Previous works presented in Chapter 4 and Section 7.3 showed that `ss6g5` sea state leads to a

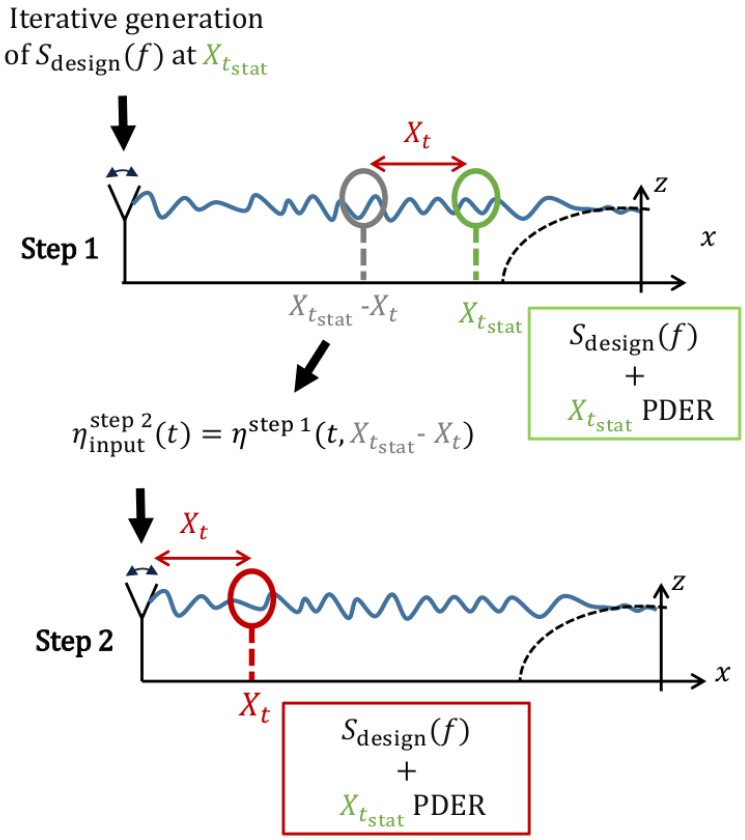

Figure 8.1 – Procedure generate a qualified wave field without the influence of the target location, for $X_{t_{stat}} > X_t$

.

significant spatial evolution of the wave statistics (see Fig. 7.9). The spectrum was accurately generated in the Towing tank at $X_t = 53\lambda_{p_{target}}$ and $X_t = 4\lambda_{p_{target}}$. The comparison of the resulting crest distributions is provided again in Fig. 8.2. Strong differences are observed. The occurrence of the extreme events are significantly larger at $X_t = 53\lambda_{p_{target}}$.

Continuing from those investigations, the procedure will be tested to reproduce the extreme $X_t = 53\lambda_{p_{target}}$ `ss6g5` wave field closer to the wave maker, at $x = 4\lambda_{p_{target}}$. This means that $X_t = 4\lambda_{p_{target}}$ and $X_{t_{stat}} = 53\lambda_{p_{target}}$. In other words, the objective is to generate at $X_t = 4\lambda_{p_{target}}$ i) the qualified `ss6g5` spectrum, and ii) the extreme distribution that was only observed at $X_{t_{stat}} = 53\lambda_{p_{target}}$.

This section will be dedicated to the first step of the study which consists in generating `ss6g5` wave fields qualified at $X_{t_{stat}} = 53\lambda_{p_{target}}$, and measured at $X_{t_{stat}} - X_t = 49\lambda_{p_{target}}$. Such

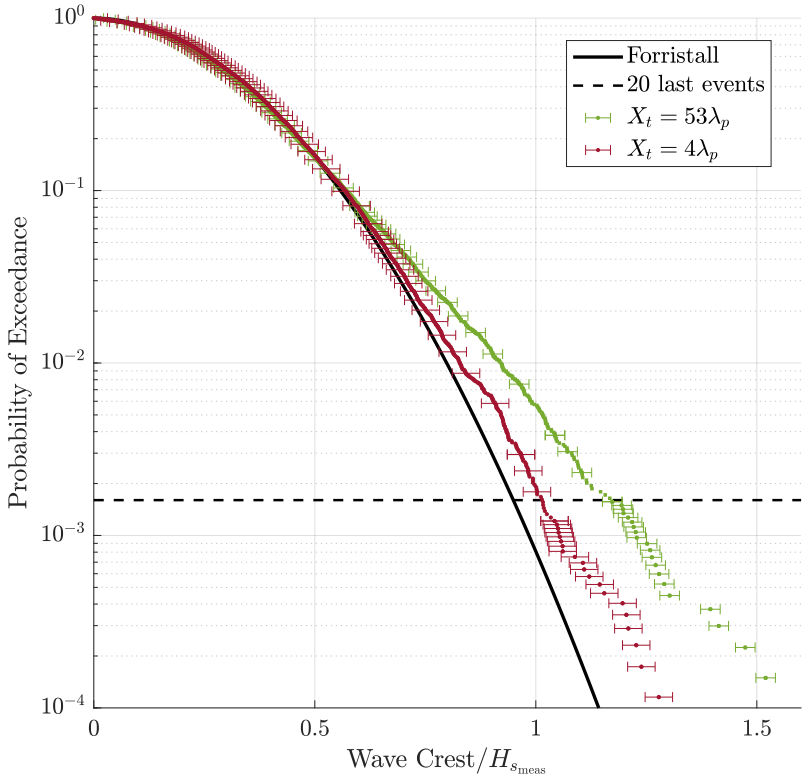

Figure 8.2 – Comparisons of `ss6g5` scale 120 sea state generated at $X_t = 4\lambda_p$ and $X_t = 53\lambda_p$ in the Towing tank (Campaigns A and D) - PDER at X_t after correction - the error bars correspond to the measurement uncertainty u_s^{meas}

data will be denoted as "$X_{t_{\text{stat}}}$ reference".

8.2.1 Experimental reference

The first available $X_{t_{\text{stat}}}$ reference is the wave field presented in Chapter 4. It consists of 30 $395T_{p_{\text{target}}}$-duration realizations at scale 120, generated in the ECN Towing tank within the frame of Campaign D. It was obtained after 4 corrective iterations of the spectrum at $53\lambda_{p_{\text{target}}}$ (see more details in Section 7.3). The corrected spectrum is provided again in Figure 8.3. Measurement probes were settled at $X_{t_{\text{stat}}} - X_t = 49\lambda_{p_{\text{target}}}$, so the recorded data can be used to generate wave maker inputs for the second step of the procedure. This wave field will now be denoted as `EXP ref`.

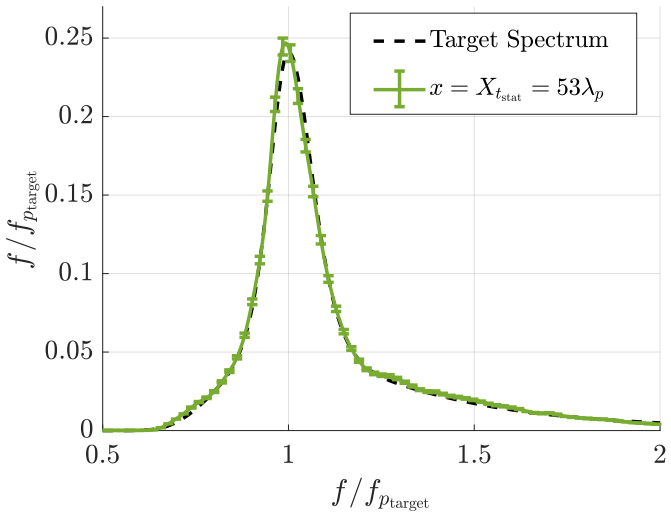

Figure 8.3 – `EXP ref: ss6g5` scale 120 sea state generated at $X_{t_{\text{stat}}} = 53\lambda_p$ in the Towing tank (Campaign D) - spectrum after correction - the error bars correspond to the measurement uncertainty u_s^{meas}

8.2.2 Numerical reference

At this point, it is important to understand that conducting the complete procedure experimentally poses significant challenges. First, it requires large-duration experiments. For instance, the generation of `EXP ref` required four iterations, each consisting of at least five 15-minute runs. Then, 30 realizations of the qualified wave field were generated. Eventually, the second step also demands 30 additional realizations. This results in a combined total of 80 realizations, equivalent to a minimum of one week of experiments.

Moreover, to use a $X_{t_{\text{stat}}}$ value that ensures statistically converged data, the first step of the procedure requires a long wave tank. It limits its application to long wave channels that are usually not available for ocean engineering experiments.

To face those issues, a viable solution is to use numerical wave propagation solvers, such as `HOS-NWT`, to generate the qualified spectrum at $X_{t_{\text{stat}}}$. Indeed the domain can be extended to any arbitrary length and the computational time needed is significantly less expensive compared to experimental campaigns. Then the second step of the procedure (i. e. the generation of the reference wave field at X_t) can be conducted either experimentally in any wave tank (the domain does not need to include $X_{t_{\text{stat}}}$) or numerically (for instance to build wave conditions for CFD wave-structure interaction studies).

Therefore, complementary to `EXP ref` data, a numerical `ss6g5` wave field qualified at

Table 8.1 – Characteristics of the spectrum at $x = X_{t_{\text{stat}}} = 53\lambda_{p_{\text{target}}}$ for all the iterations

Iter.	0	1	2	3	4
$H_s/H_{s_{\text{target}}}$ (%)	96	99	99	98	98
$T_p/T_{p_{\text{target}}}$ (%)	98	101	100	101	101
ν_w	0.142	0.141	0.135	0.138	0.136
$\max(E_S)$ (%)	32	23	12	11	5

$X_{t_{\text{stat}}} = 53\lambda_{p_{\text{target}}}$ was also generated. The data will be referred to as `HOS ref`. The characteristics of the NWT relied on the ECN ocean engineering tank and the generation scale set to 60, in the perspective of experimental validations. The length of the tank was fixed to 250 m. Note that the ECN ocean engineering tank is only 50 m long. The length of the NWT was increased to include $X_{t_{\text{stat}}} = 53\lambda_{p_{\text{target}}} = 208$ m. The numerical beach started at $x = 215$ m, preventing the reflection of the waves. Numerical probes were implemented all along the domain (every $2\lambda_{p_{\text{target}}} = 8$ m).

The domain was discretized with $N_x = 3130$ points, allowing the resolution of the wave numbers up to $k_{\max} = 25k_{p_{\text{target}}}$ (i.e. $f_{\max} = 5f_{p_{\text{target}}}$). The order of nonlinearity of the HOS method was fixed to $M = 5$ to accurately model the nonlinear phenomena at play during wave propagation. Finally, as advised in Sec. 5.2.1, the Tian breaking model was implemented, the objectives being to improve the robustness and capture the effects of possible breaking events. Note that only one or two breaking events per realization were identified.

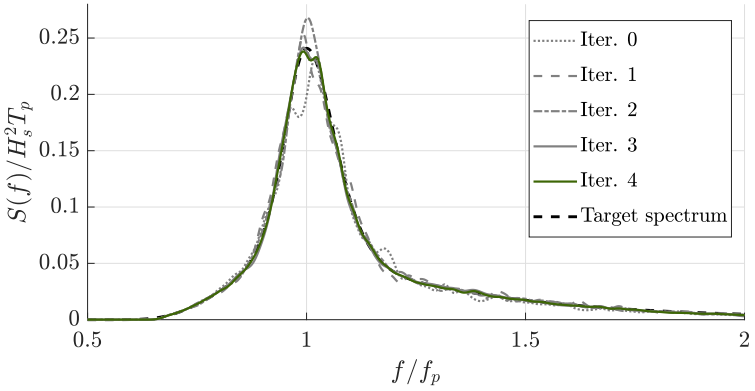

Figure 8.4 – Iterative correction of `HOS ref` spectrum at $X_{t_{\text{stat}}} = 53\lambda_{p_{\text{target}}}$

.

Figure 8.4 presents the evolution of the mean spectrum at target location from one iteration to another. Note that each corrective iteration consisted of $N_{\text{run}_{\text{iter}}} = 5$ realizations with random phases. The spectrum characteristics are given in Table 8.4. First, without any

correction (iteration 0 using $A^0_{\text{input}}(f) = A_{\text{design}}(f)$), the spectrum did not lie on its target shape (the maximum relative error, across $[0.75f_{p_{\text{target}}}; 1.5f_{p_{\text{target}}}]$, reached more than 30%). Missing energy around the peak affected the quality of the spectrum and the spectral width was larger than the target one. Similar trends were predicted in Janssen (2003), based on the NLSE and the Zakharov equations. They are the consequences of third order near-resonant interactions, broadening the spectrum. Also note that at iteration 0, H_s was slightly below $H_{s_{\text{target}}}$. This can be explained by the few breaking events (2 or 3 per realizations), activating the `HOS-NWT` breaking model.

Then, the iterative process corrected the spectrum shape at $X_{t_{\text{stat}}} = 53\lambda_{p_{\text{target}}}$. It converged step by step on the design spectrum. After 4 iterations, the maximum error $\max(E_S)$ was reduced to 5%. At the end of the process, $N_{\text{run}} = 35$ realizations of iteration 4 were generated (each of duration $\Delta T = 640T_{p_{\text{target}}}$), finalizing `HOS ref`.

8.2.3 Comparison of the references

Figure 8.5 provides the comparison of `EXP ref` and `HOS ref` wave fields. As a reminder, at $X_{t_{\text{stat}}} = 53\lambda_{p_{\text{target}}}$ the spectrum of both references matches `ss6g5` target shape (see Figure 7.8b for `EXP ref` and Figure 8.4 for `HOS ref`).

As detailed in Section 4.1, `EXP ref` is affected by side-wall friction. This results in a H_s decrease along the tank, see Fig. 8.5a. In contrast, the `HOS-NWT` model used to generate `HOS ref` does not include dissipation features, except the Tian breaking model which was almost not activated. It explains why H_s remains constant. As expected, around $x = X_t$, both `HOS ref` and `EXP ref` H_s reach $H_{s_{\text{target}}}$.

This different H_s behaviors do not seem to significantly influence the wave statistics. The spatial evolution of kurtosis and the crest distribution at $X_{t_{\text{stat}}}$ remain highly similar between `EXP ref` and `HOS ref` datasets, see Fig. 8.5c and 8.5b. It is important to note that different sets of random phases were used to generate the two wave fields. Therefore, the comparison between `HOS ref` and `EXP ref` is affected by sampling variability. Only differences that fall outside the sampling-variability intervals can be considered indicative of a mismatch between the references. This is not the case here.

As already studied in detail in Chapter 4, the kurtosis significantly increases along the tank, as the result of high-order nonlinear phenomena such as near-resonant interactions and modulational instabilities. This means that the occurrence of extreme events increases with the distance from the wave maker. Concomitantly, the crest PDER at $X_{t_{\text{stat}}}$ exhibits strong departure from the Forristall distribution for probabilities of exceedance below 5.10^{-3}. See more details

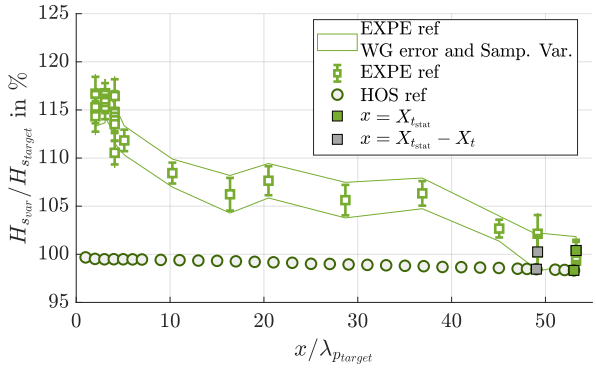

(a) H_s along the tank

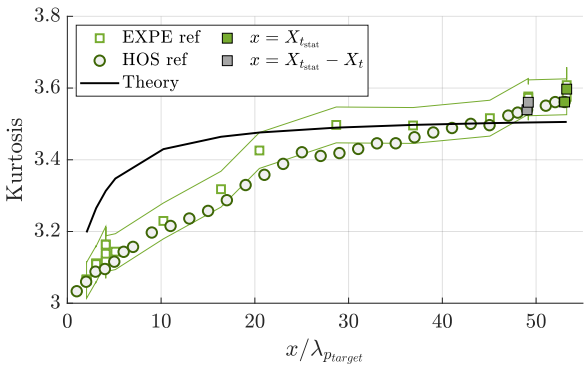

(b) Kurtosis along the tank

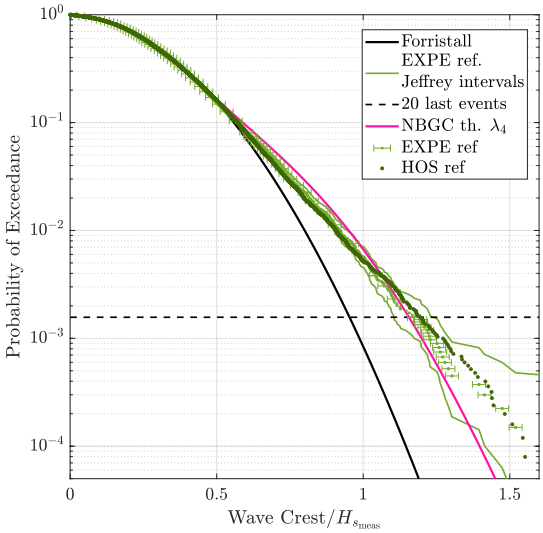

(c) Crest PDER at $X_{t_{stat}}$

Figure 8.5 – `EXP ref` and `HOS ref` comparison

and interpretations of this behavior in Section 4.2.

To conclude, the first step of the procedure was successfully carried out, numerically and experimentally. For both `HOS ref` and `EXP ref` wave fields, the spectrum at $X_{t_{stat}}$ was qualified and the associated crest PDER was extreme. The rest of the study will now detail the reproduction of those extreme wave fields closer to the wavemaker at $X_t = 4\lambda_{p_{target}}$, location which leads to non-extreme statistics when using the standard wave generation procedures, see Fig. 8.2.

8.2.4 Conversion of the wave field measurements into wave maker motion inputs

To generate the $X_{t_{\text{stat}}}$ references at X_t, we first need to convert the measurements at $X_{t_{\text{stat}}} - X_t$ into wave-maker inputs. Note that $X_{t_{\text{stat}}} - X_t$ is indicated by the grey square in Fig. 8.5. As explained in Section 1.2.2, the wave maker takes as input the Fourier transform of the desired free surface elevation time series at $x = 0$ ($\eta(t, x = 0)$). The frequency-domain wave inputs are then turned into sequences of wave-maker motions using the wave maker transfer function. In our case, the desired $\eta(t, x = 0)$ series correspond to the measurements at $X_{t_{\text{stat}}} - X_t$. They simply need to be expressed into the Fourier domain to serve as inputs for the wave maker. For the sake of brevity, the wave fields generated from $X_{t_{\text{stat}}} - X_t$ data will be denoted as `EXP ref reprod` or `HOS ref reprod` whether they come from `EXP ref` or `HOS ref` respectively.

a) Frequency cut-off in the wave maker inputs

Due to mechanical limitations, the wave makers of the two ECN tanks can not generate frequencies larger than $f_{\text{max}}^{\text{wvmk}} = 2$ Hz. Consequently the probe measurements at $X_{t_{\text{stat}}} - X_t$, converted into wave maker inputs, are cut at 2 Hz.

For the reproduction of `EXP ref` which is at scale 120, it leads to a cut off at $f = 2.2 f_{p_{\text{target}}}$. One may argue that the `EXP ref` wave field, which was generated by the 2Hz-limited Towing tank wave maker, do not contain frequencies larger than $f = 2$ Hz anyway. However, due to no nonlinear interactions, `EXP ref` measurements at $X_{t_{\text{stat}}} - X_t$ contains frequencies larger than 2 Hz, that can not be reproduced when generating `EXP ref reprod`.

Table 8.2 – Frequency cut-off $f_{\text{max}}^{\text{input}}$ applied to the wave maker inputs.

	`EXP ref` (scale120)	`EXP ref reprod` (scale120)	`HOS ref` (scale 60)	`HOS ref reprod` in a ECN tank (scale 60)	`HOS ref reprod` in `HOS-NWT` (scale 60)
$f_{\text{max}}^{\text{input}}$	2 Hz=$2.2 f_{p_{\text{target}}}$	2 Hz=$2.2 f_{p_{\text{target}}}$	1.4 Hz=$2.2 f_{p_{\text{target}}}$	2 Hz=$3.2 f_{p_{\text{target}}}$	4 Hz=$6.3 f_{p_{\text{target}}}$

Table 8.2 summarizes the cut-off frequencies $f_{\text{max}}^{\text{input}}$ applied to the inputs of the studied wave fields. All the scale-120 inputs are cut at $f = 2.2 f_{p_{\text{target}}}$. For scale-60 data, it depends. `HOS ref` was built with inputs also cut at $f = 2.2 f_{p_{\text{target}}}$, even if the `HOS-NWT` numerical wave maker can generate waves up to 4 Hz$= 6.3 f_{p_{\text{target}}}$. The $f = 2.2 f_{p_{\text{target}}}$ cut off applied to `HOS ref` inputs comes from the target `ss6g5` spectrum shape, used to build the inputs of

iteration 0, which does not contain energy for $f > 2.2f_{p_{\text{target}}}$. However, `HOS ref reprod` inputs are based on $X_{t_{\text{stat}}} - X_t$ measurements containing frequencies larger than $f = 2.2f_{p_{\text{target}}}$. Consequently, they are only limited by the wave maker capabilities (i.e. 2 Hz$= 3.2f_{p_{\text{target}}}$ if `HOS ref` is reproduced in a ECN tank, and 4 Hz$= 6.3f_{p_{\text{target}}}$ if it is reproduced numerically with `HOS-NWT`). Note that the 4 Hz `HOS-NWT` wave maker limit is a parameter that can be modified.

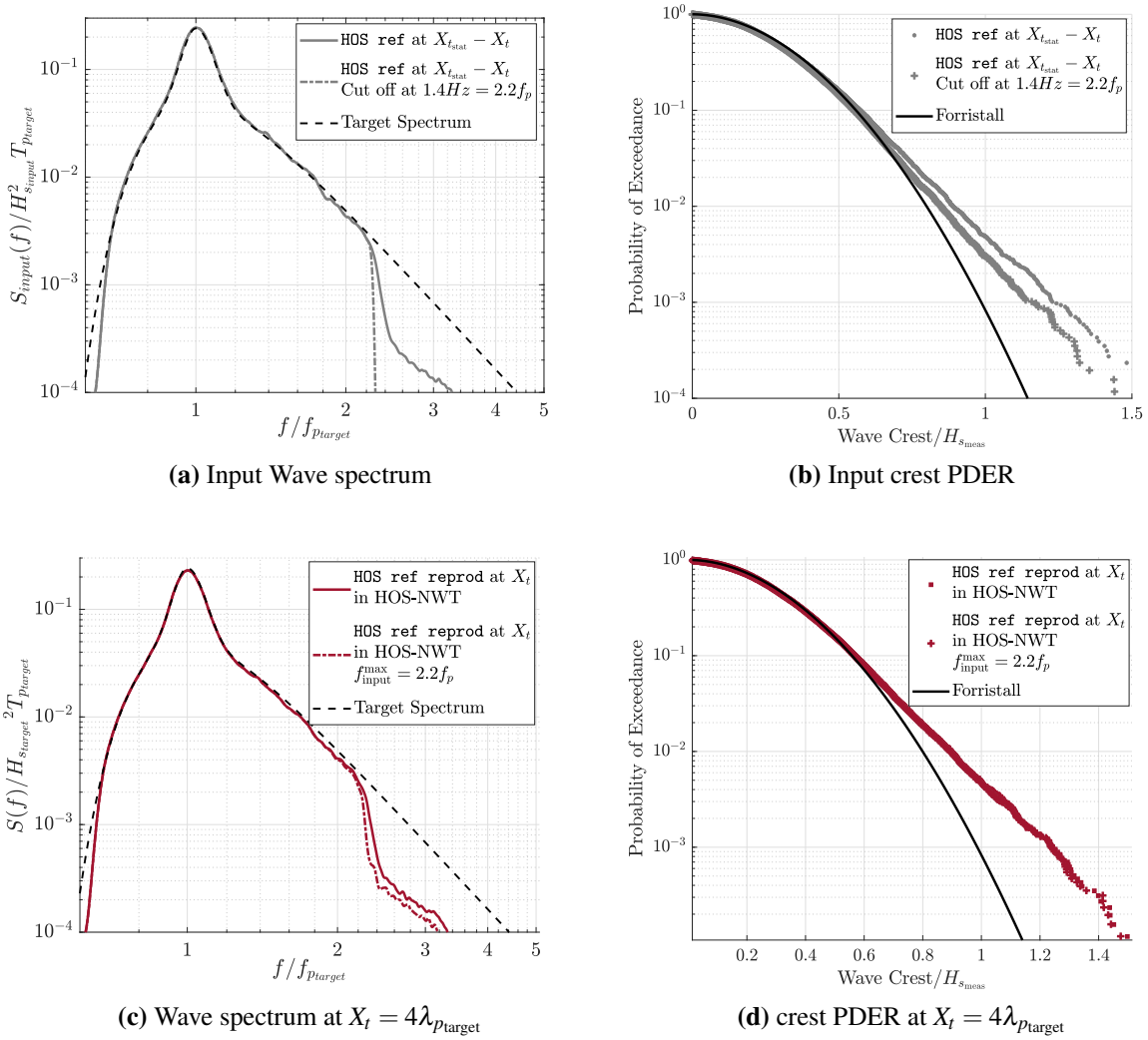

(a) Input Wave spectrum

(b) Input crest PDER

(c) Wave spectrum at $X_t = 4\lambda_{p_{\text{target}}}$

(d) crest PDER at $X_t = 4\lambda_{p_{\text{target}}}$

Figure 8.6 – Influence of $f^{\text{input}}_{\text{max}} = 2.2f_{p_{\text{target}}}$ for `HOS ref reprod` in `HOS-NWT`

Consequences of the frequency cut-off To assess the impact of the frequency cut-off $f_{max}^{input} = 2.2 f_{p_{target}}$, Figure 8.6 compares two numerical wave fields. The first corresponds to `HOS ref reprod` generated in a `HOS-NWT` domain with the implemented limitation of $f_{max}^{input} = 4$ Hz$= 6.3 f_{p_{target}}$, while the second is `HOS ref reprod` generated in the same `HOS-NWT` domain but with an imposed $f_{max}^{input} = 2.2 f_{p_{target}}$ cut off. The cut-off is observed in Fig. 8.6a which presents a comparison of the input spectra. As written above, `HOS ref` inputs are also cut at $f = 2.2 f_{p_{target}}$. However $X_{t_{stat}} - X_t$ measurements contain a bit of energy within the $f > 2.2 f_{p_{target}}$ area. It results from the nonlinear interactions that occur as the waves propagate. Additionally, Fig. 8.6b shows a decrease of the height of the extreme events in the input wave field subjected to the $f_{max}^{input} = 2.2 f_{p_{target}}$ cut off. This result was expected, see Section 1.3.4 where the influence of a frequency cut-off in wave field analysis is evaluated.

However, this discrepancy between the input wave fields does not impact `HOS ref reprod` waves. Whether the f_{max}^{input} is set to $2.2 f_{p_{target}}$ or not, the spectrum at X_t and the crest PDER at X_t remain quasi identical (Fig. 8.6c and 8.6d). An explanation might be that the frequency content larger than $2.2 f_{p_{target}}$ identified in $X_{t_{stat}} - X_t$ measurements, and cut by f_{max}^{input}, is mostly composed of bound waves. They affect the shape of wave profiles but do not influence the propagation. Moreover, they are immediately recreated when generating `HOS ref reprod`. This will be investigated more specifically in the next paragraph.

To conclude, the f_{max}^{input} cut-off imposed by the wave makers does not influence the reproduction of the $X_{t_{stat}}$ references.

b) Influence of the bound waves

As mentioned earlier, to build `EXP ref reprod` and `HOS ref reprod` inputs, the complex nonlinear wave measurements are converted into a linear sum of Fourier components. The bound waves present in the measured signals are converted into free waves by the wave maker. The aim of this paragraph is to quantify the impact on the reproduced signals.

In this respect, a more accurate procedure was tested. The idea is to remove the second-order bound waves from the free surface elevation signal, before converting it into a sum of Fourier components. As a reminder, the bound waves are linked to the skewness of the free surface elevation. Indeed they affect the wave profiles and bring asymmetry between crests and troughs. Removing the bound waves is therefore equivalent to "unskew" the data. The method used is provided in Appendix 1 of Fedele et al. (2010). It assumes a narrow-band spectrum and is based on the framework of the Non Linear Schrödinger equations for water waves. For a given time

series $\eta(t)$, the corresponding signal $\eta_1(t)$, free from the bound waves, is computed as

$$\eta_1(t) = \eta - \frac{\beta}{2}(\eta^2 - \hat{\eta}^2) + \frac{\beta^2}{8}(\eta^3 - 3\eta\hat{\eta}^2) \tag{8.1}$$

with β defined as

$$A_2\beta^2 - A_1\beta + A_0 = 0 \tag{8.2}$$

and $A_0 = \overline{\eta^3}$, $A_1 = 3\frac{\overline{\eta^4} - \overline{\eta^2\hat{\eta}^2}}{2}$, $A_2 = \frac{9\overline{\eta^5} - 21\overline{\eta^3\hat{\eta}^2} + 6\overline{\eta\hat{\eta}^4}}{8}$. $\overline{X}$ corresponds to the temporal mean operator and $\hat{X}$ to the Hilbert transform. Note that there are other procedures for removing bound waves, see for instance Barratt et al. (2020).

The method was applied to unskew `HOS ref` $X_{t_{\text{stat}}} - X_t$ measurements. The resulting data were used to generate a new version of `HOS ref reprod` which will be referred to as `HOS ref unskew reprod`.

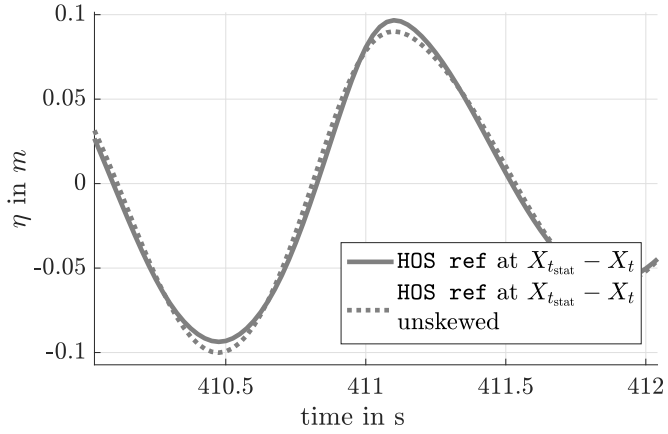

Figure 8.7 – Removing of bound waves in `HOS ref` waves sequences measured at $X_{t_{\text{stat}}} - X_t$

In Figure 8.7, a time-domain comparison is presented between the raw and the unskewed inputs. Note that no significant differences were observed when changing the time window. The wave profile of the unskewed data is symmetric relative to the mean water level. The raw measurements, which contain bound waves, present flatter troughs and shaper crests.

Subsequently, Figure 8.8 compares `HOS ref reprod` and `HOS ref unskew reprod` wave fields, numerically generated in the same `HOS-NWT` domain built from the O.E. tank geometry. The input spectra of these two wave fields are nearly identical up to $f = 2.2 f_{p_{\text{target}}}$ (see Fig. 8.8a). For higher frequencies, the unskewed dataset loses energy, suggesting that this part of the spectrum mainly contains bound waves. Complementary, Fig 8.8b compares the crest

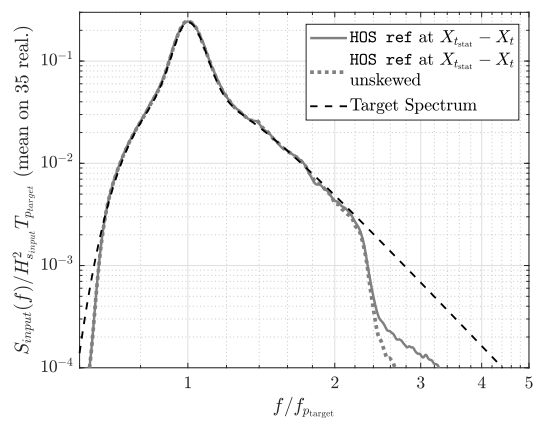

(a) Input Wave spectrum

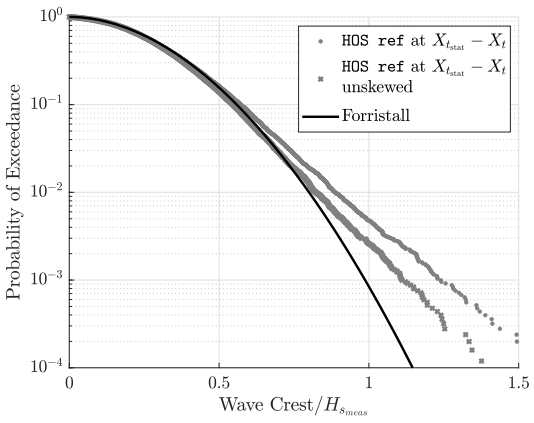

(b) Input crest PDER

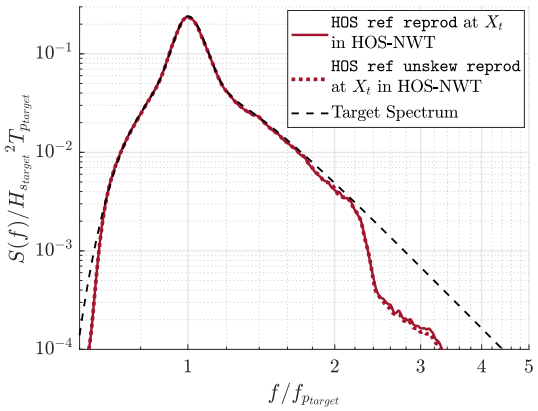

(c) Wave spectrum at $X_t = 4\lambda_{p_{\text{target}}}$

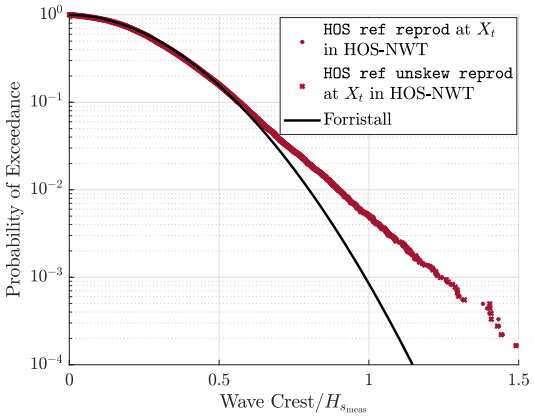

(d) crest PDER at $X_t = 4\lambda_{p_{\text{target}}}$

Figure 8.8 – Comparison of `HOS ref reprod` and `HOS ref unskew reprod` generated in a HOS numerical wave tank

distribution of the inputs. As expected, the unskewed dataset exhibits smaller crests at the same probability level.

Nevertheless, the presence or absence of bound waves in the wave maker inputs does not influence the resulting waves at X_t. `HOS ref reprod` and `HOS ref unskew reprod` have a nearly identical spectrum even for frequencies larger than $2.2f_{p_{\text{target}}}$. Moreover, they present the same crest distribution at $X_t = 4\lambda_{p_{\text{target}}}$. This shows that the bound waves removed from the unskewed inputs have been regenerated during wave propagation. It also indicates that converting `HOS ref` measurement's bound waves into free waves to construct `HOS ref reprod` inputs has no impact on the resulting wave field at X_t.

The conclusion supports the discussion from the previous paragraph. It was explained that there is no impact from a frequency cut-off at $2.2 f_{p_{\text{target}}}$. This lack of impact can be attributed to the fact that the removed frequencies are associated with bound waves. These bound waves do not affect the wave dynamics.

8.3 Step 2: Reproduction of $X_{t_{\text{stat}}}$ references at X_t

This section is dedicated to the analysis of `EXP ref reprod` and `HOS ref reprod` wave fields. To recap, these fields were built to reproduce at $x = X_t$ the exact free surface elevation time series that occurred at $X_{t_{\text{stat}}}$ during `EXP ref` and `HOS ref` generation. The main objective is to have at $x = X_t = 4\lambda_{p_{\text{target}}}$ i) the qualified design spectrum, and ii) the extreme wave statistics usually associated with $x = X_{t_{\text{stat}}} = 53\lambda_{p_{\text{target}}}$.

Consequently, the data at X_t will be compared to `EXP ref` and `HOS ref` waves at $X_{t_{\text{stat}}}$. Note that for each comparison, the analysis time windows and the sets of realizations are meticulously chosen to ensure that the same wave sequences are being compared. No sampling variability affects the comparisons.

8.3.1 Reproduction of the experimental reference

First, our attention turns to the reproductions of `EXP ref`, namely the `EXP ref reprod` wave fields. This designation refers to the wave fields derived from converting `EXP ref` measurements at $X_{t_{\text{stat}}} - X_t$ into input sequences for the wave maker. `EXP ref reprod` realizations were run experimentally in the Towing tank within the scope of Campaign D (like `EXP ref`).

Due to practical reasons, only 26 out of the 30 available seeds were run. As a result, there might be slight discrepancies between the 30-realizations `EXP ref` data presented in Fig. 8.5 and the `EXP ref` data plotted in the current section.

a) Full experimental procedure

Deterministic reproduction Figure 8.9 presents a deterministic comparison between `EXP ref` at $X_{t_{\text{stat}}}$ and `EXP ref reprod` at X_t, for a duration of 100 peak periods. No significant differences are observed when changing the time window. The `EXP ref reprod` measurements align with the `EXP ref` data. The correlation coefficient is consistently greater than 0.8 across the analyzed sequence, and almost no time shift is observed. The slight discrepancies between the two signals arise from: i) the linear conversion of `EXP ref` measured wave signals into

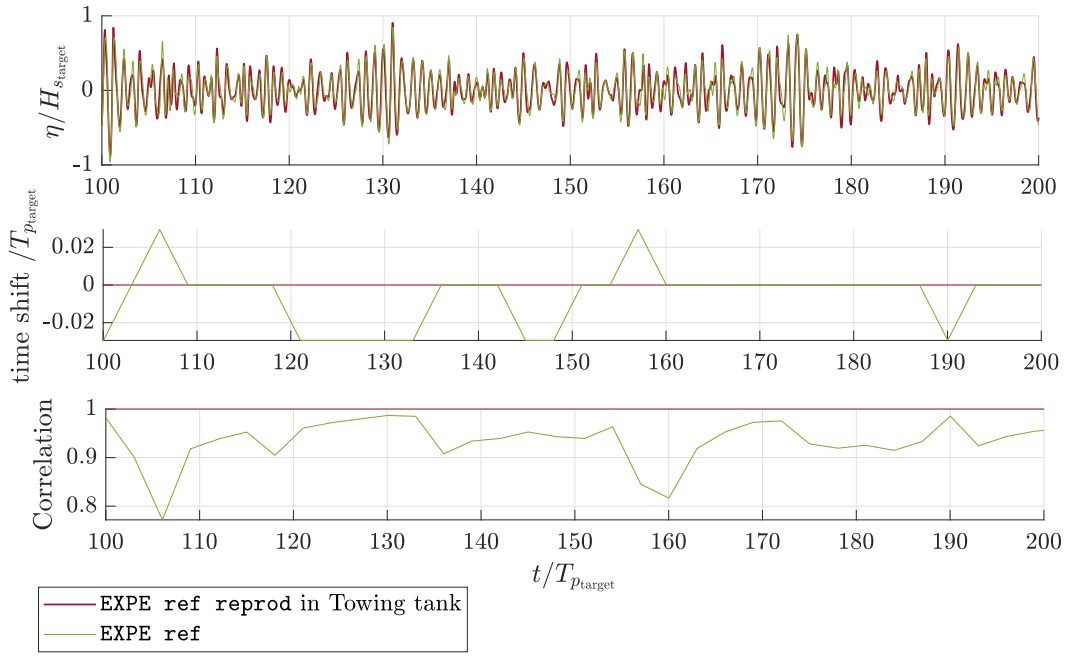

Figure 8.9 – Deterministic comparison of `EXP ref` at $X_{t_{\text{stat}}} - X_t$ and `EXP ref reprod` at X_t

`EXP ref reprod` wave maker input sequences, and ii) the Towing tank wave maker transfer function defects.

Reproduction of the spectrum Figure 8.10 presents a comparison of the stochastic quantities. We observe that the towing tank wave maker transfer function diverges from its theoretical behavior, which is used to convert the input free surface elevation series into wave maker motion sequences. The generated wave heights are slightly larger than expected. In Figure 8.10a, the `EXP ref reprod` H_s (red curve) exhibits an overshoot of 3 to 4 percent. This is also visible in the deterministic comparison in Figure 8.9, where the red curve draws slightly greater heights. Consequently, the `EXP ref reprod` spectrum at X_t is not qualified. It contains excessive energy, particularly around its peak and near $f = 1.3 f_{p_{\text{target}}}$

To overcome this issue, the iterative spectrum correction procedure (detailed in Fig 7.1) was applied to adjust `EXP ref reprod` inputs to balance the behavior of the Towing tank wave maker. Note that the correction slightly adjusts the input amplitudes, but does not modify the phases. The resulting wave field corresponds to the orange curves in Figure 8.10. The excess energy overshoot has been successfully rectified. The spectrum at X_t aligns with

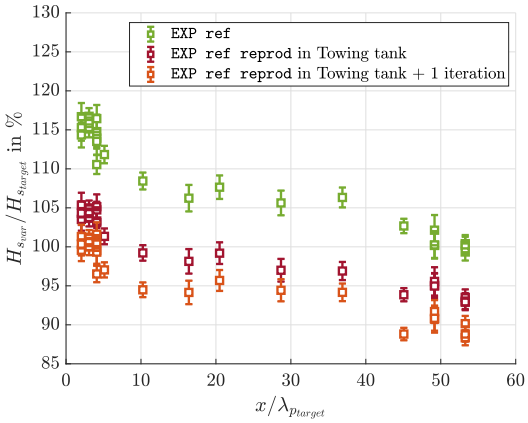

(a) H_s along the tank

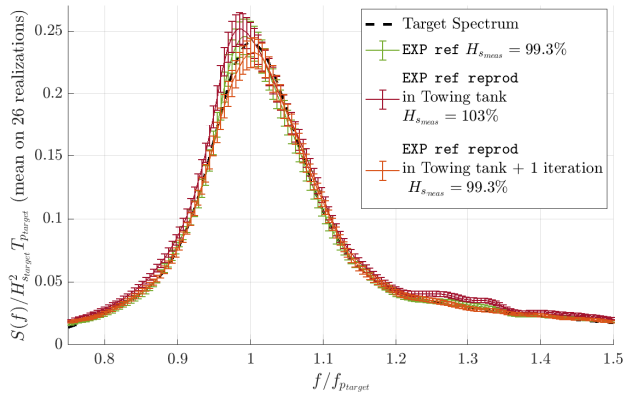

(b) `EXP ref reprod` spectrum at X_t versus `EXP ref` at $X_{t_{\text{stat}}}$

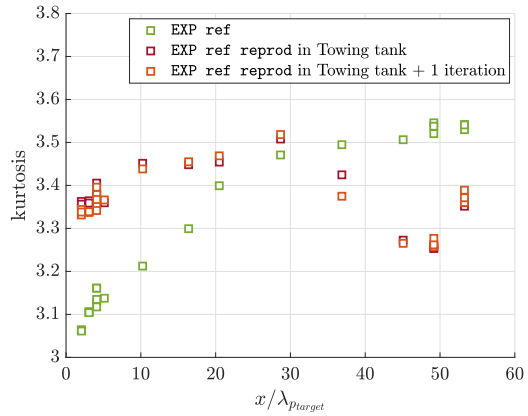

(c) kurtosis along the tank

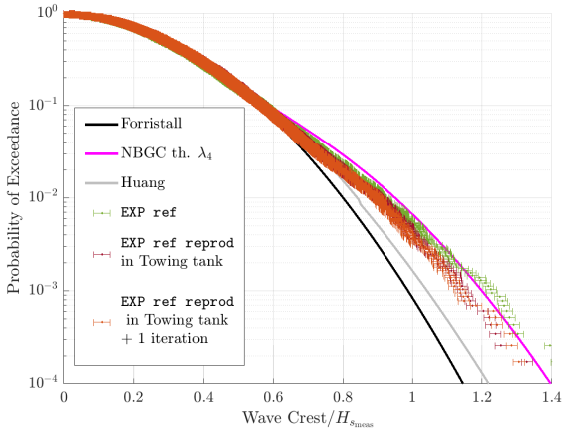

(d) `EXP ref reprod` crest PDER at X_t versus `EXP ref` at $X_{t_{\text{stat}}}$

Figure 8.10 – Comparison of `EXP ref` and `EXP ref reprod` generated in the Towing tank

the `ss6g5` target shape, within the wave gauges' uncertainty ranges. And the significant wave height reaches 99.3% of $H_{s_{\text{target}}}$ at X_t. The first objective is reached, and with an additional correction, the spectrum is qualified at $X_t = 4\lambda_{p_{\text{target}}}$.

Reproduction of the kurtosis and crest distribution Figure 8.10c presents the spatial evolution of the kurtosis along the tank. As expected, for `EXP ref reprod`, the wave maker directly generates the extreme wave field that occurs at the end of the tank for `EXP ref`. Consequently, `EXP ref reprod` kurtosis at $x = X_t = 4\lambda_{p_{\text{target}}}$ equals 3.40, instead of the 3 to 3.1 values observed at this location when using standard wave generation procedures. The 3.52 value

obtained for `EXP ref` at $x = X_{t_{\text{stat}}}$ is almost reached. The remaining difference arises due to a combination of factors including Towing wave maker defects, experimental uncertainties, and the conversion of $X_{t_{\text{stat}}} - X_t$ `EXP ref` signals into wave maker inputs. A more detailed investigation will be conducted in the upcoming subsection, based on numerical simulations. However, the effects stand limited, and a strong departure from Gaussianity is observed from the beginning of the tank thanks to the new procedure.

Figure 8.10d displays `EXP ref reprod` crest PDER obtained at $x = X_t = 4\lambda_{p_{\text{target}}}$. It nearly reaches the `EXP ref` extreme distribution measured at $x = X_{t_{\text{stat}}}$. As observed in the analysis of kurtosis, the probability of extreme events for `EXP ref reprod` is slightly smaller. This difference becomes significantly more pronounced for probabilities below 2.10^{-3}. However, the distribution is undoubtedly extreme and significantly larger than the usual PDER obtained at $4\lambda_{p_{\text{target}}}$ (see Figure 8.2). Note that the additional spectrum correction of `EXP ref reprod` does not affect the kurtosis and the crest PDER.

b) Limitations due to the Towing tank wave maker

To investigate the remaining discrepancies between the crest distributions of `EXP ref reprod` at X_t and `EXP ref` at $X_{t_{\text{stat}}}$, `HOS-NWT` simulations were conducted, reproducing the Towing tank `EXP ref reprod` experiments. The spatial discretization was set to have a maximum modeled wave number of $k_{\text{max}}^{\text{HOS}} = 25k_{p_{\text{target}}}$, and the order of nonlinearity was set to 5. This ensures an accurate nonlinear wave propagation. The numerical domain and wave maker were tuned to mimic the Towing tank geometry.

Two sets of simulations were run: i) one referred to as "`EXP ref reprod` in HOS," which used the `EXP ref reprod` input sequences, and ii) one labeled as "`EXP ref reprod` in HOS with measured Exp. WVMK" which used the recorded wave maker motions from the Towing tank experiments as inputs. The aim was to assess the impact of potential disparities between the input motions and the actual motions recorded during the `EXP ref reprod` experiments.

Figure 8.11 presents the results. The significant wave height of the two `HOS-NWT` datasets remains constant along the tank, as no dissipation model has been implemented to account for side-wall friction, which affects the experimental results. Apart from this discrepancy, "`EXP ref reprod` in HOS with measured Exp. WVMK" follows the experiments. The kurtosis, spectrum, and crest distribution are nearly identical. Additionally, the same significant wave height overshoot observed in the experimental data is also reproduced in the `HOS-NWT` results.

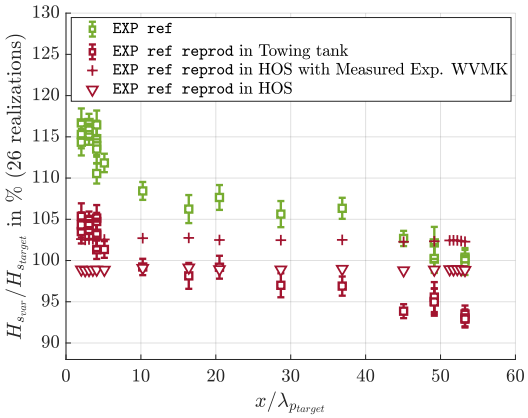

(a) H_s along the tank

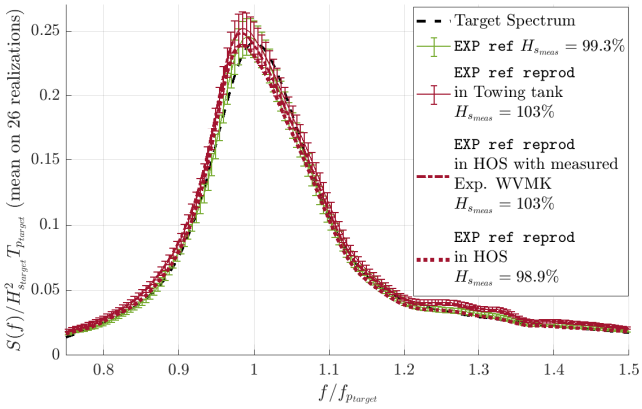

(b) `EXP ref reprod` spectrum at X_t versus `EXP ref` at $X_{t_{\text{stat}}}$

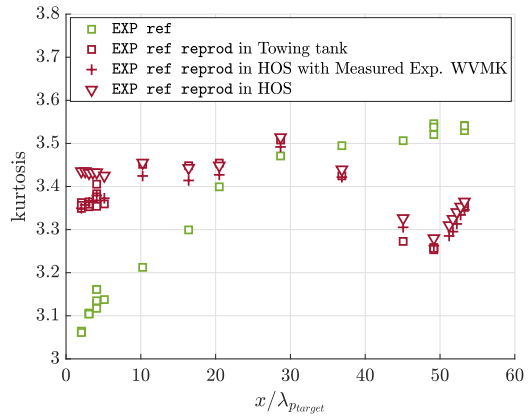

(c) kurtosis along the tank

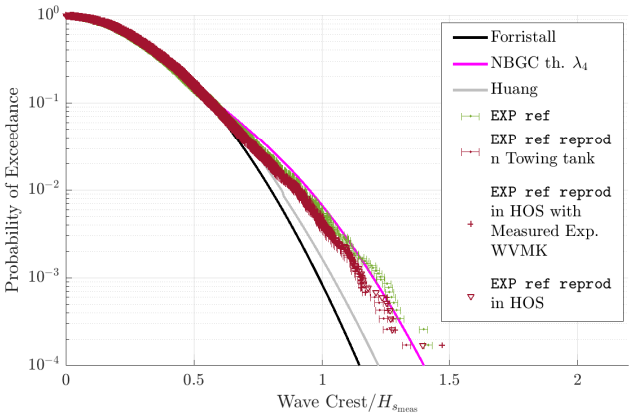

(d) `EXP ref reprod` crest PDER at X_t versus `EXP ref` at $X_{t_{\text{stat}}}$

Figure 8.11 – Influence of the Towing tank wave maker defaults on `EXP ref reprod` statistics at X_t

In contrast, when using the `EXP ref reprod` input sequences directly, the overshooting of significant wave height disappears, and the kurtosis slightly increases. This suggests that the energy overshoot and the slight reduction in the height of extreme events observed in the experimental data come from disparities between the actual wave maker motion sequences and the target wave maker motion sequences. However, the crest distribution of "`EXP ref reprod` in HOS" at X_t does not show a significant improvement and still does not reach the `EXP ref` reference measured at $X_{t_{\text{stat}}}$. The remaining errors are likely to come from the experimental uncertainties and the conversion of $X_{t_{\text{stat}}} - X_t$ `EXP ref` signals into wave maker inputs.

Conclusion The study gives an example of a fully experimental application of the procedure. Even if the accuracy of the `EXP ref reprod` waves is somewhat restricted due to experimental constraints, the objectives are reached. Both a qualified spectrum and an extreme distribution, approximately lying on the $X_{t_{\text{stat}}} = 53\lambda_{p_{\text{target}}}$ reference, were generated at $X_t = 4\lambda_{p_{\text{target}}}$. The remaining error stands within the sampling variability intervals. It only affects the height of the most extreme events which are very sensitive and occur at probabilities below the usual probabilities of design.

8.3.2 Reproduction of the numerical reference

We now address the reproduction of `HOS ref` waves, occurring at $X_{t_{\text{stat}}} = 53\lambda_{p_{\text{target}}}$, closer to the wave maker at $X_t = 4\lambda_{p_{\text{target}}}$. The resulting wave fields are denoted as `HOS ref reprod`. This designation refers to the wave fields derived from converting `HOS ref` numerical data at $X_{t_{\text{stat}}} - X_t$ into input sequences for the wave maker. `HOS ref reprod` realizations were conducted both experimentally in the Ocean Engineering tank within the scope of Campaign F, and numerically using `HOS-NWT` within the same numerical wave tank used for running `HOS ref`. Due to practical reasons, only 28 out of the 35 available seeds will be included in the plots. As a result, there might be slight discrepancies between the 35-realizations `HOS ref` data presented in Fig. 8.5 and the `HOS ref` data plotted in the current section.

Figure 8.12 presents the results. The Ocean Engineering tank's length of 50 m and the settlement of the probe network confine the experimental data within $x \in [0,5]\lambda_{p_{\text{target}}}$. As a reminder, the `HOS-NWT` domain used for conducting the numerical simulation is an extension of the Ocean Engineering tank, elongated to 250 meters, to encompass $X_{t_{\text{stat}}} = 53\lambda_{p_{\text{target}}} = 208$ m.

For both the numerical and experimental versions of `HOS ref reprod` the procedure is working well. At $x = X_t = 4\lambda_{p_{\text{target}}}$, the `ss6g5` H_s and qualified target shape are generated. Moreover, the extreme `HOS ref` distribution occurring at $X_{t_{\text{stat}}} = 53\lambda_{p_{\text{target}}}$ is also accurately reproduced.

Unlike the case of `EXP ref reprod`, no additional spectrum correction is needed and the O.E. tank wave maker perfectly reproduced the statistics. Both the fully numerical and the hybrid approaches (involving the generation of the $X_{t_{\text{stat}}}$ reference with `HOS-NWT` and its reproduction at X_t using experimental facilities) are successfully validated.

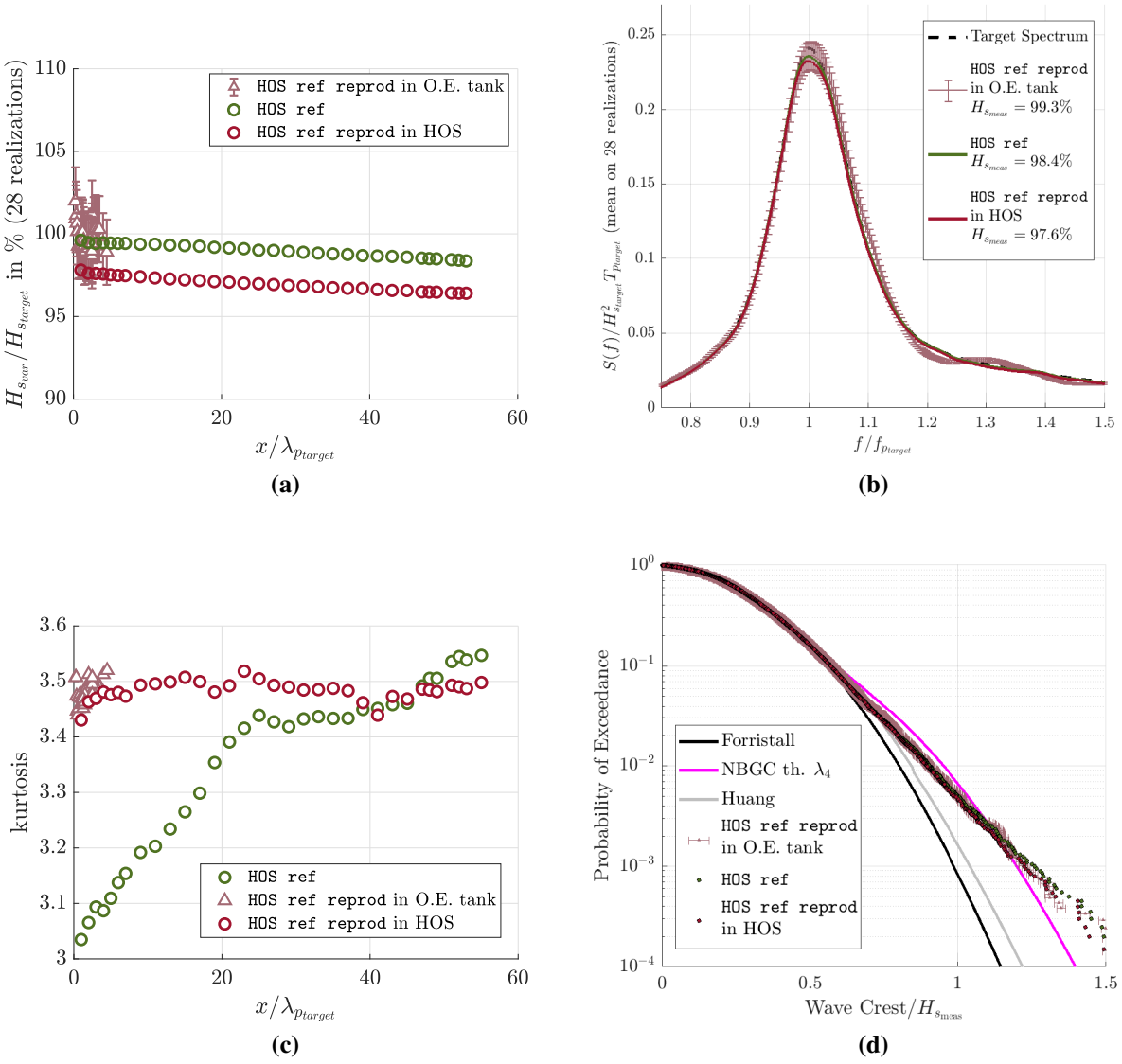

Figure 8.12 – Comparison of `HOS ref` and `HOS ref reprod` generated with `HOS-NWT` and in the O.E. tank

8.4 Conclusion

A new wave generation procedure was introduced. It allows for the generation of a qualified design spectrum associated with extreme wave statistics close to the wavemaker. The procedure was successfully tested using the typical nonlinear `ss6g5` design sea state extensively studied all along this thesis (see Chapter 4 and Section 7.3).

It relied on two main steps, each one consisting of approximately 30 realizations. First, the design spectrum was accurately generated at $X_{t_{\text{stat}}} = 53\lambda_{p_{\text{target}}}$ using the spectrum correction process introduced in Chapter 7 (Step 1). The obtained statistics were extreme, exhibiting a strong departure from the linear Gaussian distribution as well as the Forristall reference. Then, the measurements at $49\lambda_{p_{\text{target}}}$ were converted into inputs for the wave maker, and the sea state was generated at $X_t = 4\lambda_{p_{\text{target}}}$ (Step 2).

The resulting wave field was characterized by i) a qualified spectrum and ii) extreme statistics, usually associated with $X_t = 53\lambda_{p_{\text{target}}}$. When targeting directly the state at $X_t = 4\lambda_{p_{\text{target}}}$ (i.e. without using a procedure to control the statistics), the distribution usually obtained $X_t = 4\lambda_{p_{\text{target}}}$ is significantly less extreme.

The process was conducted experimentally using the ECN Towing tank, numerically based on `HOS-NWT` simulations, and using a hybrid approach involving the generation of the $X_{t_{\text{stat}}}$ reference with `HOS-NWT` (Step 1) and its reproduction at X_t using the ECN ocean engineering tank (step 2). The fully experimental application of the procedure is highly time-consuming, and the final crest distribution at X_t is slightly less extreme than the $X_{t_{\text{stat}}}$ reference. The numerical and hybrid approaches are more accurate and easier to conduct.

It is important to understand that with the state-of-the-art wave generation procedures, the statistical quantities (crest PDER, kurtosis) evolve along the tank. This was observed in the first step of the present study. The newly introduced procedure allows us to get free of this evolution, and to reproduce at a given position the statistics that usually appear further in the tank. The study opens the way to an accurate control of the wave statistics at any location in a wave tank environment.

CONCLUSION

Overview of the present work

The objective of this Ph.D. thesis was to develop wave generation and qualification procedures for accurately controlling the sea states generated through a stochastic approach, in experimental or numerical wave tanks. The framework was limited to unidirectional irregular deep-water wave conditions, and the research was exclusively focused on wave studies, without structures present in the domain.

First, the problem of irregular wave propagation was addressed from theoretical (Chapter 2), experimental (Chapters 3 and 4), and numerical (Chapter 5) points of view. Then, an existing wave generation and qualification procedure, recommended by several actors of the ocean engineering community (ITTC, 2021; NWT Preparation Workgroup, 2019) was extensively tested. The procedure aims at generating accurately a design wave spectrum at any target location X_t in the domain, by iterating on the wave-maker inputs. The limitations of the procedure were explored in detail. Then, facing the influence of X_t on the wave statistics, a new procedure was introduced to better control the statistical distributions independently of X_t.

The nonlinear potential wave solver `HOS-NWT` (Ducrozet et al., 2012), developed by Ecole Centrale de Nantes (ECN), was employed for numerical studies. Long-duration experimental campaigns were conducted using the ECN facilities, including the ECN Towing tank and the ECN Ocean engineering tank [1]. A large-size experimental database was generated and analyzed. This section summarizes the main findings.

Experimental uncertainties

In Chapter 3, following ITTC (2017a) ITTC (2008) and ISO/IEC (2008) guidelines, a strategy was developed and implemented to estimate the uncertainties that affect the quality of the experimental results. The values found are specific to the ECN facilities and the generated sea states. However, the methodology can be generalized.

Uncertainties were divided into two groups: the Type-A uncertainties (repeatability

1. `https://lheea.ec-nantes.fr/english-version/test-facilities`

issues) and the Type-B uncertainties. The Type-B group includes the measurement uncertainty, the generation uncertainty (the differences between the expected waves assuming a perfect environment and the generated waves) and the sampling variability (the differences between the statistically converged quantities and the one computed with limited data size).

Uncertainty ranges were derived for the measurement uncertainty and the sampling variability. The measurement standard uncertainty was estimated to $\approx 2\%$ for the free surface elevation. Regarding the sampling variability, it was found that i) the significant wave height is almost statistically converged with one realization only, ii) $T_{\text{analyzed}} \geq 4000T_p$ allows for the convergence of the spectrum, kurtosis, and skewness for most of the cases, iii) nonlinear wave fields exhibiting large kurtosis values require $T_{\text{analyzed}} \geq 10000T_p$.

Moreover, it was observed that spurious transverse modes can significantly affect the results. For the Towing tank experiments, strategies were implemented to remove their influence. Lastly, a repeatability study showed differences between repeated runs. The discrepancies increased with the distance from the wave maker. The ability of wave tanks to reproduce a given irregular wave sequence is limited by this phenomenon.

Experimental uncertainties should be taken into account in the wave qualification procedures. The criteria at use (see ITTC (2021); NWT Preparation Workgroup (2019)) require quality levels that are sometimes not adapted for experimental wave fields.

Wave propagation in a wave tank environment

In Chapter 4, the propagation of a narrow-band design sea state in the ECN Towing tank was studied in detail (`ss6g5`, defined in Sec. 1.2). This sea state is non-breaking and has a moderate Benjamin Feir Index value $BFI = 0.5$, which means that nonlinear interactions among the wave field components are likely to be important.

It was observed that the spectrum evolves in space due to the combined actions of side walls dissipation and nonlinear wave interactions. Moreover, the probability of extreme events increased along the tank. As a result, at the end of the domain (fifty wavelengths from the wave maker) the crest distribution, which is commonly used to assess the severity of the wave field, shows a strong departure from the reference distributions provided by the state-of-the-art wave qualification procedures (ITTC, 2021; NWT Preparation Workgroup, 2019; Det Norske Veritas, 2010). It was found that this important probability of extreme events is correlated with a time-domain rearrangement of the free surface elevation i.e. envelope modulations. This is induced by nonlinear wave interactions. The latter were tracked in the experimental data by using high-order spectra. A specific slice of the trispectrum enlightened the presence of

Benjamin Feir instabilities (Benjamin and Feir, 1967) at the end of the tank.

In addition, in Chapter 5, while comparing `HOS-NWT` numerical data with experiments, we observed that strongly-breaking conditions affect the shape of the spectrum and limit evolution in space of the wave statistics. For ocean engineering studies, all these phenomena must be taken into account by the wave generation procedures.

Control of the wave spectrum

In Chapter 7, the iterative spectrum correction procedure recommended by ITTC (2021) and NWT Preparation Workgroup (2019) guidelines was tested experimentally and numerically for various configurations: mild conditions (`ss6`), strongly-breaking conditions (`GOM`), and non-breaking conditions in a long tank where side walls induce dissipation (`ss6g5`).

Efficiency and limitations of the spectrum correction For non-breaking sea states, not affected by side walls dissipation, one iteration is enough to qualify the spectrum at X_t. With side wall dissipation, depending on the target location, 4 iterations may be needed. X_t larger than $50\lambda_{p_{\text{target}}}$ can be achieved. For strongly-breaking sea states the number of iterations is around 4, and the procedure can not achieve the generation of the target spectrum at locations larger than $6\lambda_{p_{\text{target}}}$. For these locations, the dissipation induced by breaking events is too strong. Adding energy in the wave-maker inputs triggers more breaking events and does not improve the spectrum at X_t.

The procedure was validated numerically and experimentally. No significant difference in efficiency was observed. However, we found that the spectrum accuracy of $C = \pm 5\%$ within $f \in [0.75 f_{p_{\text{target}}}; 1.5 f_{p_{\text{target}}}]$ can only be reached for numerical wave fields. In experiments, because of measurement and generation uncertainties, $C = \pm 10\%$ is more realistic.

In addition, when generating experimentally a sea state, the number of iterations needed remains the same whether calibrating the input prior experiments with `HOS-NWT` or starting from $S_{\text{input}} = S_{\text{design}}$.

Qualified spectrum and wave statistics We observed that a single qualified spectrum can be associated with different statistical behaviors, depending on i) the distance from the wave maker and ii) the spectrum tail content.

We concluded that, for non-breaking unidirectional sea states, due to high-order nonlinear interactions, the distance from the wave maker induces a rearrangement of the wave phases, modulating the envelope and increasing the probability of the extreme events, even when calibrating

the spectrum with the iterative correction procedure. Accurately controlling the spectrum is therefore not enough to control the statistics.

In addition, we observed that, $\pm 10\%$ spectrum deviations within $[0.75 f_{p_{\text{target}}}; 1.5 f_{p_{\text{target}}}]$ do not affect the statistics, but a high-frequency cut-off in the inputs (leading to differences in the spectrum tail) increases the probability of the extreme events. However, the influence of distance from the wave maker was found to be the predominant factor influencing the statistics of a qualified wave field.

Control of the wave statistics

The wave statistics, and especially the crest distribution, are of major importance for ocean engineering studies. They need to be predicted and if possible controlled whatever X_t. Therefore, to get free from the influence of X_t on the wave statistics, in Chapter 8, a new wave generation procedure was introduced. It allows for the generation of a qualified design spectrum associated with extreme wave statistics close to the wavemaker. The procedure was successfully tested using the typical nonlinear `ss6g5` design sea state extensively studied all along the thesis.

It relied on two main steps. First, the design spectrum was accurately generated at $X_{t_{\text{stat}}} = 53\lambda_{p_{\text{target}}}$ using the spectrum correction process introduced in Chapter 7 (Step 1). The obtained statistics were extreme. Then, the measurements at $49\lambda_{p_{\text{target}}}$ were converted into inputs for the wave maker, and the sea state was generated at $X_t = 4\lambda_{p_{\text{target}}}$ (Step 2).

The resulting wave field was characterized by i) a qualified spectrum and ii) extreme statistics, usually associated with $X_t = 53\lambda_{p_{\text{target}}}$. When targeting directly the state at $X_t = 4\lambda_{p_{\text{target}}}$ (i.e. without using a procedure to control the statistics), the distribution usually obtained $X_t = 4\lambda_{p_{\text{target}}}$ was significantly less extreme.

The process was conducted experimentally using the ECN Towing tank, numerically based on `HOS-NWT` simulations, and using a hybrid approach involving the generation of the $X_{t_{\text{stat}}}$ reference with `HOS-NWT` (Step 1) and its reproduction at X_t using the ECN ocean engineering tank (step 2). The fully experimental application of the procedure is more time-consuming, and the final crest distribution at X_t is slightly less extreme than the $X_{t_{\text{stat}}}$ reference. The numerical and hybrid approaches are more accurate and easier to conduct.

It is important to understand that with the state-of-the-art wave generation procedures, the statistical quantities (crest PDER, kurtosis) evolve along the tank. The newly introduced procedure allows us to get free of this evolution, and to reproduce at a given position the statistics that usually appear further in the tank.

Perspectives and proposals for future works

The studies performed in this thesis raise some questions and open the way for future works. Several topics were partially addressed and further investigations should be carried out to fine-tune the findings. In this respect, the following paragraphs provide some proposals for future works.

Estimation of experimental uncertainties First, the estimation of the experimental uncertainties (Chapter 3) can be improved. Ranges need to be derived to account for the Type-A uncertainties. To this end, specific experiments should be conducted, varying the repeated wave condition and the tank. Moreover, the increase in standard deviation among the repeated runs ($\overline{STD_{\eta}^{\text{run}}}$), observed along the tank in experiments, needs to be better understood. The next step is to reproduce it numerically with `HOS-NWT` by including residual waves and currents in the initial conditions.

Trispectrum analysis Then, in Chapter 4, Benjamin Feir's instabilities interactions were tracked with a specific slice of the trispectrum of the free surface elevation. Analyzing wave fields with high-order-spectra is still a research field at the stage of development. The interpretation of the trispectrum is complex. The number of windows required to completely remove the influence of the frequency components not resulting from interactions is known to be huge (Collis et al., 1998; Ewans et al., 2021). In this thesis, this issue was tackled by comparing the data to semi-artificial linear signals. Other methods exist and can be tested (Collis et al., 1998; Ewans et al., 2021). Moreover, the entire 3D shape of the trispectrum should be examined to see if other nonlinear interactions contribute to the increase in the probability of extreme events.

Control of the spectrum at a target location Next, the spectrum correction procedure studied in Chapter 7 can be improved. The corrective coefficients applied to the wave-maker inputs are linear. They are defined in the Fourier space as the ratio of target amplitude to measured amplitude. More complex coefficients can be derived, adapting the magnitude of the correction to the sensitivity of the measured spectrum. However, with the configurations tested in this thesis, the number of iterations does not exceed 4. An improved corrective coefficient would not result in significant time savings.

Influence of the spectrum shape on the wave statistics Besides in Chapter 7, the influence of the spectrum shape on the wave statistics was partially addressed. Additional tests are needed

to determine i) which exact part of the spectrum tail influences the statistics and ii) to what extent the spectrum deviations around the peak do not affect the statistics. Different wave conditions, including breaking waves, need to be investigated.

Control of the wave statistics at a target location In Chapter 8, a procedure was introduced to reproduce at a given position the statistics that usually appear further in the tank. A procedure also needs to be developed for the inverse problem, i.e. reproducing at a given position the statistics that usually appear closer to the wave maker. This is already subject of an ongoing internal work at ECN.

Next is the question of which crest distribution to target. For ocean engineering studies, the definition of a reference to target, independently of X_t, is still necessary. This needs to be addressed by the classification societies.

Extension to multi-directional wave conditions Lastly, in the direct continuity of this Ph.D. thesis, the scope of the studies must be extended to multi-directional sea states, which represent more realistic wave conditions.

The wave generation procedures developed in this thesis to control the sea state at a target location X_t need to be adapted. To control the spectrum, iterating on the wave-maker inputs might still work. Nonetheless, this will be more difficult to implement, as the wave maker inputs for directional wave fields are more complex. This topic is addressed at ECN with the ongoing Ph.D. thesis of Solène Darrigo.

In addition, with directional wave fields, the evolution in space of the statistics is limited. Experimental observations in tanks (Onorato et al., 2009) and theoretical predictions (Fedele, 2015) tend to say that for directional sea states, the kurtosis first increases in space, reaches a maximum value, and then decreases. In this context, a crest distribution to target also needs to be defined.

It should also be mentioned that measuring directional sea states in wave basins is not an easy task. Accurate 2D measurement systems, adapted to the model scale, are still at the stage of development. Arrays of wave gauges need to be carefully positioned to deduce the wave field directional information. For instance, this makes difficult the validation of $2D$ breaking models for nonlinear potential wave solvers such as `HOS-NWT`. This topic is addressed at ECN with the ongoing Ph.D. thesis of Ying Wang.

BIBLIOGRAPHY

G. B. Airy. *Tides and waves*. B. Fellowes, 1845.

I. Alber. The effects of randomness on the stability of two-dimensional surface wavetrains. *Proceedings of the Royal Society of London. A. Mathematical and Physical Sciences*, 363 (1715):525–546, 1978.

S. Aliyar, G. Ducrozet, B. Bouscasse, F. Bonnefoy, V. Sriram, and P. Ferrant. Numerical coupling strategy using hos-openfoam-moordyn for oc3 hywind spar type platform. *Ocean Engineering*, 263:112206, 2022.

M. A. Alkhalidi and M. A. Tayfun. Generalized boccotti distribution for nonlinear wave heights. *Ocean engineering*, 74:101–106, 2013.

T. L. Andersen, M. Clavero, M. R. Eldrup, P. B. Frigaard, and M. Losada. Active absorption of nonlinear irregular waves. In *Coastal Engineering 2018*. Coastal Engineering Research Council, 2018.

S. Y. Annenkov and V. Shrira. Evolution of kurtosis for wind waves. *Geophysical Research Letters*, 36(13), 2009.

S. Y. Annenkov and V. I. Shrira. Role of non-resonant interactions in the evolution of nonlinear random water wave fields. *Journal of Fluid Mechanics*, 561:181–207, 2006.

A. Babanin. *Breaking and dissipation of ocean surface waves*. Cambridge University Press, 2011.

M. L. Banner and W. L. Peirson. Wave breaking onset and strength for two-dimensional deep-water wave groups. *Journal of Fluid Mechanics*, 585:93–115, 2007.

D. Barratt, H. B. Bingham, P. H. Taylor, T. S. van den Bremer, and T. A. Adcock. Linearization of the wave spectrum: A comparison of methods. In *International Conference on Offshore Mechanics and Arctic Engineering*, volume 84324, page V02AT02A006. American Society of Mechanical Engineers, 2020.

X. Barthelemy, M. Banner, W. Peirson, F. Fedele, M. Allis, and F. Dias. On a unified breaking onset threshold for gravity waves in deep and intermediate depth water. *Journal of Fluid Mechanics*, 841:463–488, 2018.

V. L. Belenky, K. M. Weems, W. M. Lin, and J. R. Paulling. Probabilistic analysis of roll parametric resonance in head seas. In *Fluid Mechanics and its Applications*, volume 97, pages 555–569. Springer, 2011. ISBN 9789400714816. doi: 10.1007/978-94-007-1482-3_31.

T. B. Benjamin and J. E. Feir. The disintegration of wave trains on deep water part 1. theory. *Journal of Fluid Mechanics*, 27(3):417–430, 1967.

P. Boccotti. Quasi-determinism of sea wave groups. *Meccanica*, 24:3–14, 1989.

F. Bonnefoy. *Modélisation expérimentale et numérique des états de mer complexes*. PhD thesis, Université de Nantes, 2005.

F. Bonnefoy, A. Tikan, F. Copie, P. Suret, G. Ducrozet, G. Prabhudesai, G. Michel, A. Cazaubiel, E. Falcon, G. El, et al. From modulational instability to focusing dam breaks in water waves. *Physical Review Fluids*, 5(3):034802, 2020.

C. L. Bretschneider. *Wave variability and wave spectra for wind-generated gravity waves*. Number 118. The Board, 1959.

L. D. Brown, T. T. Cai, and A. DasGupta. Interval estimation for a binomial proportion. *Statistical science*, pages 101–117, 2001.

B. Buchner, G. Forristall, K. Ewans, M. Christou, and J. Hennig. New insights in extreme crest height distributions: A summary of the 'crest'jip. In *International Conference on Offshore Mechanics and Arctic Engineering*, volume 44342, pages 589–604, 2011.

Bureau Veritas. NI638 Guidance for Long-term Hydro-structure Calculations, 2019.

M. Canard, G. Ducrozet, and B. Bouscasse. Generation of 3hr long-crested waves of extreme sea states with hos-nwt solver. In *ASME 2020 39th International Conference on Ocean, Offshore and Arctic Engineering*. American Society of Mechanical Engineers Digital Collection, 2020.

M. Canard, G. Ducrozet, and B. Bouscasse. Experimental reproduction of an extreme sea state in two wave tanks at various generation scales. In *OCEANS 2022-Chennai*, pages 1–6. IEEE, 2022a.

M. Canard, G. Ducrozet, and B. Bouscasse. Varying ocean wave statistics emerging from a single energy spectrum in an experimental wave tank. *Ocean Engineering*, 246:110375, 2022b.

M. Casas-Prat and L. H. Holthuijsen. Short-term statistics of waves observed in deep water. *Journal of Geophysical Research: Oceans*, 115(C9), 2010.

A. Chabchoub, N. Hoffmann, M. Onorato, and N. Akhmediev. Super rogue waves: observation of a higher-order breather in water waves. *Physical Review X*, 2(1):011015, 2012.

Z. Cherneva, M. Tayfun, and C. Guedes Soares. Statistics of nonlinear waves generated in an offshore wave basin. *Journal of Geophysical Research: Oceans*, 114(C8), 2009.

Y. Choi, Y. V. Lvov, S. Nazarenko, and B. Pokorni. Anomalous probability of large amplitudes in wave turbulence. *Physics Letters A*, 339(3-5):361–369, 2005.

Y.-M. Choi, Y. J. Kim, B. Bouscasse, S. Seng, L. Gentaz, and P. Ferrant. Performance of different techniques of generation and absorption of free-surface waves in computational fluid dynamics. *Ocean Engineering*, 214:107575, 2020.

M. Christou and K. Ewans. Field measurements of rogue water waves. *Journal of physical oceanography*, 44(9):2317–2335, 2014.

W. Collis, P. White, and J. Hammond. Higher-order spectra: the bispectrum and trispectrum. *Mechanical systems and signal processing*, 12(3):375–394, 1998.

H. I. Copuroglu and E. Pesman. Analysis of flettner rotor ships in beam waves. *Ocean Engineering*, 150:352–362, 2018.

A. D. D. Craik. The origins of water wave theory. *Annual Review of Fluid Mechanics*, 36:1–28, 2004.

L. Deike, M. Berhanu, and E. Falcon. Decay of capillary wave turbulence. *Physical Review E*, 85(6):066311, 2012.

L. Deike, B. Miquel, P. Gutiérrez, T. Jamin, B. Semin, M. Berhanu, E. Falcon, and F. Bonnefoy. Role of the basin boundary conditions in gravity wave turbulence. *Journal of Fluid Mechanics*, 781:196–225, 2015.

G. Dematteis, T. Grafke, M. Onorato, and E. Vanden-Eijnden. Experimental evidence of hydrodynamic instantons: the universal route to rogue waves. *Physical Review X*, 9(4): 041057, 2019.

M. Derakhti and J. T. Kirby. Bubble entrainment and liquid–bubble interaction under unsteady breaking waves. *Journal of fluid mechanics*, 761:464–506, 2014.

M. Derakhti, J. T. Kirby, M. L. Banner, S. T. Grilli, and J. Thomson. A unified breaking onset criterion for surface gravity water waves in arbitrary depth. *Journal of Geophysical Research: Oceans*, 125(7):e2019JC015886, 2020.

Q. Derbanne, O. Menard, M. Darquier, and D. Frechou. Génération, propagation et dissipation de la houle en bassin d'essai de très grande longueur. In *Proc. of ATMA 2019*, 2009.

Det Norske Veritas. Environmental conditions and environmental loads, recommended practice dnv-rp-c205, 2010.

D. G. Dommermuth and D. K. Yue. A high-order spectral method for the study of nonlinear gravity waves. *Journal of Fluid Mechanics*, 184:267–288, 1987.

D. A. Drazen, W. K. Melville, and L. Lenain. Inertial scaling of dissipation in unsteady breaking waves. *Journal of fluid mechanics*, 611:307–332, 2008.

G. Ducrozet. *Modélisation des processus non-linéaires de génération et de propagation d'états de mer par une approche spectrale*. PhD thesis, Université de Nantes; Ecole Centrale de Nantes (ECN), 2007.

G. Ducrozet and M. Gouin. Influence of varying bathymetry in rogue wave occurrence within unidirectional and directional sea-states. *Journal of Ocean Engineering and Marine Energy*, 3:309–324, 2017.

G. Ducrozet, F. Bonnefoy, D. Le Touzé, and P. Ferrant. A modified high-order spectral method for wavemaker modeling in a numerical wave tank. *European Journal of Mechanics-B/Fluids*, 34:19–34, 2012.

G. Ducrozet, F. Bonnefoy, D. Le Touzé, and P. Ferrant. Hos-ocean: Open-source solver for nonlinear waves in open ocean based on high-order spectral method. *Computer Physics Communications*, 203:245–254, 2016.

G. Ducrozet, F. Bonnefoy, and Y. Perignon. Applicability and limitations of highly non-linear potential flow solvers in the context of water waves. *Ocean Engineering*, 142:233–244, 2017.

K. Dysthe, H. E. Krogstad, and P. Müller. Oceanic rogue waves. *Annu. Rev. Fluid Mech.*, 40: 287–310, 2008.

K. Ewans, M. Christou, S. Ilic, and P. Jonathan. Identifying higher-order interactions in wave time-series. *Journal of Offshore Mechanics and Arctic Engineering*, 143(2):021201, 2021.

E. Fadaeiazar, J. Leontini, M. Onorato, T. Waseda, A. Alberello, and A. Toffoli. Fourier amplitude distribution and intermittency in mechanically generated surface gravity waves. *Physical Review E*, 102(1), 2020a. ISSN 24700053. doi: 10.1103/PhysRevE.102.013106.

E. Fadaeiazar, J. Leontini, M. Onorato, T. Waseda, A. Alberello, and A. Toffoli. Fourier amplitude distribution and intermittency in mechanically generated surface gravity waves. *Physical Review E*, 102(1):013106, 2020b.

F. Fedele. On the kurtosis of deep-water gravity waves. *Journal of Fluid Mechanics*, 782:25–36, 2015.

F. Fedele, Z. Cherneva, M. Tayfun, and C. Guedes Soares. Nonlinear schrödinger invariants and wave statistics. *Physics of Fluids*, 22(3):036601, 2010.

F. Fedele, A. Benetazzo, and G. Z. Forristall. Space-time waves and spectra in the northern adriatic sea via a wave acquisition stereo system. In *International Conference on Offshore Mechanics and Arctic Engineering*, volume 44342, pages 651–663, 2011.

F. Fedele, J. Brennan, S. P. De León, J. Dudley, and F. Dias. Real world ocean rogue waves explained without the modulational instability. *Scientific reports*, 6:27715, 2016.

J. D. Fenton. A fifth-order stokes theory for steady waves. *Journal of Waterway, Port, Coastal and Ocean Engineering*, 111(2):216–234, 1985. ISSN 0733950X. doi: 10.1061/(ASCE) 0733-950X(1985)111:2(216).

G. Z. Forristall. Wave crest distributions: Observations and second-order theory. *Journal of physical oceanography*, 30(8):1931–1943, 2000.

G. Z. Forristall. Joint wave height and period statistics from linear simulations. *Journal of Ocean Engineering and Marine Energy*, 3(3):221–231, 2017.

S. Fouques, C. Eloïse, H.-J. Lim, J. Kim, M. Canard, G. Ducrozet, B. Bouscasse, A. Koop, B. Zhao, W. Wang, and H. Bihs. Qualification criteria for the verification of numerical waves - part 1: Potential-based numerical wave tank (pnwt). In *ASME 2021 40th International Conference on Ocean, Offshore and Arctic Engineering*. American Society of Mechanical Engineers Digital Collection, 2021.

D. R. Fuhrman, P. A. Madsen, and H. B. Bingham. A numerical study of crescent waves. *Journal of Fluid Mechanics*, 513:309–341, 2004.

E. Funke and E. Mansard. On the synthesis of realistic sea states. In *Coastal Engineering 1980*, pages 2974–2991. 1980.

C. Garrett. On cross-waves. *Journal of Fluid Mechanics*, 41(4):837–849, 1970.

T. Grafke and E. Vanden-Eijnden. Numerical computation of rare events via large deviation theory. *Chaos: An Interdisciplinary Journal of Nonlinear Science*, 29(6):063118, 2019.

M. Greco, B. Bouscasse, and C. Lugni. 3-d seakeeping analysis with water on deck and slamming. part 2: Experiments and physical investigation. *Journal of fluids and structures*, 33:148–179, 2012.

M. C. Haller and R. A. Dalrymple. Looking for wave groups in the surf zone. In *Proc. Coastal Dynamics*, volume 95, pages 81–92, 1995.

S. L. Han and T. Kinoshita. Investigation of a stochastic inverse method to estimate an external force: Applications to a wave-structure interaction. *Mathematical Problems in Engineering*, 2012, 2012. ISSN 1024123X. doi: 10.1155/2012/175036.

K. Hasselmann, T. P. Barnett, E. Bouws, H. Carlson, D. E. Cartwright, K. Enke, J. Ewing, A. Gienapp, D. Hasselmann, P. Kruseman, et al. Measurements of wind-wave growth and swell decay during the joint north sea wave project (jonswap). *Ergaenzungsheft zur Deutschen Hydrographischen Zeitschrift, Reihe A*, 1973.

S. Haver. Evidences of the existence of freak waves. In *Rogue waves*, pages 129–140. Ifremer Brest, 2001.

D. Henderson, G. K. Rajan, and H. Segur. Dissipation of narrow-banded surface water waves. In *Hamiltonian Partial Differential Equations and Applications*, pages 163–183. Springer, 2015.

W. Huang and S. Dong. Statistical description of wave groups in three types of sea states. *Ocean Engineering*, 225:108745, 2021.

Z. J. Huang and Q. Guo. Semi-empirical crest distributions of long-crest nonlinear waves of three-hour duration. In *ASME 2017 36th International Conference on Ocean, Offshore and Arctic Engineering*. American Society of Mechanical Engineers Digital Collection, 2017.

Z. J. Huang and Y. Zhang. Semi-empirical single realization and ensemble crest distributions of long-crest nonlinear waves. In *ASME 2018 37th International Conference on Ocean, Offshore and Arctic Engineering*. American Society of Mechanical Engineers Digital Collection, 2018.

R. T. Hudspeth and J. R. Medina. Wave group analysis by the hilbert transform. In *Coastal Engineering 1988*, pages 884–898. 1989.

M. Huseby and J. Grue. An experimental investigation of higher-harmonic wave forces on a vertical cylinder. *Journal of Fluid Mechanics*, 414:75–103, 2000. ISSN 00221120. doi: 10.1017/S0022112000008533.

ISO/IEC. Part 3: Guide to the expression of uncertainty in measurement, 2008.

ITTC. Guide to the expression of uncertainty in experimental hydrodynamics, 2008.

ITTC. Recommended Procedures and Guidelines - Seakeeping Experiments, 2017a.

ITTC. Recommended procedures and guidelines - uncertainty analysis, instrument calibration, 2017b.

ITTC. Recommended Procedures and Guidelines: 7.5-02-07-01.2 Laboratory Modelling of Waves, 2021.

P. A. Janssen. Nonlinear four-wave interactions and freak waves. *Journal of Physical Oceanography*, 33(4):863–884, 2003.

J. J. Jensen and J. Capul. Extreme response predictions for jack-up units in second order stochastic waves by form. *Probabilistic Engineering Mechanics*, 21(4):330–337, 2006.

I. Karmpadakis and C. Swan. A new crest height distribution for nonlinear and breaking waves in varying water depths. *Ocean Engineering*, 266:112972, 2022.

I. Karmpadakis, C. Swan, and M. Christou. Laboratory investigation of crest height statistics in intermediate water depths. *Proceedings of the Royal Society A*, 475(2229):20190183, 2019.

I. Karmpadakis, C. Swan, and M. Christou. Assessment of wave height distributions using an extensive field database. *Coastal Engineering*, 157:103630, 2020.

V. Katsardi. *Surface water waves in intermediate and shallow water depths*. PhD thesis, Department of Civil and Environmental Engineering, Imperial College London, 2007.

W. Kendall Melville. Energy dissipation by breaking waves. *Journal of Physical Oceanography*, 24(10):2041–2049, 1994.

J. Kim, A. Baquet, and H. Jang. Wave propagation in cfd-based numerical wave tank. In *International Conference on Offshore Mechanics and Arctic Engineering*, volume 58769, page V001T01A008. American Society of Mechanical Engineers, 2019.

S. Kim, B. Bouscasse, G. Ducrozet, M. Canard, G. De Hauteclocque, C. O. Housseine, and P. Ferrant. Numerical and experimental study of a form-based design wave applying the hos-nwt nonlinear wave solver. *Ocean Engineering*, 263:112287, 2022.

C. Kirezci, A. V. Babanin, and D. V. Chalikov. Modelling rogue waves in 1d wave trains with the jonswap spectrum, by means of the high order spectral method and a fully nonlinear numerical model. *Ocean Engineering*, 231:108715, 2021.

E. Kit and L. Shemer. On dissipation coefficients in a rectangular wave tank. *Acta Mechanica*, 77(3):171–180, 1989.

G. J. Komen, L. Cavaleri, M. Donelan, K. Hasselmann, S. Hasselmann, and P. Janssen. Dynamics and modelling of ocean waves. *Dynamics and Modelling of Ocean Waves, by GJ Komen and L. Cavaleri and M. Donelan and K. Hasselmann and S. Hasselmann and PAEM Janssen, pp. 554. ISBN 0521577810. Cambridge, UK: Cambridge University Press, August 1996.*, page 554, 1996.

M. Konar and H. Ding. A sustainable ocean economy for 2050: approximating its benefits and costs. *High Level Panel for a Sustainable Ocean Economy. World Resources Institute*, 2020.

W. Kusumawinahyu, N. Karjanto, and G. Klopman. Linear theory for single and double flap wavemakers. *arXiv preprint arXiv:1703.09445*, 2017.

D. Lagoutte, F. Lefeuvre, and J. Hanasz. Application of bicoherence analysis in study of wave interactions in space plasma. *Journal of Geophysical Research: Space Physics*, 94(A1): 435–442, 1989.

M. Latheef and C. Swan. A laboratory study of wave crest statistics and the role of directional spreading. *Proceedings of the Royal Society A: Mathematical, Physical and Engineering Sciences*, 469(2152):20120696, 2013.

S. Liang, Y. Zhang, Z. Sun, and Y. Chang. Laboratory study on the evolution of waves parameters due to wave breaking in deep water. *Wave motion*, 68:31–42, 2017.

G. Lindgren. Local maxima of gaussian fields. *Arkiv för matematik*, 10(1-2):195–218, 1972.

J. H. List. Wave groupiness variations in the nearshore. *Coastal Engineering*, 15(5-6):475–496, 1991.

E. Lo and C. C. Mei. A numerical study of water-wave modulation based on a higher-order nonlinear schrödinger equation. *Journal of Fluid Mechanics*, 150:395–416, 1985.

M. Longuet-Higgins. On the joint distribution of the periods and amplitudes of sea waves. *Journal of Geophysical Research*, 80(18):2688–2694, 1975.

M. S. Longuet-Higgins. On the statisticaldistribution of the height of sea waves. *JMR*, 11: 245–266, 1952.

W. Lu, J. Li, X. Li, X. Tian, X. Wu, and X. Zhang. Experimental investigation on the statistics of rogue waves under a random wave background. *Ocean Engineering*, 186:106075, 2019.

P. Lubin, S. Vincent, S. Abadie, and J.-P. Caltagirone. Three-dimensional large eddy simulation of air entrainment under plunging breaking waves. *Coastal engineering*, 53(8):631–655, 2006.

J. F. Luxmoore, S. Ilic, and N. Mori. On kurtosis and extreme waves in crossing directional seas: a laboratory experiment. *Journal of Fluid Mechanics*, 876:792–817, 2019.

H. Mase. Groupiness factor and wave height distribution. *Journal of waterway, port, coastal, and ocean engineering*, 115(1):105–121, 1989.

S. R. Massel. *Ocean surface waves: their physics and prediction*, volume 11. World scientific, 1996.

C. C. Mei, M. A. Stiassnie, and D. K.-P. Yue. *Theory and applications of ocean surface waves: Part 1: linear aspects*. World Scientific, 2005.

G. Michel, F. Bonnefoy, G. Ducrozet, G. Prabhudesai, A. Cazaubiel, F. Copie, A. Tikan, P. Suret, S. Randoux, and E. Falcon. Emergence of peregrine solitons in integrable turbulence of deep water gravity waves. *Physical Review Fluids*, 5(8):082801, 2020.

W. Mostert, S. Popinet, and L. Deike. High-resolution direct simulation of deep water breaking waves: transition to turbulence, bubbles and droplets production. *Journal of Fluid Mechanics*, 942:A27, 2022.

H. Nepf, C. Wu, and E. Chan. A comparison of two-and three-dimensional wave breaking. *Journal of Physical Oceanography*, 28(7):1496–1510, 1998.

NWT Preparation Workgroup. Year 1 report. Technical report, JIP on Reproducible CFD Modeling Practice for Offshore Applications, 2019.

M. K. Ochi and C.-H. Tsai. Prediction of occurrence of breaking waves in deep water. *Journal of Physical Oceanography*, 13(11):2008–2019, 1983.

M. Onorato, A. R. Osborne, M. Serio, L. Cavaleri, C. Brandini, and C. Stansberg. Extreme waves, modulational instability and second order theory: wave flume experiments on irregular waves. *European Journal of Mechanics-B/Fluids*, 25(5):586–601, 2006.

M. Onorato, L. Cavaleri, S. Fouques, O. Gramstad, P. A. Janssen, J. Monbaliu, A. R. Osborne, C. Pakozdi, M. Serio, C. Stansberg, et al. Statistical properties of mechanically generated surface gravity waves: a laboratory experiment in a three-dimensional wave basin. *Journal of Fluid Mechanics*, 627:235–257, 2009.

M. Onorato, S. Residori, U. Bortolozzo, A. Montina, and F. Arecchi. Rogue waves and their generating mechanisms in different physical contexts. *Physics Reports*, 528(2):47–89, 2013.

D. H. Peregrine. Water waves, nonlinear schrödinger equations and their solutions. *The ANZIAM Journal*, 25(1):16–43, 1983.

R. Pinguet. *Hydrodynamics of semi-submersible floater for offshore wind turbines in highly nonlinear waves using Computational Fluid Dynamics (CFD), and validation of overset meshing technique in a numerical wave tank*. PhD thesis, Ecole Centrale Marseille, 2021.

M. M. Rienecker and J. D. Fenton. A fourier approximation method for steady water waves. *Journal of Fluid Mechanics*, 104:119–137, 1981. ISSN 14697645. doi: 10.1017/S0022112081002851.

J.-B. Saulnier, A. Clément, F. d. O. António, T. Pontes, M. Prevosto, and P. Ricci. Wave groupiness and spectral bandwidth as relevant parameters for the performance assessment of wave energy converters. *Ocean Engineering*, 38(1):130–147, 2011.

B. R. Seiffert and G. Ducrozet. Simulation of breaking waves using the high-order spectral method with laboratory experiments: wave-breaking energy dissipation. *Ocean Dynamics*, 68(1):65–89, 2018.

B. R. Seiffert, G. Ducrozet, and F. Bonnefoy. Simulation of breaking waves using the high-order spectral method with laboratory experiments: Wave-breaking onset. *Ocean Modelling*, 119: 94–104, 2017.

M. Serio, M. Onorato, A. R. Osborne, P. Janssen, et al. On the computation of the benjamin-feir index. 2005.

L. Shemer and L. Alperovich. Peregrine breather revisited. *Physics of Fluids*, 25(5):051701, 2013.

L. Shemer and A. Sergeeva. An experimental study of spatial evolution of statistical parameters in a unidirectional narrow-banded random wavefield. *Journal of Geophysical Research: Oceans*, 114(C1), 2009.

L. Shemer, A. Sergeeva, and D. Liberzon. Effect of the initial spectrum on the spatial evolution of statistics of unidirectional nonlinear random waves. *Journal of Geophysical Research: Oceans*, 115(C12), 2010.

A. T. Skvortsov, C. Kirezci, D. Sgarioto, and A. V. Babanin. Intermittency of gravity wave turbulence on the surface of an infinitely deep fluid: Numerical experiment. *Physics Letters A*, 449:128337, 2022.

C. T. Stansberg. Wave front steepness and influence on horizontal deck impact loads. *Journal of Marine Science and Engineering*, 8(5):314, 2020. ISSN 20771312. doi: 10.3390/JMSE8050314.

G. G. Stokes. On the theory of oscillatory waves. *Trans. Cam. Philos. Soc.*, 8:441–455, 1847.

S. Støle-Hentschel, K. Trulsen, L. B. Rye, and A. Raustøl. Extreme wave statistics of counter-propagating, irregular, long-crested sea states. *Physics of Fluids*, 30(6):067102, 2018.

T. Tang and T. A. Adcock. The influence of finite depth on the evolution of extreme wave statistics in numerical wave tanks. *Coastal Engineering*, 166:103870, 2021.

T. Tang, D. Barratt, H. B. Bingham, T. S. van den Bremer, and T. A. Adcock. The impact of removing the high-frequency spectral tail on rogue wave statistics. *Journal of Fluid Mechanics*, 953:A9, 2022.

S. Tavakoli, D. Khojasteh, M. Haghani, and S. Hirdaris. A review on the progress and research directions of ocean engineering. *Ocean Engineering*, 272:113617, 2023.

M. A. Tayfun. Distribution of large wave heights. *Journal of waterway, port, coastal, and ocean engineering*, 116(6):686–707, 1990.

M. A. Tayfun and F. Fedele. Wave-height distributions and nonlinear effects. *Ocean engineering*, 34(11-12):1631–1649, 2007.

Z. Tian, M. Perlin, and W. Choi. Evaluation of a deep-water wave breaking criterion. *Physics of Fluids*, 20(6):066604, 2008.

Z. Tian, M. Perlin, and W. Choi. Energy dissipation in two-dimensional unsteady plunging breakers and an eddy viscosity model. *Journal of fluid mechanics*, 655:217–257, 2010.

Z. Tian, M. Perlin, and W. Choi. An eddy viscosity model for two-dimensional breaking waves and its validation with laboratory experiments. *Physics of Fluids*, 24(3):036601, 2012.

A. Toffoli, A. Babanin, M. Onorato, and T. Waseda. Maximum steepness of oceanic waves: Field and laboratory experiments. *Geophysical Research Letters*, 37(5), 2010.

A. Toffoli, G. Ducrozet, T. Waseda, M. Onorato, M. Abdolahpour, and F. Nelli. Ocean currents trigger rogue waves. In *The 29th International Ocean and Polar Engineering Conference*. OnePetro, 2019.

H. L. Tolman et al. User manual and system documentation of wavewatch iii tm version 3.14. *Technical note, MMAB Contribution*, 276(220), 2009.

P. S. Tromans, A. R. Anaturk, and P. Hagemeijer. A new model for the kinematics of large ocean waves-application as a design wave. In *The first international offshore and polar engineering conference*. OnePetro, 1991.

K. Trulsen and K. B. Dysthe. A modified nonlinear schrödinger equation for broader bandwidth gravity waves on deep water. *Wave motion*, 24(3):281–289, 1996.

M. Tucker, P. G. Challenor, and D. Carter. Numerical simulation of a random sea: a common error and its effect upon wave group statistics. *Applied ocean research*, 6(2):118–122, 1984.

Unctad. *Review of maritime transport 2022*. UN, 2022.

S. van Essen and W. Lafeber. Wave-induced current in a seakeeping basin. In *International Conference on Offshore Mechanics and Arctic Engineering*, volume 57748, page V07BT06A021. American Society of Mechanical Engineers, 2017.

D. A. Walker, P. H. Taylor, and R. E. Taylor. The shape of large surface waves on the open sea and the draupner new year wave. *Applied Ocean Research*, 26(3-4):73–83, 2004.

L. Wang, A. Robertson, J. Kim, H. Jang, Z. R. Shen, A. Koop, T. Bunnik, and K. Yu. Validation of CFD simulations of the moored DeepCwind offshore wind semisubmersible in irregular waves. *Ocean Engineering*, 260:112028, 2022. ISSN 00298018. doi: 10.1016/j.oceaneng.2022.112028.

P. Welch. The use of fast fourier transform for the estimation of power spectra: a method based on time averaging over short, modified periodograms. *IEEE Transactions on audio and electroacoustics*, 15(2):70–73, 1967a.

P. D. Welch. The Use of Fast Fourier Transform for the Estimation of Power Spectra: A Method Based on Time Averaging Over Short, Modified Periodograms. *IEEE Transactions on Audio and Electroacoustics*, 15(2):70–73, 1967b. ISSN 00189278. doi: 10.1109/TAU.1967.1161901.

B. J. West, K. A. Brueckner, R. S. Janda, D. M. Milder, and R. L. Milton. A new numerical method for surface hydrodynamics. *Journal of Geophysical Research: Oceans*, 92(C11):11803–11824, 1987.

V. E. Zakharov and A. B. Shabat. Exact theory of two-dimensional self-focusing and one-dimensional self-modulation of waves in nonlinear media. *Zh. Eksp. Teor. Fiz*, 61(1):118–134, 1971.

V. E. Zakharov, V. S. L'vov, and G. Falkovich. *Kolmogorov spectra of turbulence I: Wave turbulence*. Springer Science & Business Media, 2012.

Appendix

APPENDIX A

LIST OF THE EXPERIMENTAL CAMPAIGNS

This appendix summarizes the experimental campaigns that were conducted. The experiments are labeled in Table A.1, and the probe positions are illustrated in Fig. A.1 and A.2.

Table A.1 – List of the experimental campaigns

Campaign Label	Date	Tank	Generated Sea States
A	June / July 2020	Towing	`ss6g5`; `ss6`; `GOM`
B	August 2020	Ocean Engineering	`ss6`; `GOM`
C	April / May 2021	Ocean Engineering	`ss6g5`; `ss6`; `GOM`
D	February / Mars 2022	Towing	`ss6g5`; `ss6`; `GOM`
E	July 2022	Towing	`ss6`; `GOM`
F	July 2023	Ocean Engineering	`ss6g5`

In addition, Table A.2 provides a listing of the generated wave series. In this context, a "wave series" refers to a set of realizations characterized by i) an input spectrum (i.e. same target sea state and same correction adapted to X_t), ii) a scale, and iii) a tank domain. Approximately 30 realizations were generated for each wave series. The duration of a realization is approximately equivalent to 3 hours at full scale. This corresponds to 15 to 20 minutes at the model scale. The resulting total analysis duration T_{analyzed} is provided in the Table. Concomitantly, for most of the cases, numerical simulations based on `HOS-NWT` were run to replicate the experiments.

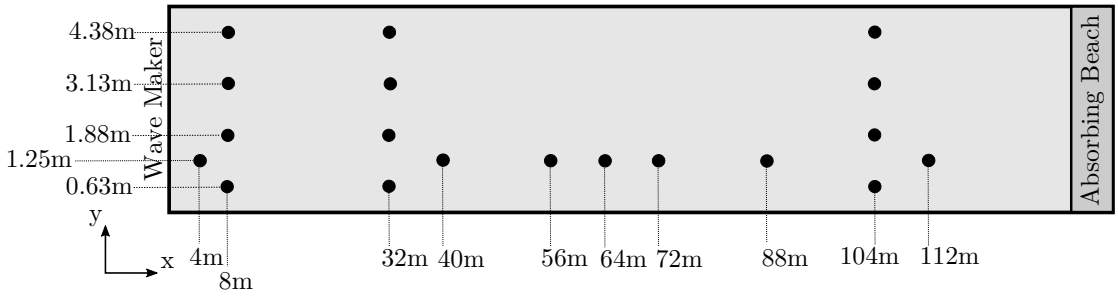

(a) Campaign A (Towing tank)

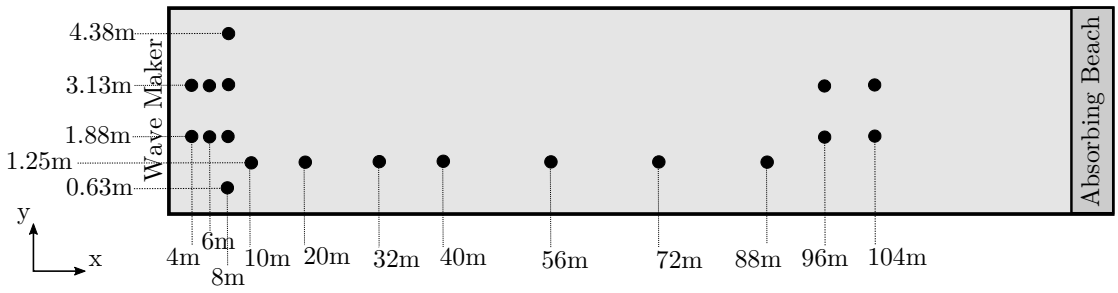

(b) Campaign D (Towing tank)

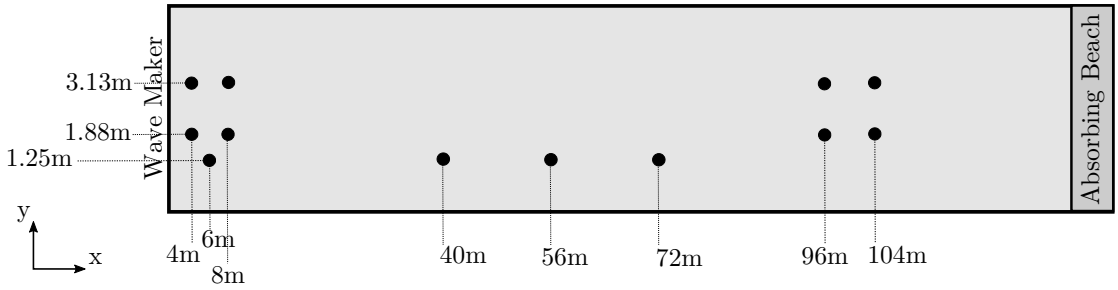

(c) Campaign E (Towing Tank)

Figure A.1 – Wave gauges positions of Towing tank campaigns.

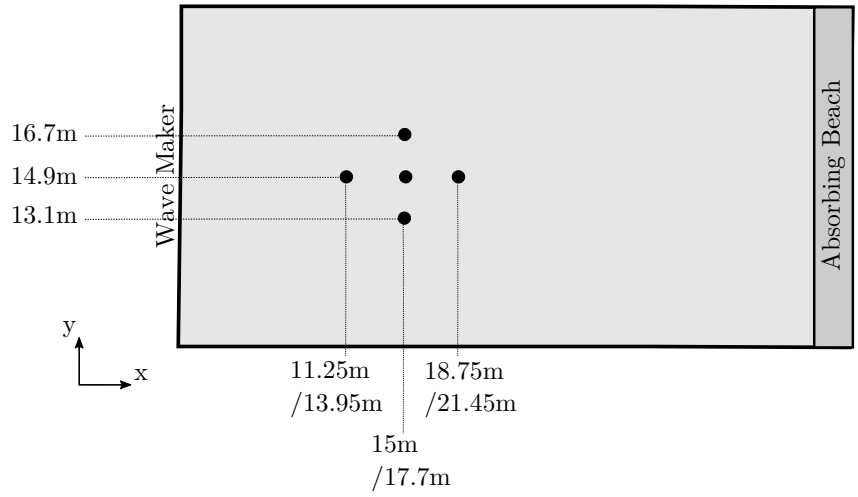

(a) Campaign B (O. E. tank)

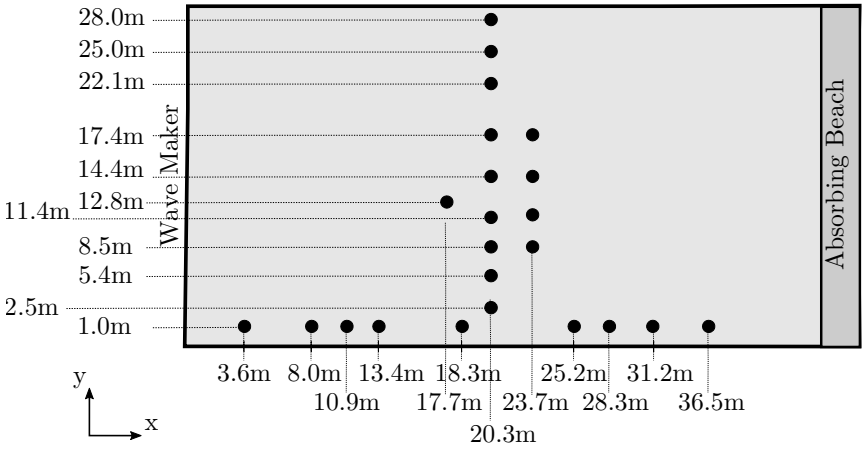

(b) Campaign C (O. E. tank)

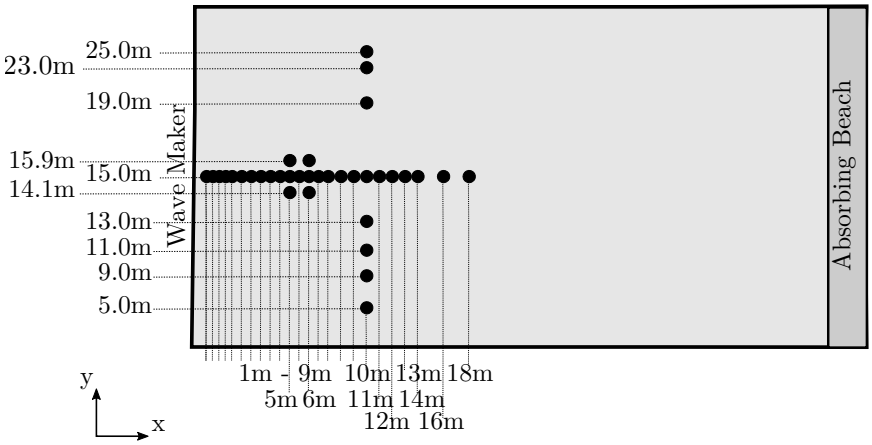

(c) Campaign F (O. E. tank)

Figure A.2 – Wave gauges positions of O.E. tank campaigns.

Table A.2 – Generated wave series. "Spect. Control" and "Stat. Control" are the spectrum and statistics control procedures introduced in Sec. 7.1 and 8.1 . "Stat. Control" procedure uses two target locations: "X_t" (the position of interest) and "$X_{t_{\text{stat}}}$" (the position used to build the target crest distribution).

Sea state	Scale	Tank	Spect. Control	Stat. Control	X_t	$X_{t_{\text{stat}}}$	HOS twin	T_{analyzed}	Campaign
GOM	188	Towing	No	No	\	\	No	$3000T_p$	D
GOM	188	Towing	Yes	No	$2\lambda_p$	\	Yes	$3000T_p$	D
GOM	94	Towing	No	No	\	\	No	$3000T_p$	D/E
GOM	94	Towing	Yes	No	$2\lambda_p$	\	Yes	$18000T_p$	D
GOM	94	O. E.	No	No	\	\	No	$14000T_p$	C/F
GOM	94	O. E.	Yes	No	$2\lambda_p$	\	Yes	$14000T_p$	C
GOM	94	O. E.	Yes	No	$6.6\lambda_p$	\	No	$14000T_p$	C
GOM	50	O. E.	Yes	No	$2\lambda_p$	\	Yes	$18000T_p$	B
ss6g5	120	Towing	No	No	\	\	No	$6000T_p$	A
ss6g5	120	Towing	Yes	No	$4\lambda_p$	\	No	$15000T_p$	A
ss6g5	120	Towing	Yes	No	$16\lambda_p$	\	No	$21000T_p$	A
ss6g5	120	Towing	Yes	No	$53\lambda_p$	\	Yes	$12000T_p$	D
ss6g5	120	Towing	Yes	Yes	$53\lambda_p$	$4\lambda_p$	Yes	$12000T_p$	D
ss6g5	120	Towing	Yes	Yes	$4\lambda_p$	$53\lambda_p$	Yes	$12000T_p$	D
ss6g5	60	O. E.	Yes	Yes	$4\lambda_p$	$53\lambda_p$	Yes	$20000T_p$	F
ss6	40	O. E.	Yes	No	$3\lambda_p$	\	Yes	$20000T_p$	B
ss6	40	Towing	Yes	No	$3\lambda_p$	\	Yes	$400T_p$ (repeat test)	A/D/E

COLLEGE SCIENCES
DOCTORAL DE L'INGENIERIE
PAYS DE LA LOIRE ET DES SYSTEMES

CENTRALE NANTES

Titre : Génération contrôlée d'états de mer irréguliers unidirectionnels dans des bassins d'essais et des simulations numériques

Mot clés : Bassin d'essais, spectre de houle, distribution de hauteur de crête, conditions de vagues, hydrodynamique, génie océanique

Résumé : L'objectif de cette thèse est d'améliorer les procédures de génération et de qualification des vagues pour les études de génie océanique. Le cadre est limité aux états de mer unidirectionnels générés dans des bassins d'essais expérimentaux et numériques. Les campagnes expérimentales ont été réalisées dans les bassins de l'ECN et les études numériques à l'aide du solveur `HOS-NWT` développé par l'ECN.

Dans la première partie de la thèse, la propagation des états de mer dans les bassins d'essais est abordée d'un point de vue théorique, expérimental et numérique. Une attention particulière est accordée à l'évolution spatiale du spectre et des statistiques. En outre, les incertitudes expérimentales sont étudiées en détail.

La deuxième partie de la thèse se concentre sur le contrôle des champs de vague à n'importe quelle position cible dans le domaine. Tout d'abord, une procédure axée sur la qualité du spectre de houle est étudiée. Ensuite, face à l'influence de la position cible sur les statistiques, une nouvelle procédure est introduite. Elle permet de mieux contrôler les distributions statistiques, indépendamment de la position cible.

Title: Controlled generation of unidirectional irregular sea states in experimental and numerical wave tanks

Keywords: Wave tank, wave spectrum, crest distribution, wave condition, hydrodynamics, ocean engineering

Abstract: The objective of this thesis is to improve the wave generation and qualification procedures in the context of ocean engineering studies. The framework is limited to unidirectional irregular sea states generated in experimental and numerical wave tanks. Experiments were carried out using the ECN facilities and numerical studies were performed using the nonlinear potential wave solver `HOS-NWT` developed by ECN.

In the first part of the thesis, the problem of irregular wave propagation in wave tank environments is addressed from theoretical, experimental, and numerical points of view. Paticular attention is paid to the evolution in space of the wave spectrum and statistics. In addition, experimental uncertainties are studied in detail.

The second part of the thesis focuses on developing methods to better control the wave fields at any target position in the domain. First, a procedure focusing on the quality of the wave spectrum is studied. Then, facing the dependence of the wave statistics on the target location, a new procedure is developed and tested to better control the statistical distributions independently of the target location.